Development of new highly conjugated molecules and their application in the field of renewable energy and biomaterials

Matteo Bessi

UNIVERSITÉ DE STRASBOURG

ÉCOLE DOCTORALE DES SCIENCES CHIMIQUES

ISIS UMR 7006

THÈSE présentée par :

Matteo BESSI

soutenue le : **06 Décembre 2018**

pour obtenir le grade de : **Docteur de l'université de Strasbourg**

Discipline/ Spécialité : Sciences Chimiques

Development of new highly conjugated molecules and their application in the field of renewable energy and biomaterials

THÈSE dirigée par :

Mme DE COLA Luisa	Professeur, Université de Strasbourg
M. TADDEI Maurizio	Professeur, Università degli Studi di Siena (Italie)

RAPPORTEURS :

Mme COLACINO Evelina	Professeur Associé, Institut Charles Gerhardt Montpellier
M. MAGGINI Michele	Professeur, Università di Padova (Italie)

AUTRES MEMBRES DU JURY :

M. MORDINI Alessandro	Directeur de Recherche, Istituto di Chimica dei Composti OrganoMetallici del CNR (Italie)
M. LAFOLET Frédéric	Maître de Conférences, Université Paris Diderot

Table of Contents

Development of Polyamidoamine Hydrogels: Towards New Stimuli-Responsive Materials

Chapter 3 - Introduction and Aim of the Work

Chapter 4 – Conductive Hydrogels

Chapter 5 – Light-Responsive Hydrogels

Annex

Résumé de Thèse

Développement de nouvelles molécules hautement conjuguées et leurs applications dans le domaine des énergies renouvelables et des biomatériaux

Ce travail se concentre sur le développement et l'incorporation de molécules conjuguées à de nouveaux matériaux fonctionnels hybrides qui seront utilisés dans une série d'applications de hautes technologies allant de capteurs bio/médicaux, à la production d'énergie renouvelable. Les deux sujets principaux de la thèse sont la synthèse de nouveaux colorants organiques pour des cellules solaires à pigment photosensibleet le développement de nouveaux hydrogels à base de polyamidoamines sensibles aux stimuli.

Développement de nouveaux colorants organiques pour des applications energétiques

- **Introduction**

Les cellules solaires à pigment photosensible (CSPP), introduits pour la première fois en 1991 par Grätzel et O'Regan,[1] ont été l'objet d'une attention croissante ces dernières années pour leur potentiel comme nouvelle photovoltaïque technologie et l'intérêt de la recherche à l'amélioration de leur efficacité et stabilité a considérablement augmenté.[2] Dans une CSPP, la lumière solaire est récoltée par des pigments, liés à un semi-conducteur grâce à un pont moléculaire. Après photoexcitation, le pigment injecte les électrons dans la bande de conduction du semi-conducteur, permettant de générer un photocourant externe à travers le dispositif. Pour ces raisons, le pigment joue un rôle clé pour la performance énergétique globale (Figure 1). Un grand nombre de colorants organiques sans métaux ont été employés dans ces dispositifs, et la plupart des colorants possèdent une structure D-π-A. Cette classe de colorants a été intensivement étudiée depuis de nombreuses années comme sensibilisateurs pour la production de dispositif CSPP[3] en raison de leur faible coût de production, leur coefficient d'extinction molaire élevé et la possibilité d'ajuster finement leur propriétés photophysiques et électrochimiques en optimisant de leur structure moléculaire.[4] Cette dernière caractéristique dépend dans la structure de bloc particulière possédée par ces pigments caractérisés par un groupe doneur riche en électrons (D) et un groupe accepteur pauvre en électrons (A), connecté par un espaceur conjugué. Chacunes de ces parties des pigments D-π-A peut être facilement modifié sans altérer les deux autres. [2,4] Ces sensibilisateurs devront être fixés sur les semi-conducteurs, afin de exploiter le processus d'injection électronique, donc un groupe d'ancrage est nécessaire et dans presque tous les cas il est coïncident avec le groupe accepteur.

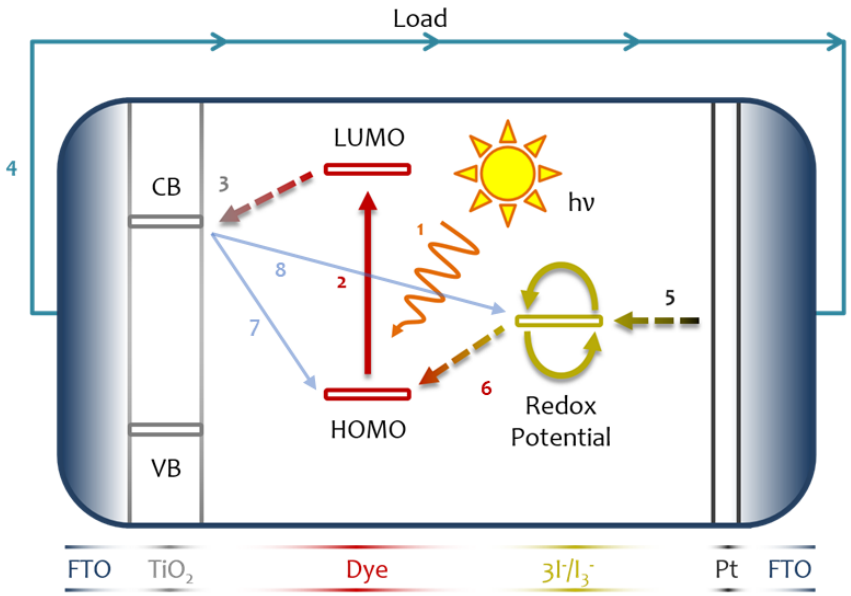

Figure 1 Processus photoélectrochimiques impliqués dans le mécanisme de travail d'un CSPP.

Le photo-reformage de matières premières renouvelables, où un composé organique agit comme un donneur d'électrons sacrificiel, promet d'être un processus valable et durable pour la production d'hydrogène.[5] TiO_2, à cause de ses bonnes propriétés, est l'un des matériaux plus étudiés pour ce type d'applications et certains systèmes tandem avec co-catalyseurs métalliques particuliers ont déjà démontré de bons résultats. Cependant, le dioxyde de titane n'est pas en mesure d'absorber la lumière visible et cela peut réduire l'efficacité de tout le processus. Pour surmonter ce problème, une possibilité est d'améliorer la récolte de lumière du système par la sensibilisation du TiO_2 avec un colorant capable d'absorber la lumière visible. Après la photoexcitation, le colorant peut injecter un électron dans le semi-conducteur (doté d'un catalyseur approprié) afin d'exploiter la réduction de l'eau à H_2 (Figure 2).[6]

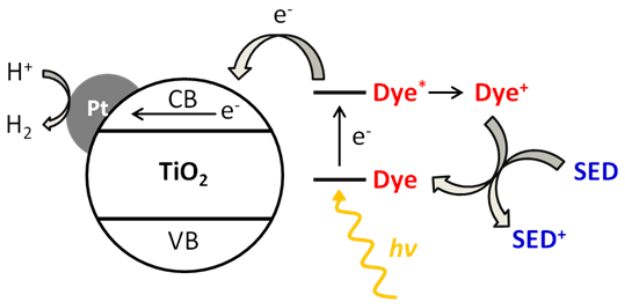

Figure 2 Représentation graphique du mécanisme de travail pour la production de H_2 sur un photocatalyseur Pt/TiO_2 sensibilisés par un pigment.

Une partie de ce travail est concentrée sur l'étude des propriétés photophysiques de pigments D-π-A particuliers développés précédemment dans notre groupe de recherche et caractérisés par la présence d'un fragment alkoxysilane dans le groupe accepteur, récemment reconnu comme l'un des groupes d'ancrage le plus stable et performant pour la CSPP.[7] Leurs propriétés photophysiques ont été analysées par spectroscopie d'absorption transitoire et ensuite leurs performances ont été évaluées sur des dispositifs réels. De plus, en raison de l'absence d'une manière simple et générale d'introduire le groupe siloxanes dans ces pigments (Figure 3), il convient de développer une méthode de synthèse alternative pour introduire sur un groupe cyanoacrylique un groupe d'ancrage silylé différent, mais ayant les même propriétés avantageuses du groupe siloxane, le silatrane (Figure 3d).

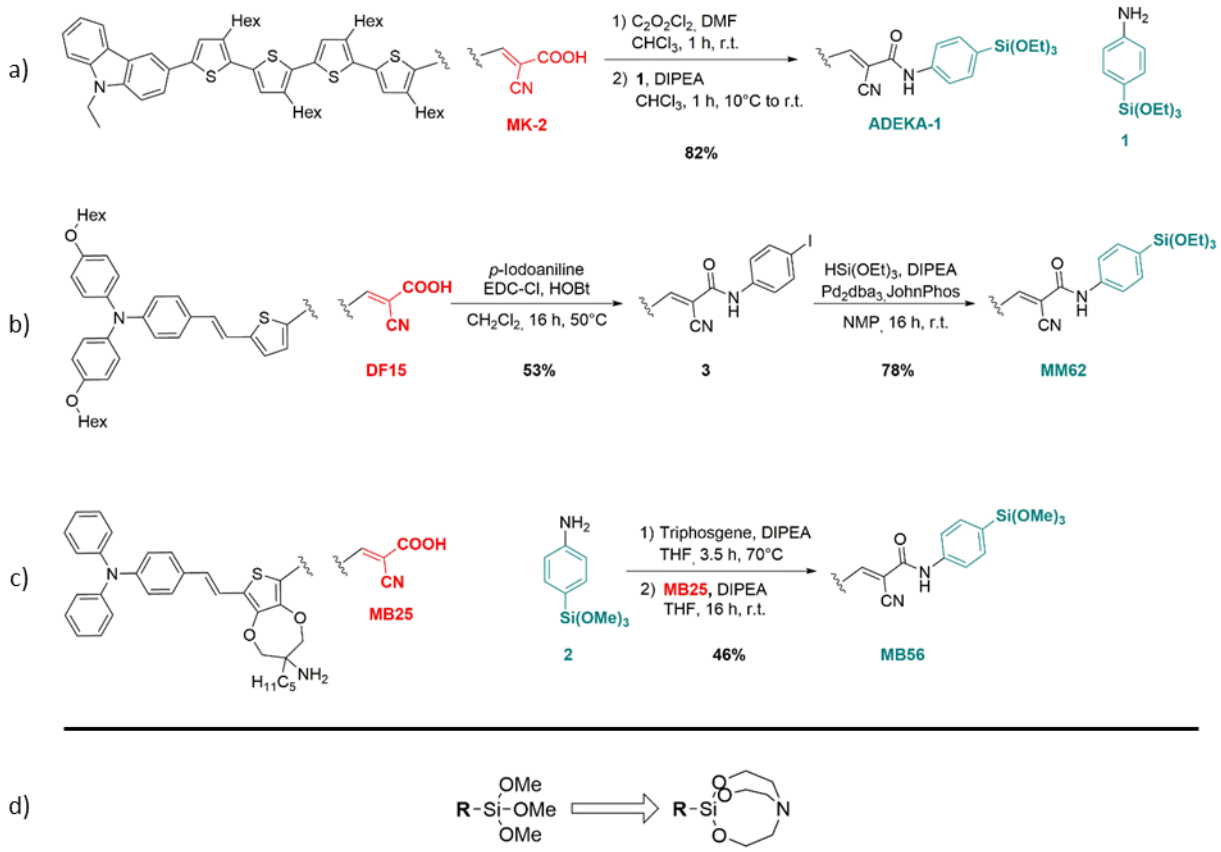

Figure 3 (a), (b), (c) Différentes voies synthétiques développées pour l'introduction du groupe siloxanes;[8](d) structure du groupe silatrane.

Ensuite, certains pigments qui ont déjà été développés pour la CSPP, donc déjà optimisés en terme d'injection d'électrons dans la couche de TiO_2, ont été testés comme photosensibilisateurs pour la production de H_2 par photo-reformage. L'intérêt pour ces pigments s'est accru au cours des dernières années, en particulier des études ont été menées sur l'effet de la structure moléculaire du pigment sur les performances globales du système, même si des études précises sur la corrélation entre la modification introduite et l'augmentation des performances sont toujours manquantes. Nous avons ensuite décidé de tester une série de pigments D-π-A ayant sur différentes positions de leur squelette plusieurs chaînes alkyles afin de tenter de corréler leur structure avec les performances du pigment pour la production du H_2, en utilisant le classique triéthanolamine (TEOA) comme donner d'électrons sacrificiel (DES).

- **Résultats et Discussion**

Les propriétés optiques et électrochimiques des pigments siloxanes et des acides cynoacryliques correspondants (Figure 4) ont été analysées afin de démontrer la possibilité de les utiliser dans des dispositifs CSPP. En particulier, leurs propriétés optiques ont été analysées tant à l'état d'équilibre, qu'avec une spectroscopie d'absorption transitoire, dans divers solvants, et après sensibilisation sur un film de TiO_2 nanocristallin. La caractérisation à l'état d'équilibre a montré comment la modification introduite sur le groupe d'ancrage avait un effet mineur sur les propriétés d'absorption du système (Tableau 1), donc des spectres d'absorption transitoire de tous les composés ont été enregistrés pour analyser aussi les propriétés d'injection d'électrons dans le semi-conducteur.

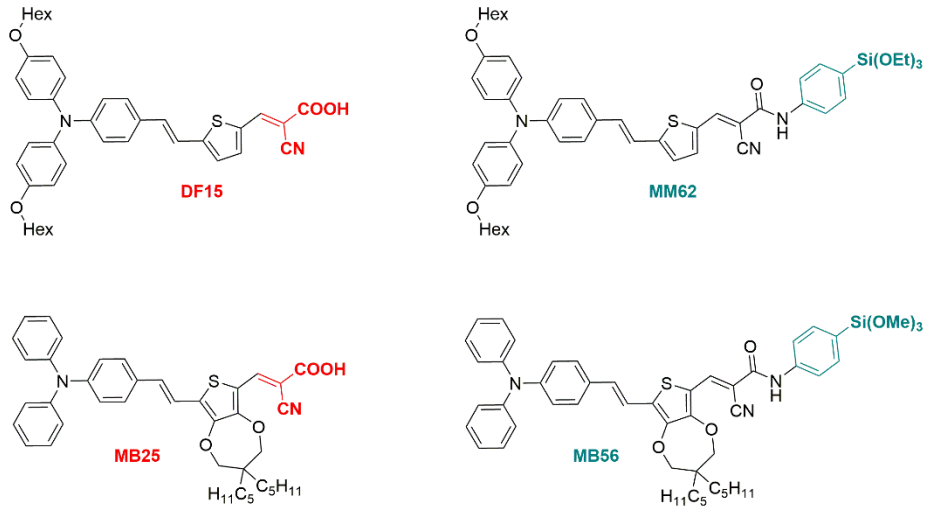

Figure 4 Structure des pigments cyanoacrylates et siloxanes analysés.

Des techniques de spectroscopie avec résolution temporelle rapides et ultra-rapides ont été utilisées pour déterminer les constantes de vitesse et les rendements quantiques des processus individuels qui se déroulent sur des films de TiO_2 sensibilisés.[9] Nous avons ensuite décidé d'enregistrer les spectres d'absorption transitoire de nos pigments, en utilisant des solvants de polarité et de polarisabilité différents, afin d'examiner l'effet de l'environnement sur les propriétés électroniques du système. L'analyse quantitative des données obtenues a été réalisée afin d'obtenir tant les constantes cinétiques, nécessaires pour décrire l'évolution dynamique du système, que les contributions spectrales correspondantes (spectres de désintégration associés à l'évolution, "EADS").[10] Pour tous les pigments (en particulier pour **DF15**), les propriétés du solvant ont démontré qu'ils avaient beaucoup d'influence sur les temps de vie des états excités et sur les formes spectrales, mais nous n'avons pas observé de différence de comportement suffisante entre les colorants siloxanes et les cyanoacrylates correspondants. Des films de TiO_2 sensibilisés avec les pigments utilisés ont été ensuite réalisés et analysés. Le temps de vie de l'état excité augmente significativement lors de l'absorption à la surface du semi-conducteur (indication de l'occurrence de l'injection électronique) et la forme spectrale de la bande d'absorption de l'état excité était qualitativement similaire pour tous les pigments (Figure 5, à gauche). Sur la base d'études antérieures concernant des colorants D-π-A similaires à **DF15**[11] et sur la comparaison entre les formes spectrales normalisées du EADS mesurées dans des solvants et sur TiO_2, la bande de l'état excité comprise dans la région 700-750 nm a été associé à la formation du cation radicalaire du pigment après de l'injection électronique dans le substrat semi-conducteur. Notamment, alors que cette bande est clairement visible dans les spectres de **DF15** et **MB25**, pour ceux des pigments silylés **MM62** et **MB56**, une seule bande très faible était présente, ce qui suggère une contribution mineur du radical cation.

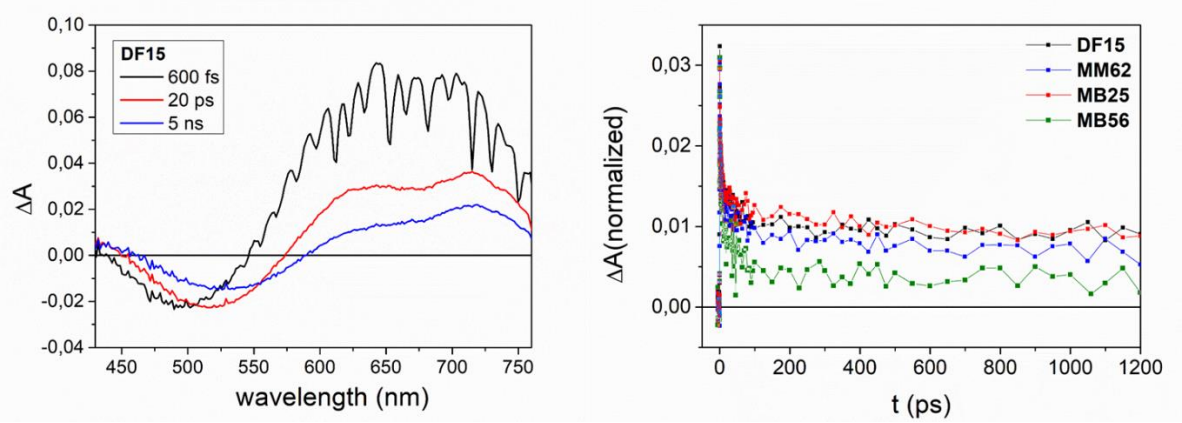

*Figure 5 (à gauche) Exemple de spectre EDAS enregistré pour le pigment **DF15** sur le film de TiO_2 et (à droite) comparaison entre les traces cinétiques normalisées des spectres EDAS relatifs enregistrés à 720 nm pour les différents colorants.*

L'analyse des traces cinétiques à une longueur d'onde >700 nm, fournit des informations sur la cinétique de recombinaison semi-conducteur-pigment et sur la quantité d'électrons injectés dans la bande de conduction du substrat. Ensuite, la quantité relative du décalage constant mesuré à >700 nm (qui peut être connectée à la quantité d'électrons injectés dans la bande conductrice du semi-conducteur[12]) a été comparée. Comme indiqué à la Figure 5 (à droite), **DF15** et **MB25** ont montré les signes résidus les plus intenses, pendant que les deux pigments silylés ont présenté une constante de décalage inférieure. Les résultats des mesures résolues en temps suggèrent que les modifications introduites sur le groupe d'ancrage pourraient affecter l'efficacité des cellules solaires préparées avec les pigments silylés en raison de la plus grande impact du processus de recombinaison, en réduisant l'efficacité de l'injection électronique si on les compare aux pigments cyanoacryliques correspondants.

Tableau 1 Résumé des propriétés photochimiques des pigments analysés et de leurs performances sur des dispositifs CSPP.

Pigment	**ε (M^{-1} cm^{-1})**	**$\lambda_{max\ abs}$ (nm)**	**$\lambda_{max\ abs.}$ sur TiO_2 (nm)**	**E_{ox} (V)**	**E_{0-0} (eV)**	**V_{oc} (mV)**	**J_{sc} (mA/cm²)**	**ff (%)**	**η (%)**
DF15[a]	34000	528	458	+0.94	2.05	686	10.86	67	4.97
MM62	24000	520	501	-	2.13	514	1.03	68	0.36
MB25	28000	514	456	+1.03	2.50	660	11.99	60	4.80
MB56	24000	510	478	+1.00	2.48	560	2.20	69	0.86
[a] Valeurs prises par la ref. 13									

Enfin, les deux pigments silylés ont été testés sur des dispositifs CSPP, et ont montré des efficacités nettement inférieures à celles des acides cyanoacryliques correspondants, contrairement à ce qui est rapporté dans la littérature scientifique pour des composés similaires.[8a] D'autre part, ces résultats sont cohérents avec ce que nous avons observé durant les expériences de spectroscopie d'absorption transitoire qui nous montrent un taux d'injection électronique plus faible et un taux de recombinaison plus rapide pour les pigments silylés après sensibilisation sur la surface de TiO_2, ce qui justifie les performances plus médiocres que leurs équivalents cyanoacryliques. Les excellents résultats obtenus par Kakiage *et al.*[8a] pourrait s'expliquer par le procédé de fabrication de cellules extrêmement raffiné qu'ils ont utilisé, comprenant l'utilisation d'une solution électrolytique complexe et de plusieurs traitements de la couche de TiO_2. Ces observations ont été indirectement confirmées par les travaux de Ziółek *et al.* sur les facteurs affectant les performances des groupes d'ancrages silylé sur CSPP.[14]

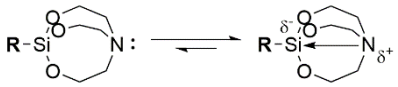

Figure 6 Liaison trans-annulaire du groupe silatrane.

Il était donc impératif de trouver un groupe alternatif au siloxane, capable de montrer les mêmes bonnes propriétés d'ancrage au TiO_2 mais en même temps qui se prête à une insertion beaucoup plus simple dans la structure du pigment. Le groupe choisi est le silatrane et, après la synthèse du squelette silatrane approprié (**4**), son introduction par couplage peptidique sur une série d'acides cyanoacryliques a été étudiée (Figure 7). La réaction a été favorisée par la structure particulière de la cage du silatrane, dans laquelle une liaison dative trans-annulaire de l'azote à l'atome de silicium, produit une espèce de silicium riche en électrons et formellement penta-coordonnée, ainsi qu'une structure plus stable[15] (Figure 6). Après une brève optimisation, la réaction s'est avérée beaucoup prometteuse et tous les pigments silatranes désirés ont été obtenus dans des bons rendements et des bonnes puretés.

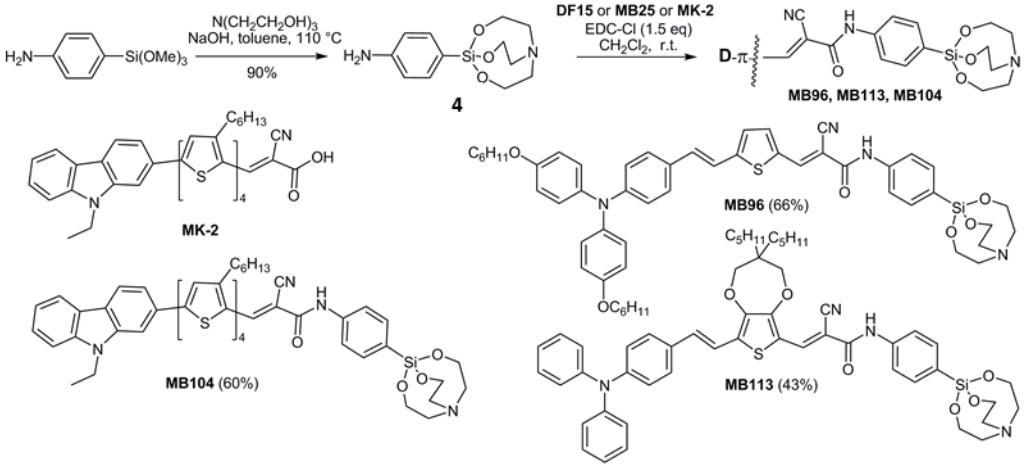

Figure 7 Synthèse et structure des nouveaux pigments silatrane.

Ensuite, une comparaison entre les propriétés spectroscopiques et d'ancrage des deux groupes a été réalisée par spectroscopie UV-Vis (en solution et après sensibilisation des pigments sur des films de TiO_2) et ATR FT-IR. Tous les pigments ont un large spectre d'absorption de la lumière et de bons coefficients d'extinction molaires; en solution de DCM (Figure 8), des valeurs très proches des maximaux d'absorption (λ_{max}) ont été observées pour tout la série, avec seulement un léger décalage vers le bleu passant de l'acide (**DF15**, **MB25**) au siloxane (**MM62**, **MB56**) et puis au silatrane (**MB96**, **MB113**). Les spectres UV des pigments absorbés sur TiO_2 sont présentés en Figure 8. Tous les pigments présentent un profil d'absorption beaucoup plus large par rapport aux spectres enregistrés en solution. Les caractéristiques d'absorption des deux classes différentes de pigments silylés après adsorption sur TiO_2 sont presque identiques, renforçant l'hypothèse selon laquelle des espèces très similaires, sinon identiques, se forment à la surface du semi-conducteur après sensibilisation avec des pigments trialkoxysilanes et silatranes.

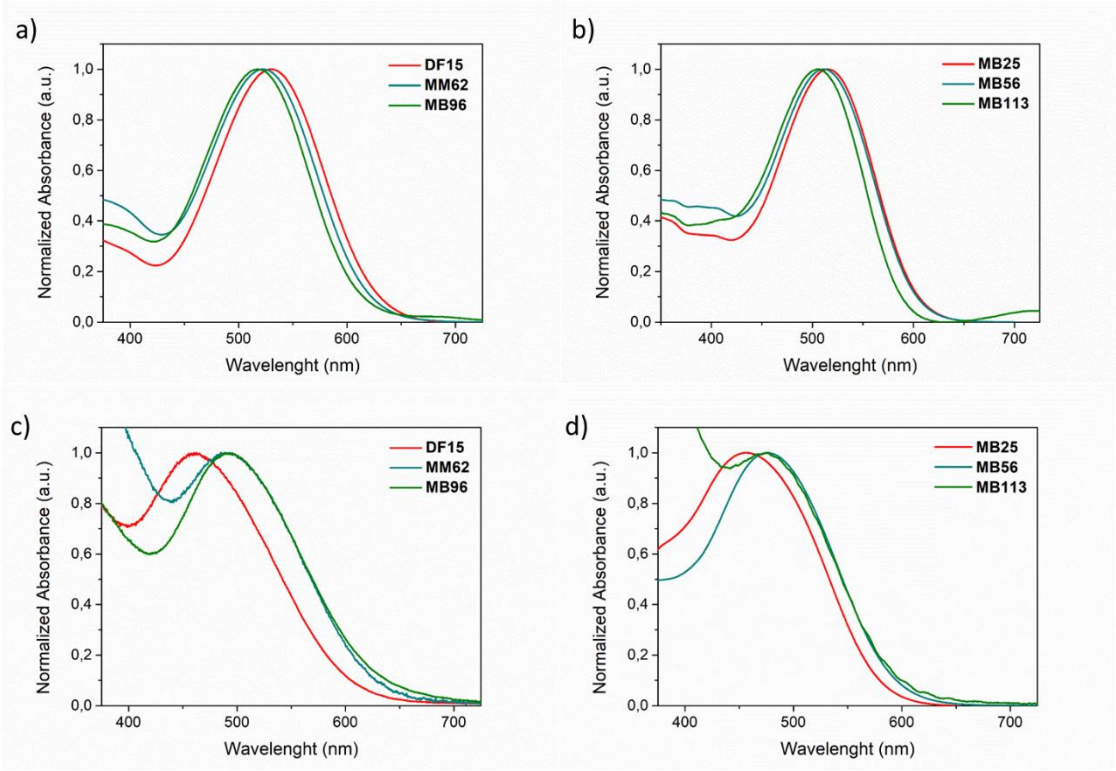

Figure 8 Spectres d'absorption UV des pigments analysés (a, b) dans une solution de DCM et (c, d) sur un film de TiO_2 après sensibilisation.

Une étude FT-IR ATR (réflectance totale atténuée) a été réalisée ensuite pour explorer la nature de la liaison établie entre les pigments et le TiO_2. La comparaison entre les spectres des deux pigments silylés **MM62** et **MB96** est remarquable: leur superposition presque parfaite (Figure 9, à droite) suggère fortement que les espèces formées sur la surface du semi-conducteur pour les deux pigments après la sensibilisation sont les mêmes. La dernière étape consiste à évaluer la stabilité relative des deux groupes d'ancrage à la surface du TiO_2. Pour ce faire, une étude de désorption en milieu aqueux a été faite et a montré qu'après seulement 30 min, plus de 60% de l'acide cyanoacrylique était éliminé du film deTiO_2, presque aucune désorption ne peut être observée pour les pigments silylés (Figure 9, à gauche).

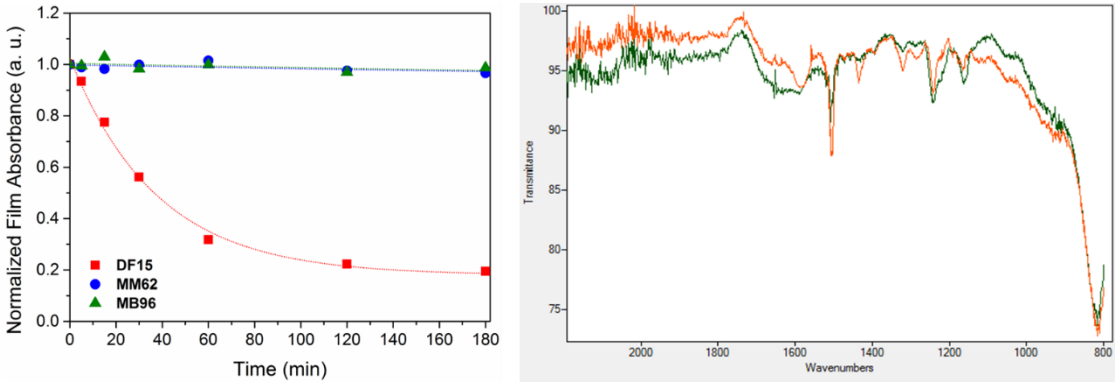

*Figure 9 (à gauche) Variation de l'absorption relative des films de TiO_2 sensibilisés avec les composés **DF15** (carrés rouges), **MM62** (cercles bleus) et **MB96** (triangles verts) après de l'exposition à la solution de désorption à 60°C; (à droite) comparaison entre les spectres FT-IR des colorants **MM62** (vert) et **MB96** (orange) après de l'ancrage sur le semi-conducteur, zoom sur la partie du spectre entre 2200 et 800 cm^{-1}.*

Ensuite, une série de pigments D-π-A avec différentes chaînes alkyles sur leur structure a été testée pour la production de H_2, en utilisant le classique TEOA comme SED (Figure 10). Le pigmentt **D5** est bien connu pour son utilisation dans les CSPP[16] et il a déjà été utilisé dans des systèmes photocatalytiques pour la

production de H_2.[17] Pour cette raison, **D5** a été utilisé comme référence et il a été comparé à trois autres pigments, **DF15**, **MB25** et **AD418**. Ces pigments ont été conçus en introduisant des modifications structurelles sur la structure du composé **D5**, telles que l'introduction de substituants riches en électrons ou des modifications sur l'espaceur π (qui peuvent influencer les propriétés d'absorption de la lumière), ou l'introduction de longues chaînes alkyles (qui en revanche peut influencer l'agrégation entre les molécules de pigment et leur effet de protection de la surface du TiO_2[18]). Les performances photocatalytiques de tous les pigments ont été comparées à la position de la fraction hydrophobe sur le squelette moléculaire de chaque structure. Avant tout, les propriétés optiques et électrochimiques de tous les pigments ont été évaluées afin de déterminer si elles sont appropriées à cette application particulière. Tous les pigments se sont révélés capables d'être utilisés pour les expériences de production d'H_2, présentant des coefficients molaires d'extinction élevés, des spectres d'absorption larges et des propriétés électrochimiques appropriées.

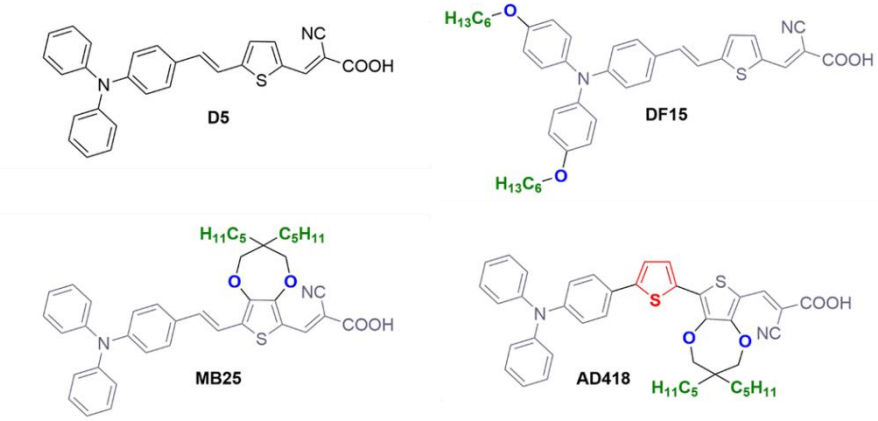

Figure 10 Différences structurelles entre les pigments testés pour la production du H_2.

Ensuite, l'expérience de production de H_2 a été réalisée. Tous les pigments ont montré une augmentation initiale du taux de production de H_2 lors des premières 1-2 heures, suivi d'une stabilisation du taux sur le long terme. Pendant que **D5** et **DF15** ont présenté une production de H_2 similaire et modérée, **MB25** et **AD418** ont montré de meilleures performances tant en termes de quantité d'H_2 produite, ainsi que de meilleurs TON, confirmant l'hypothèse selon laquelle la présence de longues chaînes alkyle sur l'espacer π (plus proche du semi-conducteur) peut protéger la surface de TiO_2 de l'approche d'autres espèces présentes dans la solution et il peut réduire l'occurrence des réactions secondaires, comme cela a déjà été rapporté pour des systèmes similaires.[19]

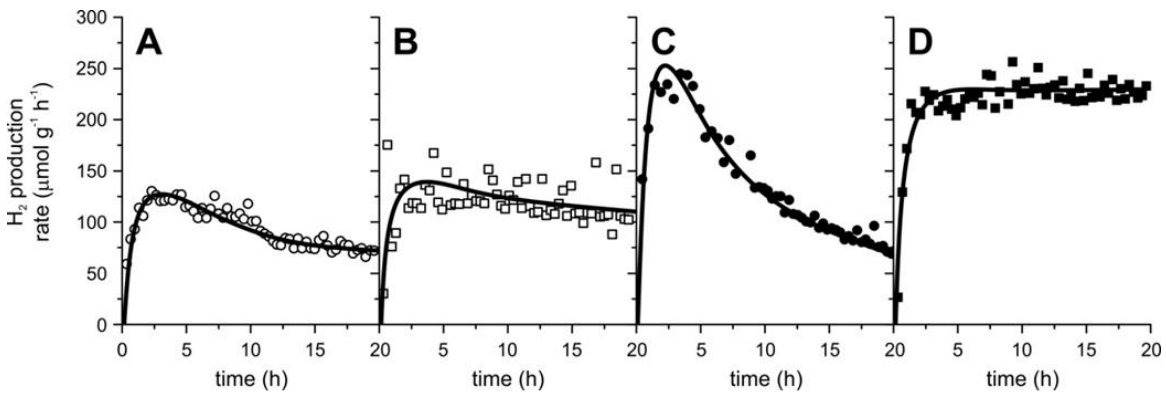

*Figure 11 Taux de production du H_2 dans les conditions d'essai pour les pigments: (A) **D5**, (B) **DF15**, (C) **MB25**, (D) **AD418**.*

La différence la plus importante entre le comportement de tous les pigments a été observée pour **MB25**: après une activité initiale élevée, il a présenté une forte réduction du dégagement du H_2, indiquant que la molécule avait subi un processus de dégradation progressif. D'un autre côté, **AD418**, qui ne s'en distingue seulement que par la nature de son espacer π, n'a montré qu'une production initiale de gaz légèrement inférieure à celle du **MB25**, mais sans enregistrer une chute massive de l'activité du dégagement du H_2. Le processus de dégradation montré par **MB25** a été ensuite analysé et expliqué par une probable attaque nucléophile sur la double liaison près de le groupe donneur de la molécule, partiellement confirmée par l'absence des phénomènes similaires sur **AD418**, dans laquelle cette double liaison a été remplacée par une liaison plus stable, un thiophène.

- **Conclusion**

Dans la première partie du travail, l'emploi de différents groupes d'ancrage silylés en CSPP a été étudié, ainsi que leurs propriétés optiques et électrochimiques. L'étude montre comment le groupe peut agir comme excellent group d'ancrage, mais seulement avec une optimisation adéquate et fine de la construction de l'appareil. Par conséquent, une nouvelle procédure générale pour insérer un groupe alternatif présentant des propriétés similaires, la silatrane, a été explorée. Son introduction sur l'infrastructure d'une série d'acides cyanoacryliques a été possible et s'est avérée plus facile et général que l'insertion du groupe trialkoxysilanique. Les deux groupes présentaient la même stabilité vers la désorption et le même comportement après la sensibilisation sur les films de TiO_2.

La deuxième partie du travail était axée sur l'utilisation de plusieurs acides cyanoacryliques pour la production photocatalytique d'hydrogène. L'expérience d'évolution de H_2 a montré comment la présence de longues chaînes hydrophobes sur l'espacer π augmente considérablement le taux de production d'hydrogène en protégeant la surface de la TiO_2 de l'approche des espèces en solution. La voie de dégradation de **MB25** pendant l'expérience a été étudiée et a été reconnue qui se déroulent sur la double liaison près de la triarylamine. Ensuite, le remplacement de la double liaison avec un thiophène (**AD418**) a permis de maintenir le même excellent taux de production de H_2 et aussi d'éliminer les processus de dégradation qui était présente pour **MB25**.

Développement d'Hydrogels Polyamidoamine: vers de nouveaux matériaux sensibles aux stimuli

- **Introduction**

Les hydrogels sont des matériaux hautement hydrophiles constitués d'un réseau de liaisons intermoléculaires covalentes ou non covalentes.[20] Depuis les premiers travaux pionniers de Wichterle et de Lim en 1960,[21] en raison de leur biocompatibilité, de leur contenu hydrique élevé, de leurs propriétés élastiques analogues à celles de tissus naturels et de leur structure poreuse, les hydrogels ont suscité ces dernières années un grand intérêt dans la science des matériaux.[22] Les hydrogels peuvent être synthétisés sous différentes formes, en fonction du réacteur utilisé pendant le processus de gélification et, également, ils peuvent changer facilement de taille et de forme en réponse à des stimuli environnementaux. Leur bonne biocompatibilité provient de leur contenu hydrique élevé, ce qui les rend également plus mous et plus élastiques. Leur capacité à gonfler et dégonfler dans un milieu dépend de nombreux facteurs, parmi lesquelles la densité de réticulation, le caractère hydrophile des chaînes polymèriques et la nature du solvant, et peut être évaluée au travers de la mesure du degré de gonflement à l'équilibre (EDS), définie selon l'équation suivante:

$$EDS = \frac{W_{wet} - W_{dry}}{W_{dry}} \times 100$$

où W_{wet} et W_{dry} sont, respectivement, le poids de l'hydrogel gonflé et lyophilisé. La valeur d'EDS mesuré pour chaque réseau dépend principalement par la densité et les caractéristiques de réticulation de l'hydrogel,[23] même si la solution environnante exerce aussi une grande influence (par exemple la valeur du pH). Les hydrogels peuvent être classés différemment,[24] en fonction de leur origine (systèmes naturels *vs.* synthétiques), de leur structure de réseau (inter-pénétrante, copolymère, homopolymère ou double), de leur méthode de réticulation (s'il est chimique ou physique), de leur charge (anionique, cationiques, amphotères ou non-ioniques) ou leur biodégradabilité (si ils sont dégradables ou non). Chaque classe de hydrogel présente des avantages et des inconvénients particuliers qui ont une grande influence sur l'application finale des matériaux.

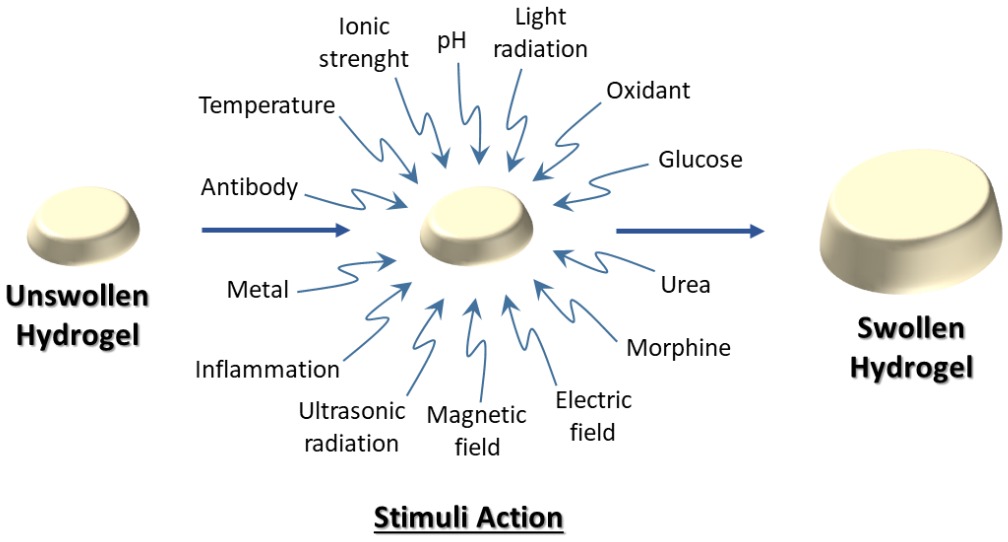

Figure 12 Représentation du comportement typique des hydrogels répondant aux stimuli.

Les hydrogels sensibles aux stimuli appartiennent à une catégorie particulière de matériaux dont la caractéristique plus représentative est de réagir aux stimuli environnementaux (physique ou chimique) en présentant des changements notables de leur taille, leur structure de réseau, leur résistance mécanique ou leur perméabilité; pour cette raison, ils sont appelés aussi des hydrogels sensibles à l'environnement ou hydrogels intelligents.[25,26] Les stimuli physiques les plus communément utilisés incluent la lumière, la pression, la température, les champs électriques ou magnétiques et les contraintes mécaniques, alors que les stimuli chimiques comprennent le pH, la force ionique et les agents chimiques. L'effet induit sur le réseau d'hydrogel par le stimulus extérieur peut souvent être observé à l'échelle macroscopique sous différentes formes, mais le changement le plus commun observé est lié à leur volume, qui est aussi lié à leur capacité d'absorption de l'eau[27] (Figure 12). Ces caractéristiques ont accru leur popularité au sein de la communauté scientifique pour leurs possibles applications dans les domaines de la recherche de nouveaux capteurs, de systèmes de délivrance de médicaments ou de prothèses souples.

Ce travail était axé sur le développement des nouveaux hydrogels sensibles aux stimuli, à partir d'une formulation d'un hydrogel biocompatible récemment mise au point.[28] Ce gel est composé d'un squelette de polyamidoamine formé sans la nécessité d'utilisation d'un initiateur par condensation d'Aza-Michael du méthylène-bis-acrylamide (MBA) et de l'acide γ-aminobutyrique (GABA), avec de la pentaethylenehexamine

(PEHA) agissant comme un agent de réticulation. De nouvelles méthodologies pour l'obtention des hydrogels polyamidoamine conducteurs et sensibles à la lumière ont été étudiées et mises au point. Les hydrogels électroconducteurs sont particulièrement intéressants parce qu'ils sont des biomatériaux composites qui rassemblent les propriétés de commutation d'oxydo-réduction et des propriétés électriques de la composante électroactive avec le transport facile de petites molécules, le niveau élevé d'hydratation et la biocompatibilité des matrices hydrogel.[29]

- **Résultats et Discussion**

La première partie présente l'introduction de certains polymères conducteurs dans le réseau d'un hydrogels. Pour commencer, l'introduction d'un polymère conducteur commun, la polyaniline (PAn), a été étudiée, en utilisant un hydrogels à base de polyacrylamide comme formulation de référence[30] (Figure 13).

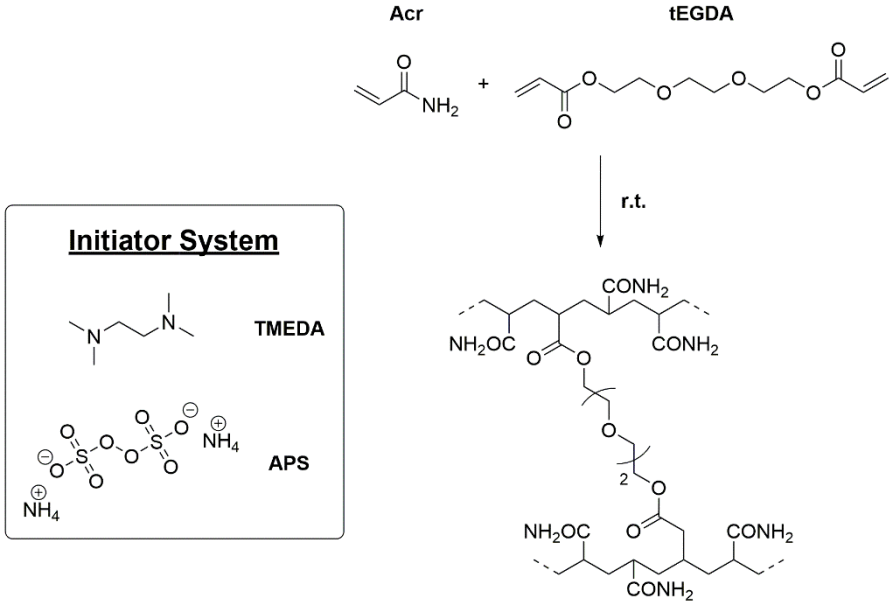

Figure 13 Représentation de la matrice d'hydrogel à base de polyacrylamide utilisée.

Le PAn peut être communément introduit en utilisant un protocole composé de deux étapes:[31] premièrement, les gels sont immergés pour 18h dans une solution du monomère du polymère conducteur ou de l'initiateur radicalaire, afin de laisser la matrice absorber le composant; ensuite, la matrice est enlevée de la solution et ensuite immergée pour quelques heures supplémentaires dans une solution de l'autre composant nécessaire à la polymérisation (Figure 14). Deux protocoles différents ont été testés et celui qui il a montré les meilleurs résultats en termes de polymère conducteur introduit dans la matrice d'hydrogel, a été choisi pour les expériences suivantes. La procédure choisie prévoit une première étape réalisée dans une solution aqueuse acide d'APS, pendant que la seconde étape dans une solution d'aniline dans l'hexane: avec ces conditions, l'APS précédemment adsorbé ne sera pas libéré dans la solution à l'extérieur du gel, garantissant la formation du polymère conducteur uniquement à l'intérieur de le réseau. Les propriétés électroniques des hydrogels conducteurs synthétisés ont été ensuite analysées et l'effet du dopage du PAn (obtenu avec l'exposition du réseau à une solution acide) a été étudié, permettant ainsi d'obtenir une augmentation d'un ordre de grandeur de la conductivité du matériau.

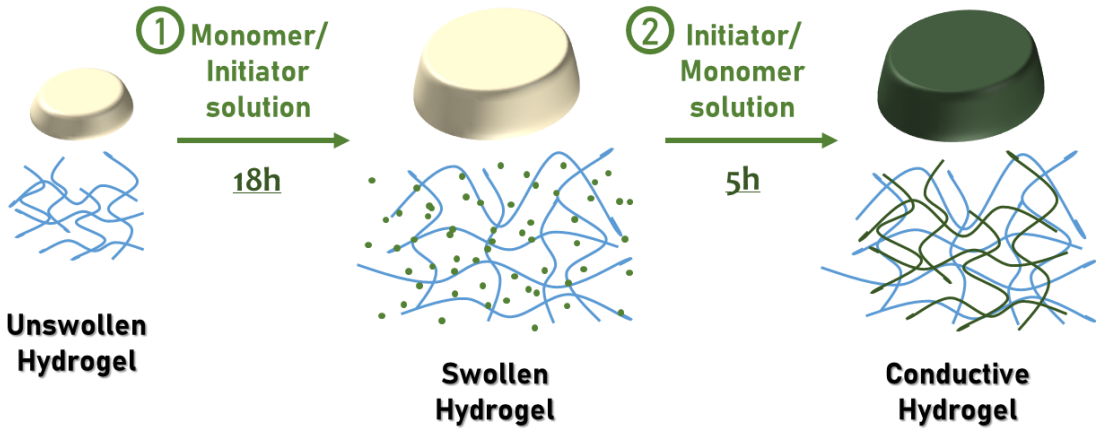

Figure 14 Représentation de la procédure en deux étapes adoptée pour l'introduction du polymère conducteur à l'intérieur de la matrice d'hydrogel.

Après avoir mis au point une procédure satisfaisante pour l'incorporation du polymère conducteur dans la matrice du gel, nous avons décidé d'étudier l'étendue de la procédure en utilisant une autre formulation d'hydrogel. La nouvelle matrice que nous avons décidé d'utiliser était un hydrogel polyamidoamine (PAA). Cette matrice particulière (Figure 15) pourrait être obtenue par réaction Aza-Michael entre la double liaison pauvre en électrons du méthylènebisacrylamide (MBA), ayant le rôle de monomère principal de la formulation, et les amines primaires de la pentaéthylènehexamine (PEHA), l'agent de réticulation, ainsi que de l'acide γ-aminobutyrique (GABA).[32] La particularité la plus notable de cette formulation est l'absence d'un initiateur: la réaction chimique utilisée pour la polymérisation peut aussi se produire spontanément à la température ambiante si le pH de la solution est suffisamment basique (8 à 9).

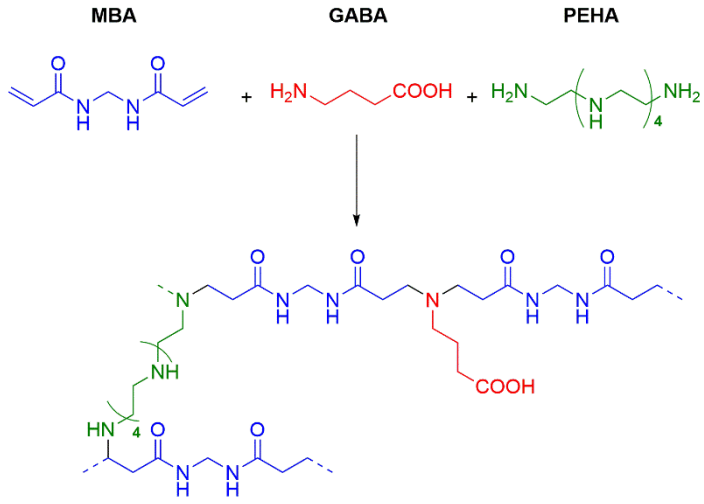

Figure 15 Représentation de la structure du hydrogel de PAA.

Pour introduire le PAn dans des hydrogels de PAA, la même procédure que celle déjà développée pour la matrice à base de polyacrylamide a été testée. Étonnamment, après la première étape de la procédure (le gonflement dans la solution d'APS) tous les échantillons utilisés sont devenus plus foncés et plus petit. En particulier, deux échantillons ont été complètement décomposés dans la solution, ce qui nous a permis de conclure que la matrice était dégradée par réaction avec du APS dans des conditions acides, selon une voie similaire à celle du mécanisme de la réaction de Cope[33] (Figure 16).

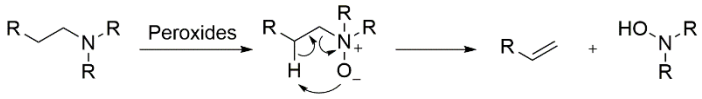

Figure 16 Mécanisme de la réaction de Cope.

Ensuite, pour surmonter le problème, une optimisation des conditions de polymérisation fut nécessaire, afin de permettre la polymérisation de l'aniline sans provoquer la dissolution de la matrice d'hydrogel. L'optimisation a été réalisée en testant différents ordres pour l'addition des deux réactifs dans les deux étapes, pour différentes durées et à différents pH. L'évaluation de la résistance du matériau et du changement de poids de la matrice après l'introduction du fragment conducteur a permis d'identifier les meilleures conditions: la première étape a été réalisée pendant 18h dans une solution aqueuse d'aniline 0,1 M (pH 7) et la deuxième pendant 5h dans une solution acide (HCl 1 M) d'APS 0,1 M. Ensuite, la morphologie (Figure 17) et les propriétés électroniques des hydrogels conducteurs obtenus ont été évaluées à l'aide d'une méthode à la sonde à quatre points (Tableau 2).

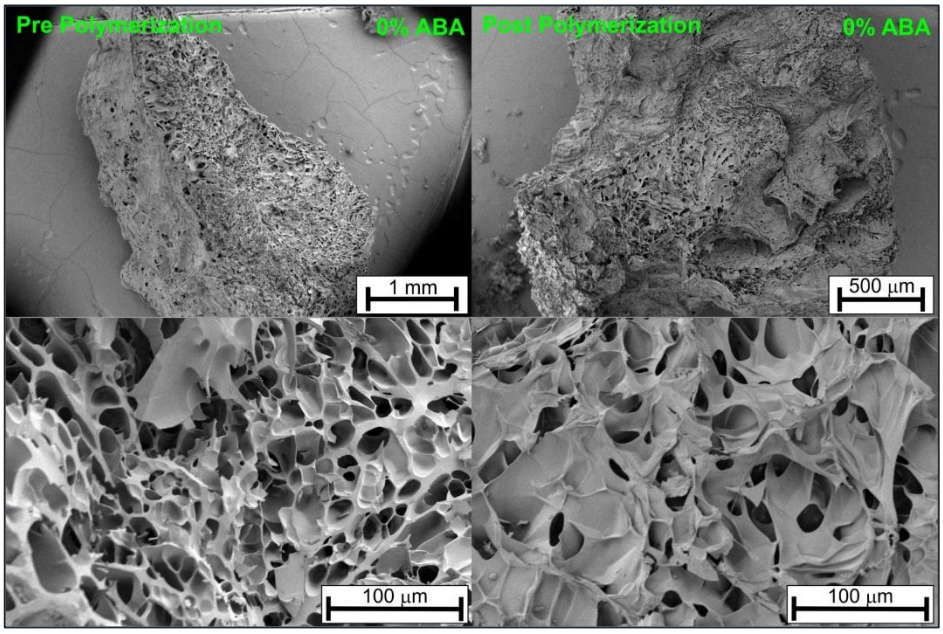

Figure 17 SEM de l'hydrogel pur (à gauche) et conducteur (à droite).

Ensuite, il a été exploré la possibilité d'utiliser d'autres types de polymères conducteurs, en particulier le polypyrrole (PPy) et le polyéthylènedioxithiophène (PEDOT), qui sont bien connus pour être des matériaux polymères hautement conducteurs. La principale raison de ce choix a été la possibilité de réaliser la polymérisation du milieu conducteur dans des conditions plus modérées, sans devoir utiliser des oxydants forts ou des solutions acides. L'incorporation a été réalisée en utilisant une procédure en deux étapes similaire à celle optimisée précédemment pour l'introduction de la polyaniline dans l'hydrogel à base d'acrylamide. Donc, la première étape a été réalisée dans la solution aqueuse de l'oxydant ($FeCl_3$) et la deuxième dans une solution organique des monomères.[34] La matrice de gel s'est révélée capable de résister aux conditions d'oxydation et n'a montré aucun signe de dégradation après une nuit dans à solution de $FeCl_3$; l'incorporation des deux polymères conducteurs, donc, a été réalisée avec succès. Ensuite, les caractéristiques électroniques des différents hydrogels conducteurs ont été enregistrées et comparées à celles rapportées dans la littérature. Les valeurs obtenues étaient d'un ordre de grandeur supérieur à celui du PAA-hydrogel non-conducteur, ce qui montre bien la bonne amélioration des propriétés électroniques du matériau composite. Les valeurs de conductivité les plus élevées ont été obtenues avec l'incorporation du PEDOT et de la PAn après le dopage; la comparaison aussi avec le hydrogel contenant le PPy a montré

clairement comment la nature du polymère conducteur introduit dans la matrice pouvait beaucoup influencer les propriétés électroniques du matériau composite (Tableau 2). Malheureusement, même dans nos meilleures conditions, la conductivité observées reste toujours inférieure d'un ordre de grandeur à celle des hydrogels conducteurs les plus performants développés pour les applications énergétiques[35,36] (0,11-0,88 S/cm), même si les valeurs étaient conformes aux valeurs moyennes observée pour ce type de matériaux[37,38] (0,1-10 mS/cm).

Tableau 2 Résumé de la conductivité enregistrée de tous les différents hydrogels conducteurs développés.

Polymère Conducteur	Conductivité (mS/cm)
Polyaniline	3.4
Polyaniline (dopage)	15.4
Polypyrrole	0.2
Polypyrrole (dopage)	3.2
PEDOT	12.6
Pur	1.0×10^{-3}

L'étape suivante consistait à créer une liaison covalente entre la partie conductrice et la matrice d'hydrogel dans le but d'augmenter l'affinité entre les deux réseaux différents et les propriétés globales de l'hydrogel conducteur. Pour créer la liaison, un monomère du polymère conducteur approprié fonctionnalisé avec une amine primaire a été inséré dans le squelette du réseau pendant la synthèse de l'hydrogel, en remplaçant le GABA dans la formulation. Les molécules choisies étaient la 4-aminobenzylamine (**ABA**) pour le PAn et la 3- (1*H*-pyrrol-1-yl) propane-1-amine (**1-PPA**) pour le PPy (Figure 18). La synthèse du composé **1-PPA** devait être conçue puis réalisée car il n'est pas disponible dans le commerce.

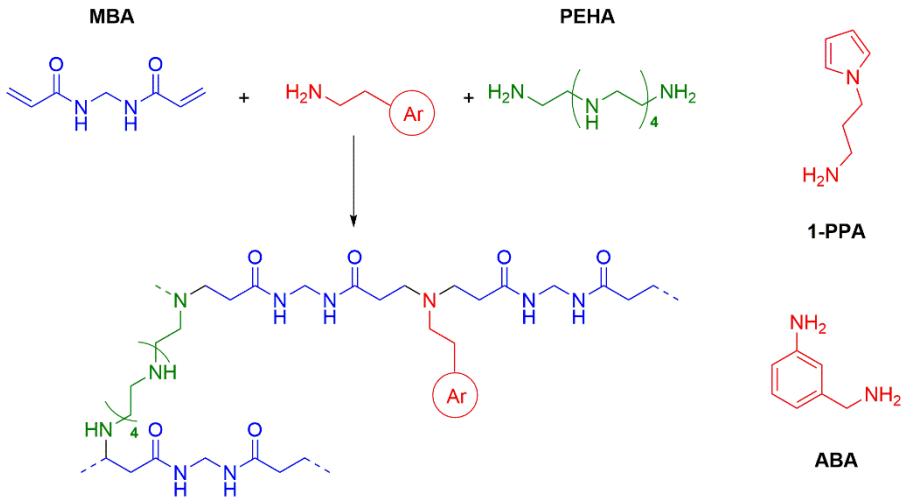

*Figure 18 Représentation des modifications de la structure d'hydrogel de polyamidoamine introduites et structure des additifs **1-PPA** et **ABA**.*

Enfin, des hydrogels chargés avec les deux composés **ABA** et **1-PPA** ont été synthétisés (Figure 19) et, par la suite, les deux polymères conducteurs PAn et PPy ont été polymérisés à l'intérieur en utilisant les méthodologies précédemment développées. Les caractéristiques électroniques des matériaux hybrides ont été mesurées et un criblage de l'effet sur les propriétés physiques du système pour différentes charges d'**ABA** dans les hydrogels a été réalisé. L'introduction des fractions hydrophobes dans le réseau d'hydrogels a montré une réduction de la valeur d'EDS du matériau avant et après la polymérisation du milieu conducteur,

sans affecter sensiblement les propriétés électroniques. En fait, des valeurs extrêmement similaires de conductivité à celles précédemment enregistrées pour les hydrogels conducteurs sans liaison covalente ont été obtenues pour ces nouveaux matériels (1,7 - 4,1 mS/cm).

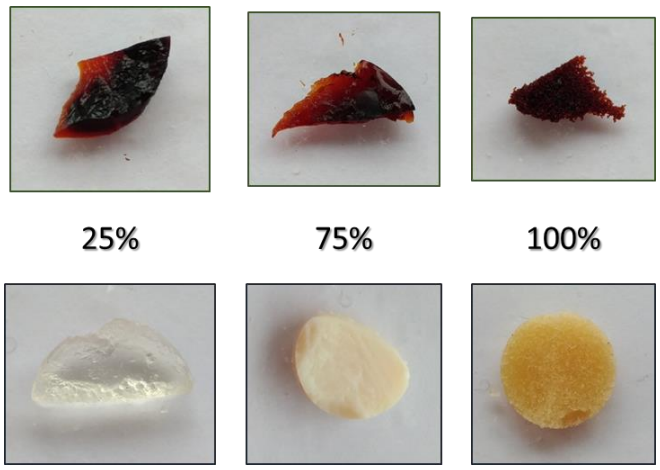

*Figure 19 Aspect des hydrogels contenant une quantité différente d'**ABA** (% entre chaque paire d'images) avant (en bas) et après (en haut) la polymérisation du milieu conducteur.*

La dernière partie du travail a été centrée sur la synthèse et à la caractérisation d'un hydrogel sensible à la lumière, dans lequel une partie photoactive favorise une altération des propriétés hydrophiles/hydrophobes du gel par oxydation sélective des chaînes latérales. En tant que partie photosensible, C_{60}, qui est connu pour être capable de produire de l'oxygène singulet après l'exposition à la lumière UV[39] avec un rendement quantique élevé[40] et qui peut être facilement fonctionnalisé avec différents substituants,[41] a été choisi. Ensuite, la méthionine a été identifiée comme le substrat oxydable le plus approprié: elle possède un fragment hydrophobe contenant du soufre (capable de s'oxyder), un groupe amine primaire (pour participer à la réaction d'Aza-Michael utilisée pour la constitution de la matrice d'hydrogel de polyamidoamine) et aussi un acide carboxylique, qui la rend extrêmement similaire au co-monomère GABA utilisé dans la formulation originale du gel. De plus, l'oxydation de la méthionine au sulfoxyde correspondant a déjà été accomplie en utilisant de l'oxygène singulet produit par des dérivés du fullerène,[42] et il a déjà été démontré qu'elle peut améliorer le caractère hydrophile de certains systèmes polymèriques.[43] La stratégie utilisée pour charger les nouveaux additifs dans la matrice était analogue à celle déjà expérimentée avec succès avec **ABA** et **1-PPA**, consistant à remplacer le GABA dans la formulation originale (Figure 20). Pour cette raison, la synthèse d'un dérivé du fullerène approprié, fonctionnalisé avec un groupe amine, était nécessaire; le composé **C_{61}-NH_2**, a ensuite été conçu et synthétisé en utilisant une réaction de Bingel comme étape clé.[44]

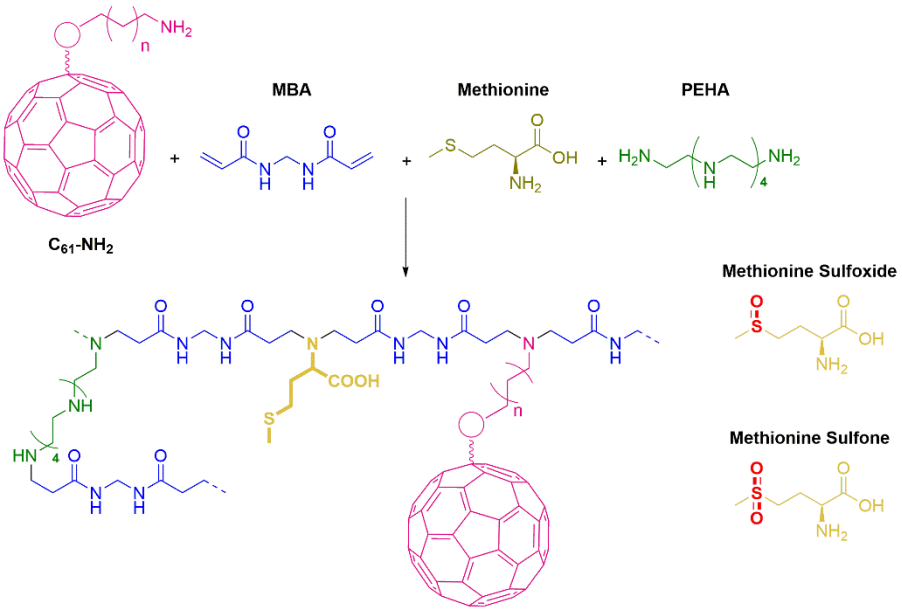

Figure 20 Représentation de la formulation d'hydrogel avec la méthionine et le composé ***C_{61}-NH_2***.

Afin de prouver la faisabilité de l'idée, la première étape consistait à déterminer la différence de propriétés physiques entre deux matériaux construits avec le même processus, mais incorporant des composés contenant du soufre avec états d'oxydation différents, un sulfure et un sulfoxyde. Deux lots différents de gels, l'un contenant uniquement de la méthionine et l'autre contenant uniquement le sulfoxyde de la méthionine, ont été préparés et l'EDS a été mesuré pour les deux matériels. Les valeurs enregistrées ont montré que, en passant par la méthionine hydrophobe au sulfoxyde correspondant (plus hydrophile), le contenu hydrique d'hydrogels a augmenté considérablement, confirmant ainsi notre première hypothèse. Les deux matériaux différents ont ensuite été caractérisés au moyen de techniques XPS (Figure 21), SEM et ATR-IR pour la comparaison successive avec les données obtenues pour l'hydrogel sensible à la lumière.

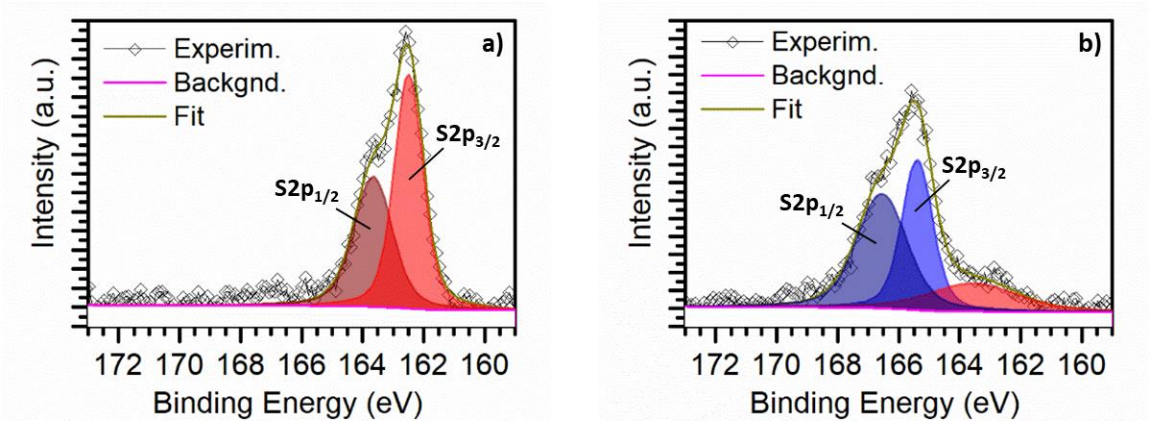

Figure 21 Spectres XPS du soufre d'hydrogels avec (a) la méthionine et (b) la méthionine sulfoxyde. Les zones colorées correspondant à l'ajustement de donner des différents composants du soufre, en rouge la forme réduite (sulfure) et en bleu l'oxydé (sulfoxyde).

Ensuite, le nouvel hydrogel photosensible contenant le dérivé du fullerène C_{61}-NH_2 et la méthionine a été synthétisé sans problème, effectuant la gélification dans l'obscurité afin d'éviter de déclencher la production de l'espèce oxydante avant les mesures. Le matériau a prouvé de ne être pas capable de relâcher l'adduit du C_{60} même dans des solvants organiques et la caractérisation précédemment effectuée pour les systèmes analogues a été répétée, en choisissant l'analyse XPS comme instrument principal pour la détection semi-quantitative de l'oxydation du sulfure. Ensuite, l'expérience d'oxydation

a été réalisée en exposant plusieurs échantillons de l'hydrogel sous une lampe à mercure de forte puissance pendant 20h, en permettant la production de l'espèce oxydante par le dérivé du fullerène et donc l'oxydation de la méthionine. Comme contrôle, la même expérience a été également réalisée sur des échantillons de l'hydrogel original (avec uniquement du GABA). L'analyse EDS, SEM et XPS par tous les hydrogels a été effectué après l'expérience et comparés à la caractérisation effectuée avant l'irradiation (Figure 22).

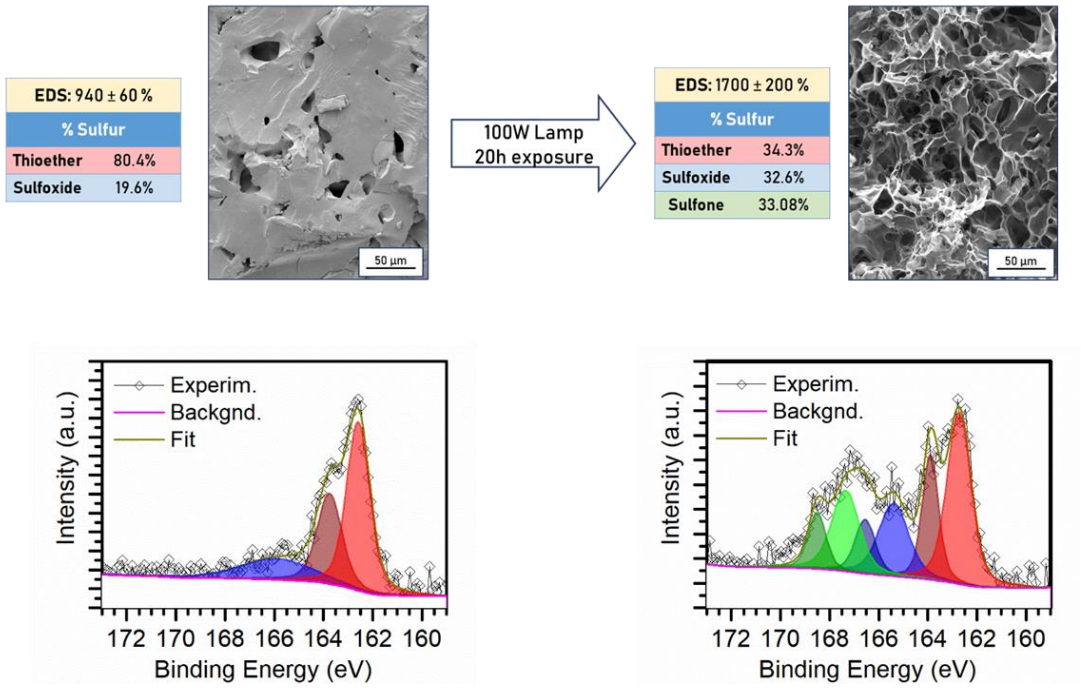

Figure 22 Résumé des propriétés de l'hydrogel photosensible avant et après l'exposition à la lumière.

Alors que l'EDS de l'hydrogel original n'a pas changé sensiblement de celui enregistré avant l'expérience, dans le cas de l'hydrogel sensible à la lumière, le paramètre a augmenté considérablement après l'irradiation. L'absence d'altérations du réseau originale a prouvé que la matrice était capable de résister aux conditions de l'expérience sans être dégradée. D'autre part, l'augmentation de la valeur EDS enregistrée par le nouvel système était le signal d'un changement important dans la structure de l'hydrogel, ce qui a été successivement confirmé par les analyses SEM et XPS. En particulier, le spectre XPS du soufre (Figure 22) a montré une augmentation des formes oxydées de la méthionine aux dépens de la forme réduite, qui ne représentant plus que le 34% du soufre total présent dans l'hydrogel. L'apparition d'une autre paire de pics ayant une énergie plus élevée que celle du sulfoxyde de méthionine a été attribuée à la forme encore plus oxydée de méthionine, sa sulfone, comme confirmé par comparaison avec d'autres travaux rapportés dans la littérature.[45] Ensuite, l'analyse SEM a mis en évidence le changement macroscopique de la structure du matériau: après l'irradiation, la formation d'un réseau très poreux a été observée, ce qui correspond à l'augmentation de la valeur du EDS qui a été enregistré. Les pores étaient répartis uniformément dans le matériau et semblaient être interconnectés entre eux.

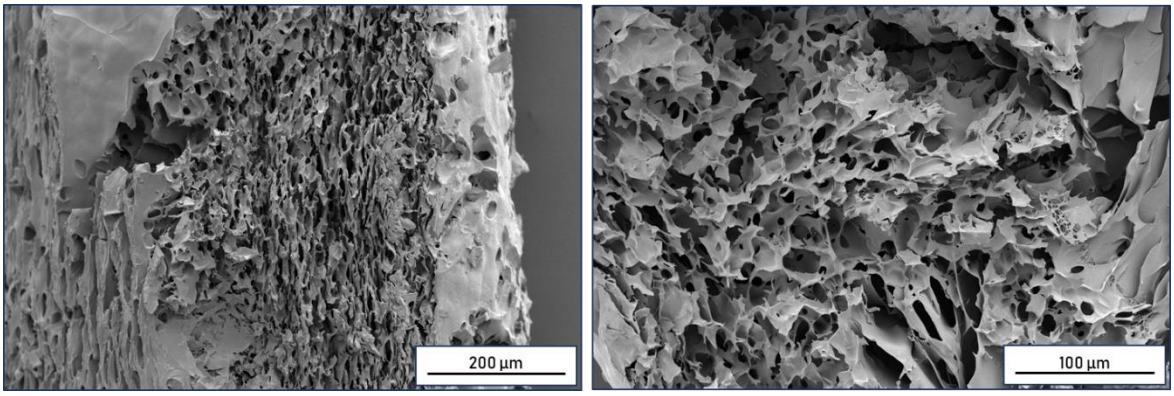

Figure 23 Images SEM de l'hydrogel à base de méthionine après traitement avec KO_2.

Enfin, un échantillon d'hydrogel à base de méthionine a été utilisé pour vérifier si le même effet observé sur les propriétés physiques et la structure du matériel à base du méthionine/fullerène après l'irradiation pouvait être obtenu en l'absence de fullerène au moyen d'une oxydation chimique classique. Le composé choisi pour le test était le KO_2, un oxydant fort commun. L'échantillon a été conservé dans une solution d'oxydant et, après 16h d'immersion, l'hydrogel n'a présenté aucun changement significatif de la valeur de l'EDS si on les comparait aux échantillons non-traités. Les analyses SEM et XPS ultérieures effectuée sont montré une oxydation non-homogène du réseau, ce qu'il pourrait justifier l'absence d'incrément de la valeur du EDS. Les différents modes d'oxydation observés au XPS et au SEM peuvent être liés au fait que l'oxydation favorisée par les molécules des fullerènes dans l'hydrogel sensible à la lumière avait lieu in situ, pendant que le KO_2 devait diffuser à l'intérieur de la matrice à partir de la solution externe pour permise l'oxydation. Cette différence a conduit à une oxydation plus efficace dans le cas d'hydrogel avec le fullerène, ce qui s'est traduit par une valeur EDS plus élevée et une structure plus poreuse observée dans le SEM.

- **Conclusion**

Dans la première partie des travaux, l'introduction de polymères conducteurs à l'intérieur d'une matrice d'hydrogel préexistante a été étudiée et la polymérisation du second réseau a été optimisée. Avec la procédure choisie, il a été possible d'obtenir des hydrogels conducteurs fabriqués avec différents polymères conducteurs. Les propriétés électroniques des nouveaux matériaux ont été analysées et ont révélé être cohérentes. Ensuite, l'introduction d'une liaison covalente entre la matrice hydrogel et la partie conductrice a été exploitée au moyen de l'introduction de composés fonctionnels appropriés pendant la synthèse de l'hydrogel. Les modifications ont montré que les propriétés physiques ont été modifiées plutôt que les propriétés électroniques de la matière finale, réduisant la capacité d'absorption d'eau en raison de leur nature hydrophobe, sans provoquer de changement substantiel de la conductivité du matériau.

Ensuite, dans la deuxième partie, le développement d'un nouvel hydrogel sensible à la lumière a été réalisé. Le matériau a été construit autour d'un système tandem où un dérivé aminé du C60 approprié, lié au réseau d'hydrogel, après l'absorption de la lumière et la production d'oxygène singulet, a été en mesure d'oxyder les fragments de méthionine présents en le sulfoxyde correspondant plus hydrophile. L'oxydation a été prouvée par l'analyse de XPS et a conduit à l'incrément de la valeur d'EDS du matériel.

▪ References

[1] O'Regan, B.; Grätzel, M. *Nature* **1991**, *353*, 737.
[2] Hagfeldt, A.; Boschloo, G.; Sun, L.; Kloo, L.; Pettersson, H. *Chem. Rev.* **2010**, *110*, 6595
[3] (a) Lee, C-.P.; Lin, R.Y-.Y.; Lin, L-Y.; Li, C-.T.; Chu, T-.C.; Sun, S-.S.; Lin, J.T.; Ho, K-.C. *RSC Adv.* **2015**, *5*, 23810; (b) Lee, C-.P.; Li, C-.T.; Ho, K-.C *Mater Today* **2017**, *20*, 267.
[4] Ooyama, Y.; Harima, Y. *ChemPhysChem.* **2012**, *13*, 4032
[5] Willkomm, J.; Orchard, K.L.; Reynal, A.; Pastor, E.; Durrant, J.R.; Reisner, E. *Chem. Soc. Rev.* **2016**, *45*, 9
[6] Cecconi, B.; Manfredi, N.; Montini, T.; Fornasiero, P.; Abbotto, A. *Eur. J. Org. Chem.* **2016**, *31*, 5194
[7] Kakiage, K.; Aoyama, Y.; Yano, T.; Oya, K.; Fujisawa, J.-I.; Hanaya, M. *Chem. Commun.* **2015**, *51*, 15894.
[8] (a) Kakiage, K.; Aoyama, Y.; Yano, T.; Otsuka, T.; Kyomen, T.; Unno, M.; Hanaya, M. *Chem. Commun.* **2014**, *50*, 6379; (b) Bessi M.; Monini M.; Calamante M.; Mordini A.; Sinicropi A.; Di Donato M.; Iagatti A.; Foggi P.; Zani L.; Reginato G. *Synthesis* **2017**, *49*, 3975.
[9] Martın, C.; Ziolek, M.; Douhal, A. *J. Photochem. Photobiol. C* **2016**, *26*, 1; (b) Sobus, J.; Karolczak, J.; Komar, D.; Anta, J.A.; Ziolek, M. *Dyes Pigments* **2015**, *113*, 692.
[10] Van Stokkum, I.H.M.; Larsen, D.S.; Van Grondelle, R. *Biochim. Biophys. Acta* **2004**, *1657*, 82.
[11] (a) Wiberg, J.; Marinado, T.; Hagberg, D.P.; Sun, L.; Hagfeldt, A.; Albinsson, B. *J. Phys. Chem. C* **2009**, *113*, 3881; (b) Sobus, J.; Kubicki, J.; Burdzinski, G.; Ziołek, M. *ChemSusChem* **2015**, *8*, 3118.
[12] Wiberg, J.; Marinado, T.; Hagberg, D.P.; Sun, L.; Hagfeldt, A.; Albinsson, B. *J. Phys. Chem. C* **2009**, *113*, 3881
[13] Franchi, D.; Calamante, M.; Reginato, G.; Zani, L.; Peruzzini, M.; Taddei, M.; Fabrizi De Biani, F.; Basosi, R.; Sinicropi, A.; Colonna, D.; Di Carlo, A.; Mordini, A. *Tetrahedron* **2014**, *70*, 6285.
[14] Sobus, J.; Gierczyk, B.; Burdzinski, G.; Jancelewicz, M.; Polanski, E.; Hagfeldt, A.; Ziołek, M. *Chem. Eur. J.* **2016**, *22*, 15807
[15] Frye, C.L.; Vogel, G.E.; Hall, J.A. *J. Am. Chem. Soc.* **1961**, *83*, 996.
[16] Hagberg, D.P.; Edvinsson, T.; Marinado, T.; Boschloo, G.; Hagfeldt, A.; Sun, L. *Chem. Commun.* **2006**, 2245.
[17] Tiwari, A.; Pal, U. *Int. J. Hydr. En.* **2015**, *40*, 9069.
[18] Dessì, A.; Calamante, M.; Mordini, A.; Peruzzini, M.; Sinicropi, A.; Basosi, R.; Fabrizi de Biani, F.; Taddei, M.; Colonna, D.; Di Carlo, A.; Reginato, G.; Zani, L. *Chem. Commun.* **2014**, *50*, 13952.
[19] Lee, J.; Kwak, J.; Ko, K.C.; Park, J.H.; Ko, J.H.; Park, N.; Kim, E.; Ryu, H.; Ahn, K.T.; Lee, J.Y.; Son, S.U. *Chem. Commun.*, **2012**, ***48***, 11431.
[20] Peppas, N.A.; Hilt, J.Z.; Khademhosseini, A.; Langer, R. *Adv. Mater.* **2006**, *18*, 1345
[21] Wichterle, O.; Lim, D. *Nature* **1960**, *185*, 117.
[22] Luo, Y.; Kirker, K.R.; Prestwich, G.D. *J. Control. Release* **2000**, *69*, 169.
[23] Fatin-Rouge, N.; Milon, A.; Buffle, J.; Goulet, R.R.; Tessier, A. *J. Phys. Chem. B* **2003**, *107*, 12126.
[24] Ullah, F.; Bisyrul, M.; Othman, H.; Javed, F.; Ahmad, Z.; Akil, H. *Mat. Sci. Eng. C* **2015**, *57*, 414.
[25] (a) Peppas, N.; Bures, P.; Leobandung, W.; Ichikawa, H. *Eur. J. Pharm. Biopharm.* **2000**, *50*; 27; (b) Gil, S.; Hudson, S.M. *Prog. Polym. Sci.* **2004**, *29*, 1173.
[26] Koetting, M.C.; Peters, J.T.; Steichen, S.D.; Peppas, N.A. *Mater Sci. Eng. R Rep.* **2015**, *93*, 1
[27] (a) Koettinga, M.C.; Petersa, J.T.; Steichenb, S.D.; Peppas, N.A. *Mater. Sci. Eng. R* **2015**, *93*, 1; (b) Echeverria, C.; Fernandes, S.N.; Godinho, M.H.; Borges, J.P.; Soares, P.I.P. *Gels* **2018**, *4*, 54.
[28] Fiorini, F.; Prasetyanto, E.A.; Taraballi, F.; Pandolfi, L.; Monroy, F.; López-Montero, I.; Tasciotti, E.; De Cola, L. *Small* **2016**, *12*, 4881
[29] A. Guiseppi-Elie, *Biomaterials* **2010**, *31*, 2701
[30] Saha, S.; Sarkar, P.; Sarkarb, M.; Girib, B. *RSC Adv.* **2015**, *5*, 27665.
[31] Dai, T.; Quing, X.; Wang, J.; Shen, C.; Lu, Y. *Compos. Sci. Technol.* **2010**, *70*, 498.
[32] (a) Fiorini, F.; Prasetyanto, E.A.; Taraballi, F.; Pandolfi, L.; Monroy, F.; López-Montero, I.; Tasciotti, E.; De Cola, L. *Small* **2016**, *12*, 4881; (b) Rizzi, V.; Fiorini, F.; Lamanna, G.; Gubitosa, J.; Prasetyanto, E.A.; Fini, P.; Fanelli, F.; Nacci, A.; DeCola, L.; Cosma, P. *Adv. Sustainable Syst.* **2018**, *2*, 1700146.
[33] March, J. "*Advanced Organic Chemistry: Reactions, Mechanisms, and Structure*" (3rd ed.), New York: Wiley, **1985**.
[34] (a) Zhang, J.; She, Y.; Lu, B.; Zhou, Y.; Fu, K. *Chinese J. Polym. Sci.* **1993**, *11*, 337; (b) Zhang, X.; Bai, R. *Langmuir* **2003**, *19*, 10703; (c) Mawad, D.; Lauto, A.; Wallace, G.G. "*Conductive Polymer Hydrogels*", in "*Polymeric Hydrogels as Smart Biomaterials*" **2016**, Springer; (d) Du, R.; Xu, Y.; Luo, Y.; Zhang, X.; Zhang, J. ***Chem. Commun.*** **2011**, ***47***, 6287.
[35] Pan, L.; Yu, G.; Zhai, D.; Lee, H. R.; Zhao, W.; Liu, N.; Wang, H.; Tee, B. C.-K.; Shi, Y.; Cui, Y.; Bao, Z. *Proc. Natl. Acad. Sci. U.S.A.* **2012**, *109*, 9287
[36] (a) Yao, B.; Wang, H.; Zhou, Q.; Wu, M.; Zhang, M.; Li, C.; Shi, G. *Adv. Mater.* **2017**, *29*, 1700974.
[37] Zhao, Y.; Liu, B.; Pan, L.; Yu, G. *Energy Environ. Sci.* **2013**, *6*, 2856.
[38] (a) Xia, Y.; Zhu, H. *Soft Matter* **2011**, *7*, 9388; (b) Chen, L.; Kim, B.; Nishino, M.; Gong, J.P.; Osada, Y. *Macromolecules* **2000**, *33*, 1232.
[39] Prat, F.; Stackow, R.; Bernstein, R.; Qian, W.; Rubin, Y.; Foote, C.S. *J. Phys. Chem. A* **1999**, *103*, 7230

[40] (a) Stasheuski, A.S.; Galievsky, V.A.; Stupak, A.P.; Dzhagarov, B.M.; Choi, M.J.; Chung, B.H.; Jeong, J.Y. *Photochem. Photobiol.* **2014**, *90*, 997; (b) Franskevych, D.; Palyvoda, K.; Petukhov, D.; Prylutska, S.; Grynyuk, I.; Schuetze, C.; Drobot, L.; Matyshevska, O.; Ritter, U. *Nanoscale Res. Lett.* **2017**, *12*, 40.

[41] (a) Hirsch, A.; Bellavia-Lund, C. "*Fullerenes and Related Structures*" in "*Topics in Current Chemistry*", Berlin: Springer, **1993**; (b) Diederich, F.N. *Pure Appl. Chem.* **1997**, *69*, 395; (c) Prato, M. *J. Mater. Chem.* **1997**, *7*, 1097.

[42] Carofiglio, T.; Donnola, P.; Maggini, M.; Rossetto, M.; Rossi, E. *Adv. Synth. Catal.* **2008**, *350*, 2815.

[43] Napoli, A.; Valentini, M.; Tirelli, N.; Müller, M.; Hubbell, J.A. *Nat. Mater.* **2004**, *3*, 183.

[44] Bingel, C. *Chem. Ber.* **1993**, *126*, 1957.

[45] Zhang, G.; Yuan, S-.S.; Li, Z-.M.; Longa, S-.R.; Yang, J. *RSC Adv.* **2014**, *4*, 23191.

Development of new organic dyes for energy applications

Chapter 1

Introduction and Aim of the Work

1.1. The energy issue

With the beginning of the modern era and the industrial revolution the economic system of the entire world changed dramatically, leading to a huge increase of the energy demand and the extensive exploitation of natural resources. In particular, in recent years the great development of the so-called "emerging countries" (especially China and India) significantly increased the world energy demand, as depicted in Figure 1.1, with an increase of 2.3% in 2017 (doubled compared to 2016) and of more than 40% compared to 2000 (see Figure 1.1).[1]

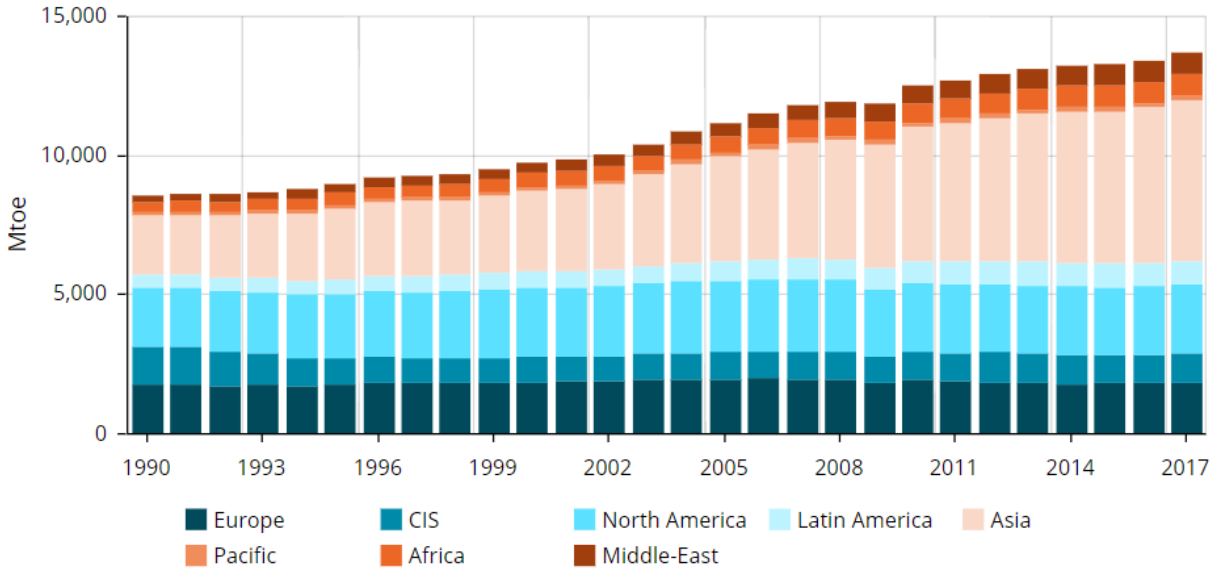

Figure 1.1 World energy consumption 1990-2017 (1000 Mtoe ≈ 11.63 TWh).[1]

A relevant example is still China that, after few years with nearly zero energy growth, in 2017 was the leader country in the energy consumption increment rank, with +3.3% on the previous year. With these premises and taking into account the growth of the urbanization in Africa and the increment of world population (expected to be 9.2 billion in 2040), a further increase of the energy demand of 30% is estimated by 2040.[2] Nowadays, the main energy sources are still fossil fuels (79.5% in 2016, Figure 1.2) that, apart from being non-renewable and therefore affected by a limited availability on the long term, are the main responsible of the greenhouse effect due to the emissions of CO_2 deriving from their combustion. For these reasons, the development of alternative energy sources is fundamental to satisfy the future global energy demand.

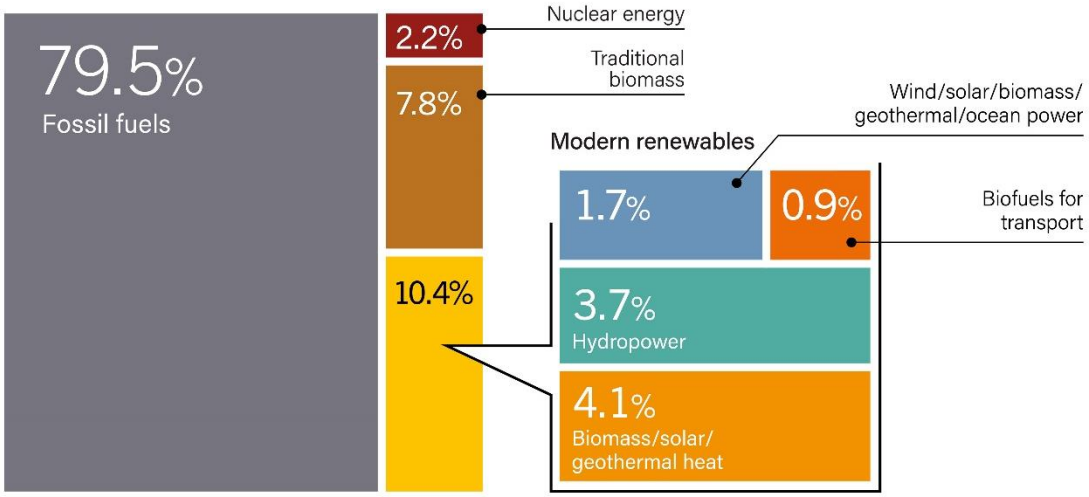

Figure 1.2 Global energy consumption by source in 2016.[3]

Renewable sources, such as biomass, hydropower, bio-heat, wind and solar energy, could be an ideal solution to the global energy problem since they are practically inexhaustible (in term of human timescale) and should have a lower impact on the environment compared to fossil sources. Accordingly, huge financial investments in the field have already been done, making them the fastest-growing energy source in terms of deployed power with a projected increment of 40% in the total energy supply by 2040 (Figure 1.2).[2] Among them, the most important at the moment is still hydropower (producing more than one third of total energy from renewable resources), but wind and solar energy are those growing most rapidly, with an increment, respectively, of 11% and 33% in respect to 2016 (for comparison, hydropower achieved "only" a +2% increase).[3]

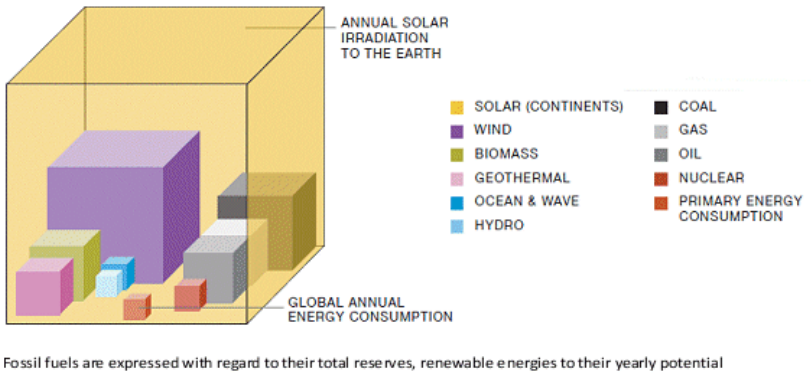

Figure 1.3 Energy reserves of the principal energetic resources of the planet.[4]

Solar energy in particular is considered to have the highest potential to become the world main energy source in the future (see Figure 1.3).[5] The annual solar radiation that reaches the Earth is estimated to be ≈ 15.2×10^5 TWh, orders of magnitude larger than any other resource present on the planet, and also considering a realistic amount of exploitable power around 600 TW, using solar cells with a global conversion efficiency of just 10% could already guarantee enough energy to satisfy three times the Earth energetic needs.[6]

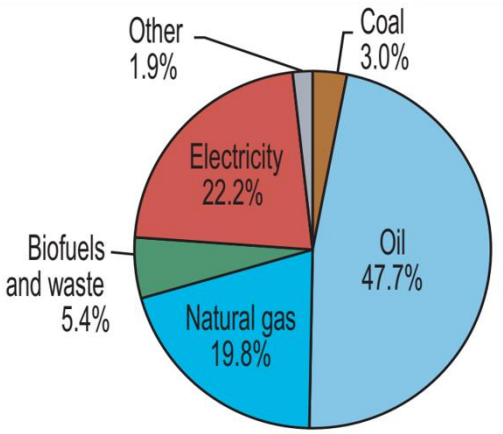

Figure 1.4 World total final consumption by fuels in 2015.[7]

A serious drawback in the use of renewable sources is that currently they are mostly used to produce electricity but not fuels. This will be a great limitation in the future because, even assuming that electricity produced from renewable sources could become the main energy source of the planet, it will still be very improbable that the use of fuels will be totally abandoned. Indeed, as we can see in Figure 1.4, current energy consumption is made of electricity only for the 22%, while almost 80% is in form of fuels.[7] This problem, mixed with the environmental issue and the control of CO_2 emissions, leads to the need of a clean, easy to store, safe, non-toxic alternative for the near future. Among all the candidates, hydrogen is considered a promising choice since it produces water as by product, thus its carbon footprint is zero. However the use of hydrogen as fuel suffers from some serious limitations, such as the absence of a large-scale technology for its production and storage, or transportation issues, linked to the risk of leaking and explosion (it has the highest energy density by weight, but also a low energy density by volume). Unfortunately, on the Earth free H_2 cannot be found and it has to be obtained from another source in order to be employed, such as water, through molecular splitting. However, the reaction is thermodynamically and kinetically disfavored, water splitting in fact requires a free energy ΔG^0 of 237 KJ mol^{-1} or 2.46 eV per mol of hydrogen produced.[8] To overcome this limit without losing the benefit of introducing an environmentally friendly fuel, the use of renewable sources, such as solar energy, to produce hydrogen is the only realistic option.

1.2. Semiconductors & The Photovoltaic Technology

One of the technologies that can be used to trap and convert solar energy into a different energy form, is photovoltaics (PV), which allows direct transformation of sunlight into electricity without the production of waste, even though the amount of waste generated during the manufacturing process of the devices and after their end-of-life, is not negligible.[9] Apart from the environmental issue, PV technology suffers from some drawbacks such as the not-constant power production and the relatively high cost of converted energy (0.20 – 0.30 $/KWh) compared to the electricity generated from coal or natural gas (0.09-0.14 and 0.06-0.12 $/KWh, respectively).[10] While until the 90s this technology remained mostly confined into specialized applications, in the new Millennium the start of the mass-production of these devices allowed to spread their use in several sectors of the society and the development of new systems increased exponentially (Figure 1.5). The basis for the most common PV devices are semiconductors, because they can exhibit the photoelectric effect, according to which after irradiation with light, an electron is emitted.

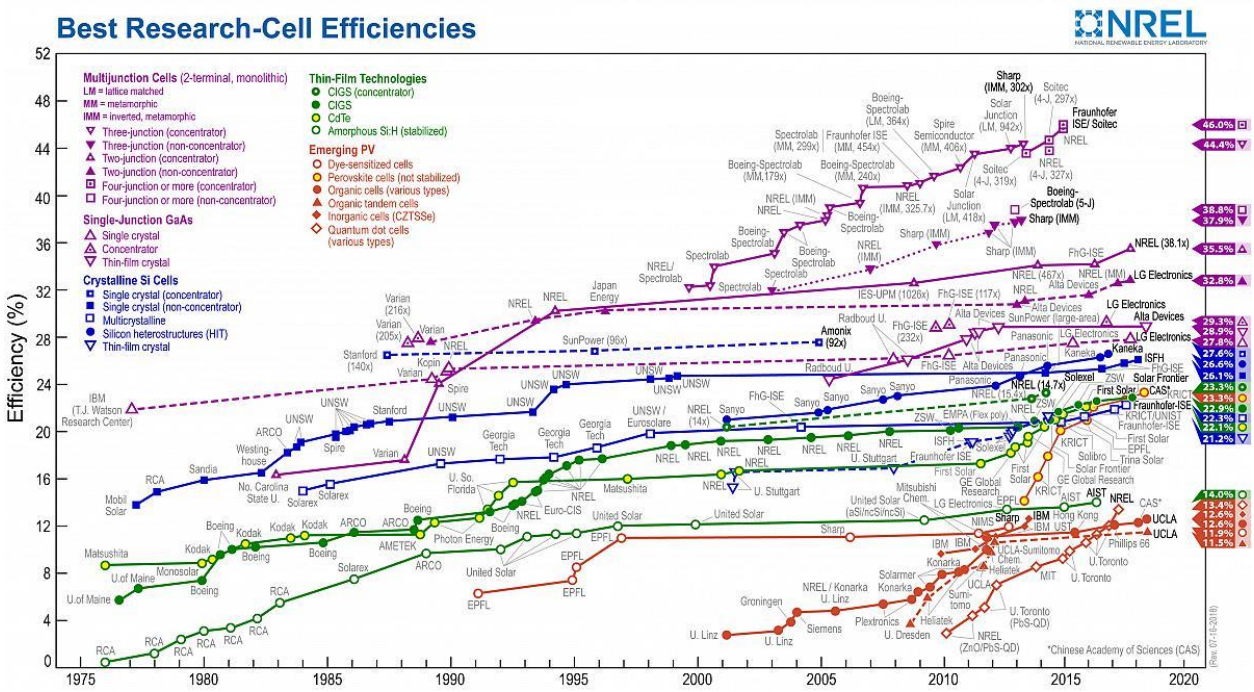

Figure 1.5 Evolution of the photovoltaic technology.[11]

Semiconductors, in their natural state, are poor conductor materials with an electrical resistance halfway between those of the conductors and the insulators. The reason of their low conductivity lies in their electronic structure. To generate an electric current a flow of electrons is required, but this cannot happen in the valence band because it is filled, while the existing band gap with the empty conductive band, at room temperature, allow only a small amount of charge to be promoted and be able to flow, resulting in a poor conductivity in standard condition (Scheme 1.1).[12]

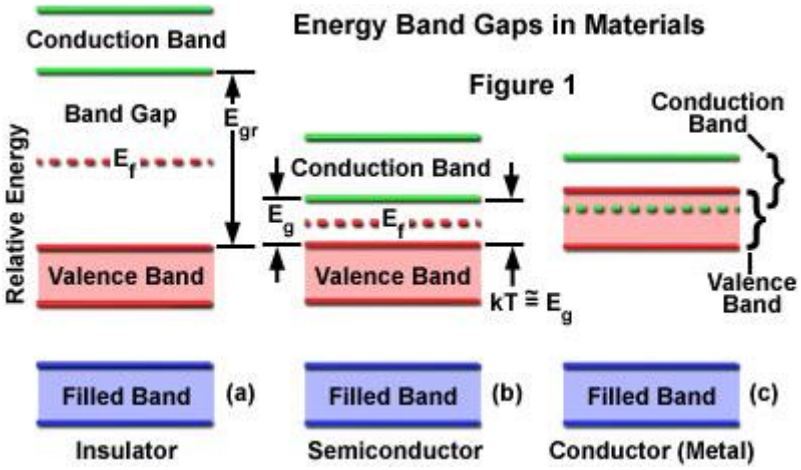

Scheme 1.1 Description of the electronic bands in insulator, semiconductor and conductor materials.[13]

However, the conducting properties of these materials can be easily altered either by varying the temperature (increasing it will increment the number of charges promoted to the conductive band), using light (photoelectric effect), by applying an external field (a process called "gating"[14]) or by the controlled introduction of impurities into the crystal structure ("doping"[12]). In particular, the doping process (Figure 1.6) greatly enhances the number of charge carriers within the material either by creating free holes ("*p*-type doping", realized by introduction of atoms with less electrons than the main

material) or with free electrons ("*n*-type doping", with atoms having more electrons). When two layers with different doping are put in contact, a semiconductor junction is created.

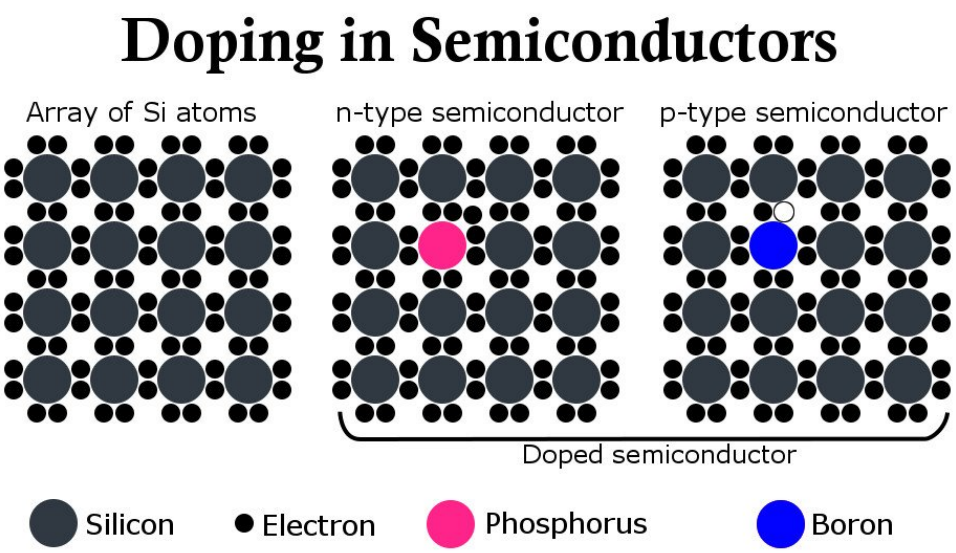

Figure 1.6 Representation of the doping into silicon crystals.[15]

For these reasons, semiconductors are widely used in electronic devices from the last decades of 20th century, even if the first practical applications date back to the early 1900s, in diodes, transistors and integrated circuits,[16] that nowadays are still some of the main applications for these materials. Semiconductors have been widely used also in PV devices from the very beginning, in 1954, with the construction of the first silicon-based solar cell at Bell Laboratories.[17] These materials usually play a key role in this kind of devices and they have been the target of intense studies focused on the increment of the efficiencies and the reduction of the manufacturing cost of final cells. For that reason, solar cells can be classified in three different categories based on the semiconductor used in their construction, which then determine the working mechanism and the final physical properties of the device.

- **First Generation: Silicon-based Solar Cells**

Historically the first type of PV cells ever invented, nowadays they are also the most diffused on mass-production scale. Depending from the nature of the starting material used, monocrystalline or polycrystalline silicon, the characteristics of the final device can be different either in manufacturing cost and efficiency. The modules are composed by several *p*-*n* junction cells connected either in parallel or in series; a single junction consists of two layers of crystalline silicon doped with an element of Group III (typically B or Al) for the positive side and with atoms of Group V (P or As are the most common) for the negative one. An electric field is created when the electrons naturally flow from the *n*-side to the positive one. Absorption of a photon on the surface of the silicon wafer promotes an electron to the semiconductor conduction band that first migrates on the *n*-junction and then, through an external circuit, recombines with a vacancy present on the *p*-side.[18] These cells exhibit high efficiency (respectively, 22-23% for monocrystalline silicon-based and 18-19% polycrystalline silicon-based solar cells, for a definition of photovoltaic efficiency see below) and long durability but the cost of the high quality silicon needed for their fabrication is still quite high. Furthermore, they also require a specific orientation towards the sunlight to be able to work at their maximum efficiency.

- **Second Generation: Thin-Film Solar Cells**

The so-called "thin-film" solar cells owe their name to the fact that they are much thinner than the silicon-based solar cells. With the first generation of photovoltaic devices they share the working mechanism, that it is still based on a *p*-*n* junction, but are composed of different materials. In this case, the *n*-side is usually composed by cadmium sulfide (CdS), while various inorganic semiconductors can be employed as the photoactive *p*-side material, influencing both the efficiency and the total cost of the cell. The most commonly used materials for the positive layer are: a) Amorphous silicon,[19] which is the most developed and cheap technology, but also the one providing the lowest efficiency; b) Cadmium telluride (CdTe),[20] which has a good cost/efficiency ratio, although the toxicity of the material could be a limiting factor for its use on large scale; c) Copper indium gallium selenide (CIGS),[21] which has an extremely high absorption coefficient that allows to build very thin cells with good efficiency and a reasonable cost, however the components are still toxic and quite rare; d) Gallium arsenide (GaAs): cells made with this alloy reached the top world value in terms of efficiency of a single-junction device, but the high cost of the active material relegates their use only in extremely high-tech applications (i.e. in spacecrafts). Although some of these technologies can compete with monocrystalline silicon-based solar cells in terms of efficiencies, they still lag behind in terms of installations, representing approximately only 10% of the global PV market.

1.2.1. Third Generation: Emerging Photovoltaics

Emerging photovoltaics represent new types of solar cells theoretically able to surpass the Shockley-Queisser limit, i.e. the maximum efficiency output for a classical PV device, which is around 30-40%, depending on the semiconductor band gap.[22] There are few methods to overcome this limit. One possibility is to build multi-junction solar cells containing several thin layers of photoactive materials with different band gaps, in order to absorb a wider range of light wavelengths. Alternatively it is necessary to build devices based on a different working mechanism. This last option also implies the possibility to employ new materials with different optical and electronic properties compared to traditional semiconductors, indeed a huge research effort has been made in the search of these alternatives. In particular, both the two most promising technologies of this generation, Dye Sensitized Solar Cells (DSSC) and Perovskite Solar Cells, are based on different semiconductors materials than those described above. While DSSCs have a different working mechanism compared to classical PV cells (see Chapter 1.3.1), perovskite-based ones[23] are composed by a *p*-*i*-*n* junction in which the photoactive material is an hybrid compound with generic formula $AlkNH_3PbX_3$ and crystalline structure analogous to that of natural perovskite ($CaTiO_3$) (Figure 1.7). This compound (the "i" of the junction) generates the charge carriers which migrate to the corresponding electrode passing through the *p*- and *n*-layer, respectively the hole transport material (HTM, the most used one is an organic compound called spiro-OMeTAD) and the electron transport material (ETM, typically TiO_2). Despite being the most promising among all third generation solar technologies, in particular due to a maximum efficiency well beyond 20%,[24] this technology has some serious drawbacks related to the use of toxic Pb-containing materials and the poor long-term stability of the devices, especially in presence of water.

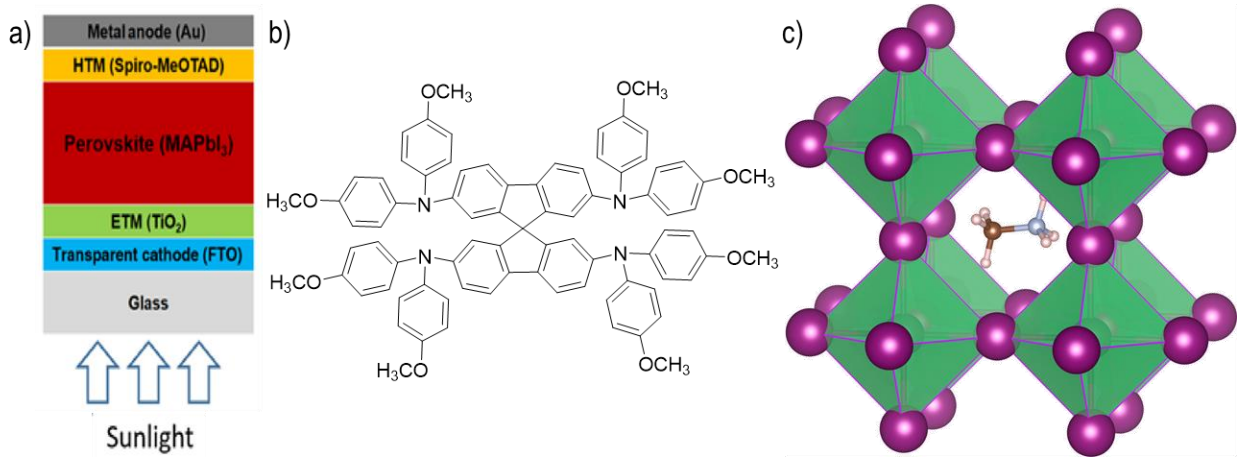

Figure 1.7 (a) Scheme of a Perovskite solar cell; (b) Spiro-OMeTAD structure; (c) $CH_3NH_3PbX_3$ crystal structure.[25]

In this context, where the best performing compounds are either expensive or toxic, the use of a material which is stable, nontoxic and commercially available at low price is a valid alternative. For these reason, the use of TiO_2 and ZnO, two oxides that perfectly fit the profile for efficient and cheap semiconductors, have been extensively studied during the past years. Regarding the photovoltaic technologies, they have been particularly used in both perovskite and DSSC, where TiO_2 is the most used semiconductor. The excellent results obtained in the field of DSSC have also been extended to other possible applications for energy production, as for instance in the photocatalytic H_2 production.

1.2.2. Traditional Water Splitting

The main difficulty arising from the production of hydrogen from water splitting is the need to couple one-photon reactions to multi-electrons processes. In fact, while usually only one electron can be made available after the absorption of one photon, two electrons per molecule of hydrogen and four electrons per molecule of oxygen evolved are needed during the water splittin process. Therefore, to perform the electrochemical photolysis of water, there are two main approaches: not integrated systems (such as a PV system coupled with an electrolyzer (in which a flow of electrons is granted by the solar cell), or integrated systems, which consist of photocatalytic technologies and photoelectrochemical cells. While the second class of devices is still in a laboratory scale, the first one has been studies for longer time and the production of H_2 with these methods is already possible, although the costs are still too high to be compared with hydrogen produced by methane reforming.[26] For that reason, this technology is employed only when high purity hydrogen is needed. In recent years the focus moved from the optimization of the tandem PV-electrolyzer systems (in which field good performances have already been reached) to the use of the photocatalysis, considered promising since it is able to directly convert the sunlight to chemical energy, skipping the electricity production step. In view of the difficulty to find a material able to act both as catalyst and light-harvester, the research focused on the development of multicomponent systems, where these two roles are fulfilled by separated components. Starting from 1972, with the work of Honda and Fujishima[27] on water splitting using a *n*-type TiO_2 electrode (acting as photoactive material) connected to a platinum black electrode, the use of semiconductors in this field was deeply studied for their capability to either interact with light and being able to ensure a good charge transport, including oxides, sulfides, nitrides and hydroxides.[28] While the record in quantum efficiency (56% in H_2 production) was established for $NiO/NiTaO_3$ under UV irradiation,[29] TiO_2 still plays a prominent role as semiconductor for this application. Even though its activity and quantum efficiency

are lower than those of many other materials, its photo- and chemo- stability, conjugated with low cost and low environmental impact, make TiO_2 the most used semiconductor in the field.[30]

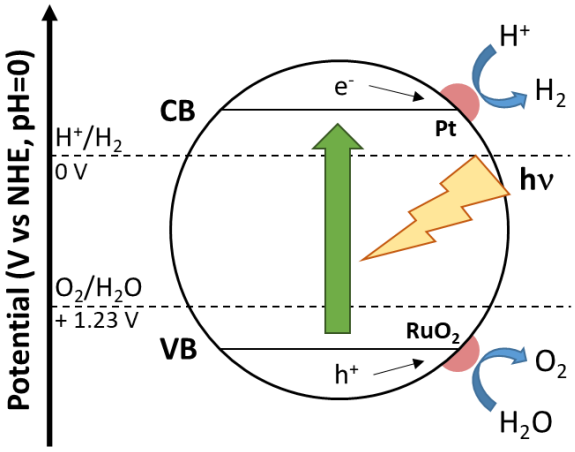

Figure 1.8 Water splitting mechanism on semiconductors with noble metals loading (RuO_2 is an oxidation catalyst)

The working mechanism for water splitting over a semiconducting photocatalyst mediated by suitable redox co-catalysts is briefly represented in Figure 1.8. To make the photocatalytic reactions work, the CB potential of the semiconductor has to be more negative than the redox potential of the couple H^+/H_2, while the VB energy level has to be more positive than the redox potential of O_2/H_2O. After the absorption of a photon with an energy equal or higher than the band gap, a e^-/h^+ couple is generated. Then, charge separation occurs (e^- in the CB, while h^+ in the VB) and the two species migrate from the bulk to the surface of the semiconductor, where are transferred to the proper catalyst as the main responsible for the two redox reactions.[31] A semiconductor alone can perform water splitting if it has the right energy potential for both the conduction and the valence band, but the coupling with proper catalysts make the process more efficient.

One of the main drawbacks related to this kind of applications is TiO_2 large energy band gap (around 3.0-3.2 eV), requiring a UV radiation to allow the promotion of one electron to the conduction band, that is only the 10% of the total light output of the Sun. A possibility to enhance titania light-harvesting properties is to sensitize it with a compound able to absorb also the visible and IR radiation, in order to cover most of the Sun emission spectrum. Then, in order to make use of the augmented light-absorption capability, the excited sensitizer has to be able to transfer electrons to the semiconducting layer where it is adsorbed. This process, called electron injection, can occur only if the LUMO energy level of the adsorbed compound is higher than the energy of the TiO_2 conducting band. Finally, to be able to exploit this process over and over again and allow the continuous flow of electrons from the sensitizer, it has to be regularly reduced by another species.

In the following sections the applications of sensitized TiO_2 films in photovoltaic devices will be discussed. In particular, the use in DSSCs and in processes for H_2 production will be presented along with their working principles.

1.3. Dye-sensitized Solar Cells

Introduced for the first time in 1991 by Grätzel and O'Regan,[32] dye-sensitized solar cells are considered one of the most promising alternatives to the classical silicon-based solar panels, even if nowadays they are challenged by the quick development of the perovskite technology (originally introduced as a variation of the typical DSSC structure[33]). The DSSC working mechanism is completely different form the other photovoltaic technologies and directly inspired by natural photosynthesis; for these reasons these devices possess unique features compared to the other PV cells, such as an easy manufacturing, low cost (absence of high quality materials and rare elements), excellent performances under ambient indoor light (with maximum efficiency close to 32%, near the theoretical limit[34]) and high temperature and great flexibility in terms of weight, colors, shape and transparency. While the efficiency are still lower that the classic PV (14.3% in laboratory test for a single dye[35] versus 26.3% for a silicon heterojunction[36]), the other particular characteristics open to their use for indoor application and in small electronic objects.

1.3.1. Structure & Working Mechanism

A classical DSSC device is composed by five main components[6,37] (Scheme 1.2).

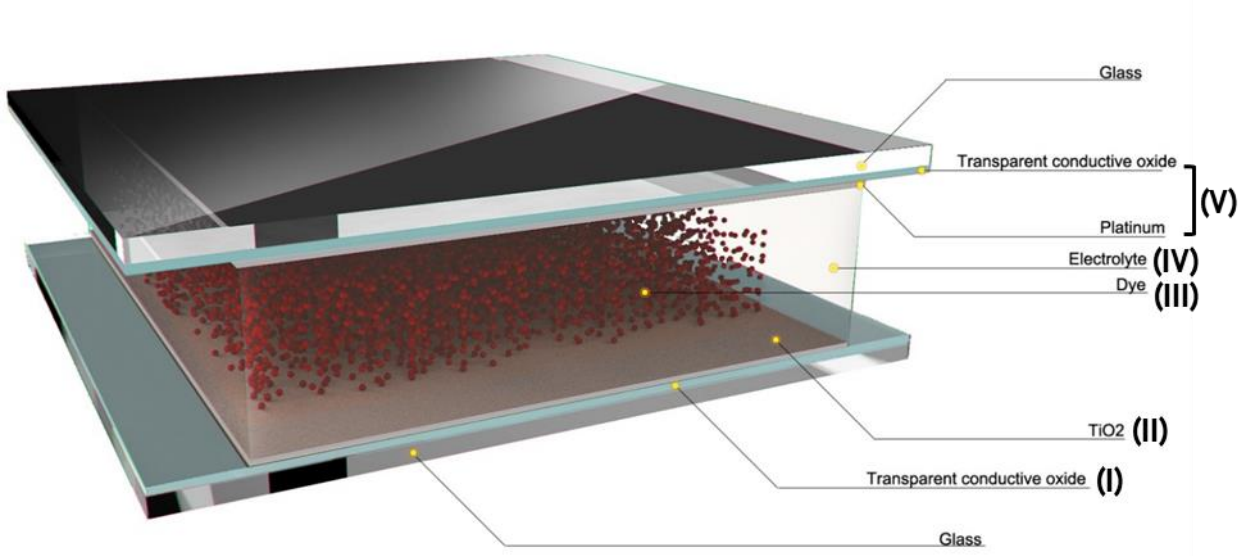

Scheme 1.2 Structure of a dye sensitized solar cell.[38]

- The conductive substrate (**I**), that is composed by a glass electrode coated with a transparent conductive oxide and is the most expensive component of the entire cell. The most used conductive materials are tin oxide doped with fluorine (FTO) and indium-tin oxide (ITO), while common alternatives are polymeric films[39] or metallic fibers.[40]
- A semiconducting-thin film (**II**) that is deposed on top of the substrate and together with it constitutes the photoanode of the cell. The semiconductors used are in the mesoporous crystalline form in order to maximize the available surface area for dye sensitization. The most common choice is TiO_2 in its anatase form, obtained by means of hydrothermal growth, because it has the more suitable band gap for this application; changing the conditions of particles preparation allows to tune their size, shape and diameter. After

mixing with polymeric additives, the obtained paste is deposited onto the conducting substrate and sintered at 450°C in order to remove the organic components and to make the electric connections between titania nanoparticles. The film usually has an average thickness of 5-15 μm and a huge internal surface of about 1000 cm^2 for conducting substrate unit area (cm^2). In several cases, the entire photoanode receives some additional treatments, i.e. deposition of blocking[41] or light-scattering[42] layers or overcoating with $TiCl_4$,[43] in order to maximize cell efficiency. Common alternatives to the TiO_2 are zinc oxide (ZnO),[44] that has a higher electron mobility but lacks in chemical stability, SnO_2[45] or Nb_2O_5.[46]

- A photosensitizer[6,37] (**III**) that is necessary in order to maximize the light-harvesting properties of the device and to start the generation of electric current. To be able to work, the photosensitizer needs to be permanently linked to the semiconductor. The sensitization is realized by immersion of the photoanode in an organic solution of the proper dye for several hours. A wide library of compounds has been developed, from natural dyes[47] to transition metal complexes[48], though chlorophyll-like pigments[49] and every category has demonstrated merits and disadvantages (Figure 1.9). In particular, the category of the metal-free D-π-A dyes will be presented and their properties discussed (see Chapter 1.5).

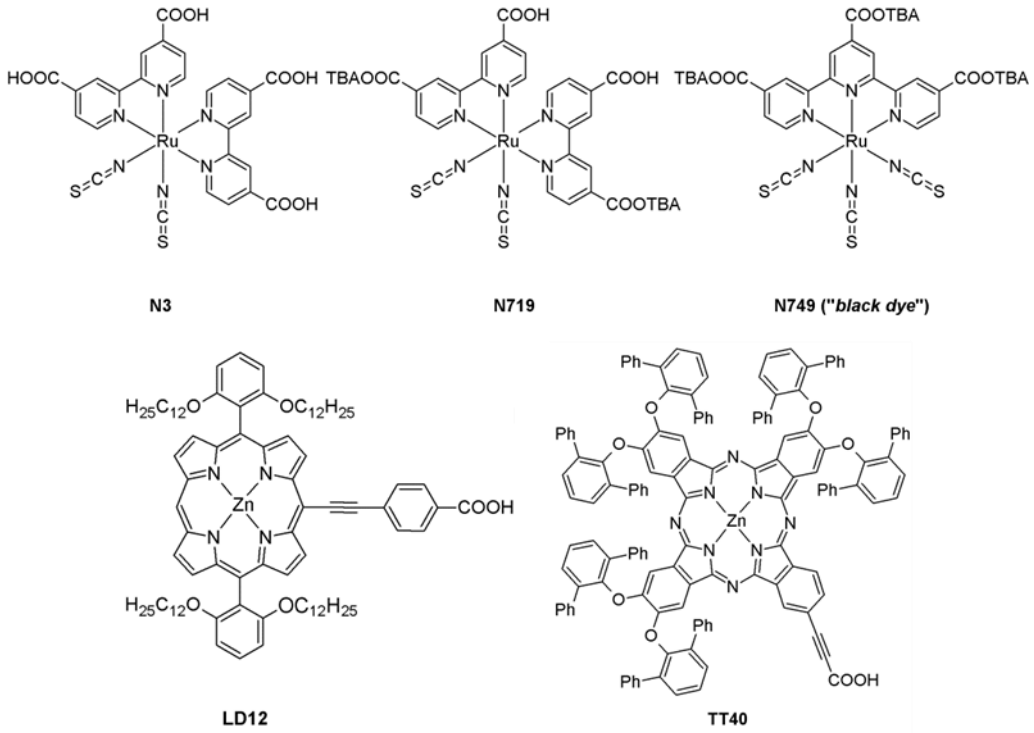

*Figure 1.9 Some examples of transition-metal complexes (**N3**, **N719**,**N749**)[48], porphyrin (**LD12**)[49a] and phthalocyanine (**TT40**)[49b] dyes used in DSSC.*

- An electrolytic solution (**IV**) that is used to fill the space between the two electrodes and ensure the electronic communications between them. To be used in DSSC, the electrolyte has to fulfill some requirements, such as to exhibit a long-term stability in the operations conditions, not to cause the desorption or the degradation of the sensitizer and not to display a huge absorption in the range of visible light. Nowadays, liquid electrolytes are still the most commonly used due to their high conductivity, low viscosity and easy preparation, but their drawbacks, such as the potential leaking and evaporation of the solvent, led to the employment of alternative systems, such as quasi-solid-state electrolytes[50] and solid-state

transport materials[51]. Usually, the liquid electrolytes are composed by a high-boiling point liquid (like nitriles or ionic liquids) in which a redox couple is dissolved.[6] Iodide/triiodide is the simplest redox couple to be used because it has a good solubility in organic media, a suitable redox potential, high conductivity and low cost. More recently, metalorganic $[Co]^{2+/3+}$ complexes have also been applied: thanks to the possibility to tune their redox potential through modifications of the ligands, they showed very good results and have been recognized among the best performing redox couples for DSSC.[52] In addition, in several cases additives (i.e. the 4-*tert*-butylpyridine, TBP[53]) are introduced in the electrolyte solution to optimize DSSC performances by means of various mechanisms.

- The counterelectrode (**V**) that is usually constituted by a conductive glass substrate coated with a nanometric layer of platinum. Due to the high price of the platinum, the research of low cost alternatives is very popular and use of many highly conductive materials such as carbon nanotubes[54] (CNT) and conductive polymers[55] has already been described.

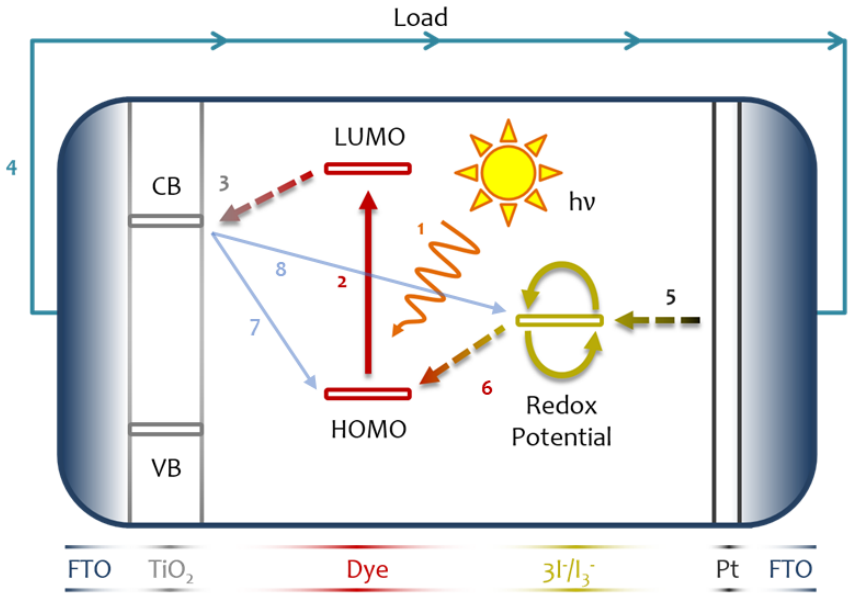

Figure 1.10 Photoelectrochemical processes involved in the working mechanism of a DSSC.

The working mechanism of a DSSC is reported in Figure 1.10.[6,37] Initially the photosensitizer absorbs sunlight (**1**), promoting an electron from the HOMO to the LUMO (**2**). The excited dye then injects the electron into the conductive band of the semiconductor (**3**) with an estimated time for the process of 100 ps.[56] Then the electrons flow through the external circuit (**4**) and arrive to the counterelectrode, on which the redox couple present in the electrolyte is reduced (**5**). Finally, the circuit is closed with the regeneration of the dye in its ground state by the redox mediator in its reduced form (**6**). This last process requires that the ground state oxidation potential of the dye is lower (more positive) than the redox potential of the mediator to achieve a good regeneration.

In the cells, during the cycles, are always present also some side-processes that limit the device performances, the most important of which is the recombination of the injected electrons both with the oxidized dye (**7**) or the redox couple (**8**).

1.3.2. Cells Characterization

The characterization of a DSSC device requires measurement of a series of defined parameters that allow the comparison between different cells.[6,37] They will be shortly present in the next sections.

- **Incident Photon-to-current Conversion Efficiency (IPCE)**

The IPCE is defined as the ratio between the number of electrons that flow through the external circuit and the number of incident photons striking the device for any given wavelength, and is given by Equation (1).

$$\mathrm{IPCE}(\%) = 1240\ (\mathrm{eV\ nm})\ \frac{\mathrm{J_{ph}\ (mA\ cm^{-2})}}{\lambda\ (\mathrm{nm})/\ \mathrm{I(mW\ cm^{-2})}} \qquad \text{Eq. (1)}$$

λ and I are respectively the wavelength and the intensity of the monochromatic light, while J_{ph} is the generated photo-current. The plot of the IPCE vs the excitation wavelength is a very useful tool to evaluate a new photosensitizer for DSSC (Figure 1.11). The IPCE is either strictly related to some intrinsic characteristic of the dye, the light-harvesting properties and the injection quantum yield, as well to other external factors, such as the amount of dye adsorbed on the semiconductor and the electron transfer process through the external circuit. The maximum IPCE value for DSSC is capped around 80-85%, while experimentally is impossible to reach the 100% due to the loss in absorption and reflection caused by the FTO conductive glass.

- **Photocurrent/voltage curves (J/V curves)**

The global performances of a complete cell can be evaluated by measuring the photocurrent/voltage curve (Figure 1.11) under simulated sunlight in standard conditions of range of wavelengths and power (in particular, usually the standard terrestrial spectra AM 1.5 under 100 mW cm^{-2} of irradiance is used). Recording the J/V curve is quite useful because all the device key parameters (V_{oc}, J_{sc}, *ff* and η) can be extracted from that graph.

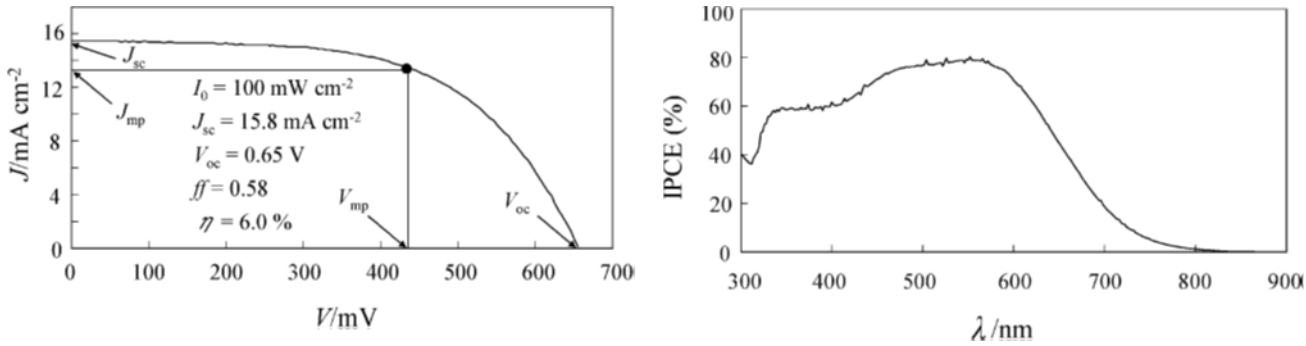

Figure 1.11 Example of a typical J/V curve (left)[37] and of a typical IPCE spectra (right)[57] of a DSSC.

- **Open-circuit voltage (V_{oc})**

The V_{oc} parameter is the difference in electric potential between the two electrodes while the cell is irradiated and the circuit is open. It can be calculated from the following equation:

$$\mathrm{V_{oc}} = \left[\frac{\mathrm{E_{CB}}}{\mathrm{e}} + \frac{\mathrm{k_b T}}{\mathrm{e}} \ln\left(\frac{\mathrm{n}}{\mathrm{N_{CB}}}\right)\right] - \mathrm{E_{REDOX}} \qquad \text{Eq. (2)}$$

In the equation, E_{cb} is the energy level of the conduction band of the semiconductor used in the anode, *e* is the elementary charge, K_b is the Boltzmann constant, *T* is the absolute temperature, *n* is the number

of electrons in the TiO_2, N_{cb} is the effective density of the conduction band states and finally E_{redox} is the redox potential of the electrolyte. The maximum V_{oc} value depends on the difference between the potential of the conduction band (E_{cb}/e, the potential related to the TiO_2 Fermi level, usually in the range between -0.5 and -0.4 V *vs.* NHE) and the electrolyte redox potential. If the redox couple is I^-/I_3^- (E_{redox} = 0.4 V *vs.* NHE), then the maximum theoretical V_{oc} value stands between 0.8-0.9 V, but usually the electron recombination processes that happen at the titania interface (channels **7** and **8** in Figure 1.10) reduce this value.

Another factor affecting the V_{oc} value is the molecular dipole at the dye/TiO_2 interface: having a dipole moment pointing away from the surface leads to a decrease in the potential of the TiO_2 conduction band, increasing the V_{oc}.[58] This phenomenon can be reversed by the use of additives, like 4-*tert*-butylpyrine (TBP), that by means of an opposite effect are able to shift the TiO_2 E_{cb} to more negative values.

- **Short-circuit photocurrent density (J_{sc})**

J_{sc} is the photocurrent per unit area (mA cm^{-2}) when a DSSC under irradiation is short-circuited (it happens when the electrical impedance and the difference in electric potential are close to zero), and represents the maximum value of photocurrent density produced. The J_{sc} value is strongly related to the dye photophysical and electrochemical properties. For these reasons, to increase the J_{sc}, a proper dye design is mandatory, in order to maximize its interaction with the semiconductor and to adjust its spatial orientation on the TiO_2 surface.

- **Fill factor (*ff*)**

The fill factor is defined as the ratio between the cell maximum power output ($J_{mp}V_{mp}$) and the product of J_{sc} and V_{oc} and it is given by the Equation (3).

$$\mathrm{ff} = \frac{J_{mp}V_{mp}}{J_{sc}V_{oc}} \qquad \text{Eq. (3)}$$

On the J/V curve (Figure 1.11) is represented by the ratio between the area of the rectangle having J_{sc} and V_{oc} dimensions, and that described by $J_{mp}V_{mp}$. The maximum theoretical value is 1, corresponding to an ideal diode behavior, but experimentally the *ff* is reduced due to the power dissipation events occurring in the various interfaces present inside the real cell. For these reasons, this value is strongly related to the device practical fabrication.

- **Solar energy-to-electricity conversion efficiency (η)**

The η value gives a global evaluation of all the processes that are present inside the cell and for that reason is often the value use to compare different cells. It is defined as the ratio between the DSSC maximum electrical output and the energy of the incident sunlight (I_0, generally 100 mW cm^{-2} in the standard AM 1.5 conditions).

$$\eta\ (\%) = \frac{J_{sc}\ (\mathrm{mA\ cm^{-2}})V_{oc}\ (\mathrm{V})\mathrm{ff}}{I_0\ (\mathrm{mW\ cm^{-2}})} \qquad \text{Eq. (4)}$$

η values can be increased by optimization of all the other parameters that have been previously described and are present in Equation (4), most of which depend on the properties of the photosensitizer used and its electronic communication with the other components of the cell. For these reasons, molecular optimization of the dye is a crucial process for obtaining highly performing DSSCs.

1.4. Photocatalytic H_2 Production

In recent years water splitting has been the object of many studies but its efficiency is still very low and far from reaching a real viability.[59] The process suffers from serious drawbacks mainly due to its working mechanism, for the complex research of a suitable photocatalyst capable to catalyze both the two processes, but also related to the production of two different gases (H_2 and O_2) in the same reactor, requiring introduction of an additional gas separation procedure. Moreover, optimization of catalyst or sensitizer is often carried out by considering only one semi-reaction, in order to simplify the system avoiding the dependence from the partner process; to do that, sacrificial electron donors (SED) or acceptors (SEA) are used to mimic the effect of the other semi-reaction[60] (Figure 1.12).

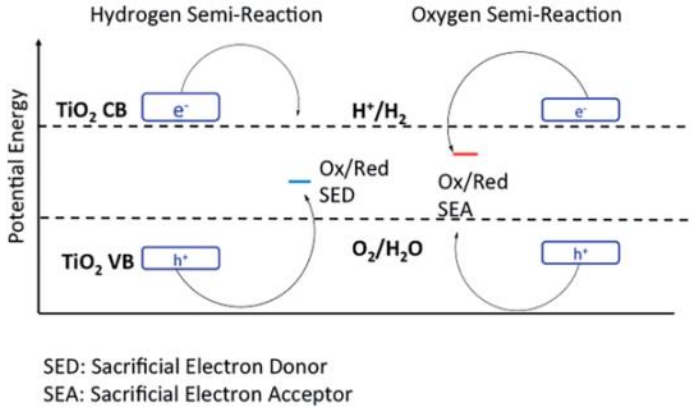

Figure 1.12 Mechanism for hydrogen and oxygen production in presence of sacrificial agents.[61]

Although photocatalytic H_2 production is possible also with the employment of a single semiconductor,[62] several systems described in the literature have been inspired by the working mechanism of DSSC and are composed by a semiconductor, a sensitizer, a catalyst and a sacrificial electron donor (SED).[63]

- **Semiconductor**: The main role of the semiconductor is to ensure the communication between the molecular components of the system and the catalyst. For this reason, it has to be chemically and physically stable in the working conditions, have an accessible surface area, high charge mobility and fast electron injection rates.[64] The materials that show almost all these features are the metal oxides, but they generally have a large band gap and then are able to absorb only UV light (Figure 1.13). Cu_2O and metal chalcogenides, that have a narrow energy gap, have been used alone, but these materials suffer from photo-corrosion in water and their properties are difficult to tune.[65] For these reasons, usually the semiconductors are sensitized with a dye capable to increase the light-harvesting properties of the system, to reduce the side reactions given by highly reactive VB holes following direct band gap excitation and increase the semiconductors stability. In analogy to DSSC, the most studied and employed semiconductor is TiO_2, in the form of micrometer sized agglomerates of nanoparticles; indeed, the conductive network created by the nanoparticles can facilitate charge transfer and reduce recombination phenomena.[66]

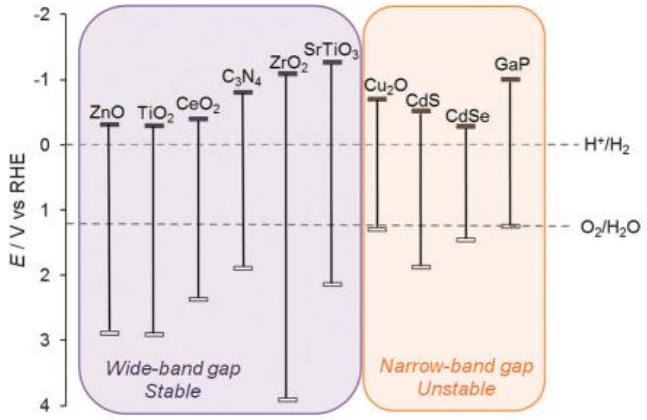

Figure 1.13 Conduction band and valence band potential (in V vs. RHE) compared to the electrochemical standard potentials of water oxidation and proton reduction.[67]

- **Sensitizer**: The photophysical and electrochemical requirements a dye has to fulfill in order to be suitable for photocatalytic H_2 production are very similar to those needed in DSSCs, namely efficient electron injection, broad range of light absorption, high molar extinction coefficient and stability during multiple redox cycles. For these reasons, usually the most commonly employed dyes are similar to those showing the best performances in DSSC, displaying some modifications in order to increase the hydrophilicity or enhance the anchoring stability in presence of water.[63,68] Apart from D-π-A dyes, metal-based dyes (i.e. ruthenium complexes), porphyrins and natural dyes have been widely employed. More recently, other alternatives have been tested, such as carbon dots[69], but despite the first promising results, their photophysical properties have still to be explored.
- **Catalyst**: Directly responsible for the H_2 production, is defined by three key parameters, the onset potential for catalytic reduction (E_{red}), the turnover number (TON) and the turnover frequency (TOF) at a given potential.[70] E_{red} is particularly important because it has to be more positive than the CB potential of the semiconductor and determines the overpotential needed for the reaction.[71] A larger difference in potentials between E_{red} and the CB it results in faster catalytic rates. Platinum and other noble metals[72] are the most studied catalysts because they possess all the requirements: they are thermodynamically stable and reversible towards the proton reduction (and also water oxidation) and they require a small overpotential to be able to work. However, these materials have some drawbacks, for example they are rare and expensive a factor that hamper the scale-up of the devices. A recent alternative is constituted by molecular catalysts inspired by the hydrogenases (natural enzymes able to drive proton reduction to molecular hydrogen) based on transition metals for their low cost and atom efficiency, but for the moment stability and immobilization issues hamper their use.[73] Regarding the use of platinum, usually it is deposited as nanoparticles on the surface of the semiconductor either by impregnation[74] or photodeposition.[75]
- **Sacrificial Electron Donor (SED)**: The choice of the SED for phocatalytic H_2 production is quite delicate because in addition to dye regeneration, the SED also plays a key role in defining the pH of the solution (their optimal working condition is with a pH close to their pK_a value) and it can interfere with all the reactions that lead to H_2 evolution.[76] It has to be pointed out that, depending on the particular interaction, this last problem can either lead to non-innocent interactions that reduce the catalytic performances or to additional H_2 evolution given by the SED oxidation.[77] The most commonly used electrondonors are triethanolamine (TEOA) and EDTA, but a wide range of compounds have been used, including organic acids (i.e. ascorbic acid or formic acid),

alcohols (mostly MeOH[61,78]) and inorganic ions or redox couples (i.e. sulfite or IO_3^-/I^- and Fe^{2+}/Fe^{3+})[68]. In particular, the use of SED from renewable feedstocks (such as EtOH[79]) in recent years gained huge attention due to the possibility of carry out the scale-up of these devices with limited environmental impact.

Finally, it has to be mentioned that also the pH of the aqueous solution has to be taken in account because it virtually influences all the interactions and the components of the system. For such reason, it is a key parameter for determining the activity. In fact, the pH influence the dye redox potential, its photophysical characteristics and anchoring capabilities, as well as the catalyst activity[103,80] and the SED redox activity[81], so its value has to be carefully decided while planning an experiment.

1.4.1. Working Principles

The working mechanism of photocatalyzed H_2 production resembles the that of DSSCs, with the difference that the TiO_2 does not transfer the electrons to an external circuit, but instead to the catalyst responsible for the H_2 generation.[61]

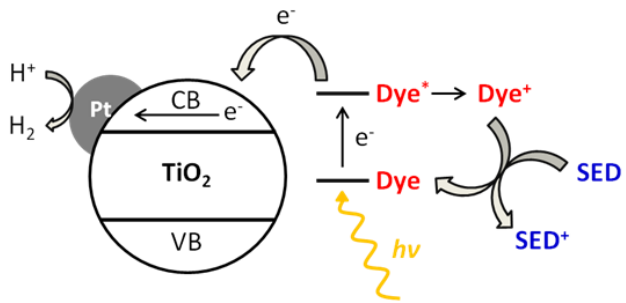

Figure 1.14 Graphical representation of the working mechanism for H_2 production over dye-sensitized Pt/TiO_2 photocatalysts.[79]

The working mechanism is depicted in Figure 1.14, while the reactions involved in a typical photocatalytic system for H_2 production are described by the following equations:

$$Pt/TiO_2/Dye \longrightarrow Pt/TiO_2/Dye^* \quad (1)$$

$$Pt/TiO_2/Dye^* \longrightarrow Pt/TiO_2(e^-)/Dye^{+\cdot} \quad (2)$$

$$Pt/TiO_2(e^-)/Dye^{+\cdot} + SED \longrightarrow Pt/TiO_2(e^-)/Dye \quad (3)$$

$$Pt/TiO_2(e^-)/Dye \longrightarrow Pt(e^-)/TiO_2/Dye \quad (4)$$

$$Pt(e^-)/TiO_2/Dye + H^+ \longrightarrow Pt(e^-)/TiO_2/Dye + \tfrac{1}{2}\, H_2 \quad (5)$$

$$Pt/TiO_2/Dye^* \longrightarrow Pt/TiO_2/Dye + h\nu \quad (6)$$

$$Pt/TiO_2(e^-)/Dye^{+\cdot} \longrightarrow Pt/TiO_2/Dye \quad (7)$$

The process starts with the excitation of the dye after absorption of a light photon (**1**), followed by injection of an electron into the conduction band of the semiconductor (**2**), with subsequent generations of a charge separated state. The dye is then immediately reduced by the SED to the ground state (**3**), while the electron is transferred from TiO_2 to the photocatalyst (**4**). Finally, the catalyst carries out protons reduction, producing molecular hydrogen (**5**). Many other pathways can take place during the process, reducing the overall

performances of H_2 production. Two of these parasitic pathways are especially responsible for limiting the efficiency of the whole process, namely the radiative relaxation of the dye to the ground state, hindering electron injection (**6**) and the hole-electron recombination between the semiconductor and the dye, due to slow proton reduction or dye regeneration (**7**). Both these side reactions have to be minimized in order to enhance the performances and the durability of the system. As in DSSCs, a proper tuning of the FMO energy levels of the dye is essential in order to make the system able to work. The energy of the dye LUMO level has to be higher (more negative *vs.* NHE) than the energy level of the CB of the semiconductor, because a potential difference between them is a requirement for an efficient electron transfer. The HOMO level also plays a strategic role in the whole mechanism because the regeneration process is a focal step of the entire process and a fast reduction of the dye from the SED must take place in order to guarantee an efficient activity and stability of the whole photocatalytic system. In this context, the affinity of the dye towards the aqueous solution plays a critical role too, because it influences the interaction with the water-dissolved SED and in turn the rate of the regeneration process.

1.4.2. Efficiency Parameters

Compared to DSSCs, the parameters that determine the performances for H_2 production are always relative to the reaction time. In fact, usually, the shape of the H_2 production graph *vs.* time is not a linear line, but consist in a different curve, which means that either there is an induction period for the first hours of reaction or the manifestation of a deactivation phenomenon. For that reasons, the rate of H_2 production is often used and the comparison between efficiencies obtained with different irradiation time experiments cannot be done. In the case of dye-sensitized system also the dye loading has to be taken into account to calculate efficiency (because it is the expression of the active sites) and then a normalization of the value of gas evolved or of the evolution rate on the weight of catalyst used is advisable. The most important parameters are presented in the next sections.[61,63,68]

- **Turnover number (TON) and turnover frequency (TOF)**

The TON value is the equivalent to that normally used catalysis. It is given by Equation (5).

$$\mathrm{TON} = \frac{\text{number of reacted electrons}}{\text{number of active sites}} = \frac{2 \times \text{moles of produced } H_2}{\text{moles of dye loaded}} \qquad \text{Eq. (5)}$$

The second part of the equation is the approximation that is really used after a measurement, since a molecule of hydrogen should be produced by the reduction of two protons. The TON depends strongly on the experimental conditions, in particular on the light source and its intensity, and has to be referred to the irradiation time (i.e. TON (5h) or TON (20h)). Along the TON, also the TOF value is used to compare different catalyst. It quantifies the activity level of the system by the number of catalytic cycle occurring at the center per unit of time and it is practically given by the following equation:

$$\mathrm{TOF} = \frac{\mathrm{TON}}{\text{unit of time}} \qquad \text{Eq. (6)}$$

- **Apparent (AQY) and Intrinsic (IQY) quantum yield**

The value of this parameter is one of the most used for comparing different catalytic systems because it is less dependent from the experimental conditions and is given by Equation (7).

$$\mathrm{AQY} = \frac{\text{number of reacted electrons}}{\text{number of incident photons}} = \frac{2 \times \text{number of } H_2 \text{ molecules}}{\text{number of incident photons}} \qquad \text{Eq. (7)}$$

As the TON, also the AQY is "translated" in measurable terms. It is called "Apparent QY" because not all the incident photons can be actively used by the catalyst and it is the equivalent of the IPCE for DSSCs. The number of incident photons can be experimentally measured by placing a silicon photodiode in place of the photoreactor. Due to its definition, this value is independent from the nature of the light used and can then be used also to compare dyes with different light-harvesting properties.

$$\mathrm{IQY} = \frac{\text{number of reacted electrons}}{\text{number of absorbed photons}} \qquad \text{Eq. (8)}$$

The intrinsic quantum yield (IQY) is given by the Equation (8) and express the real quantum yield of the process. However, the evaluation of the absorbed photons is quite difficult due to the light scattering that occurs while employing a heterogeneous catalyst and for this reasons is rarely used. The value of AQY corresponds to the IQY when all the striking photons are absorbed by the system.

- **Solar-to-hydrogen efficiency (STH) and Light-to-fuel efficiency (LFE)**

These two values are similar and both express the global efficiency of the system, intended as the conversion ratio of solar energy into chemical energy; they are the equivalent to the η parameter in DSSC.

$$\mathrm{STH}\ (\%) = \frac{F_{H_2} \times \Delta G^0_{H_2}}{S \times A_{irr}} \qquad \text{Eq. (9)}$$

$$\mathrm{LFE}\ (\%) = \frac{F_{H_2} \times \Delta H^0_{H_2}}{S \times A_{irr}} \qquad \text{Eq. (10)}$$

Where F_{H2} is the flow of H_2 produced (in mol s^{-1}), ΔG^0_{H2} and ΔH^0_{H2} are respectively the free Gibbs energy and the enthalpy associated to the H_2 combustion (respectively 237 × 103 J mol^{-1} and 285.8 × 103 J mol^{-1}), *S* is the total incident light irradiance (in W cm^{-2}) and A_{irr} is the irradiated area (in cm^2). Both parameters are rarely used because, differently than the η parameter in DSSCs, which is univocally defined for a PV device, their values depend from irradiation time and so can be compared only between systems that have been exposed to the light for the same time. Usually their value are low (inferior to 1%) and comparable to the efficiency of natural photosynthesis.[82]

In this PhD work we focused into the study of a particular category of sensitizer, called D-π-A dyes and the development of new molecules with this particular structure that can find application as key component in photo-activated devices. In the next section the properties of this particular category of dyes will be presented.

1.5. D-π-A Dyes

This class of dyes is composed by organic metal-*free* molecules characterized by a particular *push-pull* structure. They have been intensively studied since many years, especially for application as sensitizers for DSSC production,[83] due to their low production costs, high molar extinction coefficients and the possibility to finely adjust their photophysical and electrochemical properties by optimizing their molecular structure. This last feature relies on the particular block structure possessed by these dyes characterized by an electronrich donor group (D) and an electronpoor acceptor moiety (A), connected by a π-conjugated spacer (Figure 1.15). Of course such sensitizers need to be attached to the semiconductor, in order to let the process of electron injection to occur, thus an anchor moiety is needed

which is in almost all the case coincide with the acceptor group. Each of this three parts of the D-π-A dyes can be easily modified without altering the other two.[6,37]

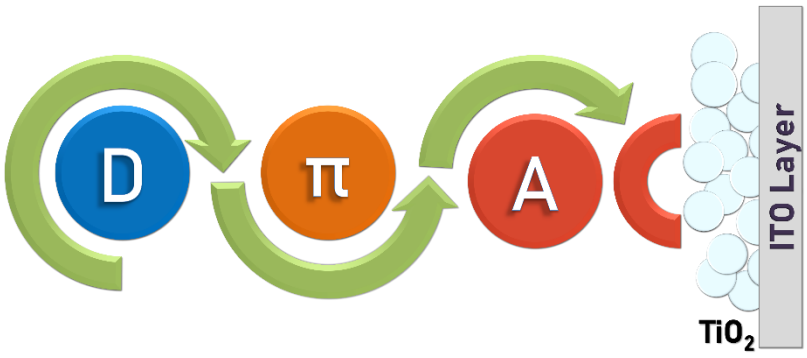

Figure 1.15 Representation of a D-π-A dye structure.

This particular design confers peculiar characteristics to the dyes, since having two groups with opposite electronic properties leads to a better localization of the frontier molecular orbitals (FMO) on these two parts of the molecule, the HOMO mostly localized on the donor part and the LUMO mostly located on the acceptor moiety. As a consequence, after light absorption an intramolecular charge transfer (ICT) between the two parts is observed, due to the electronic connection guaranteed by the π-spacer; in that way the electron density is transferred near the semiconductor surface and electrons can be injected into its conduction band.[32,37] Tuning the energy levels of both HOMO and LUMO, as well as increasing the light-harvesting properties of the molecule, can be achieved by replacing the electronrich and electronpoor part with stronger/weaker groups or by increasing the conjugation length of the π-spacer. Once the injection occurred, the spatial separation between the positive part of the oxidized dye, located on the donor, and the TiO_2 layer reduces also the possibility of recombination of the electrons in the conductive band with the dye radical cation. Aggregation of these compounds on the titania surface is one of the principal drawbacks in their use, together with the poor light absorption in the IR region. To minimize these effects, hindered groups such as long alkyl chains can be inserted in the planar structure of the dye or bulky co-adsorbents such as the chenodeoxychloic acid (CDCA, Figure 1.16) can be added to the dye solution used for electrode staining.[84]

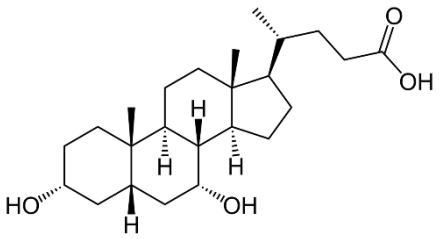

Figure 1.16 Structure of the chenodeoxychloic acid.

The most common structures used to optimize the design of these dyes (depending on their applications) will be presented below.

- **Donor Groups**

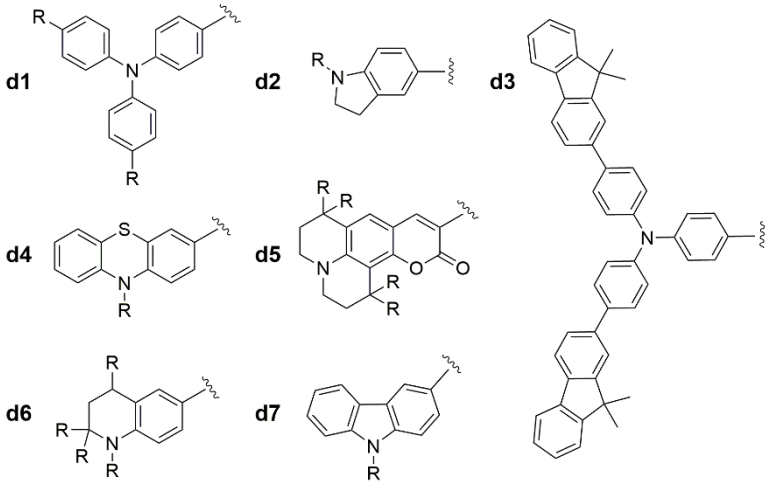

Figure 1.17 Examples of some donor groups structures.

The most used moieties are reported in Figure 1.17. The functionalization with additional donor groups (like –OR or -NR_2 groups) of this part of the molecule allows to tune the HOMO energy levels (mainly delocalized on the donor part) and consequently the absorption spectrum of the final compound. Another common modification is the introduction of bulky groups, in order to reduce dye aggregation. Triarylamines (**d1**,**d3**) are the most used donor groups due to their excellent electronic properties and the ease of functionalization. Used since 2004,[85] they have been functionalized in the 4,4' positions either with long alkyl,[86] alkyloxy[87] and thioalkyl[88] chains or further aromatic[89] and heteroaromatic[90] rings, *i.e.* the fluorenyl group[91] (**d3**), able to stabilize cation and anion radicals. The indoline group[92] (**d2**) is one of the best performing donor groups due to its outstanding electron-donating capability, influencing the maximum absorption peak as well, and simple synthesis. Indoline dyes exhibit also good stability and high molar extinction coefficients. Other donor groups widely used in recent years and worth to be mentioned are phenothiazine[93] (**d4**), coumarine[94] (**d5**), tetrahydroquinoline[95] (**d6**), exhibiting also a strong absorption in the IR region, and carbazole[96] (**d7**).

- **π-Spacers**

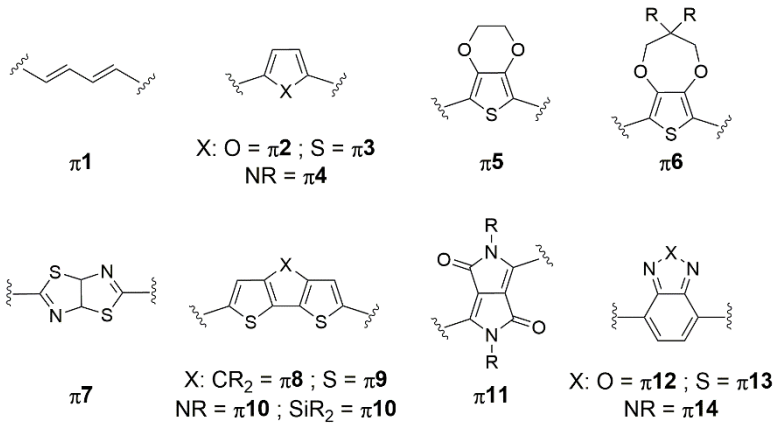

Figure 1.18 Examples of some π-spacer groups structures.

The π-bridge allows the electron conjugation between the other two moieties of the molecule and is the main responsible for the light-harvesting properties of the dye; extending the conjugation in fact shifts the maximum absorption peak and increases the molar extinction coefficient. For these reasons, many

different structures have been used as spacers (Figure 1.18), from single (hetero)aromatic rings[97] (**π2-4**) (i.e. thiophene is widely used due to its good polarizability, which facilitates charge transfer process) to polycyclic structures[98] (**π7-14**) (that can greatly enhance the absorption spectra), passing thought the use of a simple series of conjugated *E* double bonds (**π1**) (which are however less efficient as can undergo photoisomerization processes[95]). Use of electronrich rings, such as ethylendioxythiophene[99] (EDOT) (**π5**) or propylenedioxythiophene[100] (ProDOT) (**π6**) is also quite common because they can shift the maximum absorption peak of the molecule. The ProDOT ring is particularly interesting because during its synthesis it can be easily functionalized with alkyl chains on the central carbon between the two CH_2O groups. Introduction of bulky groups on the planar π-spacer is commonly used in order to reduce dye aggregation.

- **Acceptor/Anchoring Groups**

This moiety plays two main roles in the dye structure, it is in fact both responsible for bonding on the semiconductor surface, as well as for electron injection. Usually the same group that acts as acceptor is also the anchoring one, but this is not compulsory because the sole requirements for a good injection is that the TiO_2 and the acceptor part have to be spatially close; indeed, electron transfer can happen also if only weak interactions occur between the two partners.[101] This is, for example, the case of the dye **NI7** (Figure 1.19), in which the strong anchoring moiety is not the acceptor part, constituted by a pyridine which only has to be spatially close to the semiconductor surface in order to be able to inject the electrons into the CB.[102]

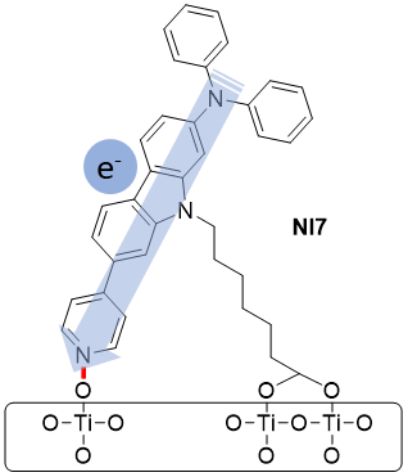

*Figure 1.19 Proposed anchoring and electron injection processes for the dye **NI7**.[102]*

The traditional anchors used in D-π-A dyes are cyanoacrylic (**a1**) and carboxylic acids (**a2**), due to the good electron injection and the strong ester linkage with the semiconductor they guarantee.[6,103] The cyanoacrylic acids, due to their stronger electron-acceptor character are the most used ones and for this reason are also often used as references to test the properties of new anchoring groups. Their principal drawback relies in their poor stability in the presence of water due to hydrolysis. For such reason, research on different anchoring groups capable to form a stronger bond with TiO_2 in those conditions is very active and multiple structures and groups have been tested (Figure 1.20). In particular, alkoxysilane (**a4**) are the object of the research of this PhD and their properties will be discussed in the next chapter.

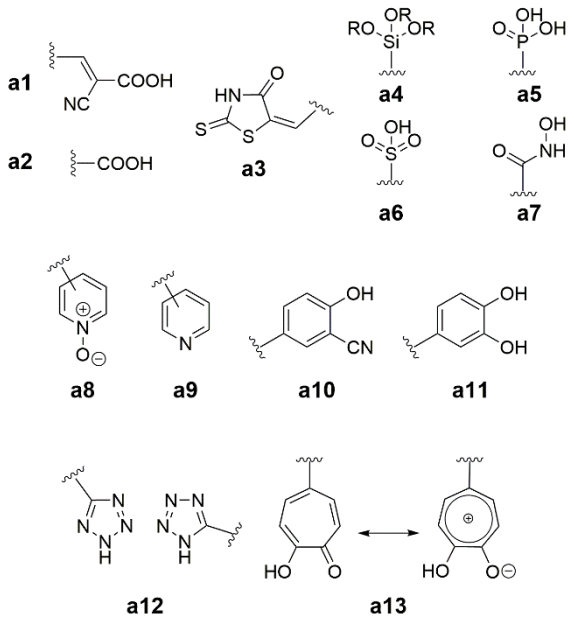

Figure 1.20 Examples of some acceptor groups structures.

Phosphoric[104] (**a5**) and sulfonic acids[105] (**a6**) have been employed due to their similarity to the carboxylic acid structure while being able to establish multiple bonds with the titania surface, increasing the stability of the linkage; however, both groups showed slow injection rate due to the tetrahedral structure of the anchoring moiety, which interrupts the electronic conjugation.[106] 2-hydroxybenzonitrile[107] (**a10**) can establish as well strong bonds with the -OH groups on the surface of the semiconductor, however slow injection rates were obtained. Another possibility lies in the use of Lewis coordination bonds instead of Brønsted acid-base interactions. Rhodamines[108] (**a3**) and, especially, hydroxamic acids[109] (**a7**), which are also used as bidentate ligands for metals and metal oxides, have been shown to establish a strong water-resistant bond with TiO_2, and the latter have also showed good performances in the electron injection process. Another possibility is the use of pyridine[110] (**a9**) and pyridine N-oxide[111] (**a8**), which display a strong interaction of their nitrogen atom with the titanium centers of TiO_2 (accompanied by the interaction of the O atom in the N-oxide) , allowing once again an efficient electron transfer and a bathochromic shift of light absorption. These good properties can also be enhanced by introducing additional electron withdrawing groups such as carboxylic acids or nitrile groups. However, usually the loading of these dyes on TiO_2 is lower compared to similar cyanoacrylic dyes due to the lower number of binding sites available on the semiconductor. Other functions that have been recently employed as anchoring groups are tetrazoles[112] (**a12**) (considered an analogous of the carboxylate group due to their similar physical and electronic properties) and tropolone[113] (**a13**) (that has already been used as chelating ligand, since after deprotonation can act both as acceptor and anchoring group). Finally, a different way to perform the electron injection can be achieved by the use of cathecols[114] (**a11**). This group in fact is able to inject electrons directly from the ground state into the conduction band of the semiconductor (the so-called "Type-II" injection process[37]) after photoexcitation, providing also a bathochromic shift of the absorption spectra of the dye and a good stability of the anchoring. However this group exhibits strong recombination phenomena, lowering cell efficiencies and hampering its more widespread use.

1.6. Aim of the work

As we have already discussed, the photosensitizer plays a key role in the working mechanism of photoactivated processes such as DSSC and photocatalytic hydrogen production. Its optimization is crucial in order to exploit efficient light conversion systems and the aim of this PhD work was the study of the effect of modifications on the dyes backbone in order to enhance the performances of the final devices.

Regarding the DSSC, the focus was into the introduction of particular silylated anchoring group, that already showed excellent photovoltaic performances into the device, along with an extremely good stability of the dye towards the desorption from the TiO_2 film.[35] This particular feature is very interesting because, also if do not affect the immediate performances of the solar cell, it can extend the lifetime of the final device and therefore increase the economic and environmental sustainability of the technology. For that reason, we decided to study the reason behind their good performances and to research if other silylated moieties can be employed as well, in order to broaden the use of these particular groups in the field of the solar cells.

In the second part of this section, the use of these dyes will be extend to another field, the photoactivated hydrogen production. The particular characteristics of this kind of dye, regarding the easy tunability of their properties, are in fact perfect for the optimization of this new kind of device, due to the complexity of the system. For that reason, a better understanding of the role of the modifications on the backbone of the dyes is needed. We decide then to study the impact that some common modifications have on the rate of hydrogen production in this kind of SED-assisted systems.

1.7. References

[1] *Global Energy Statistics Yearbook* **2018**, yearbook.enerdata.net

[2] (a) *BP Energy Outlook* **2018**, bp.com/energyoutlook; (b) *IEA World Energy Outlook 2017*, iea.org/weo2017

[3] *REN21 Global Status Report* **2018**, ren21.net

[4] *Solar generation 6, EPIA.* www.greenpeace.org/international/Global/international/publications/climate/2011/Final%20SolarGeneration%20VI%20full%20report%20lr.pdf

[5] Schiermeier, Q.; Tollefson, J.; Scully, T.; Witze, A.; Morton, O. *Nature* **2008**, *454*, 816.

[6] Hagfeldt, A.; Boschloo, G.; Sun, L.; Kloo, L.; Pettersson, H. *Chem. Rev.* **2010**, *110*, 6595.

[7] *Key World Energy Statistics* **2017**, www.iea.org

[8] Armaroli, N.; Balzani, V. *ChemSusChem* **2011**, *4*, 2.

[9] Parisi M. L., Maranghi S., Basosi R. *Ren. Sust. Energy Rev.* **2014**, *39*, 124.

[10] Energy Information Administration, Annual Energy Outlook 2011. DOE/EIA-0383(2010)

[11] *NREL, Photovoltaic Efficiency Chart*, www.nrel.gov/pv/assets/images/efficiency-chart-20180716.jpg

[12] Neamen, D. "Semiconductor Physics and Devices", ed. McGraw-Hill, **2003**.

[13] http://www-opto.e-technik.uni-ulm.de/lehre/cs/

[14] Achuthan, M.K.; Bhat, K.N. *"Fundamentals of semiconductor devices"*, ed. Tata McGraw-Hill, **2007**, pp. 475.

[15] https://www.scienceabc.com/innovation/how-does-a-semiconductor-work.html

[16] Shockley, W. "*Electrons and holes in semiconductors : with applications to transistor electronics*", ed. R. E. Krieger Pub. Co., **2015**.

[17] "April 25, 1954: Bell Labs Demonstrates the First Practical Silicon Solar Cell"**,** *APS News*, **2009**, *18*, 4.

[18] Wenham S.R., Green M. A. *Prog. Photovolt. Res. Appl.* **1996**, *4*, 3.

[19] Wronski C.R. *Conference Record of the 28 th IEEE Photovoltaic Specialists Conference, Anchorage, AK*, IEEE: New York, **2000**, p 1-6.

[20] (a) Britt J., Ferekides C. *Appl. Phys. Lett.* **1993**, *62*, 2851; (b) Ullal H.S. *Proc. 28th IEEE PVSC*, **2000**, 418.

[21] Green M. A. *Third Generation Photovoltaics: Advanced Solar Energy Conversion*; Springer-Verlag: Berlin, Heidelberg, **2003.**

[22] Shockley W., Queisser H. J. *J. Appl. Phys.* **1961**, *32*, 510.

[23] a) Kim D.W., Shin S.S., Lee S., Cho I.S., Kim D.H., Lee C.W., Jung H.S., Hong K.S. *ChemSusChem* **2013**, *6*, 449. b) Park N.-G. *Mater. Today* **2015**, *18*, 65.

[24] Yang W.S., Noh J.H., Jeon N.J., Kim Y.C., Ryu S., Seo J., Seok S.I. *Science*, **2015**, *348*, 1234.

[25] Eames, C.; Frost, J.M.; Barnes, P.R.F.; O'Regan, B.C.; Walsh, A.; Islam, M.S. *Nat. Commun.* **2015**, *6*, 7497.

[26] Ebbesen, S.D.; Jensen, S.H.; Hauch, A.; Mogensen, M.B. *Chem. Rev.* **2014**, *114*, 10697.

[27] Fujishima, A.; Honda, K. *Nature* **1972**, *238*, 37.

[28] Osterloh, F.E. *Chem. Mater.* **2008**, *20*, 35.

[29] Kato, H.; Asakura, K.; Kudo, A. *J. Am. Chem. Soc.* **2003**, *125*, 3082.

[30] (a) Chen, X.; Shen, S.; Guo, L.; Mao, S.S. *Chem. Rev.* **2010**, *110*, 6503; (b) Kudo, A.; Miseki, Y. *Chem. Soc. Rev.* **2009**, *38*, 253.

[31] Ma, Y.; Wang, X.L.; Jia, Y.S.; Chen, X.B.; Han, H.X.; Li, C. *Chem. Rev.* **2014**, *114*, 9987.

[32] O'Regan, B.; Grätzel, M. *Nature* **1991**, *353*, 737.

[33] Park, N. -G. *Mater. Today* **2015**, *18*, 65.

[34] Cao, Y.; Liu, Y.; Zakeeruddin, S.M.; Hagfeldt, A.; Grätzel, M. *Joule* **2018**, *2*, 1108.

[35] Kakiage, K.; Aoyama, Y.; Yano, T.; Oya, K.; Fujisawa, J.-I.; Hanaya, M. *Chem. Commun.* **2015**, *51*, 15894.

[36] Yoshikawa, K.; Kawasaki, H.; Yoshida, W.; Irie, T.; Konishi, K.; Nakano, K.; Uto, T.; Adachi, D.; Kanematsu, M.; Uzu, H.; Yamamoto, K. *Nat. Energy* **2017**, *2*, 17032.

[37] Ooyama, Y.; Harima, Y. *ChemPhysChem.* **2012**, *13*, 4032.

[38] http://www.sf-tec.com/en/p3-2.asp?id=143

[39] (a) Lee, K. S.; Lee, H. K.; Wang, D. H.; Park, N.-G.; Lee, J. Y.; Park, O O.; Park, J. H. *Chem. Commun.* **2010**, *46*, 4505; (b) Yoo, K.; Kim, J.-Y.; Lee, J. A.; Kim, J. S.; Lee, D.-K.; Kim, K.; Kim, J. Y.; Kim, B. S.; Kim, H.; Kim, W. M.; Kim, J. H.; Ko, M. J. *ACS Nano* **2015**, *9*, 3760; (c) Chen, T.; Qiu, L.; Cai, Z.; Gong, F.; Yang, Z.; Wang, Z.; Peng, H. *Nano Lett.* **2012**, *12*, 2568.

[40] Yun, M. J.; Cha, S. I.; Seo, S. H.; Lee, D. Y. *Sci. Rep.* **2014**, *4*, 5322.

[41] Ito, S.; Liska, P.; Comte, P.; Charvet, R. L.; Pechy, P.; Bach, U.; Schmidt-Mende, L.; Zakeeruddin, S. M.; Kay, A.; Nazeeruddin, M. K.; Grätzel, M. *Chem. Commun.* **2005**, 4351.

[42] Zhang, Z. P.; Ito, S.; O'Regan, B.; Kuang, D. B.; Zakeeruddin, S. M.; Liska, P.; Charvet, R.; Comte, P.; Nazeeruddin, M. K.; Pechy, P.; Humphry-Baker, R.; Koyanagi, T.; Mizuno, T.; Grätzel, M. *Z. Phys. Chem.* **2007**, *221*, 319.

43 Sommeling, P. M.; O'Regan, B. C.; Haswell, R. R.; Smit, H. J. P.; Bakker, N. J.; Smits, J. J. T.; Kroon, J. M.; van Roosmalen, J. A. M. *J. Phys. Chem. B* **2006**, *110*, 19191.

44 Saito, M. ; Fujihara, S. *Energy Environ. Sci.* **2008**, *1*, 280.

45 Onwona-Agyeman, B. ; Kaneko, S.; Kumara, A. ; Okuya, M.; Murakami, K.; Konno, A.; Tennakone, K. *Jpn. J. Appl. Phys. Part 2* **2005**, *44*, L731.

46 Guo, P.; Aegerter, M. A. *Thin Solid Films* **1999**, *351*, 290.

47 (a) Hemalatha, K.V; Karthick, S.N.; Justin Raj, C.; Hong, N.-Y.; Kim, S.-K.; Kim, H.-J. *Spectrochim. Acta Part A, Mol. Biomol. Spectrosc.* **2012**, *96*, 305; (b) Zhang, D.; Lanier, S.M.; Downing, J.A.; Avent, J.L.; Lum, J.; McHale, J.L. *J. Photochem. Photobiol. A* **2008**, *195*, 72; (c) Arifin, Z.; Soeparman, S.; Widhiyanuriyawan, D.; Suyitno, S. *Int. J. Photoenergy* **2017***, Article ID 2704864,* https://doi.org/10.1155/2017/2704864.

48 (a) Nazeeruddin M.K., Kay A., Rodicio I., Humphry-Baker R., Mueller E., Liska P., Vlachopoulos N., Grätzel M., *J. Am. Chem. Soc.* **1993**, *115*, 6382; (b) Nazeeruddin M.K., Zakeeruddin S. M., Humphry-Baker R., Jirousek M., Liska P., Vlachopoulos N., Shklover V., Fischer C. H., Grätzel M. *Inorg. Chem.* **1999**, *38*, 6298; (c) Nazeeruddin M. K., Pechy P., Grätzel M. *Chem. Commun.* **1997**, 1705.

49 (a) Chang Y.-C., Wang C.-L., Pan T.-Y., Hong S.-H., Lan C.-M., Kuo H.-H., Lo C.-F., Hsu H.-Y., Lin C.-Y., Diau E. W.-G. *Chem. Commun.* **2011**, *47*, 8910; (b) Ragoussi M.-E., Cid J.-J., Yum J.-H., de la Torre G., Di Censo D., Grätzel M., Nazeeruddin M. K., Torres T. *Angew. Chem.* **2012**, *124*, 4451; *Angew. Chem. Int. Ed.* **2012**, *51*, 4375.

50 (a) Wu, J.; Hao, S.; Lan, Z.; Lin, J.; Huang, M.; Huang, Y.; Fang, L.; Yin, S.; Sato, T. *Adv. Funct. Mater.*, **2007**, *17*, 2645; (b) Wu, J.; Lan, Z.; Lin, J.; Huang, M.; Hao, S.; Sato, T.; Yin, S. *Adv. Mater.* **2007**, *19*, 4006; (c) Di Noto, V.; Lavina, S.; Giffin, G. A.; Negro, E.; Scrosati, B. *Electrochim. Acta* **2011**, *57*, 4; (d) Yang, W.; Söderberg, M.; Eriksson, A. I. K.; Boschloo, G. *R. RSC Adv.* **2015**, *5*, 26706.

51 (a) Li, D.; Qin, D.; Deng, M.; Luo, Y.; Meng, Q. *Energy Environ. Sci.* **2009**, *2*, 283; (b) Li, B.; Wang, L.; Kang, B.; Wang, P.; Qiu, Y. *Sol. Energy Mater. Sol. Cells* **2006**, *90*, 549; (c) Zhang, W.; Cheng, Y.; Yin, X.; Liu, B. *Macromol. Chem. Phys.* **2011**, *212*, 15; (d) Cao, Y.; Saygili, Y.; Ummadisingu, A.; Teuscher, J.; Luo, J.; Pellet, N.; Giordano, F.; Zakeeruddin, M.S.; Moser, J-.E.; Freitag, M.; Hagfeldt, A.; Grätzel, M. *Nat Commun.* **2017**, *8*, 15390.

52 (a) Nusbaumer, H.; Moser, J.; Zakeeruddin, S.; Nazeeruddin, M.; Grätzel, M. *J. Phys. Chem. B* **2001**, *105*, 10461; (b) Nelson, J.; Amick, T.; Elliott, C. *J. Phys. Chem. C* **2008**, *112*, 18255; (c) Boschloo, G.; Hagfeldt, A. *Acc. Chem. Res.* **2009**, *42*, 1819.

53 (a) Nazeeruddin, K.; Kay, A.; Rodicio, I.; Humphry-Baker, R.; Mueller, E.; Liska, P.; Vlachopoulos, N.; Grätzel, M. *J. Am. Chem. Soc.* **1993**, *115*, 6382; (b) Boschloo, G.; Hagman, L.; Hagfeldt, A. *J. Phys. Chem. B* **2006**, *110*, 13144.

54 Suzuki, K.; Yamaguchi, M.; Kumagai, M.; Yanagida, S. *Chem. Lett.* **2003**, *32*, 28.

55 Yeh, M.-H.; Lin, L.-Y.; Lee, C.-P.; Wei, H.-Y.; Chen, C.-Y.; Wu, C.-G.; Vittal, R.; Ho, K.-C. *J. Mater. Chem.* **2011**, *21*, 19021.

56 Harima, Y.; Kawabuchi, K.; Kajihara, S.; Ishii, A.; Ooyama, Y.; Takeda, K. *Appl. Phys. Lett.* **2007**, *90*, 103515.

57 Ooyama, Y.; Harima, Y. *Eur. J. Org. Chem.* **2009**, 2903.

58 Kim, B.-G.; Chung, K.; Kim, J. *Chem. Eur. J.* **2013**, *19*, 5220.

59 (a) Hisatomi, T.; Kubota, J.; Domen, K. *Chem. Soc. Rev.* **2014**, *43*, 7520; (b) Kudo, A.; Miseki, Y. *Chem. Soc. Rev.* **2009**, *38*, 253.

60 Chen, X.; Shen, S.; Guo, L.; Mao, S.S. *Chem. Rev.* **2010**, *110*, 6503.

61 Cecconi, B.; Manfredi, N.; Montini, T.; Fornasiero, P.; Abbotto, A. *Eur. J. Org. Chem.* **2016**, *31*, 5194.

62 (a) Navarro Yerga, R.M.; Consuelo Àlvarez Galvàn, M.; della Valle, F.; Villoria de la Mano, J.A.; Fierro, J.L.G. *ChemSusChem* **2009**, *2*, 471; (b) Chen, X.; Mao, S.S: *Chem. Rev.* **2007**, *107*, 2891.

63 Willkomm, J.; Orchard, K.L.; Reynal, A.; Pastor, E.; Durrant, J.R.; Reisner, E. *Chem. Soc. Rev.* **2016**, *45*, 9.

64 Young, K.J.; Martini, L.A.; Milot, R.L.; Snoeberger, R.C.; Batista, V.S.; Schmuttenmaer, C.A.; Crabtree, R.H.; Brudvig, G.W. *Coord. Chem. Rev.* **2012**, *256*, 2503.

65 Osterloh, F.E. *Chem. Soc. Rev.* **2013**, *42*, 2294.

66 Park, Y.; Kim, W.; Monllor-Satoca, D.; Tachikawa, T.; Majima, T.; Choi, W. *J. Phys. Chem. Lett.* **2013**, *4*, 189.

67 Xu, Y.; Schoonen, M.A.A. *Am. Mineral.* **2000**, *85*, 543.

68 Zhang, X.; Peng, T.; Song, S. *J. Mater. Chem. A* **2016**, *4*, 2365.

69 Yu, H.; Zhao, Y.; Zhou, C.; Shang, L.; Peng, Y.; Cao, Y.; Wu, L.-Z.; Tung, C-.H.; Zhang, T. *J. Mater. Chem. A* **2014**, *2*, 3344.

70 Artero, V.; Saveant, J-.M. *Energy Environ. Sci.* **2014**, *7*, 3808.

71 Armstrong, F.A.; Hirst, J. *P. Natl. Acad. Sci. USA* **2011**, *108*, 14049.

72 López, C.R.; Melián, E.P.; Méndez, J.A.O.; Santiago, D.E.; Rodríguez, J.M.D.; González, O.; Díaz, M. *J. Photocatal. Photobiol. A* **2015**, *312*, 45.

73 (a) Kaeffer, N.; Massin, J.; Lebrun, C.; Renault, O.; Chavarot-Kerlidou, M.; Artero, V. *J. Am. Chem. Soc.* **2016**, *138*, 12308; (b) McKone, J.R.; Lewis, N.S.; Gray, H.B. *Chem. Mater.* **2014**, *26*, 407.

74 (a) Zou, J-.J. ; Liu, C-.J. ; Yu, K-.L.; Cheng, D-.G.; Zhang, Y-.P.; He, F.; Du, H-.D.; Cui, L. *Chem. Phys. Lett.* **2004**, *400*, 520; (b) Fu, X.; Long, J.; Wang, X.; Leung, D.Y.C.; Ding, Z.; Wu, L.; Zhang, Z.; Li, Z. *Int. J. Hydrogen Energ.* **2008**, *33*, 6484.

75 Yoshida, H.; Hirao, K.; Nishimoto, J.I.; Shimura, K.; Kato, S.; Itoh, H.; Hattori, T. *J. Phys. Chem. C* **2008**, *112*, 5542.

76 Lakadamyali, F.; Kato, M.; Reisner, E. *Faraday Discuss.* **2012**, *155*, 191.

77 Ni, M.; Leung, M.K.H.; Leung, D.Y.C.; Sumathy, K. *Renew. Sust. Energ. Rev.* **2007**, *11*, 401.

78 (a) Li, X.; Cui, S.; Wang, D.; Zhou, Y.; Zhou, H.; Hu, Y.; Liu, J-.G.; Long, Y.; Wu, W.; Hua, J.; Tian, H.; *ChemSusChem* **2014**, *7*, 2879; (b) Balasubramanian, S.; Wang, P.; Schaller, R.D.; Rajh, T.; Rozhkova, E.A. *Nano Lett.* **2013**, *13*, 3365.

79 Dessì, A.; Monai, M.; Bessi, M.; Montini, T.; Calamante, M.; Mordini, A.; Reginato, G.; Trono, C.; Fornasiero, P.; Zani, L. *ChemSusChem* **2018**, *11*, 793.

80 Cobo, S.; Heidkamp, J.; Jacques, P-.A.; Fize, J.; Fourmond, V.; Guetaz, L.; Jousselme, B.; Ivanova, V.; Dau, H.; Palacin, S.; Fontecave, M.; Artero, V. *Nat. Mater.* **2012**, *11*, 802.

81 Reynal, A.; Pastor, E.; Gross, M.A.; Selim, S.; Reisner, E.; Durrant, J.R. *Chem. Sci.* **2015**, *6*, 4855.

82 Barber, J. *Chem. Soc. Rev.* **2009**, *38*, 185.

83 (a) Lee, C-.P.; Lin, R.Y-.Y.; Lin, L-Y.; Li, C-.T.; Chu, T-.C.; Sun, S-.S.; Lin, J.T.; Ho, K-.C. *RSC Adv.* **2015**, *5*, 23810; (b) Lee, C-.P.; Li, C-.T.; Ho, K-.C *Mater Today* **2017**, *20*, 267.

84 Liu D., Fessenden R.W., Hug G. L., Kamat P.V. *J. Phys. Chem. A* **1997**, *101*, 2583.

85 Kitamura, T.; Ikeda, M.; Shigaki, K.; Inoue, T.; Anderson, N.A.; Ai, X.; Lian, T. Q.; Yanagida, S. *Chem. Mater.* **2004**, *16*, 1806.

86 Zeng, W.; Cao, Y.; Bai, Y.; Wang, Y.; Shi; Y.; Zhang, M.; Wang, F.; Pan, C.; Wang, P. *Chem. Mater.*, **2010**, *22*, 1915.

87 Yella, A.; Lee, H. W.; Tsao, H.N.; Yi, C.; Chandiran, A.K.; Nazeeruddin, M.K.; Diau, E.W.G.; Yeh, C.Y.; Zakeeruddin, S.M.; Grätzel, M. *Science* **2011**, 334, 629.

88 Robson, K.C.D.; Hu, K.; Meyer, G.J.; Berlinguette, C.P. *J. Am. Chem. Soc.* **2013**, *135*, 1961.

89 Chang, Y.J.; Chow, T.J. *Tetrahedron* **2009**, *65*, 4726.

90 Shi, J.; Huang, J.; Tang, R.; Chai, Z.; Hua, J.; Qin, J.; Li, Q.; Li, Z. *Eur. J. Org. Chem.* **2012**, 5248.

91 Choi, H.; Raabe, I.; Kim, D.; Teocoli, F.; Kim, C.; Song, K.; Yum, J.-H.; Ko, J.; Nazeeruddin, M.K.; Grätzel, M. *Chem. Eur. J.* **2010**, *16*, 1193.

92 (a) Horiuchi, T.; Miura, H.; Uchida, S. *Chem. Commun.* **2003** 3036; (b) Wu, Y.; Marszalek, M.; Zakeeruddin, S.M.; Zhang, Q.; Tian, H.; Grätzel, M.; Zhu, W. *Energy Environ. Sci.* **2012** *5*, 8261; (c) Yang, J.; Ganesan, P.; Teuscher, J.; Moehl, T.; Kim, Y.J.; Yi, C.; Comte, P.; Pei, K.; Holcombe, T.W.; Nazeeruddin, M.K.; Hua, J.; Zakeeruddin, S.M.; Tian, H.; Grätzel, M. *J. Am. Chem. Soc.* **2014** *136*, 5722.

93 (a) Tian, H.; Yang, X.; Chen, R.; Pan, Y.; Li, L.; Hagfeldt, A.; Sun, L. *Chem. Commun.* **2007**, 3741; (b) Manfredi, N.; Cecconi, B.; Abbotto, A. *Eur. J. Org. Chem.* **2014**, 7069.

94 (a) Hara, K.; Kurashige, M.; Dan-oh, Y.; Kasada, C.; Shinpo, A.; Suga, S.; Sayama, K.; Arakawa, H. *New J. Chem.* **2003**, *27*, 783; (b) Wang, Z.S.; Cui, Y.; Dan-Oh, Y.; Kasada, C.; Shinpo, A.; Hara, K. *J. Phys. Chem. C* **2008**, *112*, 17011.

95 Chen, R.; Zhao, G.; Yang, X.; Jiang, X.; Liu, J.; Tian, H.; Gao, Y.; Liu, X.; Han, K.; Sun, M.; Sun, L. *J. Mol. Struct.* **2008**, *876*, 102.

96 (a) Koumura, N.; Wang, Z.-S.; Mori, S.; Miyashita, M.; Suzuki, E.; Hara, K. *J. Am. Chem. Soc.* **2006**, *128*, 14256; (b) Koumura, N.; Wang, Z.-S.; Miyashita, M.; Uemura, Y.; Sekiguchi, H.; Cui, Y.; Mori, A.; Mori, S.; Hara, K. *J. Mater. Chem.* **2009**, *19*, 4829; (c) Lai, H.; Hong, J.; Liu, P.; Yuan, C.; Li, Y.; Fang, Q. *RSC Adv.*, **2012**, *2*, 2427.

97 (a) Kitamura, T.; Ikeda, M.; Shigaki, K.; Inoue, T.; Anderson, N.A.; Ai, X.; Lian, T.; Yanagida, S. *Chem. Mater.* **2004**, *16*, 1806; (b) Hara, K.; Kurashige, M.; Ito, S.; Shinpo, A.; Suga, S.; Sayama, K.; Arakawa, H. *Chem. Commun.* **2003**, 252; (c) Hagberg, D.P.; Edvinsson, T.; Marinado, T.; Boschloo, G.; Hagfeldt, A.; Sun, L. *Chem. Commun.* **2006**, 2245; (d) Li, R.; Lv, X.; Shi, D.; Zhou, D.; Cheng, Y.; Zhang, G.; Wang, P.; *J. Phys. Chem. C* **2009**, *113*, 7469.

98 (a) Li, R.; Liu, J.; Cai, N.; Zhang, M.; Wang, P. *J. Phys. Chem. B* **2010**, *114*, 4461; (b) Ko, S.; Choi, H.; Kang, M.-S.; Hwang, H.; Ji, H.; Kim, J.; Ko, J.; Kang, Y. *J. Mater. Chem.* **2010**, *20*, 2391, (c) Zhu, X.; Tsuji, H.; Yella, A.; Chauvin, A.-S.; Grätzel, M.; Nakamura, E. *Chem. Commun.* **2013**, *49*, 582.

99 (a) Liu, W.-H.; Wu, I.-C.; Lai, C.-H.; Lai, C.-H.; Chou, P.-T.; Li, Y.-T.; Chen, C.-L.; Hsu, Y.-Y.; Chi, Y. *Chem. Commun.* **2008**, 5152; (b) Chen, B.-S.; Chen, D.-Y.; Chen, C.-L.; Hsu, C.-W.; Hsu, H.-C.; Wu, K.-L.; Liu, S.-H.; Chou, P.-T.; Chi, Y. *J. Mater. Chem.* **2011**, *21*, 1937.

100 (a) Dessì, A.; Calamante, M.; Mordini, A.; Peruzzini, M.; Sinicropi, A.; Basosi, R.; Fabrizi de Biani, F.; Taddei, M.; Colonna, D.; Di Carlo, A.; Reginato, G.; Zani, L. *Chem. Commun.* **2014**, *50*, 13952; (b) Dessì, A.; Calamante, M.; Mordini, A.; Peruzzini, M.; Sinicropi, A.; Basosi, R.; Fabrizi de Biani, F.; Taddei, M.; Colonna, D.; Di Carlo, A.; Reginato, G.; Zani, L. *RSC Adv.* **2015**, *5*, 32657.

101 Ooyama, Y.; Shimada, Y.; Inoue, S.; Nagano, T.; Fujikawa, Y.; Komaguchi, K.; Imae, I.; Harima, Y. *New J. Chem.* **2011**, *35*, 111.

102 Ooyama, Y.; Nagano, T.; Inoue, S.; Imae, I. Komaguchi, K.; Ohshita, J.; Harima, Y. *Chem. Eur. J.* **2011**, *17*, 14837.

103 Zhang, L.; Cole, J. M. *ACS Appl. Mater. Interfaces*, **2015**, *7*, 3427.

104 (a) Pechy, P.; Rotzinger, F.P.; Nazeeruddin, M.K.; Kohle, O.; Zakeeruddin, S.M.; Humphry-Baker, R.; Grätzel, M. *J. Chem. Soc., Chem. Commun.* **1995**, 65; (b) Mulhern, K.R.; Orchard, A.; Watson, D.F.; Detty, M.R. *Langmuir* **2012**, *28*, 7071; (c) Abate, A.; Perez-Tejada, R.; Wojciechowski, K.; Foster, J.M.; Sadhanala, A.; Steiner, U.; Snaith, H.J.; Franco, S.; Orduna, J. *Phys. Chem. Chem. Phys.* **2015**, *17*, 18780.

105 Yao, Q.-H.; Shan, L.; Li, F.-Y.; Yin, D.-D.; Huang, C.-H. *New J. Chem.* **2003**, *27*, 1277.

106 Guerrero, G.; Alauzun, J. G.; Granier, M.; Laurencin, D.; Mutin, P. H. *Dalt. Trans.* **2013**, *42*, 12569.

107 Li, S.-F.; Yang, X.-C.; Cheng, M.; Zhao, J.-H.; Wang, Y.; Sun, L.-C. *Tetrahedron Lett.* **2012**, *53*, 3425.

108 (a) Mao, J.; He, N.; Ning, Z.; Zhang, Q.; Guo, F.; Chen, L.; Wu, W.; Hua, J.; Tian, H. *Angew. Chem. Int. Ed.* **2012**, *51*, 9873; (b) Zhang, J.; Li, H.-B.; Zhang, J.-Z.; Wu, Y.; Geng, Y.; Fu, Q.; Su, Z.-M. *J. Mater. Chem. A* **2013**, *1*, 14000.

109 (a) McNamara, W.R.; Snoeberger, III R.C.; Li, G.; Richter, C.; Allen, L.J.; Milot, R.L.; Schmuttenmaer, C.A.; Crabtree, R. H.; Brudvig, G.W.; Batista, V.S. *Energy Environ. Sci.* **2009**, *2*, 1173; (b) McNamara, W. R.; Milot, R. L.; Song, H.; Snoeberger III, R. C.; Batista, V.S.; Schmuttenmaer, C. A.; Brudvig, G. W.; Crabtree, R. H. *Energy Environ. Sci.* **2010**, *3*, 917; (c) Koenigsmann, C.; Ripolles, T.S.; Brennan, B. J.; Negre, C.F.; Koepf, M.; Durrell, A.C.; Milot, R.L.; Torre, J.A.; Crabtree, R.H., Batista, V.S.; Brudvig, G.; Bisquert, J.; Schmuttenmaer, C. *Phys. Chem. Chem. Phys.* **2014**, *16*, 16629.

110 (a) Ooyama, Y.; Inoue, S.; Nagano, T.; Kushimoto, K.; Ohshita, J.; Imae, I.; Komaguchi, K.; Harima, Y. *Angew. Chem. Int. Ed.* **2011**, *50*, 7429; (b) Franchi, D.; Calamante, M.; Reginato, G.; Zani, L.; Peruzzini, M.; Taddei, M.; Fabrizi De Biani, F.; Basosi, R.; Sinicropi, A.; Colonna, D.; Di Carlo, A.; Mordini, A. *Tetrahedron* **2014**, *70*, 6285; (c) Mao, J.; Wang, D.; Liu, S.-H.; Hang, Y.; Xu, Y.; Zhang, Q.; Wu, W.; Chou, P.-T.; Hua, J. *Asian J. Org. Chem.* **2014**, *3*, 153.

111 (a) Wang, L.; Yang, X.; Li, S.; Cheng, M.; Sun, L. *RSC Adv.* **2013**, *3*, 13677; (b) Cecconi, B.; Mordini, A.; Reginato, G.; Zani, L.; Taddei, M.; Fabrizi de Biani, F.; De Angelis, F.; Marotta, G.; Salvatori, P.; Calamante, M. *Asian J. Org. Chem.* **2014**, *3*, 140; (c) Wang, L.; Yang, X.; Zhao, J.; Zhang, F.; Wang, X.; Sun, L. *ChemSusChem* **2014**, *7*, 2640.

112 (a) Massin, J.; Ducasse, L.; Toupance, T.; Olivier, C. *J. Phys. Chem. C* **2014**, *118*, 10677; (b) Selvam, R.; Prakash, G.; Subramanian, K. *RSC Adv.* **2016**, *6*, 109054; (c) Chermahini, Z.J.; Chermahini, A.N.; Dabbagh, H.A.; Rezaei, B.; Irannejad, N. *J. Iran. Chem. Soc.* **2017**, *14*, 1549.

113 Higashino, T.; Fujimori, Y.; Sugiura, K.; Tsuji, Y.; Ito, S.; Imahori, H. *Angew. Chem. Int. Ed.* **2015,** *54***,** 9052.

114 (a) Tae, E. L.; Lee, S. H.; Lee, J. K.; Yoo, S. S.; Kang, E. J.; Yoon, K. B. *J. Phys. Chem. B* **2005**, *109*, 22513; (b) An, B.-K.; Hu, W.; Burn, P. L.; Meredith, P. *J. Phys. Chem. C* **2010**, *114*, 17964; 8c) Ooyama, Y.; Yamada, T.; Fujita, T.; Harima, Y.; Ohshita, J. *J. Mater. Chem. A* **2014**, *2*, 8500.

Chapter 2

Results and Discussion

2.1. Synthesis of Silylated Anchoring Groups for DSSC Application

2.1.1. Background

As already shown, the dye plays a key role in the working mechanism of a DSSC, being able to influence all the properties of the final solar cells, which are not only limited to photovoltaic performances but also include, for example, the durability and transparency of the device. The durability in particular is a crucial factor for the diffusion and the commercialization of this technology as a real counterpart to first generation photovoltaic devices. There are two main processes that could cause a crash of a DSSC, namely the UV-heat stress, possibly leading to the degradation of the various cell components, and the defects in sealing that could lead to the electrolyte leaking or the intrusion of water inside the device. Solving such problems represents a huge technical challenge, as demonstrated by the large number of existing studies concerning the optimization of manufacturing conditions.[1,2] Regarding the dye, the most critical problem could be the presence of water because, apart from the possibility to cause short-circuits inside the cell, it could either lead to dye degradation or its desorption from the semiconductor surface. This is particularly true for the dyes bearing a cyanoacrylic acid moiety that, as already pointed out, is currently the most used anchoring group. Indeed, as demonstrated by a recent study[3], the combined action from both intense light and water in the presence of metal oxides could lead to the degradation of the double bond of the cyanoacrylic acid moiety and the consequent desorption of the dye (Scheme 2.1).

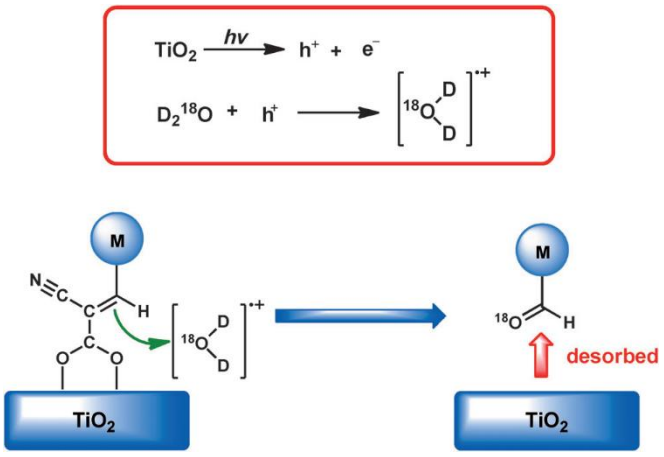

Scheme 2.1 Proposed mechanism for the cyanoacrylic acid degradation in DSSC.[3]

The research of new anchoring groups characterized by higher stability in these conditions is therefore very active and directly linked to the sensitizers molecular structure. Among all the anchoring groups already used in DSSCs,[4] our attention focused onto the siloxane, a group with general formula $Si(OR)_3$, in which R are alkyl chains, that was already shown to be able to establish a strong bond with metal oxides surfaces.[5] The bond formation mechanism is still debated, but the commonly accepted theory implies that after hydrolysis of the OR group, the obtained silanol can form a covalent ester bond on the metal oxide surface after the elimination of a molecule of water (Figure 2.1).[6]

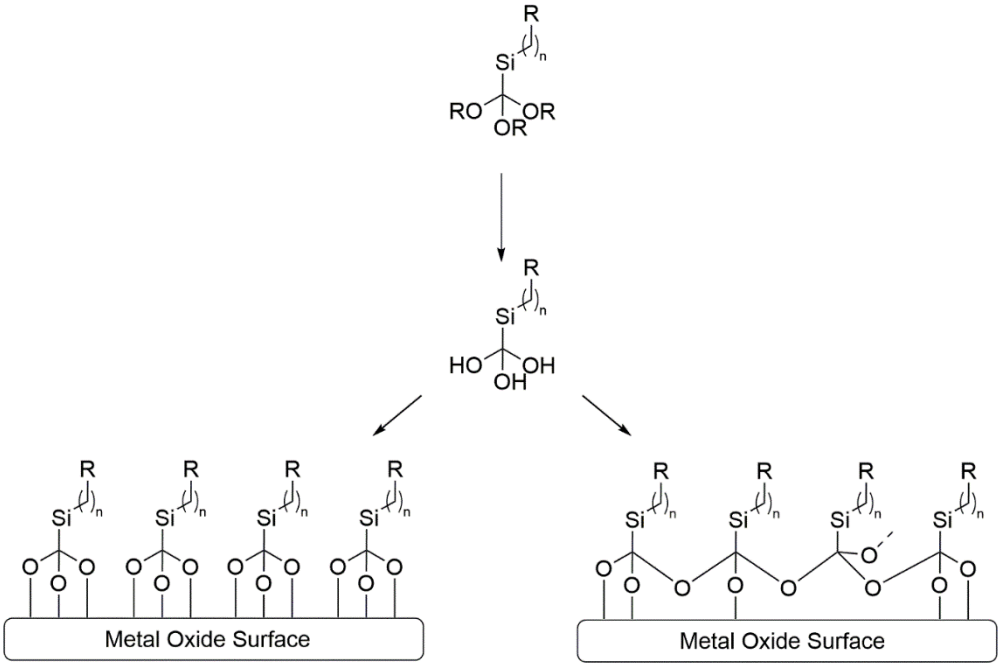

Figure 2.1 Proposed mechanism for the bond formation between the siloxane and the semiconductor surface.[6b]

In the literature, various papers regarding the synthesis of dyes bearing the siloxane group can be found,[6b,7,8] but it is only with the most recent works of *Hanaya et al.*[9,10] that a breakthrough in the use of silyl-anchoring dyes in DSSC was reached. In the first work of the series, the authors synthetized a new dye called **ADEKA-1** (Figure 2.2) as a derivation of the more famous cyanoacrylic dye **MK-2**[11] and showed that it had an excellent stability on the titania surface and was able to provide DSSCs of high efficiency (over 12.5%), greater also than the corresponding cyanoacrylic acid. The presence of a strong electron-acceptor moiety and an extended π-spacer system explain the better results obtained compared to the dye previously synthetized by the same group, **SFD-5** (Figure 2.2). The co-sensitization of **ADEKA-1** with this latter dye or with cyanoacrylate **LEG4** (Figure 2.2), accompanied by a thorough optimization of the cell parameters (i.e. electrolyte composition, pre-staining treatment of the semiconductor surface), allowed to reach even better efficiencies in the final devices (over 14% for the system **ADEKA-1**/**LEG4**). Finally in their last work, they also exploited the possibility to enhance another important parameter of a DSSC device, the V_{oc}, by synthetizing a new coumarine dye called **ADEKA-3** (Figure 2.2) with optimized FMOs energy levels in order to work with an electrolyte solution that has the redox couple Br^-/Br_3^- as main component; with that system they were able to reach a value over 1.4 V for the V_{oc} of the complete devices.[10c]

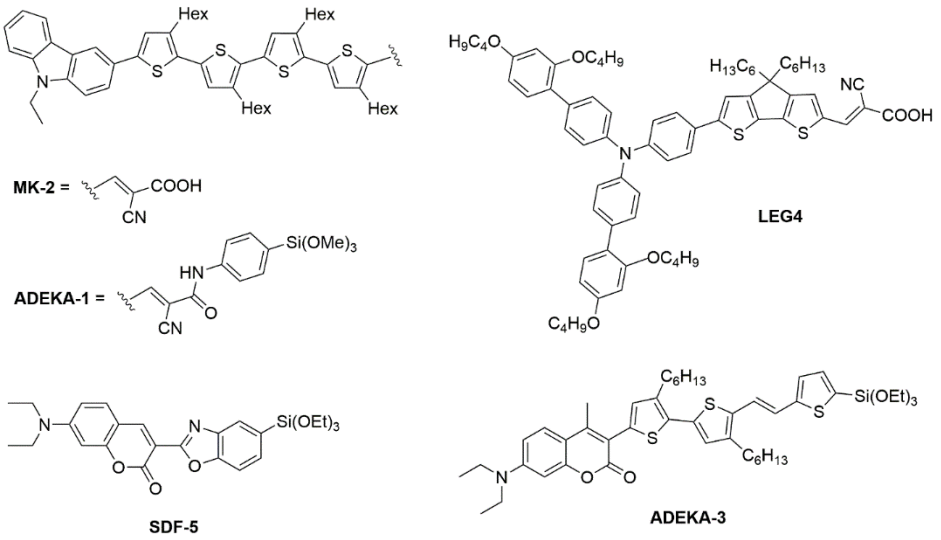

Figure 2.2 Structure of the siloxane dyes synthetized by Hanaya et al.[9,10c]

In a previous study conducted in the laboratory where this work was carried out, two new siloxane dyes were synthetized starting from the corresponding cyanoacrylic acids.[12] However, the introduction of the silylated group as described for **ADEKA-1**,[10a] by transforming the acid to the corresponding acyl chloride with subsequent reaction with the 4-(triethoxysilyl)aniline (**1**), has turned out not to be straightforward and general as it seemed to be and the development of a different synthetic route for both the two new dyes, **MM62** and **MB56**, was necessary (Scheme 2.2). The difficulties encountered in the synthesis and the purification of these dyes stimulated us to look for a new valid anchoring group as an alternative to the siloxane.

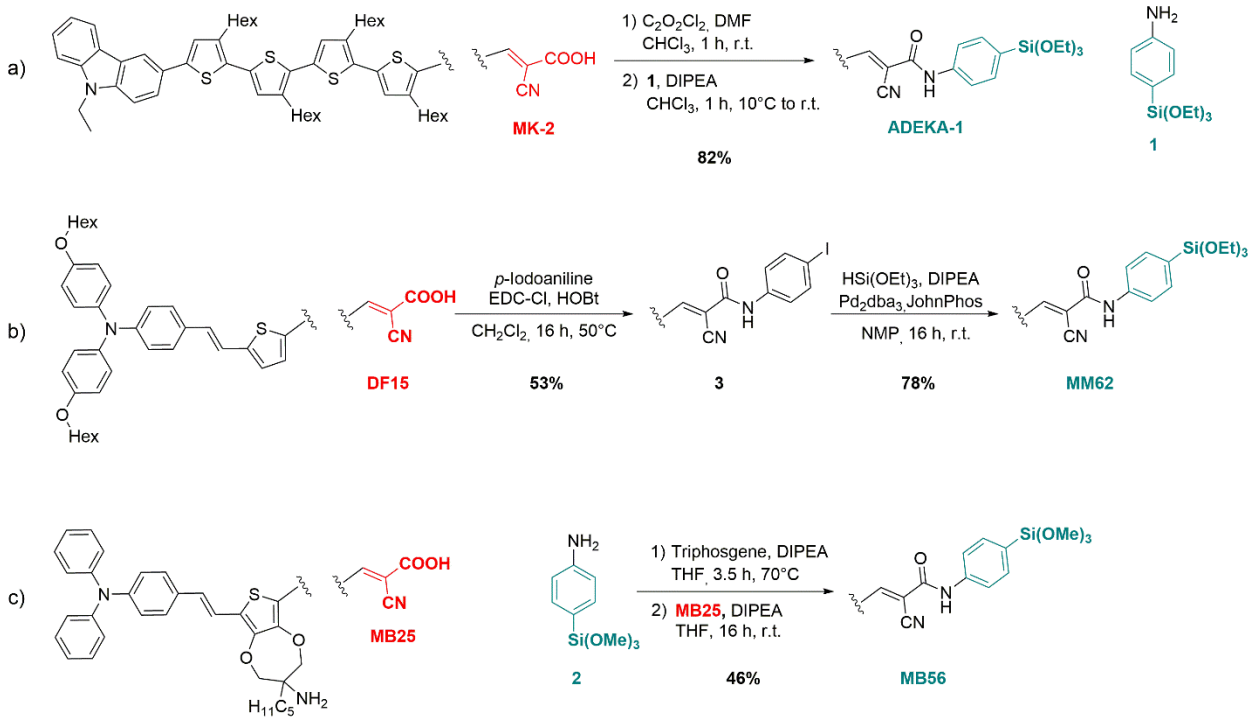

Scheme 2.2 Different synthetic pathways for the introduction of the siloxane moiety.[10a,12]

The first part of this PhD work was then focused on investigating the photophysical properties of trialkoxysilane dyes **MM62** and **MB56**, which were prepared as shown in Scheme 2.2. The two compounds were analyzed by means of transient absorption spectroscopy and their performances in DSSC were evaluated. Furthermore we developed a simple and general way to introduce on a cyanoacrylic dye a different silylated anchoring group having the same advantageous properties as the siloxane. The group we chose was the silatrane moiety (Figure 2.3a), which is, in fact, relatively stable under a wide range of pH values,[13] can withstand many common reaction conditions and can be easily purified with column chromatography on silica gel, but it can still be hydrolyzed on the titania surface to form the same stable covalent bond as the siloxane group, without exhibiting the tendency to form polymeric species (typical of the alkoxysilane deviratives).[14] For these reasons, there were already examples on the use of this group for the sensitization of metal oxides surfaces with heterogeneous catalysts,[15] tetra-aryl porphyrins[16] and organometallic dyes,[14] while its introduction in the structure of metal-free organic dyes had never been reported so far. We decided to introduce the silatrane moiety on a series of cyanoacrylic acids in order to compare the new dyes with their already developed siloxane analogs, and therefore designed the three dyes **MB96**, **MB104** and **MB113** (Figure 2.3b).

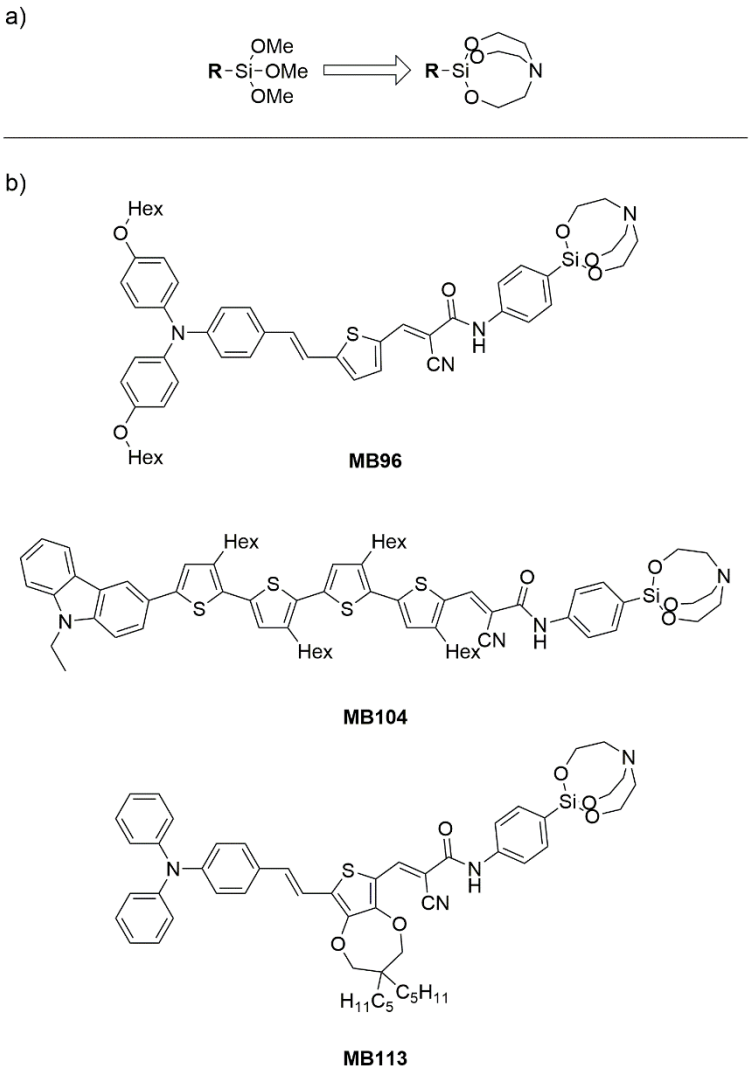

Figure 2.3 Structure of (a) the silatrane cage, (b) the target dyes.

2.1.2. Studies on the Siloxane Dyes MM62 and MB56

2.1.2.1. Siloxanes Characterization

The optical and electrochemical properties of the siloxane dyes were analyzed in order to prove the possibility of their employment in real DSSC devices. In particular, their optical properties were analyzed both with steady-state measurements and with transient absorption spectroscopy.

- **Steady-State Spectroscopic Characterization and Electrochemical Measurements**

The absorption spectra* of the siloxane dyes **MM62** and **MB56** have been recorded in dichloromethane (DCM), benzene and acetonitrile (ACN) solution and compared with those recorded for the corresponding cyanoacrylic dyes **DF15** and **MB25**. The obtained spectra are showed in Figure 2.4.

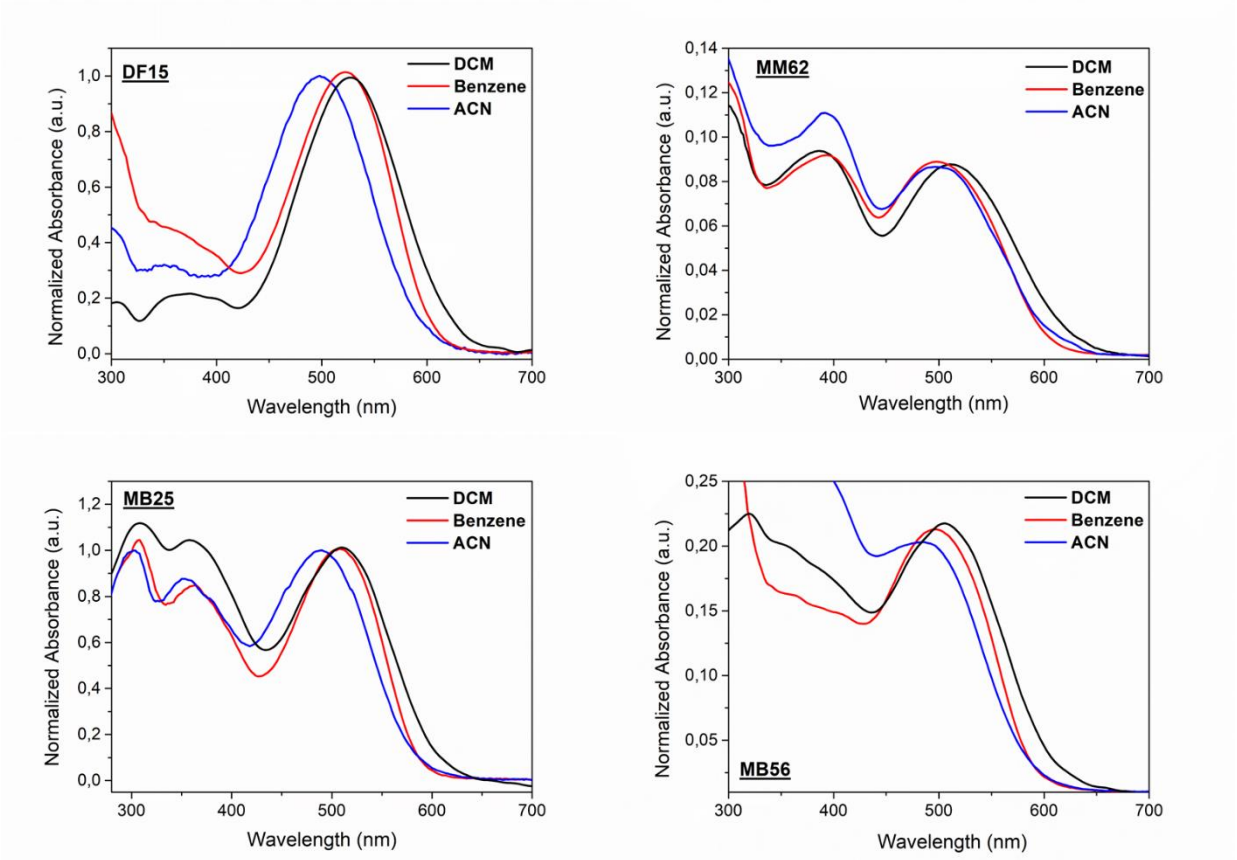

*Figure 2.4 Absorption spectra in solution (DCM, benzene, ACN) of compounds **DF15**, **MM62**, **MB25** and **MB56**.*

Both **DF15** and its trialkoxysilane derivative **MM62** showed a strong absorption band in the visible region, peaked near 500 nm, with the exact position of the maximum absorption depending from the solvent used. In case of **DF15**, in DCM it exhibited an absorption peaks at 528 nm with a broad red-tail, in benzene a λ_{max} at 515 nm (with a decreased red-tail if compared to the DCM solution), while in ACN the absorption maximum was peaked at 495 nm, thus showing dependence both on polarity and polarizability of the external medium. Similar trend was observed for **MM62**, thus demonstrating that

* The spectroscopic characterization was performed by Mariangela Di Donato of LENS (European Laboratory for Non-Linear Spectroscopy, University of Florence).

the modification of the anchoring part of the molecule did not affect to a large extent the nature of its electronic state. In the case of the couple **MB25**-**MB56**, an analogous behavior was observed, with the absorption spectra also showing the appearance of two higher energy bands besides the band at 500 nm. This last comparison confirmed that modification of the anchoring part of the molecule had a minor effect on the steady-state absorption.

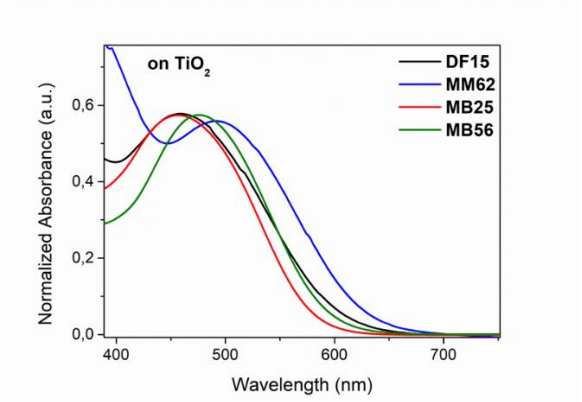

*Figure 2.5 Absorption spectra of dyes **DF15**, **MM62**, **MB25** and **MB56** on TiO_2 film.*

Then, the spectra of the dyes adsorbed on a nanocrystalline TiO_2 film were recorded (Figure 2.5). The staining conditions used for the sensitization were not the same for all the compounds examined: while for the acids it is sufficient to dip the films overnight in a toluene solution of the dyes at r.t., for the silylated compounds it is necessary to immerse the films in a toluene solution of the dyes heated up to 70°C for several hours. The difference in staining conditions depends on the reactions that have to take place for the sensitization to occur: while for the carboxylic acids only a deprotonation is needed, for the silylated dyes the hydrolysis of the SiO-R groups to the corresponding silanols has to happen (Figure 2.1), a reaction that requires more energy to occur. All the recorded spectra appeared blue-shifted if compared with the respective absorption measured in DCM solution; in particular, the blue-shift was extremely pronounced in case of the cyanoacrylic acids (the maximum absorption shifts at 458 nm both in case of **DF15** and **MB25**), which is most probably due to deprotonation of the carboxylic group on the surface. In the other cases, the blue-shift observed with respect to the solution may be caused by the formation of H-aggregates on the surface, which is commonly observed in DSSC photoanodes prepared without the addition of any anti-aggregating agent.[17]

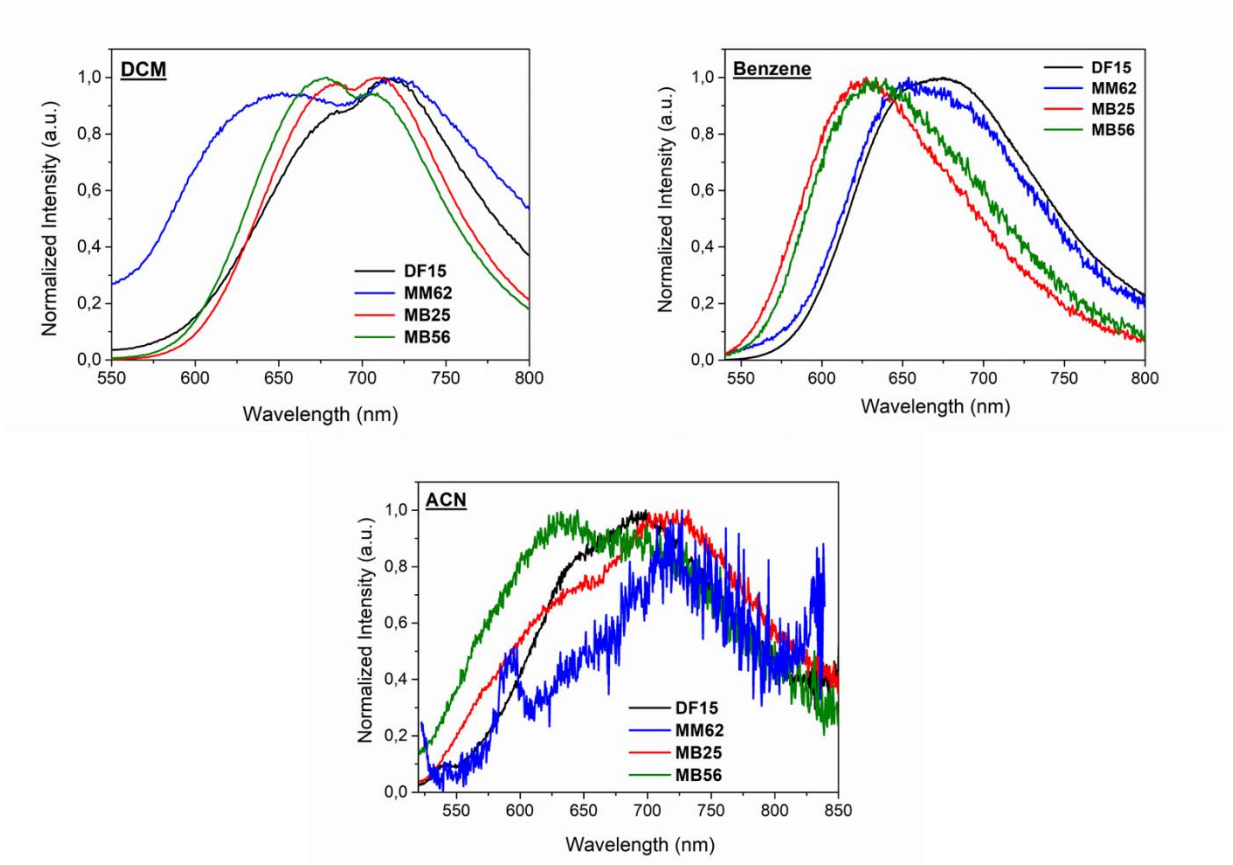

Figure 2.6 Normalized fluorescence spectra of all the analyzed dyes in DCM, benzene and ACN.

Fluorescence spectra of all dyes in the three analyzed solvents are reported in Figure 2.6. In all cases, fluorescence spectra are very broad and usually blue shifted in benzene with respect the two other solvents. For **DF15** and its alkoxysilane derivative **MM62**, fluorescence yields increased in benzene compared to the other two solvents, while a very low fluorescence was observed in acetonitrile. Both **MB25** and **MB56** showed fluorescence of comparable intensity in benzene and dichloromethane and lower fluorescence intensity was observed in acetonitrile also for these dyes.

*Table 2.1 Spectroscopic and electrochemical data for dyes **DF15**, **MM62**, **MB25** and **MB56** in DCM.*

Dye	**$\varepsilon^{[a]}$ ($M^{-1}\,cm^{-1}$)**	**$\lambda_{max\ abs.}^{[a]}$ (nm)**	**$\lambda_{max\ emi.}^{[a]}$ (nm)**	**$\lambda_{max\ abs.}$ on TiO_2 (nm)**	**$E_{ox.}^{[b]}$ (V)**	**$E^*_{ox.}^{[c]}$ (V)**	**$E_{0\text{-}0}^{[d]}$ (eV)**
DF15	34000	528	624	458	+0.94	-1.09	2.05
MM62	24000	520	721	501	-	-	2.13
MB25	28000	514	605	456	+1.03	-1.02	2.50
MB56	24000	510	679	478	+1.00	-1.08	2.48

[a] DCM solution; [b] Potentials vs. NHE; [c] Calculated from $E_{ox} - E_{0\text{-}0}$; [d] Estimated from the intersection of normalized absorption and emission spectra.

Cyclic voltammetry† measurements were carried out in DCM to determine the ground-state oxidation potentials (Table 2.1) of the dyes. All the potentials were comprised in the 0.94-1.03 V range, therefore being positive enough to ensure regeneration by the iodide/triiodide redox couple (*ca.* 0.5 V vs. NHE[18]). As already seen, the modifications on the anchor part of the structure, did not cause major changes to the dyes electrochemical characteristics. Finally, by subtraction of the optical band-gaps ($E_{0\text{-}0}$) to the ground-state oxidation potentials ($E_{ox.}$), it was possible to calculate the excited state oxidation potentials (Table 2.1; $E^{*}_{ox.} = E_{ox.} - E_{0\text{-}0}$). These values resulted being always more negative than the TiO_2 conduction band edge (*ca.* –0.4 eV vs. NHE), which means that electron injection from the excited state of the dye to the conduction band of the semiconductor could occur properly during cell operation.

- **Transient Absorption Spectroscopy Analysis**

Fast and ultrafast time-resolved spectroscopy techniques have often been employed to determine the rate constants and quantum yields of the individual processes taking place on sensitized TiO_2 films.[17a] Starting from these premises, we decided to record transient absorption spectra of our dyes, using solvents differing both in polarity and polarizability in order to investigate the effect of the external medium on the system electronic properties of the system. Dyes **DF15** and **MM62** were excited either at 400 and 520 nm (on the two different absorption peaks recorded before), however, changing the excitation conditions had no remarkable effect on the measured transient absorption spectra and on the dynamic evolution of the excited states. On the other hand, **MB25** and **MB56** have been excited at 480 nm (on their maximum absorption peak), in order to reach the lower excited state of the molecule. In all the cases (especially for **DF15**), both the excited state lifetimes and the spectral shapes were greatly influenced by the solvent properties. The quantitative analysis of the data obtained by the ultrafast transient absorption experiments has been performed by global analysis, in order to retrieve both the kinetic constants associated, necessary to describe the dynamic evolution of the system, and the corresponding spectral contributions (evolution associated decay spectra, EADS).[19] Figure 2.7 reports the EADS and the kinetic traces registered at the maximum of the excited state absorption band obtained by analyzing the transient absorption data recorded for all the dyes in the analyzed solvents, together with the fit obtained by global analysis.

† Cyclic voltammetry measurements were performed by Dr. Fabrizia Fabrizi de Biani (University of Siena).

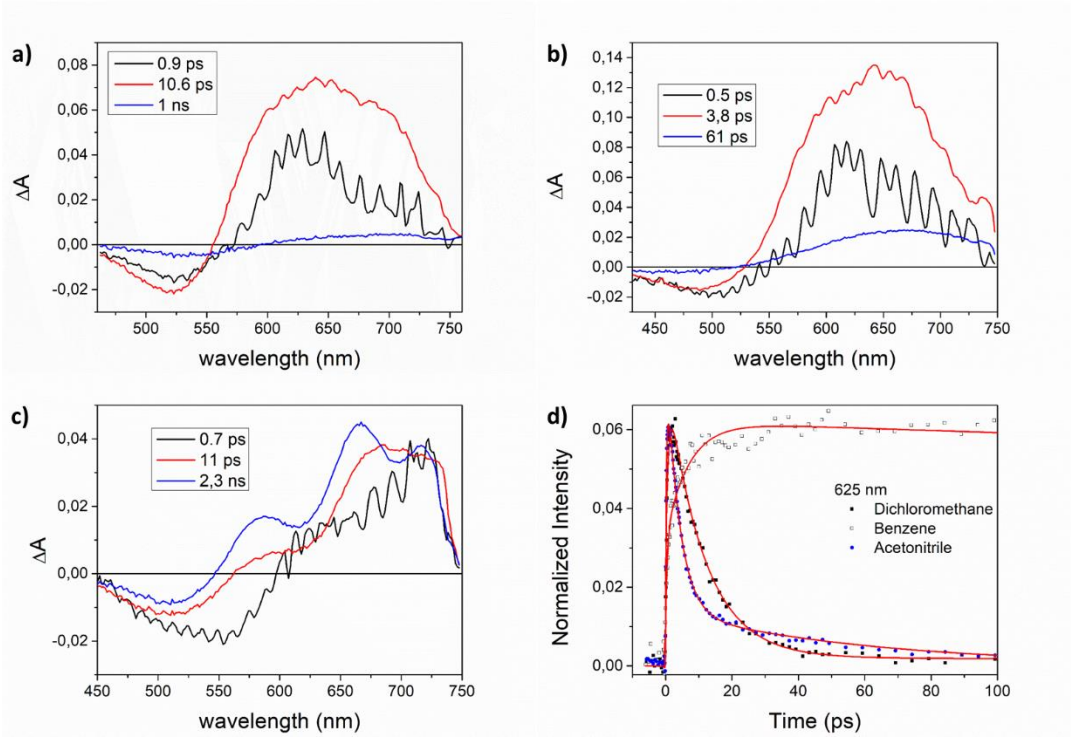

*Figure 2.7 EADS obtained by the global analysis of transient data recorded for **DF15** in (a) ACN, (b) DCM, (c) benzene; panel (d) reports the kinetic traces at 625 nm registered for **DF15** in the three solvents (scattered points). Red lines underlying the kinetic traces lines on panel d represent the fit resulting from global analysis.*

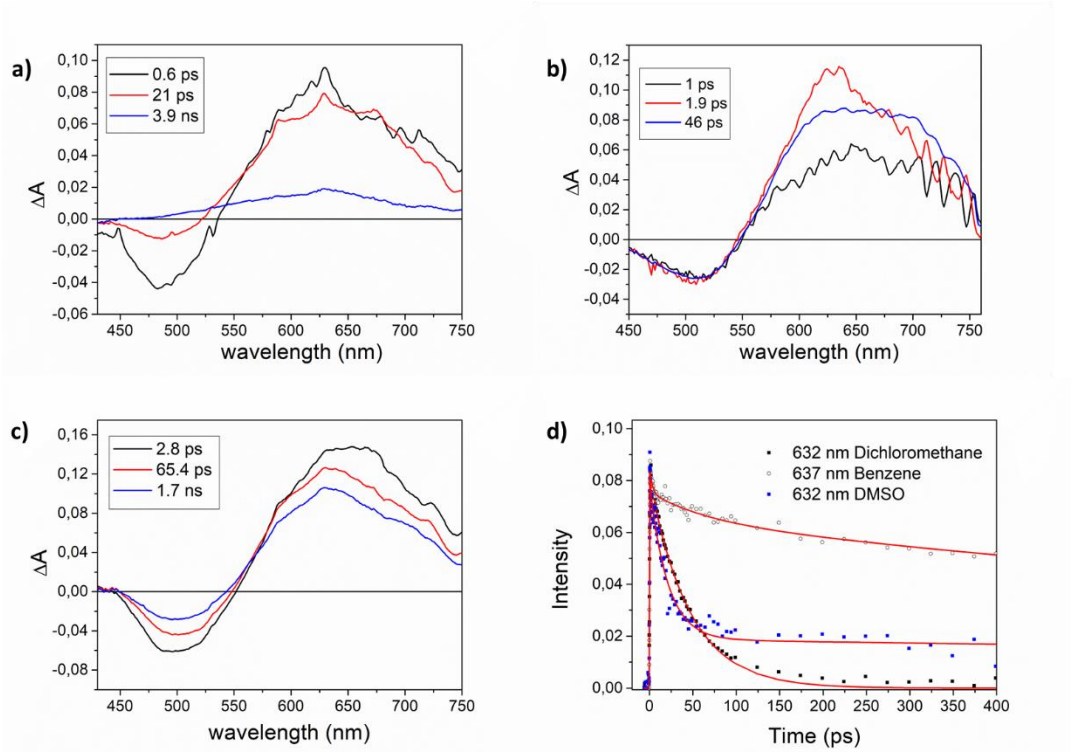

*Figure 2.7 EADS obtained by the global analysis of transient data recorded for **MM62** in (a) DMSO, (b) DCM, (c) benzene; panel (d) reports the kinetic traces at 625 nm registered for **MM62** in the three solvents (scattered points). Red lines underlying the kinetic traces lines on panel d represent the fit resulting from global analysis*

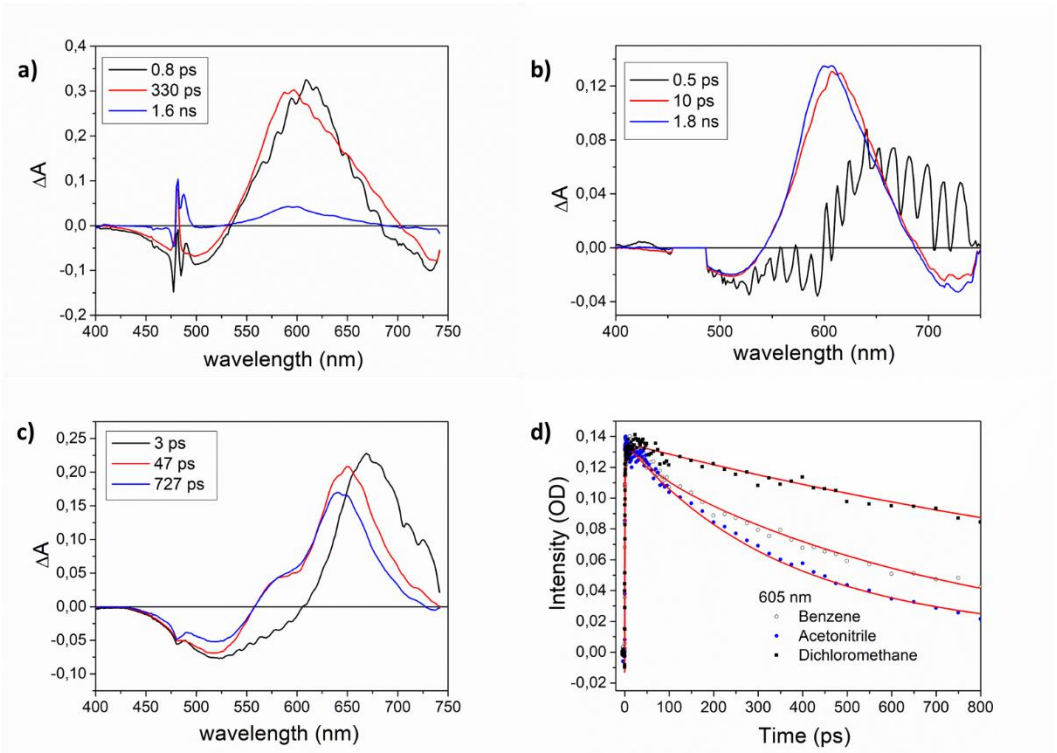

*Figure 2.7 EADS obtained by the global analysis of transient data recorded for **MB25** in (a) ACN, (b) DCM, (c) benzene; panel (d) reports the kinetic traces at 625 nm registered for **MB25** in the three solvents (scattered points). Red lines underlying the kinetic traces lines on panel d represent the fit resulting from global analysis*

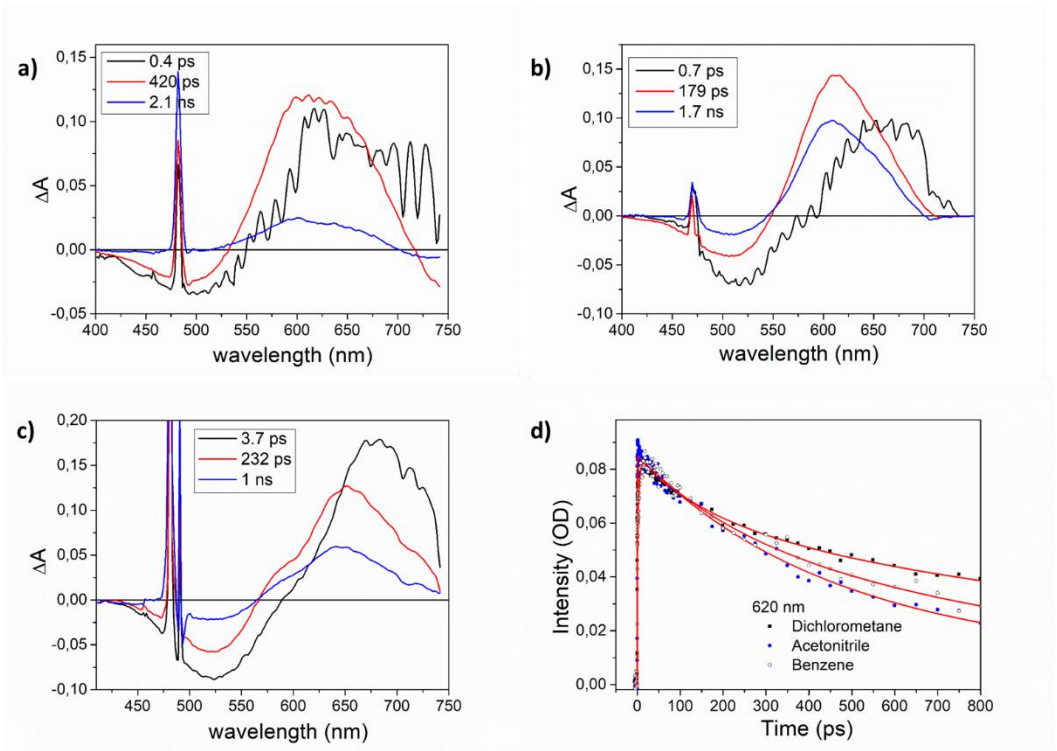

*Figure 2.7 EADS obtained by the global analysis of transient data recorded for **MB56** in (a) ACN, (b) DCM, (c) benzene; panel (d) reports the kinetic traces at 625 nm registered for **MB56** in the three solvents (scattered points). Red lines underlying the kinetic traces lines on panel d represent the fit resulting from global analysis*

In the majority of cases three kinetic components have been necessary in order to accurately fit the kinetic traces. For all molecules, the excited state absorption band rose in intensity and broadened towards 650-750 nm on *ca.* 1 ps timescale (black to red evolution in Figure 2.7 panels a, b and c). On a short timescale after excitation, several processes could occur, concerning both the relaxation of the initially excited state and reorganization of the solvent. In analogy with what observed in similar dyes presenting a D-π-A structure,[17a] the occurring of the spectral evolution on a few ps timescale could be indicative of the evolution from an initial local excited state to an excited state with charge transfer character. The transient absorption spectra of **DF15** and **MM62** reported in Figure 2.7 were qualitatively very similar. In both cases, a very broad excited state absorption band could be noticed, besides a negative feature corresponding to the bleaching of the ground state absorption. In case of **MM62** the measurement of the transient absorption spectra in ACN was not possible, due to the extremely low solubility of the dye in this solvent. In order to have an idea of the effect of solvent polarity on the excited state properties of this molecule, a transient spectrum in another polar solvent, DMSO (where the molecule was more soluble), was registered. The lifetimes obtained by global analysis for all the investigated compounds in the different solvents are summarized in Table 2.2.

Table 2.2 Time constants resulting from the analysis of transient absorption data.

Dye	DCM			ACN			Benzene		
	τ_1 (ps)	τ_2 (ps)	τ_3 (ps)	τ_1 (ps)	τ_2 (ps)	τ_3 (ps)	τ_1 (ps)	τ_2 (ps)	τ_3 (ps)
DF15	0.7	10.9	735	0.5	3.8	61.0	0.5	7.0	215
MM62	1.0	1.9	46	0.6[a]	21.0[a]	3900[a]	2.8	65.4	1700
MB25	0.5	10	1800	0.8	330	1600	3.0	47.0	727
MB56	0.7	179	1700	0.4	420	2100	3.7	232	1000
[a] Values referred to the DMSO solution.									

In DCM, the excited state absorption band significantly decayed on a 10 ps timescale, while the residual signal recovered in ca 750 ps timescale for **DF15**. On the other hand, in case of **MM62** in DCM an additional evolution on a 2 ps timescale was observed, which could be ascribed to vibrational relaxation, being accompanied by a slight blue-shift and narrowing of the excited state absorption band. The following decay of the excited state absorption occurred on a 46 ps timescale. When measurements were repeated in a more polar solvent (ACN for **DF15**, DMSO for **MM62**), the observed spectral shapes and the dynamic evolution of the transient signals were qualitatively similar to what already observed in DCM. The difference was an overall acceleration of the excited state evolution and of the recovery of the ground state. In fact, in the case of **DF15**, the excited state signals mostly recovered in 3.8 ps (with a residual decay occurring in 60 ps), while for **MM62**, the ground state recovery occurred respectively in 7.6 and 21 ps. On the other hand, when measurements were performed in benzene, the excited state absorption band appeared more structured for **DF15**, while was again very broad in the case of **MM62**. In this solvent, excited state relaxation was significantly slower that what previously observed in more polar media, in agreement with the increased fluorescence yield already observed. For both **DF15** and **MM62**, besides an initial evolution occurring on a <1 ps timescale, which could be ascribed to the relaxation of an initially hot excited state, a further dynamics evolution was observed on a 7-10 ps timescale. The associated spectral changes mostly consisted in a blue-shift, narrowing

and increasing in intensity of the excited state absorption band, which induced to associate this dynamic evolution to vibrational cooling and solvent induced structural relaxation of the excited state. In the case of **MM62** the transient spectra in benzene were qualitatively similar to those already observed in DCM and DMSO, but a significant increase of the excited state lifetime is observed. Although with several specific differences, for all the compounds, the overall excited lifetime was dependent on the solvent polarity, resulting quite short in ACN (DMSO for **MM62**), intermediate in DCM and significantly longer in benzene. This observation suggested that the excited state stabilized upon visible excitation in polar media had a significant charge transfer nature, as already reported in case of push-pull dyes.[20] As already noticed from steady-state absorption spectra, the two dyes exhibited a strong similarity in the transient absorption spectral shapes and in the trend observed for the solvent effect on the excited state lifetime, confirm that modification of the anchoring group has a minor effect on the excited state electronic distribution.

On the contrary, in the case of **MB25** and **MB56**, several differences could be noticed. Although the spectral shape of the transient spectra of these two molecules was qualitatively similar to that observed for **DF15**, the excited state absorption band was narrower and slightly red-shifted for **MB56**. Furthermore, the solvent effect was less pronounced: in all solvents the excited state lifetime was on the ns timescale, and appeared to be only slightly longer in DCM as compared with ACN and benzene. This observation brought to the conclusion that the excited state reached upon excitation at 520 nm in both **MB25** and **MB56** had less charge transfer character as compared with the previously analyzed compounds, by the effect of the differences on the backbone in these systems if compared with **DF15**. This was due to a more delocalized electron density in the ground state which determines a minor electron density shift in the excited state.

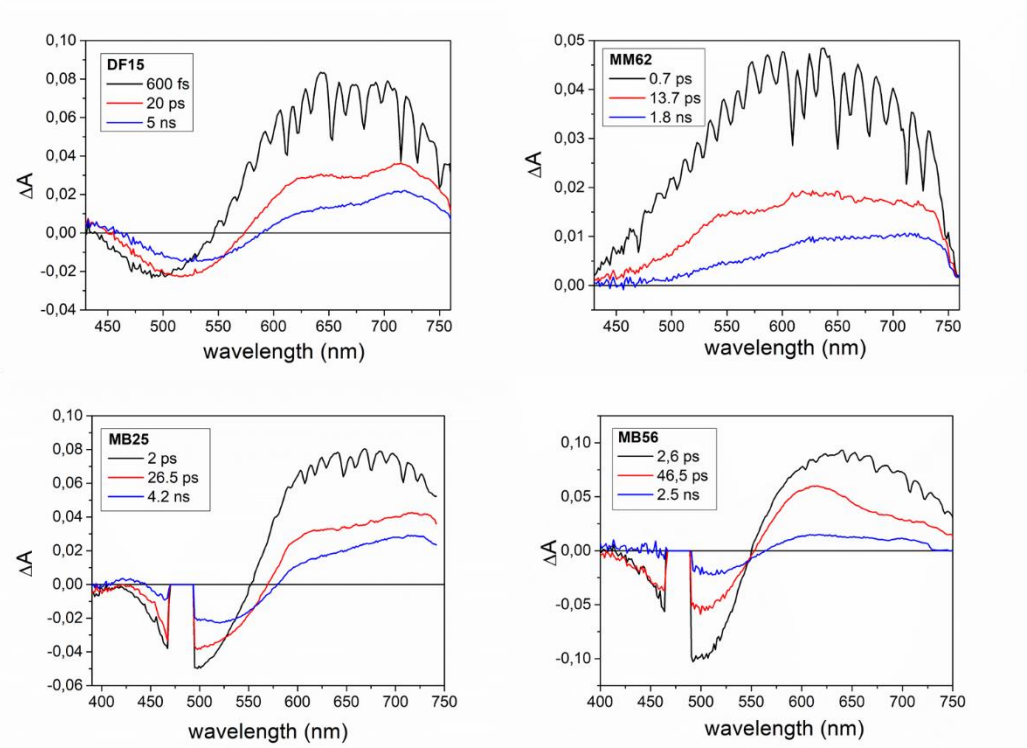

Figure 2.8 EADS obtained by the global analysis of transient data recorded for all the investigated dyes when absorbed on a TiO_2 film.

Finally, TiO_2 film sensitized with all the dyes object of the study were analyzed and the relative transient absorption spectra are reported in Figure 2.8. In all cases, the excited state lifetime increased significantly upon absorption on the semiconductor surface (indication of the occurrence of the electron injection) and, with the exception of **MM62** (that showed an extremely broad excited state absorption band), the spectral shape of the excited state absorption band was qualitatively similar for all dyes. Soon after excitation, a very broad absorption band appeared in the spectra, which partly decreased in intensity on a 0.5-2 ps timescale. On the same timescale, the spectral shape of the excited state band became more structured, allowing to distinguish a double peak structure. Based on previous studies on similar D-π-A dyes with analogous structure as **DF15**[21] and on the comparison between the normalized spectral shapes of the last EADS measured in solvents and on TiO_2, the excited state band peaking on the 700-750 nm region could be associated to the formation of the dye radical cation upon electron injection into the semiconductor substrate. Notably, while this band could be clearly seen in the spectra of **DF15** and **MB25**, in those of the silylated dyes **MM62** and **MB56** only a very weak band was present, suggesting a lower contribution by the radical cation. In any cases, analysis of the transient absorption spectra suggests that the electron injection process occurs at least in part on a very short timescale for all dyes.

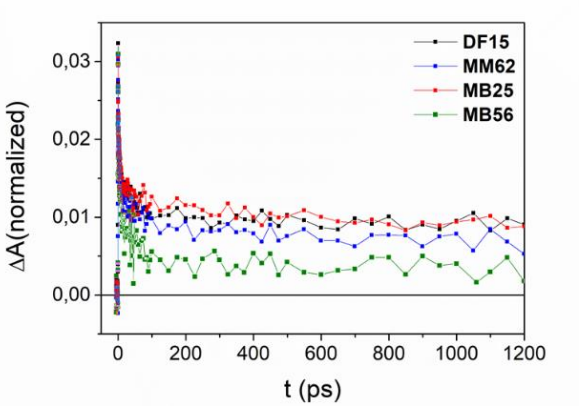

Figure 2.9 Comparison between the normalized kinetic traces of the relative EDAS spectra recorded at 720 nm for the different molecules.

The analysis of the kinetic traces at wavelength >700 nm, due to the cation absorption, could give information on the semiconductor-dye recombination kinetics and on the amount of injected electrons reaching the conduction band of the substrate. As it can be seen in Figure 2.9, the kinetic traces registered at 720 nm for all dyes show a fast bi-exponential decay component and a long lasting offset. The fast decay was associated with rapid charge recombination due to the electrons injected on the surface state of the semiconductor, or to cation quenching due to dye aggregation on the surface, in line with what was already observed for similar D–π-A dyes.[22] A small qualitative dependence on the anchoring group can be observed: after the substitution of the cyanocrylic moiety with the phenylalkoxysilane group, in fact, the timescale of fast recombination shortened to *ca.* 14 ps (for **MM62** and **MB56**) from the initial *ca.* 20 ps in the case of **DF15** and **MB25**, possibly as the effect of the increased conjugation of the anchoring group, or of a different absorption geometry on the semiconductor surface.[23] The value of residual signal that was observed is related to the amount of charge carrier that were successfully separated in the process and did not recombine with the dye molecule itself,[21c] as well the longer component of the decay (the longer it is, higher is the amount of electrons that recombine[24]). It has to be pointed out that the relatively large amount of the fast decay component could result from the preparation procedure adopted for the colored films, which did not involve the addition of any anti-aggregating agent to the dye solution, the use of any electrolyte (that

can induce modifications both on the electron injection and charge recombination timescale)[17a] and to the fact that TAS measurements have been performed by directly exposing the film to air.

In order to evaluate the electron injection capabilities of the dyes, the relative amount of the constant offset measured at >700 nm (which can be connected to the amount of electrons injected into the semiconductor CB)[21a] were compared. As reported in Figure 2.9, **DF15** and **MB25** showed the most intense residual signal, while two silylated dyes exhibited a lower constant offset (only slightly smaller with respect to **DF15** for **MM62**, while reduced to almost 1/3 of the value measured for the corresponding cyanoacriylic acid for **MB56**). The outcomes of time resolved measurements suggested that the modifications introduced on the anchoring group could affect the efficiency of solar cells prepared with the silylated dyes due the larger extent of the recombinative process, possibly affecting the efficiency of the electron injection if compared to the corresponding cyanoacrylic dyes.

2.1.2.2. Computational Analysis

A theoretical analysis of the silylated dyes **MM62** and **MB56** was also performed in order to rationalize the electronic structure of the compounds and to characterize their excited state energy and charge transfer capabilities. The analysis was based on DFT/TD-DFT calculations‡ and, once again, the results were compared with those of the corresponding cyanoacrylic dyes. Both the isolated and the anchored dye were considered, using, in the second case, a model (composed by a TiO_2 cluster) to simulate the electronic properties and the FMOs of the semiconductor.

- **Isolated Dye**

In the calculations, the pentylic chains of dyes **MB25** and **MB56** were replaced by simple methyl groups to reduce the computational burden, without affecting the nature of the conjugated system. The dyes structures were optimized by means of TD-DFT calculations, which were performed as reported in the Experimental Section (see below). The energy values of the FMOs and their shape were calculated for all the computed structures (**DF15**, **MM62**, **MB25** and **MB56**) and the wave function plots of the corresponding orbitals are shown in Figure 2.10.

‡ TD-DFT calculations were performed by Prof. Adalgisa Sinicropi (University of Siena).

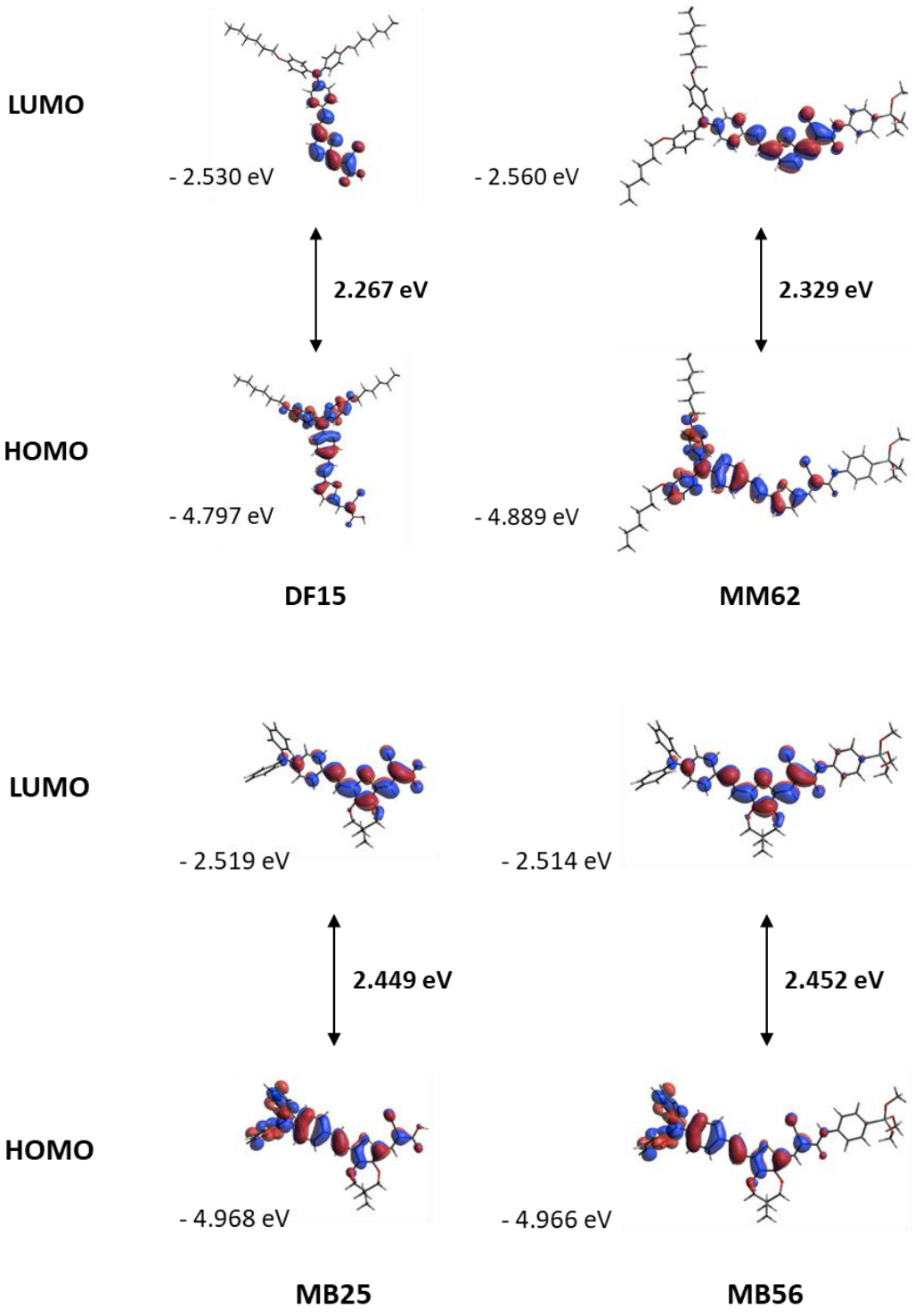

*Figure 2.10 Wave function plots of the HOMO and LUMO orbitals of compounds **DF15**, **MM62**, **MB25** and **MB56**.*

The plots showed the typical FMOs distributions of a D-π-A dye, with a HOMO mainly localized on the donor part and the π-spacer, while the LUMO was mostly localized on the acceptor part. In particular, in the case of **MM62** and **MB56** can be seen how the electron density of LUMO level remains substantially located on the cyanoacrylic moiety, without any significant contribution arising from the siloxane anchoring group, which limits the intramolecular charge-transfer nature of the excitation process. Anyway, the modification on the anchoring group did not cause any significant change of the shape and the energy values of the FMOs.

Table 2.3 TD-DFT (CAM-B3LYP/6-31G and, in brackets, MPW1K/6-31G*) computed absorption maxima (λ^a_{max}), energy (E_{exc}), oscillator strengths f and composition in terms of molecular orbitals for the lowest singlet-singlet excitation[#] of **DF15**, **MB25**, **MB56** and **MM62** in DCM, benzene and ACN.*

Dye	Solvent	λ^a_{max} (nm)	E_{exc} (eV)	*f*	Transition H→L
DF15	DCM[a]	489 (517)	2.53 (2.40)	1.594 (1.517)	77% (90%)
	Benzene	487 (513)	2.54 (2.41)	1.607 (1.539)	77% (89%)
	ACN	487 (515)	2.54 (2.41)	1.583 (1.501)	77% (90%)
MM62	DCM	480 (505)	2.58 (2.46)	1.819 (1.750)	77% (89%)
	Benzene	480 (504)	2.58 (2.46)	1.820 (1.760)	77% (89%)
	ACN	478 (502)	2.59 (2.47)	1.819 (1.746)	77% (89%)
MB25	DCM	477 (497)	2.60 (2.49)	1.505 (1.494)	80% (91%)
	Benzene	475 (493)	2.61 (2.51)	1.519 (1.518)	80% (90 %)
	ACN	476 (496)	2.61 (2.50)	1.491 (1.475)	80% (91%)
MB56	DCM	479 (499)	2.59 (2.48)	1.733 (1.721)	80% (90%)
	Benzene	477 (495)	2.60 (2.50)	1.741 (1.741)	80% (90%)
	ACN	478 (498)	2.60 (2.49)	1.728 (1.710)	80% (90%)
[a] Values taken from ref.25					

TD-DFT absorption maxima (λ^a_{max}), vertical excitation energies (E_{exc}) and oscillator strengths (*f*) in DCM, benzene and ACN are shown in Table 2.3. Calculations showed how the main visible band in the spectrum of all dyes is due to a HOMO → LUMO transition and, in agreement with experimental values, the vertical excitation energies were computed in the 2.52-2.63 eV and 2.40-2.51 eV ranges at the CAMB3LYP/6-31G* and MPW1K/6-31G* levels of theory, respectively. In addition, the deprotonated form of **DF15** was also computed at the CAM-B3LYP/6-311+G(2d,p) level of theory and its data were compared to those of the neutral form (Table 2.4).

*Table 2.4 TD-DFT (CAM-B3LYP/6-311+G(2d,p)) computed absorption maxima (λ^{a}_{max}), excitation energy (E_{exc}), oscillator strengths (f) and composition in terms of molecular orbitals for the lowest singlet-singlet excitation of **DF15** and of its deprotonated form in DCM, benzene and ACN.*

Dye	Solvent	λ^{a}_{max} (nm)	E_{exc} (eV)	*f*	Transition H→L
DF15	DCM	508.97	2.4360	1.5944	77%
	Benzene	506.64	2.4472	1.6050	77%
	ACN	506.75	2.4467	1.5829	77%
Deprotonated DF15	DCM	439.42	2.8215	1.5348	73%
	Benzene	428.20	2.8955	1.5707	83%
	ACN	443.24	2.7972	1.5065	72%

The computed difference in vertical excitation energy between neutral and deprotonated form was in line with the observed blue-shift of the absorption maximum in the UV-Vis. spectra after sensitization on TiO_2 film (if compared to the data obtained in solution), confirming that the deprotonated acid was the active anchoring group.

- **Absorbed Dye**

The optimized geometries of dyes on TiO_2 are shown in Figure 2.11, in comparison with their calculated arrangement in solution.

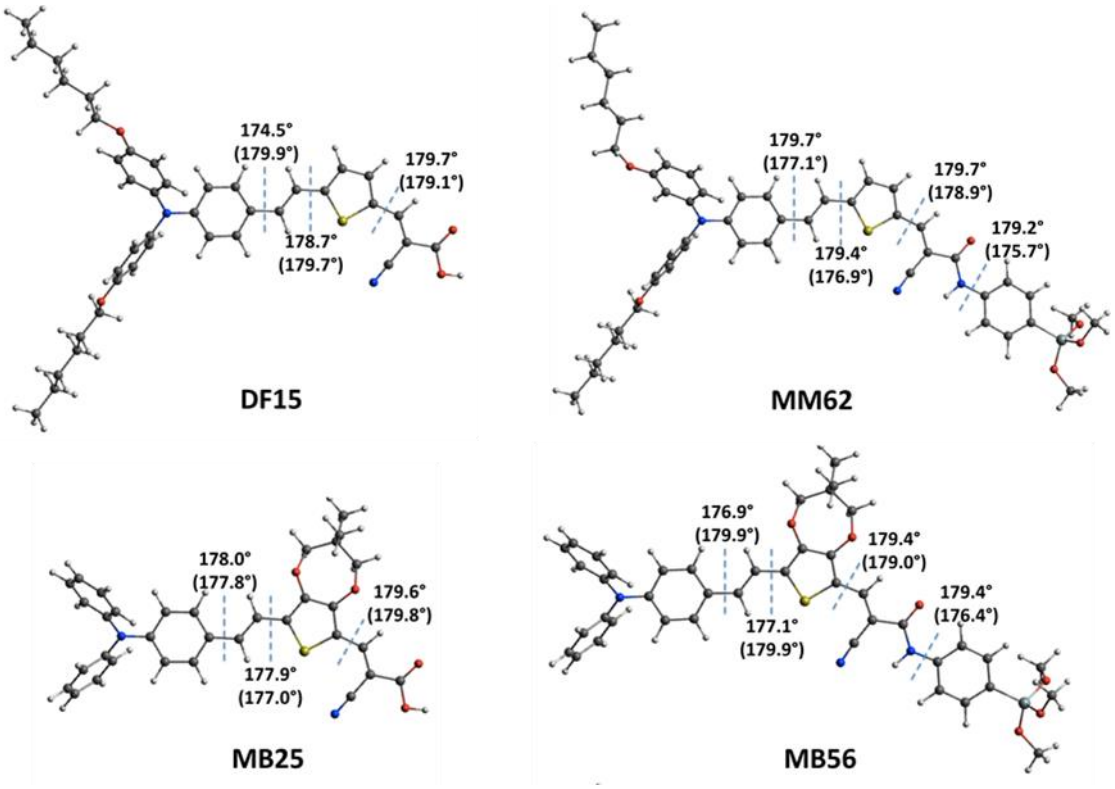

*Figure 2.11 Geometries and dihedral angles of dyes **DF15**, **MM62**, **MB25** and **MB56** isolated and adsorbed on TiO_2 (in parenthesis).*

As can be seen, the geometries of the dyes do not show any major change upon binding to TiO_2. In particular, the dihedral angles between the donor and the π-conjugated units and between the spacer and the cyanoacrylic groups did not significantly deviate from planarity upon binding the semiconductor, meaning that the degree of π-conjugation was conserved. As a consequence, the energy values of the HOMOs for the isolated **DF15**, **MM62**, **MB25** and **MB56** dyes are comparable with those for the same dyes after sensitization (Figure 2.12).

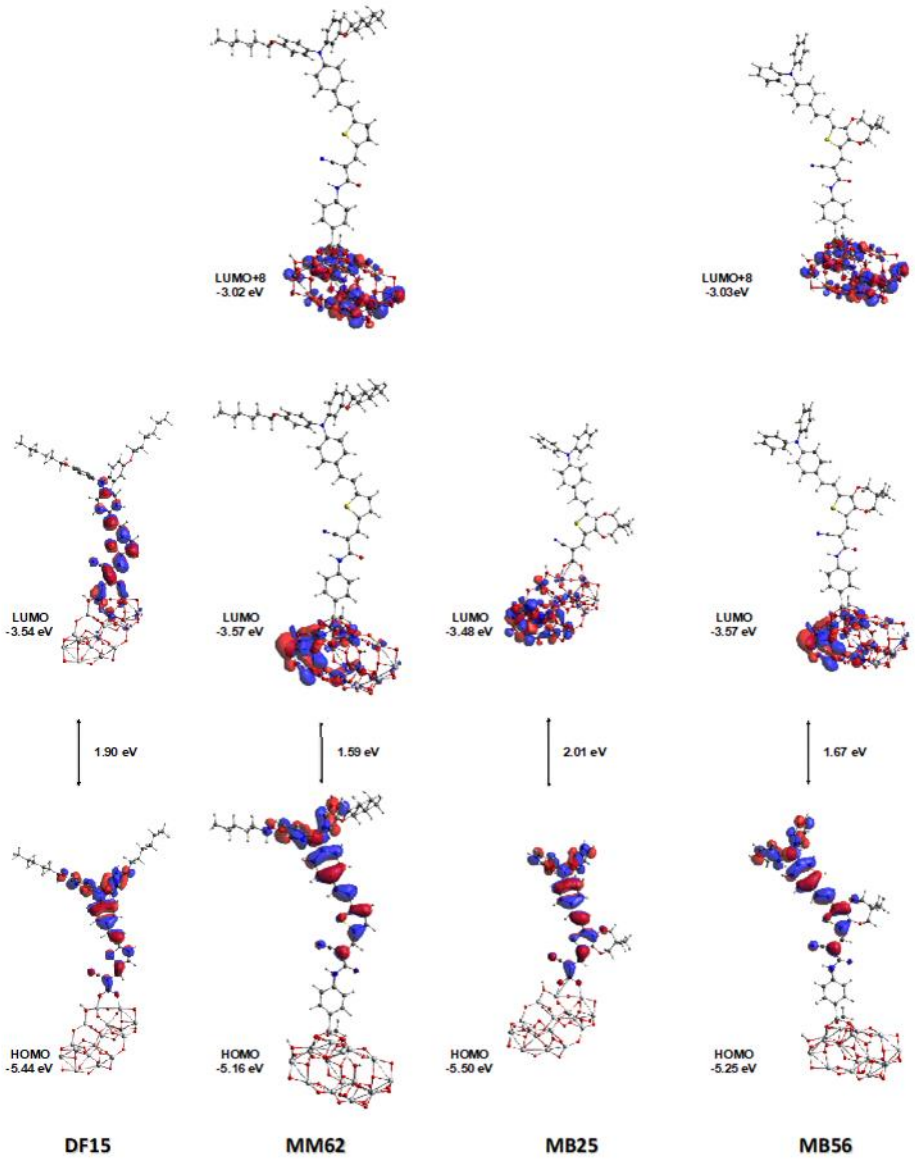

*Figure 2.12 Wave function plots and energies of the frontier molecular orbitals of compounds **DF15**, **MM62**, **MB25** and **MB56** on TiO_2.*

The LUMO energy levels, instead, were considerably stabilized when bound to TiO_2, thus reducing the HOMO→LUMO energy gap, which was confirmed by the red-shifted absorption maximum computed for all the dye/TiO_2 systems (see Table 2.5). Nevertheless, as previously reported,[26] the observed blue- or red-shift of the absorption maximum in going from dye/solvent to dye/TiO_2 systems is rather mainly caused by the protonation state of the dye in solution and by the dye aggregation which, in turn, depends on the dye packing on the surface and thus it is not predictable. For these reasons, and contrarily to the predicted reduced energy gap, a blue-shift is observed in the experimental UV-Vis. dyes absorption spectra after sensitization (see Figure 2.5). To complete the set of TD-DFT calculation

and learn more about the electronic differences, absorption maxima (λ^a_{max}), vertical excitation energies (E_{exc}) and oscillator strengths (f) for the all the cyanoacrylic and siloxane dyes on TiO_2 were computed, and are shown in Table 2.5; for comparison, the same values obtained for all the compounds in DCM solution are also reported at the CAM-B3LYP/6-311G(d,p) level of theory.

*Table 2.5 TD-DFT[#] computed absorption maxima (λ^a_{max}), energy (E_{exc}), oscillator strengths f and composition in terms of molecular orbitals for the lowest singlet-singlet excitation of **DF15**, **MM62**, **MB25** and **MB56** in DCM and upon binding TiO_2.*

Dye		λ^a_{max} (nm)	E_{exc} (eV)	f	**Transition**
DF15	TiO_2	528	2.35	2.111	H→L 78%
	DCM	490	2.53	1.595	H→L 77%
MM62	TiO_2	459	2.71	1.864	H→L+8 78%
	DCM	481	2.58	1.819	H→L 77%
MB25	TiO_2	493	2.52	1.950	H→L 69%
	DCM	479	2.61	1.506	H→L 80%
MB56	TiO_2	455	2.72	1.810	H→L+8 82%
	DCM	480	2.58	1.736	H→L 80%
[#] For dyes/TiO_2: CAM-B3LYP/6-311G(d,p) level in which the standard LANL2DZ basis set was used for the Ti atom; for dyes in DCM: CAM-B3LYP/6-311G(d,p) level.					

2.1.2.3. Photovoltaic Measurements[§]

Strip DSSC cells (3.6 cm^2) containing the acid **MB25** and its silylated derivative **MB56** as sensitizers and a small-scale test DSSC (0.25 cm^2) sensitized with **MM62** were assembled in order to evaluate and compare their photovoltaic performances. The standard organometallic dye **Z907**[27] was used as reference (Figure 2.13).

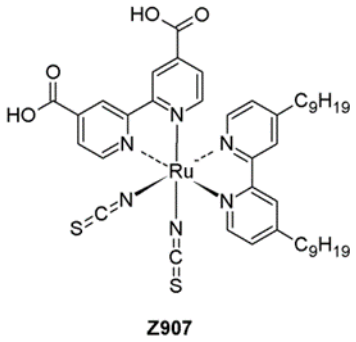

Z907

*Figure 2.13 Structure of the reference dye **Z907**.*

[§] All the photovoltaic measurements were carried out by Dr. Daniele Colonna and Prof. Aldo di Carlo (C.H.O.S.E., University of Rome "Tor Vergata").

Considering the obtained value for the molar extinction coefficient of the studied dyes, the cells were prepared with transparent photoanodes having thickness of 6 μm (using commercial Dyesol 18NR-T paste), without any other treatment on the semiconductor film. A commercial electrolyte solution based on the most classical I^-/I_3^- redox couple (Dyesol HPE) was employed in the cells without the use of any other additive. Typical J/V curves measured on the transparent solar cells are shown in Figure 2.14, while the photovoltaic performance parameters are reported in Table 2.6.

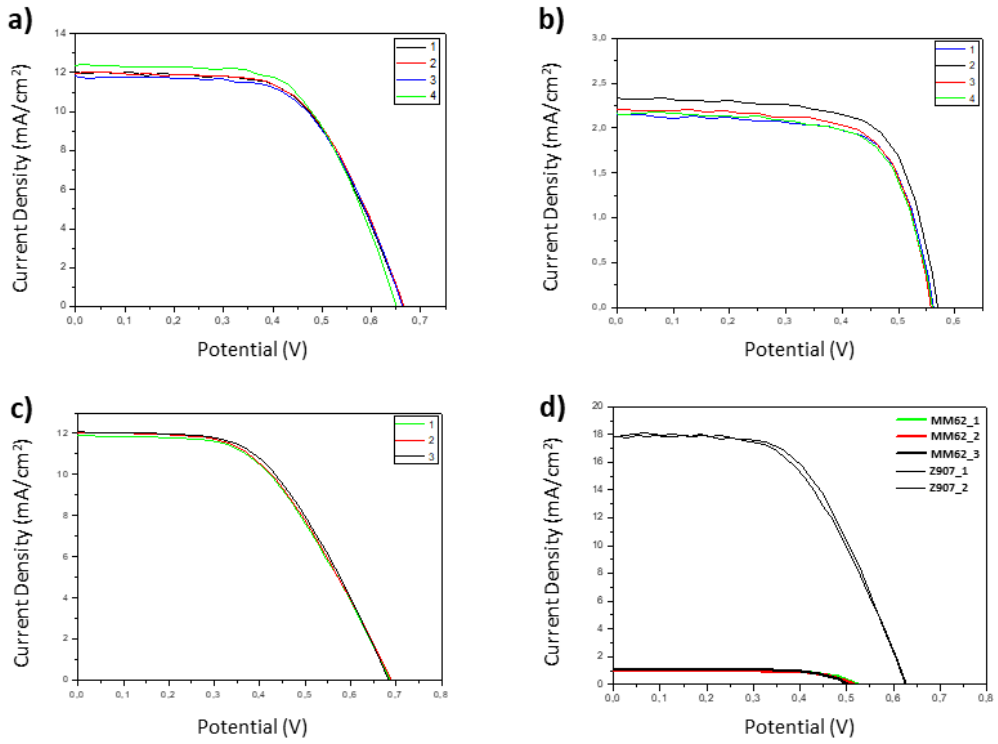

*Figure 2.14 Typical J/V curves for transparent strip cells built with dyes (a) **MB25**, (b) **MB56**, (c) **Z907** and for small-scale test cells sensitized with (d) **MM62** and **Z907**.*

*Table 2.6 Photovoltaic parameters for transparent DSSCs built with dyes **MB25**, **MB56**, **MM62** and **Z907**.*

Dye	**V_{oc} (mV)**	**J_{sc} (mA/cm²)**	***ff*** **(%)**	**η (%)**
MB25 (strip)	660	11.99	60	4.80
MB56 (strip)	560	2.20	69	0.86
Z907 (strip)	688	12.00	52	4.28
DF15 (small-scale)[a]	686	10.86	67	4.97
MM62 (small-scale)	514	1.03	68	0.36
Z907 (small-scale)	628	17.92	57	6.37
[a] Values taken from ref. 25				

As can be seen from Table 2.6, the two silylated dyes exhibited notably lower efficiency when compared either to the reference dye **Z907** or the corresponding cyanoacrylic acid. This effect can be seen for both the two different series of dyes sharing the same backbone and both in the small-scale test devices and in the strip cells. In particular, the recorded value for the J_{sc} in the case of the silylated dyes was six to ten times lower than those of the corresponding cyanoacrylic acids. As example, in Figure 2.15 is reported the IPCE spectra of the two dyes **MB25** and **MB56**: both of them showed a peak around 460 nm, but while **MB25** exhibited a values for IPCE of 61%, **MB56** showed only a value of 5%.

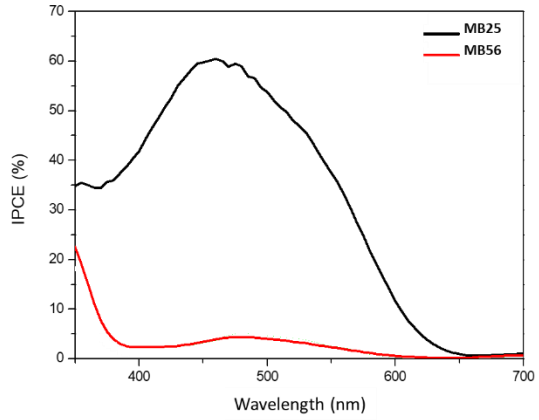

*Figure 2.15 IPCE spectra for strip cells build with dyes **MB25** and **MB56**.*

This unexpected result seems to be in contrast with what was observed by *Kakiage et al.* with their silylated dye **ADEKA-1**, which was reported to have better efficiency of the related cyanoacrylic acid **MK-2**.[10a] On the other hand, such a result is in agreement with what we observed in the transient absorption spectroscopy experiments which showed us lower electron injection rate and the slightly faster recombination rate for the silylated dyes after sensitization on the TiO_2 surface, which justify a worse performances than their cyanoacrylic equivalents. The excellent results obtained by *Kakiage et al.* could be probably explained by the extremely refined cell fabrication procedure they employed, comprising use of a complicated, multicomponent electrolyte solution and treatment of the TiO_2 layer with several different metal oxides and co-adsorbents (establishing an "anti-recombination" layer). Such observations can be also related to the work of *Ziółek et al.* on the factors affecting the performances of silylated anchoring group on DSSC.[21b] In that study, the synthesis and the purification of **ADEKA-1** were optimized and the effect of the dye purity, along with the presence of additives in the electrolyte solution and of pre-treatment on the semiconductor surface, was studied. Indeed, the presence of co-adsorbents and capping agents was observed to strongly reduce the fast-recombination this kind of anchoring group suffers, due to the suppression of the coupling between the injected electrons and the dye molecules. In addition, the bulky co-adsorbent molecules impose a perpendicular orientation on the TiO_2 surface to the sensitizer, which plays a critical role on the final performances. Indeed, a twisted anchoring geometry (possibly caused by the high flexibility of the anchoring group) could reduce the distance between the donor part of the dye and the TiO_2, thus promoting the recombination process.[23] For that reason, a perpendicular geometry of the dye on the TiO_2 surface is preferable. In their case, in the best conditions, cells built with **ADEKA-1** displayed performances comparable to those obtained by devices sensitized with the corresponding acid **MK-2**, but were not able to surpass the results of the carboxylate. Probably, the high electronic coupling between the dye and the TiO_2, along with the great flexibility conferred by the long phenyl-alkoxysilane group are the main causes of the not satisfactory performances we obtained with this anchoring moiety in DSSCs. This last observation shows how the siloxane group could be a great anchoring group for DSSC application, but only when a huge work of

optimization of the staining conditions and of the electrolyte solution is carried out, in order to speed up the electron injection and slow down the recombination processes.

2.1.3. Development of the New Silatrane Dyes

2.1.3.1. Validation of the Siloxane Synthesis

In a previous study,[28] two new synthetic procedures for the introduction of the siloxane moiety on cyanoacrylic acids were developed using dyes **DF15** and **MB25** as starting materials (Scheme 2.3), respectively, as the previously reported procedure[10a] used to prepared **ADEKA-1** proved to be not general. In order to validate the new procedures, we attempted then the synthesis of dye **ADEKA-1** (Scheme 2.4 and Scheme 2.5).

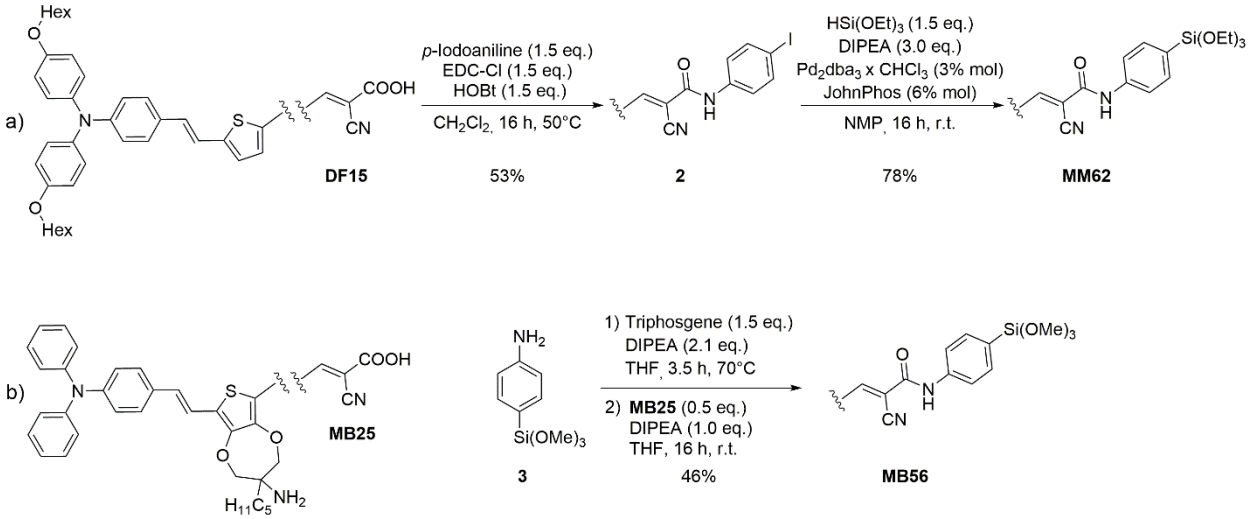

*Scheme 2.3 Synthetic procedures developed for preparing the dyes (a) **MM62** and (b) **MB56**.*

Thus, we performed a simple peptide coupling between acid **MK-2** and 4-iodoaniline, mediated by EDC-Cl; after purification by column chromatography, amide **4** was collected with a reasonable yield (Scheme 2.4). Unfortunately when then following step was attempted to obtain the I-Si exchange by treatment of amide **4** with triethoxysilane in the presence of a Pd-based catalyst and DIPEA as a base, we obtained the product of the dehalogenation (**5**) as the main product of the reaction. Such a process, which is known to occur sometimes under the reaction conditions used[29] hampered the possibility to extend the protocol to our model compound **MK-2**. The second protocol, developed for the preparation of siloxane **MB56** (Scheme 2.3b), was also tested. In this case we need to perform two consecutive steps with the in situ formation of the isocyanate of amine **3** by reaction with triphosgene in basic THF, followed by interception of the latter with carboxylic acid **MK-2** to give the corresponding amide (Scheme 2.5).

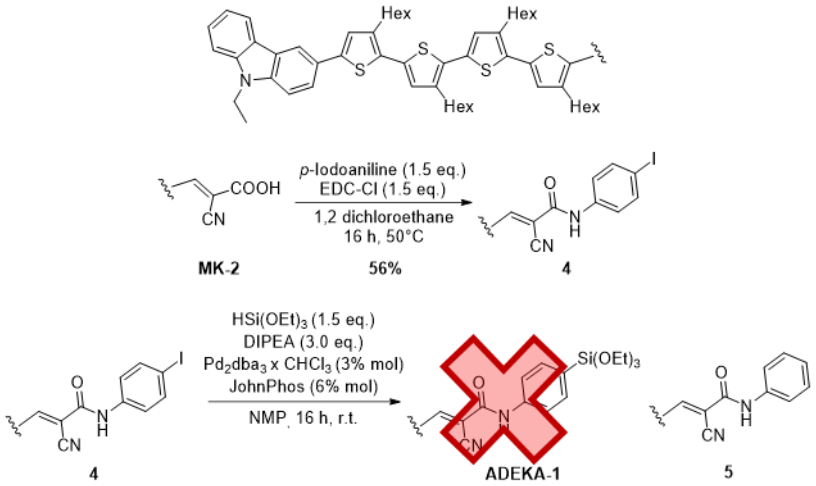

*Scheme 2.4 Attempted synthesis of **ADEKA-1** using the same procedure employed to prepare **MM62**.*

Unfortunately, also in this case, the formation of the right product was not observed, and only acid **MK-2** was recovered after purification by column chromatography. An attempt to rise the temperature of the second step from r.t. to 50°C, did not give any better result.

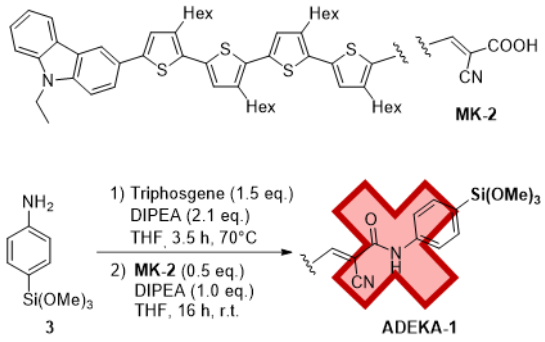

*Scheme 2.5 Attempt in the synthesis of **ADEKA-1** using the same pathway as **MB56**.*

2.1.3.2. Silatrane Synthesis

As we have already anticipated, at this stage of the work we decided to exploit the possibility to look for a new valid anchoring group alternative to the siloxane, in order to overcame the difficulties in the synthesis and the purification of silylated dyes encountered so far.

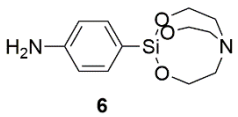

Figure 2.16 Chosen silatrane precursor.

We decided to use the silatrane moiety (Figure 2.16) which can be easily synthetized from the corresponding siloxane in one step.[30] Such moiety is expected to be more stable due to the particular characteristic to establish a trans-annular dative bond from the nitrogen to the silicon atom, producing a formally penta-coordinated electron-rich silicon species.[31]

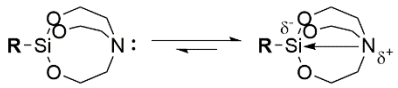

Figure 2.17 Trans-annular bonding in silatrane.

In particular we decided to focus on the preparation of phenyl derivative **6**, which was successfully synthetized with high yield using a procedure already reported in literature.[30] Trialkoxysilane **3** was reacted in boiling toluene with triethanolamine (TEOA) and after filtration of the solution, compound **6** was obtained in high purity as a white solid (Scheme 2.6). This reagent was then used to prepare silatrane **MB96**.

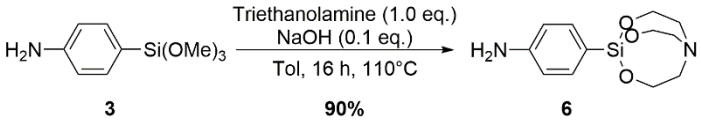

Scheme 2.6 Synthesis of the silatrane precursor.

Indeed we knew from a precedent work that the introduction of the silylated group by peptide coupling between precursor **3** and acid **DF15** (Scheme 2.7) was not an efficient process. Due to the low nucleophilicity of the aniline nitrogen and the tendency of siloxane to hydrolyze to the corresponding hydroxysilane, the only product of the reaction was the methyl ester of acid **DF15**. However, we reasoned that the presence of the silatrane cage could overcome both the problems encountered with the siloxane: the trans-annular bond, in fact, makes the aniline nitrogen more nucleophilic (by pushing a negative charge towards the aromatic ring), while the presence of the cage strongly reduces the possibility to get hydrolysis of a Si-C bond, minimizing the esterification side-reaction.

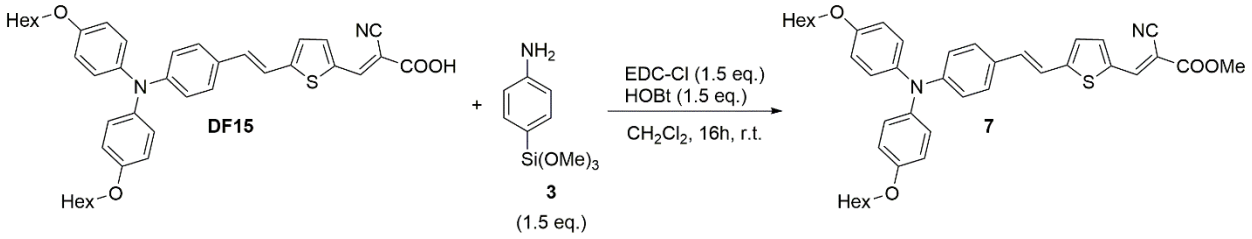

*Scheme 2.7 Attempt in the synthesis of **MM62**, formation of the methyl ester.*

Thus, the peptide coupling between a cyanoacrylic acid and aniline **6** was investigated. Initially, the reaction was tested on dye **DF15** as reference compound (Scheme 2.8).The conditions employed are summarized in Table 2.1. First of all, EDC-CI (Figure 2.18) was employed as coupling agent in DCM at r.t.; differently from our previous studies,[12] in this case the use of HOBt was avoided because control reactions demonstrated that its presence was irrelevant for the reaction outcome.

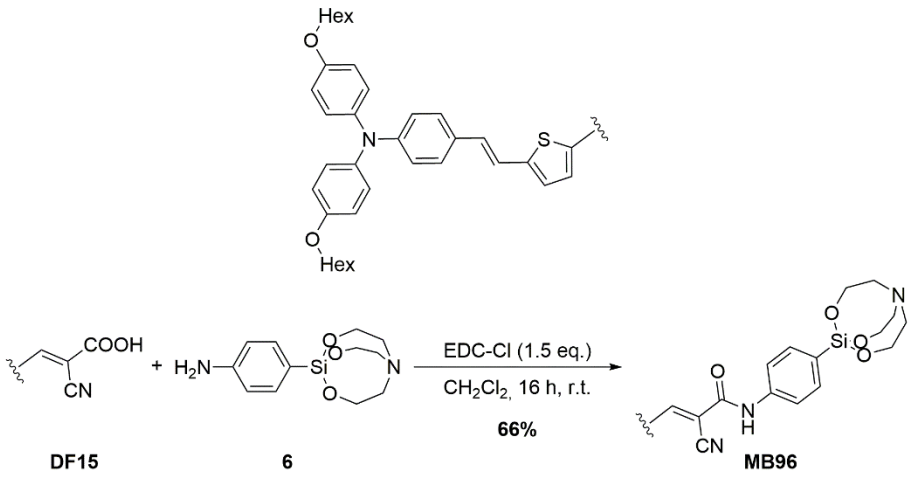

*Scheme 2.8 Synthesis of dye **MB96**.*

The reaction proceeded much more cleanly than in the case of the corresponding siloxane and, after a classic purification by flash column chromatography, the desired silatrane **MB96** was obtained in good yield and purity. Before trying the protocol on other acids, a small screening of the reaction conditions was carried out in an attempt to maximize the yield. In particular, two further coupling agents, PyBOP and TBTU (Figure 2.18), were used without changing the other reaction parameters, and an increase of the reaction temperature to 50°C was tested, still using EDC-Cl as reagent.

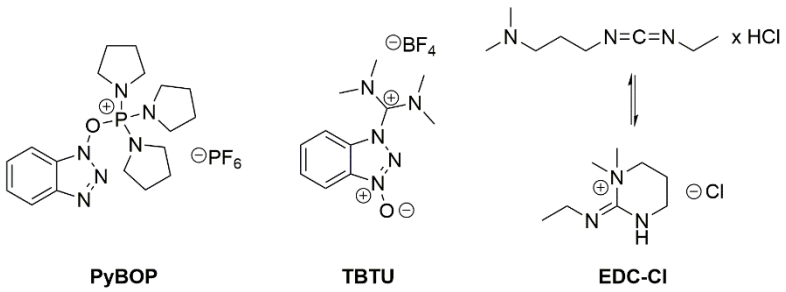

Figure 2.18 Structure of the peptide coupling agents.

As can be seen in Table 2.7, increasing the temperature led to a drop of the yield, while changing the coupling agent did not yield the desired product, but actually promoted a different reaction pathway. Indeed, when PyBOP and TBTU were used, a different compound was produced (while still some of the starting acid was recovered) which, after purification and NMR analysis, turned out to be the product of silatrane desilylation after formation of the amide bond (compound **5** in Scheme 2.4).

*Table 2.7 Optimization of the peptide coupling conditions between aniline **6** and dye **DF15**.*

Entry	**Coupling Agent**	**Temperature**	**Solvent**	**Yield**
1	EDC-Cl	r.t.	DCM	66%
2	EDC-Cl	50°C	1,2 dichloroethane	40%
3	TBTU	r.t.	DCM	-
4	PyBOP	r.t.	DMC	-

Based on these results, the reaction on other two cyanoacrylic acids was performed according to the best conditions (Entry 1 in Table 2.7), and the synthesis of silatranse **MB104** and **MB113** was achieved with good yield after purification by flash column chromatography, showing how this method is more general than those already employed for the introduction of the siloxane group (Scheme 2.9).

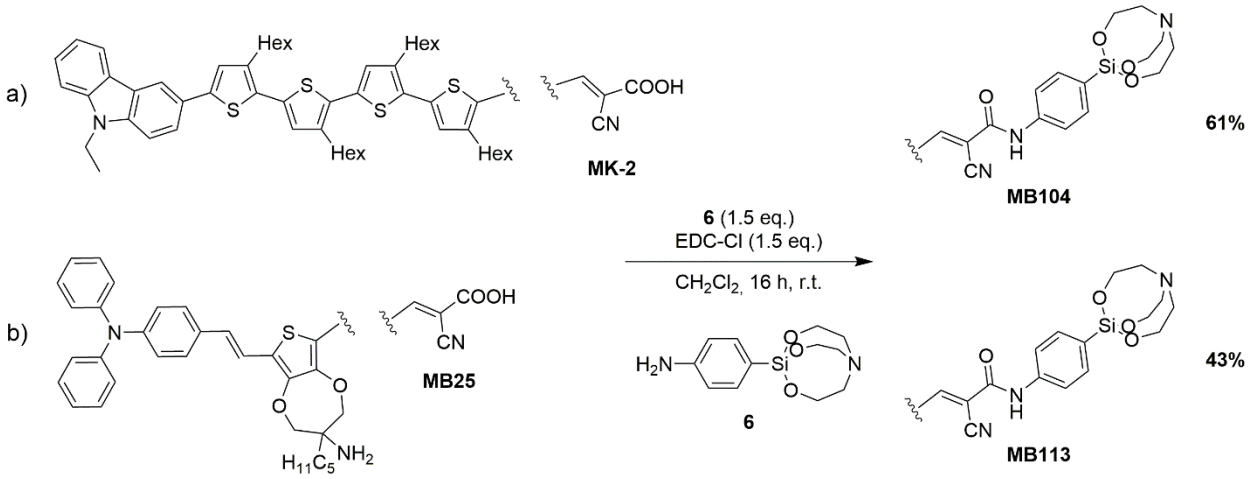

*Scheme 2.9 Synthesis of dyes **MB104** and **MB113**.*

2.1.4. Dyes Characterization

Once the synthesis of cyanoacrylic silatrane derivatives was carried out, their spectroscopic properties were analyzed. To prove that silatrane is a valid alternative to siloxane, a comparison between the spectroscopic and anchoring properties of the two groups was carried out. In particular, the species present on TiO_2 surface after dye adsorption were analyzed and compared for both silylated groups, in order to prove that the same (or a very similar) covalent adduct was formed in both cases.

Regarding the spectra recorded in solution, the concentration of the dye used was ≈2.0×10^{-5} M, while for the sensitization a concertation around 1×10^{-4} M was used. All the dyes exhibit a broad light absorption spectrum and good extinction molar coefficients; the spectra are shown in Figure 2.19, along with the superimposition of the correspondent cyanoacrylic acids and siloxanes, while relevant data are reported in Table 2.8.

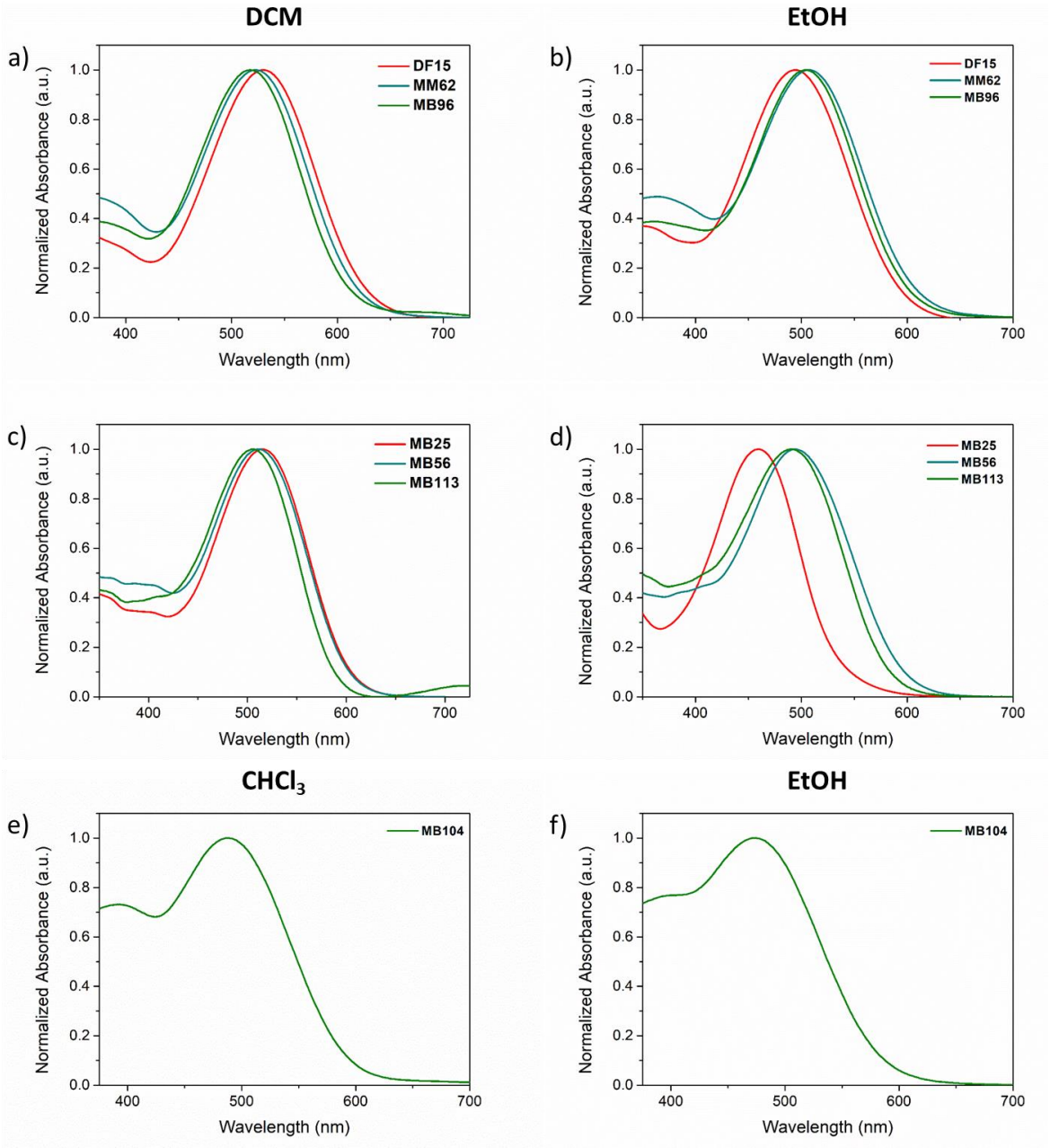

Figure 2.19 UV-Vis spectra of the carboxylic acid (red line), siloxane(blue line) and silatrane (green line) dyes in CH_2Cl_2, $CHCl_3$ and EtOH solution.

It can be seen that in CH_2Cl_2 solution very close values of maximum absorption wavelengths (λ_{max}) were observed along all the series , with just a slight blue shift moving from the acid (**DF15**, **MB25**) to the siloxane (**MM62**, **MB56**) and then to the silatrane (**MB96**, **MB113**). In the case of the siloxane obtained from acid **MK-2** (**ADEKA-1**), in $CHCl_3$ it can be seen that its λ_{max} is red shifted compared to the acid, while the introduction of the silatrane cage (**MB104**) on the structure causes a blue shift of the absorption maximum, going back to the same value as the acid (**MK-2**). The molar extinction coefficient, on the other hand, showed a different trend: it decreased going from the carboxylic acid to the siloxane, while it increased again moving to the silatrane (reaching a value even higher than that of the corresponding acid in the case of **MB96**). The data related to **ADEKA-1** follow once again, with the ε increasing when moving from the acid to the siloxane and then decreasing again going to the silatrane.

Table 2.8 Relevant UV-Vis spectroscopic data of the investigated dyes, both in solution and adsorbed on TiO_2.

Dye	DCM Solution		EtOH Solution		TiO_2 film
	λ_{max} (nm)	ε (M^{-1} cm^{-1})	λ_{max} (nm)	ε (M^{-1} cm^{-1})	λ_{max} (nm)
DF15[a]	530	35000	493	26900	457
MM62	523	22900	508	13800	493
MB96	518	42500	504	42300	490
MB25	515	27900	459	34300	457
MB56	511	22800	494	24500	475
MB113	506	27300	491	27100	476
	$CHCl_3$ Solution		EtOH Solution		TiO_2 film
MK-2	491	35800	-	-	441[b]
ADEKA-1	507[c]	43500[c]	-	-	512[c]
MB104	491	37200	473	35300	478
[a] Taken from ref. 30; [b] Taken from ref. 11b; [c] Taken from ref. 9.					

Regarding the data collected in EtOH solution, it can be seen that the molar extinction coefficient shows the same trend already observed in the chlorinated solvent solution, while the maximum absorption wavelength, on the other hand, follows a totally different evolution. In fact, in EtOH it is the λ_{max} of the acids to be significantly blue shifted compared to those of the silylated compounds (whose values are instead much closer to those observed in DCM solution). This solvatochromic effect is related to the interactions that can occur between molecules having acidic functional groups and protic solvents (i.e. hydrogen bonds or dissociation processes). In particular, if a deprotonation equilibrium takes place, it will cause an increment of the net negative charge on the acceptor group of the molecule, resulting in a destabilization of the LUMO and a blue shift of the λ_{max} compared to those registered in aprotic solvents, where this process cannot happen. Despite that, the differences recorded between the dyes sharing the same backbone were not very high (the molar extinction coefficients remained on the same order of magnitude, while the maximum shift in λ_{max} is 35 nm, observed between **MB25** and **MM62** in EtOH), suggesting that the electronic and photophysical properties remained stable and were not significantly affected by the changes in the anchoring group.

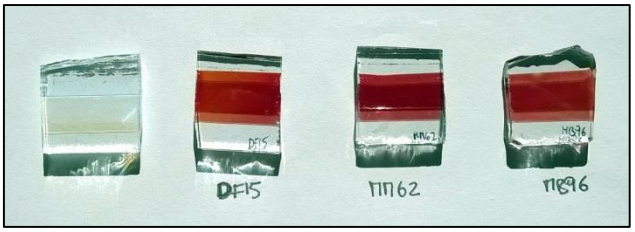

*Figure 2.20 TiO_2 films on glass sheets, from left to right: untreated; sensitized with **DF15**; sensitized with **MM62**; sensitized with **MB96**.*

After the evaluation of the optical properties in solution, to verity that silatrane can be considered a proper anchoring group, dyes **MB96**, **MB104** and **MB113** were adsorbed on nanocrystalline TiO_2 films deposed on glass sheets and then their optical properties were compared to those of sensitized films obtained from the corresponding acid and siloxane dyes. The staining conditions used for the sensitization were not the same for all the compounds examined: while for the acids it is sufficient to dip the films overnight in a toluene solution of the dyes at r.t., for the silylated compounds it is necessary to immerse the films in a toluene solution of the dyes heated up to 70°C for several hours. The difference in staining conditions depends on the different reactions that have to take place for sensitization to occur: while for the carboxylic acids only a deprotonation is needed, for the silylated dyes hydrolysis of the SiO-R groups to the corresponding silanols needs to happen (see Figure 2.1), a reaction requiring more forcing conditions. As a visual example, the stained films obtained for the series of dyes **DF15**, **MM62** and **MB96** together with the original untreated TiO_2 layer are shown in Figure 2.20.

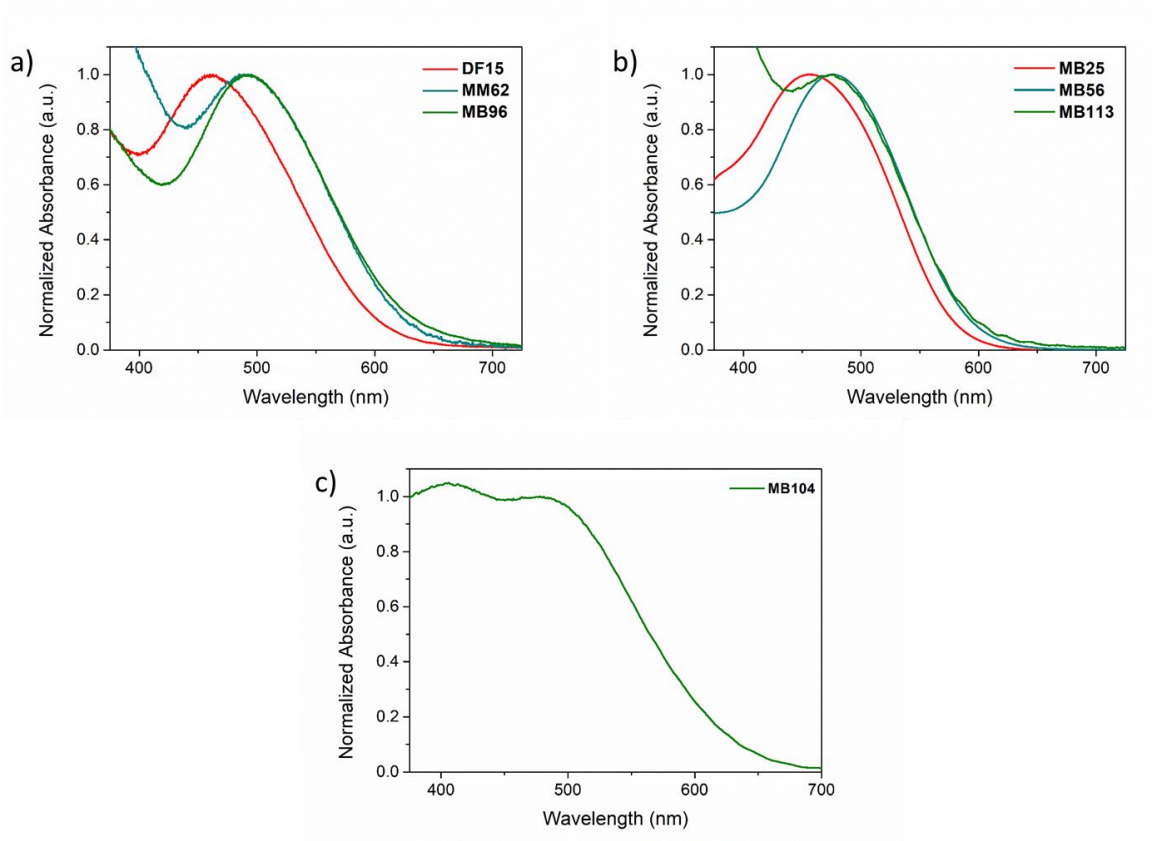

Figure 2.21 UV-Vis spectra of the carboxylic acid (red line), siloxane (blue line) and silatrane (green line) dyes absorbed on TiO_2.

The recorded UV-Vis spectra of the dyes absorbed on TiO_2 are shown in Figure 2.21. All dyes showed a much broader absorption profile compared to the spectra recorded in solution while the absorbance maxima exhibited a trend similar to that observed in EtOH solution. In this case, the bathochromic shift observed for the silylated dyes compared to the corresponding acids can be explained either by the deprotonation of the carboxylic moiety occurring upon sensitization, or by the less pronounced formation of aggregates on the semiconductor surface due to the reduced amount of adsorbed dye molecules (see below). Remarkably, the absorption characteristics of the two different classes of silylated dyes after the compounds were adsorbed on TiO_2 were almost identical, strengthening the hypothesis that the very similar (if not identical) species are formed on the semiconductor surface after sensitization with trialkoxysilane and silatrane dyes.

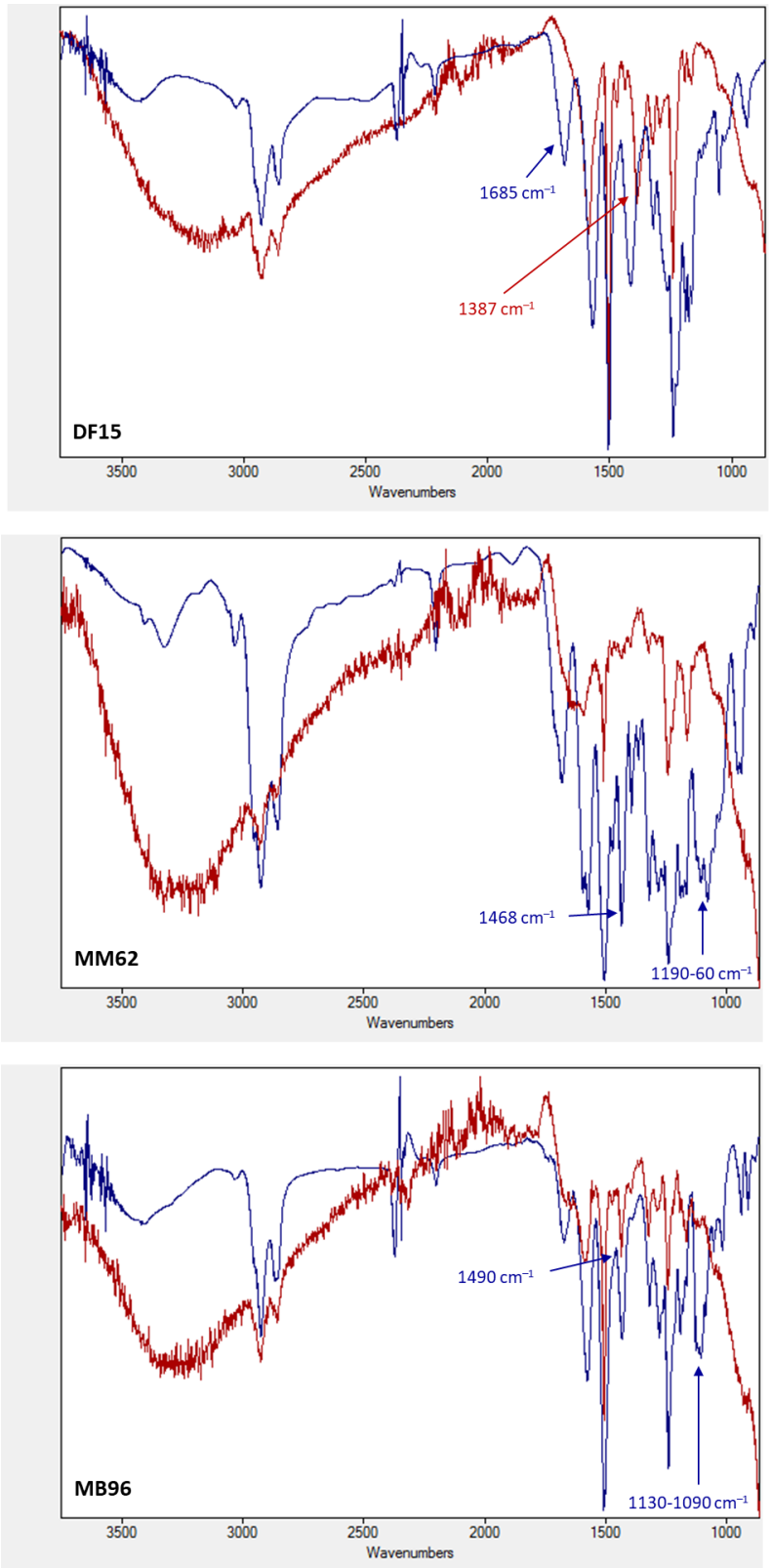

*Figure 2.22 ATR FT-IR spectra of dyes **DF15**, **MM62** and **MB96** (blue: powder; red: adsorbed on TiO_2).*

To obtain further proof of that, an ATR (Attenuated Total Reflectance) FT-IR study was carried out to explore the nature of the bond established between dyes **DF15**, **MB56** and **MB96** and TiO_2 (Figure 2.22). Sensitization of the pristine TiO_2 powder was carried out in conditions analogous to those employed for the coloration of semiconductor films used for the UV analysis. The only difference was that staining was

conducted under stirring in order to obtain a more homogeneous dispersion of the powder in the solvent. After adsorption on TiO_2 some important changes related to the modification of the anchoring groups could be recognized in the spectra, which are summarized in Table 2.9.

*Table 2.9 Diagnostic peaks in the ATR FT-IR spectra of isolated and adsorbed dyes **DF15**, **MM62** and **MB96**.*

Dye	**Isolated compound ν (cm^{-1})**	**Adsorbed on TiO_2 ν (cm^{-1})**
DF15	1685 (C=O str.)	1387 (COO^- symm. str.)
MM62	1468 (C-H bend.) 1190-1160 (4 peaks, C-O str.)	not present not present
MB96	1130-1090 (4 peaks, C-O str.)	not present

Deprotonation of acid **DF15** could be easily recognized from the disappearance of the band related to C=O stretching (1685 cm^{-1}) and the appearance at 1387 cm^{-1} of a new peak that can be attributed to the symmetric stretching of the new species that was formed, the COO^- group.[16] In the case of the silylated compounds, the signal related to the actual anchoring group (the related silanols) could not be detected in the spectrum, but the hydrolysis of the siloxane and silatrane groups could be easily recognized. In the spectra of **MM62**, the two sets of signals related to the trialkoxysilane moiety, located at 1468 cm^{-1} (C-H bending of the CH_2 units of the alkoxysilane group) and 1190-1160 cm^{-1} (4 peaks, C-O stretching of the alkoxysilane group),[16] present in the spectrum of the isolated dye, disappear after adsorption on TiO_2, indicating the hydrolysis of the alkylic moieties of the molecule. Instead, in the case of the dye **MB96**, only the disappearance of the group of four peaks at 1130-1090 cm^{-1} (C-O stretching of the silatrane group) can be observed because in the spectra of the pristine compound, the peak around 1450 cm^{-1} (C-H bending of the CH_2 units of the silatrane group) is concealed by a strong signal at 1500 cm^{-1} and thus its disappearance in the spectrum of the adsorbed compound could only be inferred by the relative thinning of that peak. Finally, remarkable is the comparison between the spectra of the two silylated compound **MM62** and **MB96**: their almost perfect superimposition (Figure 2.23), in fact, strongly suggests that the species formed on the semiconductor surface after the sensitization is the same for both dyes.

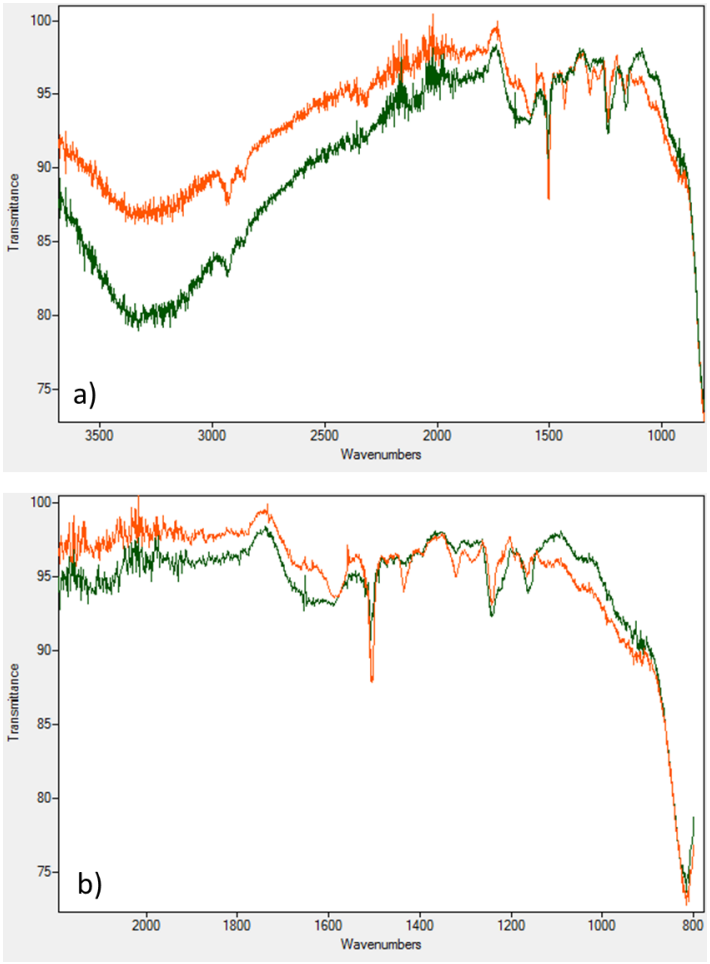

*Figure 2.23 Comparison between the FT-IR spectra of the dyes **MM62** (green) **MB96** (orange). (a) Full spectral range; (b) zoom in the 2200-800 cm^{-1} portion of the spectrum, highlighting the similarity of the observed bands.*

The next step was to evaluate the relative stability of the different anchoring groups on the TiO_2 surface and the dye loading that was achieved upon sensitization. The first parameter was assessed by desorption studies in aqueous environment. In particular, sensitized films of dyes **DF15**, **MM62** and **MB96** were immersed in a ACN/H_2O 1:1 (v/v) mixture, which was heated up to 60°C, and then, after fixed time intervals, they were extracted from the solutions, carefully washed with EtOH and directly analyzed with a UV-Vis spectrophotometer. Such procedure was selected to simulate a working DSSC environment after the infiltration of water inside the device.[10a]

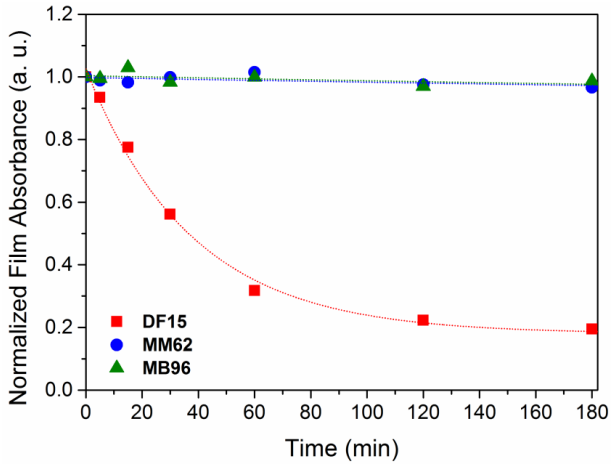

*Figure 2.24 Variation of the relative absorbance of TiO_2 films sensitized with compounds **DF15** (red squares), **MM62** (blue circles) and **MB96** (green triangles) upon exposure to the desorption mixture at 60°C.*

As can be seen in Figure 2.24, while in the case of **DF15** after just 30 min more than 60% of the dye is removed from the TiO_2 film, almost no desorption can be observed for the silylated dyes **MM62** and **MB96**. The difference became even more pronounced with the progression of the experiment, with only approximately 20% of the acid **DF15** still anchored to the semiconductor surface after 3h, while almost the entire amount of dyes **MM62** and **MB96** was still retained. Once again, the two silylated compounds showed the same behavior and in their case to observe a significant drop of the absorbance of dye loaded on TiO_2 the experiment had to be continued overnight (in the morning, a loss around the 20-30% of the initial absorption was detected).

*Table 2.10 Dye loading for the series **DF15**, **MM62** and **MB96**.*

Dye	Film Area (cm^2)	Dye Loading (mol cm^{-2})
DF15[a]	1.44	3.70×10^{-7}
MM62		0.48×10^{-7}
MB96		1.01×10^{-7}
[a] Taken from ref. 25.		

Finally, the total amount of dyes absorbed on a reference TiO_2 film was determined by means of a quantitative desorption method. The principle is identical to that already used in the previous stability evaluation, with the difference that this time the experiment is carried out until complete detachment of the dye from the film. Due to the strong bond established between the silylated groups with the TiO_2, it was necessary to use a base in the desorption mixture, that was constituted by a 0.1 M solution of KOH in THF/EtOH 1:9 (to ensure that both the dye and the base could be dissolved). The sensitized TiO_2 films were immersed in the desorption mixture for several days at 50°C, and the absorbance of the resulting solutions was compared with that of reference dyes solutions in order to quantify the released amount of dye by means of UV-Vis absorbance intensity. As can be seen in Table 2.10, the estimated amount of attached **DF15** was much higher compared to the two other dyes of the series. This can be possibly related to the bulkier structure of the phenyl-silylated anchoring moieties compared to the cyanoacrylic acid, that can shield the nearest areas of the semiconductor surface from attachment of other dye molecules. Noteworthy is the difference in dye loading between **MM62** and **MB96**, with the latter exhibiting an almost double value compared to the corresponding siloxane. In this case,

the difference can be attributed in the different tendency of the two silylated moieties to form oligomers: siloxanes are known[14] for being able to polymerize on metal oxides surfaces and this characteristic can increase the area covered by dye molecules not bonded to the semiconductor, reducing the total amount of compound that can be able to inject electrons on the TiO_2 film.

2.2. Rational Design of Triarylamine-based Dyes for Sustainable H_2 Production

2.2.1. Background

As we have already shown, the working mechanism of photocatalyzed H_2 production resembles the that of DSSCs , at least in its first step. For this reason many dyes that have been tested for H_2 production are similar to those already used in DSSCs and the same can be stated for the most common modifications to the dye structure. The molecular design of the dye in this kind of dye-sensitized systems is particularly crucial, because their photocatalytic performances do not depend only from the relative redox potential of the sensitizer and the SED, but also from the kinetics of all the electron transfer processes taking place in the system.[32] For these reasons, D-π-A dyes, with their particular architecture that allows a fine tuning of their properties and an excellent versatility, have been recognized among the most promising sensitizers for photocatalytic H_2 production.[33] The interest in this particular dyes has grown in the last years, especially investigations on the effect of the dye molecular structure on the global performance of the system. Apart from the classical screening of the different groups that can be used in the various sections of the dye, a great deal of attention was also dedicated to the role played by other modifications, such as the introduction of hydrophobic/hydrophilic chains or the incorporation of additional donor groups in different parts of the molecule and the use of multiple anchoring groups.

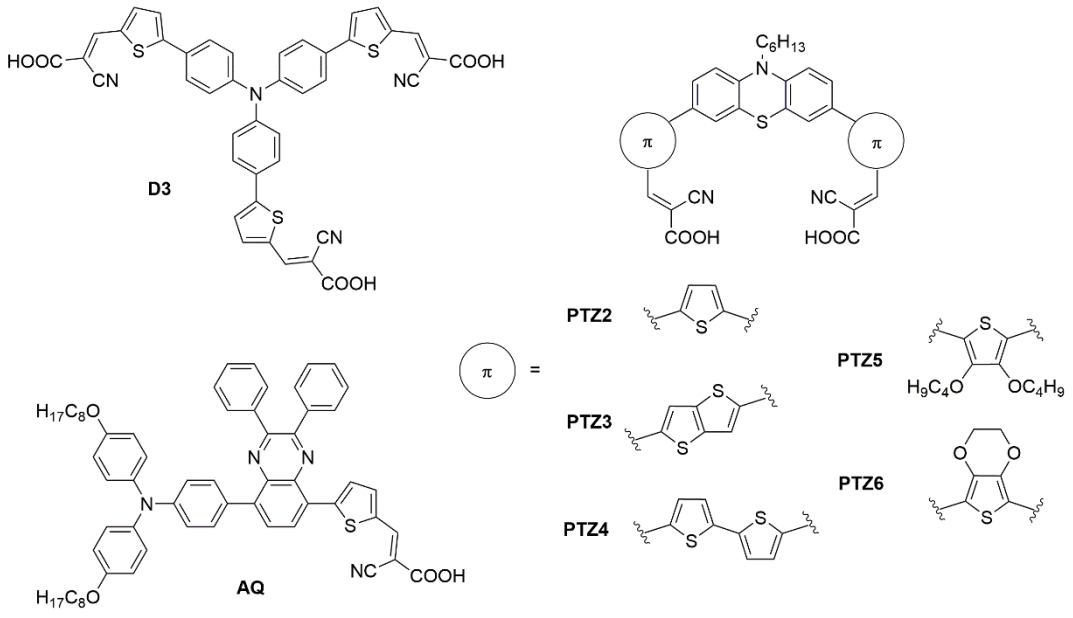

Figure 2.25 Examples of modification on the anchoring group and on the π-spacer.[34,38b,39]

Having multiple anchoring groups on the same dye[34,35] (Figure 2.25) can have a double effect by both increasing the electron deficiency of the molecule (in order to have a more efficient ICT process) and enhancing the stability of the bond on the TiO_2 surface. Besides, the use of multiple anchoring group can also help to improve the dye orientation on the semiconductor, a factor that has already been established to play a role in the performances of the system.[36] Another possibility for enhancing the efficiency is to introduce modifications to the π-spacer, the part of the molecule mainly responsible for light absorption. As in DSSC, increasing the conjugation,[37] introducing different polycyclic structures[38] and introducing an additional acceptor moiety within the conjugated bridge[39] can either increase the light-harvesting properties of the molecule (by shifting and broadening the absorption spectra) and produce a higher rate for the ICT process.

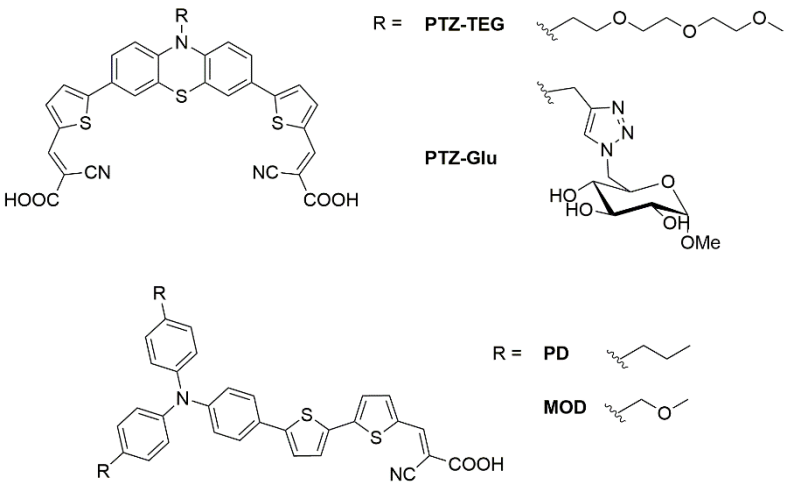

Figure 2.26 Examples of different hydrophilic and hydrophobic bulky groups used in dyes for H_2 production.[40b,41]

Another common modification employed in this kind of photocatalytic system is the introduction of hydrophilic group on the dyes backbone. In fact in order to be regenerated, the dye has to interact with the water soluble SED that is present in solution. The presence of a hydrophilic moiety on the sensitizer can facilitate the interaction and speed up the regeneration process, that is one of the most crucial of the entire system. Classic glycolated chains (i.e. tris(ethylene glycol) monomethyl ether, **PTZ-TEG** in Figure 2.26) have been employed to reach this goal,[36,40] but recently the use of carbohydrates has shown even better results in term of wettability of the dye-sensitized TiO_2 film (**PTZ-Glu** in Figure 2.26).[41]

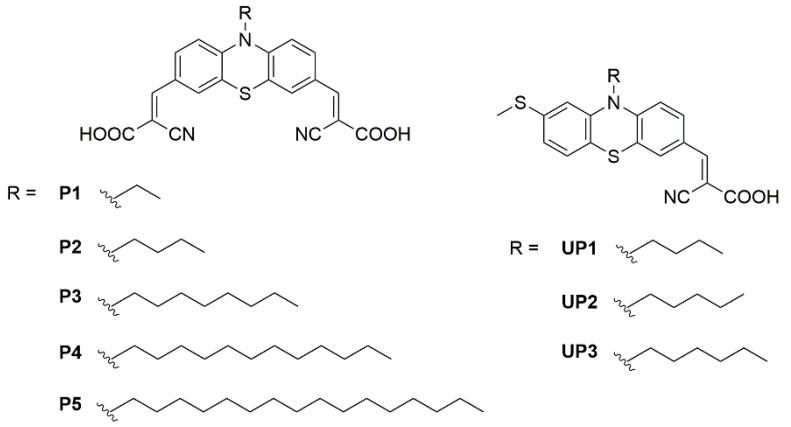

Figure 2.27 Different alkyl chains employed and compared.[35,36]

Interpreting the effect of using hydrophobic chains is more complex: if, on one hand, their introduction on the donor part of the molecule (directly pointed to the solution) was already demonstrated to hamper the efficiency in H_2 production[40b] (i.e. **PD** is 3 times more efficient than **MOD** into H_2 evolution, Figure 2.26), on the other hand their use, analogously to what already observed in DSSCs, could both reduce dye aggregation (preventing fast charge recombination between the spatially close dye molecules) and shield the semiconductor surface from the water approaching, preventing the deactivation/desorption of the anchored dye. While there are already some examples regarding the use of alkylic chains in sensitizers for H_2 production[37,42] and studies about the influence of their length in the photocatalytic activity[35,36,40a,b] (**P** and **UP** series, Figure 2.27), a particular investigation about the effect that different position of hydrophobic chains can have on the global efficiency of the system, is still missing. In this part of the PhD work we decided to test a series of D-π-A dyes (Figure 2.28) having different alkyl chains on different position of their backbone in order to try to rely the structure, in particular the position of the hydrophobic chains, with the efficiency of the dye for H_2 production. The classic TEOA was used as SED.

2.2.2. Dyes Characterization

Among the dyes chosen for this study, **D5** is well-known for its use in DSSCs[43] and it has been also already employed into dye sensitized photocatalytic systems.[38a] For such reason, **D5** was used as reference and compared to three other dyes, **DF15**, **MB25** and **AD418**, which are reported in Figure 2.28. The dyes were designed introducing some structural modification , in particular, **DF15** and **MB25** were both derived from **D5**, the first by introducing two electron donor hexyloxy chains on the terminal triarylamine group, and the second by replacing the thiophene moiety on the π-spacer with an electronrich ProDOT ring bearing two *n*-pentyl chains. Dye **AD418**, instead, differed from **MB25** by the nature of its π-bridge, featuring a thiophene ring between the triarylamine moiety and the ProDOT ring instead of a simple double bond. While modifications such as the introduction of electron rich substituents or changes on the π-spacer can only affect the light-harvesting properties of the compound, the presence of long alkyl chains influence the aggregation between dye molecules and their shielding effect on the TiO_2 surface. To this end, the presence of two alkyl chains on the ProDOT ring can be particularly effective, due to the quaternary geometry of the carbon they are bound to.[44]

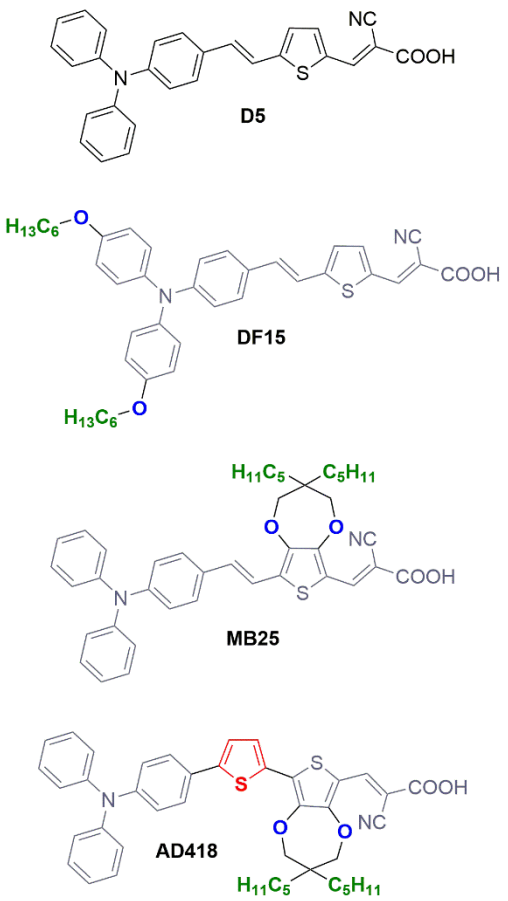

Figure 2.28 Highlight of the structural differences between the dyes object of the study.

The optical and electrochemical properties of all dyes were evaluated to understand if they were suitable for this particular application. The UV-Vis spectra of all compounds are shown in Figure 2.29; as can be seen, **DF15**, **MB25** and **AD418** exhibit a red shift in the absorption maximum compared to **D5** due to the presence of additional electron donor groups on their molecular backbone, which enhance the donor-acceptor nature typical of D-π-A dyes. The effect is more pronounced in **DF15** because the alkoxy chains are directly located on the donor part of the molecule.

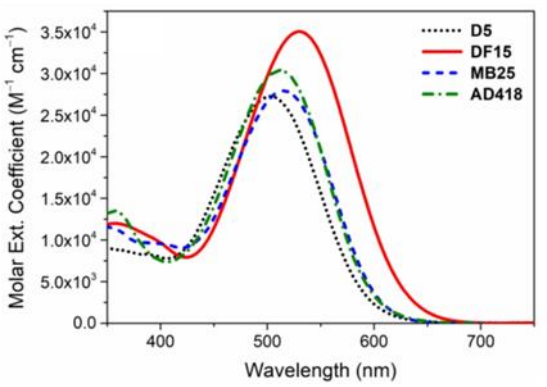

*Figure 2.29 UV-Vis absorption spectra of: (a) compounds **D5**, **DF15**, **MB25** and **AD418** in dichloromethane solution.*

To check if the good light-harvesting properties of the selected dyes are conserved upon sensitization of the semiconductor, they were adsorbed over benchmark TiO_2 P25 powder previously loaded (by photodeposition[38b]) with Pt (the catalyst). The THF solution of each dye was mixed with a suspension of the nanoparticles in EtOH for 12h in the dark, then the powder was retrieved by filtration; in all cases the isolated solution was colorless, indicating that the dye was fully loaded on the nanoparticles. Then, diffuse reflectance spectra (DRS) of the sensitized Pt/TiO_2 were collected and analyzed (Figure 2.30). The spectra showed a strong absorption band in the range 400-650 nm, confirming that all the dyes were successfully loaded onto the powder.

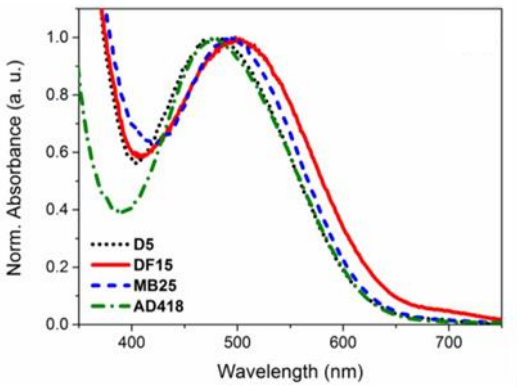

Figure 2.30 Normalized DRS spectra of the compounds adsorbed on the Pt/TiO_2 catalyst used for hydrogen production tests.

Concerning the first series, **DF15** and **MB25** showed a similar behavior as in solution, their λ_{max} in fact is red shifted compared to **D5** (even if with a smaller difference), while the spectrum recorded for **AD418** it is almost superimposable to that of **D5**.

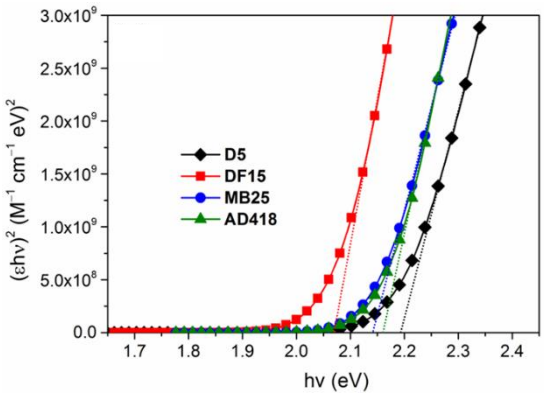

*Figure 2.31 Tauc plots for compounds **D5**, **DF15**, **MB25**, **AD418**.*

Table 2.11 Optical and electrochemical properties of the employed dyes.

Dye	λ_{max} [nm]	ε [M^{-1} cm^{-1}]	$E_{0\text{-}0}$ [eV][a]	λ_{max} Pt/TiO_2 [nm]	E_{ox} [V][b]	E_{HOMO} [eV][c]	E_{LUMO} [eV][c,d]
D5	501[e]	27300	2.19	478	+1.09[f]	–5.69	–3.50
DF15	530[e,g]	35040[g]	2.07	498	+0.94[g]	–5.54	–3.47
MB25	515[e]	27925	2.14	490	+1.03	–5.63	–3.49
AD418	512[e]	30400	2.16	475	+1.05	–5.65	–3.49

[a] Estimated from the corresponding Tauc plot; [b] Potentials vs. NHE; [c] Values relative to a vacuum, using a potential value of 4.6 ± 0.2 eV for NHE vs. vacuum[45]; [d] Values calculated using the following equation: $E_{LUMO} = E_{HOMO} – E_{0\text{-}0}$; [e] Measured in DCM solution; [f] Value taken from ref. 46; [g] Values taken from ref. 25.

To determine the optical band gaps of the analyzed compounds, the Tauc plots of all the dyes were collected (Figure 2.31). The optical band gap can then be directly determined from the value of the intercept on the x-axis of the line fitting the straight region of the plot.[47] These values are summarized in Table 2.11, along with the dyes electrochemical properties, evaluated by means of cyclic voltammetry. The tendency already observed in the spectra of dyes **D5**, **DF15**, **MB25** and **AD418** was confirmed by the electrochemical experiments, with the presence of the electron rich groups on the last three compounds of the series causing a negative shift of the E_{ox} (ground-state oxidation potential) compared to the value recorded for **D5**. On the other hand, the energy of their LUMO level did not change significantly compared to that of **D5**, and was always higher than the CB level of the TiO_2 (-4.0 V vs. vacuum), allowing the electron injection process to happen.

2.2.3. Performances Evaluation

H_2 production experiments** were carried out in classic conditions, that is using TEOA as SED, fixing the pH at 7.0 and using only visible light ($\lambda > 420$ nm, obtained with a glass filter), in order to eliminate the contribution of light absorption by the TiO_2 nanoparticles. The optimal dye loading was set at 10 μmol g^{-1}, after an optimization of the experimental conditions. The sensitized Pt/TiO_2 nanoparticles were then put into the TEOA solution under inert atmosphere and the suspension was irradiated with a Xe lamp; the evolved H_2 was collected and its quantity was measured by GC; the LFE (light-to-fuel efficiency) of the catalytic system was calculated after 3h and 20h of irradiation. The H_2 evolution rates for all the dyes are shown in Figure 2.32, while the TON and LFE values are reported in Table 2.12.

** The H_2 production experiments were carried out by Dr. Matteo Monai (University of Trieste).

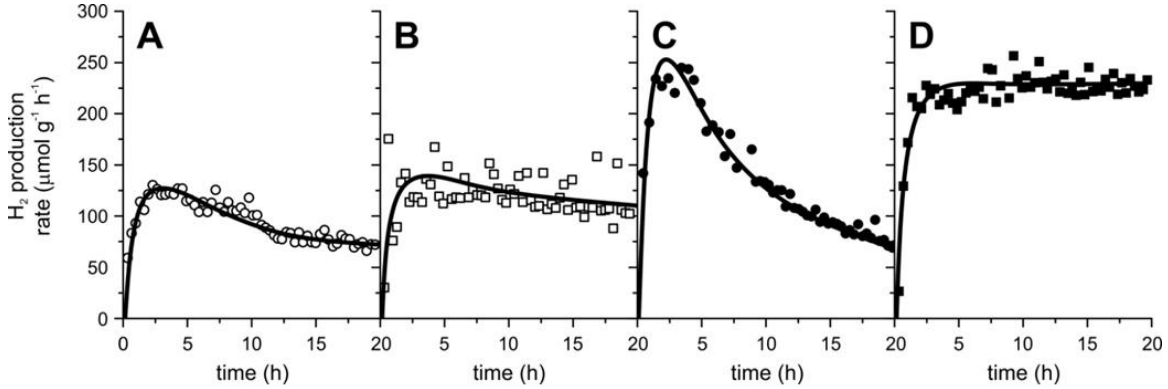

*Figure 2.32 H_2 production rates in the experimental conditions for the dyes: (A) **D5**, (B) **DF15**, (C) **MB25**, (D) **AD418**.*

Regarding the dyes all of them showed an initial increase of the H_2 production rate in the first 1-2h of experiment (due to chromatographic effects and to the activation of the passivated Pt under irradiation[38b]) and then a subsequent stabilization of the rate on the long term. While **D5** and **DF15** in particular exhibit similar moderate H_2 production, **MB25** and **AD418** showed better performances both in terms of amount of H_2 evolved and TON. The reason for the close values observed for **DF15** and **D5** can be found in the difference in optical and electrochemical properties they showed: while **DF15** has a better light-harvesting ability, **D5** has a more positive redox potential, which can facilitate the dye regeneration process (see Table 2.11). The biggest difference among their behavior was the decreasing of the H_2 evolution rate, in fact, by comparing the LFE_{20} it can be seen that the value related to **D5** is about the 25% lower than the one registered for **DF15**. This can be ascribed to the presence of quenching processes in the case of **D5** that were significantly reduced in the case of **DF15**: the presence of the long alkyl chains on its backbone, in fact, can shield the TiO_2 surface from the approach of other species present solution and reduce the occurrence of side-reactions, as it has already been reported for similar systems.[35] **MB25** showed a particular behavior: after a high initial activity (as can be seen from LFE_{03}, doubled compared to those of **D5** and **DF15**), it presented a sharp drop of H_2 evolution with its LFE_{20} reaching similar value to those of the previous two dyes. The excellent activity at the beginning of the experiment (compared to **DF15**) suggested that moving the bulky chains from the donor to the π-spacer was a good idea: having those hydrophobic groups in the middle of the molecule instead on its terminal part, in fact, can favor the approach of the SED to the dye and then its regeneration, while the TiO_2 surface still remained covered from the approach of undesired species (such as radicals and partially oxidized TEOA derivatives) present in solution. The subsequent activity drop indicated that the molecule underwent a progressive degradation process (in fact the H_2 production did not reach a *plateu,* but instead continued to drop also after 20h). On the other hand, **AD418** (which shared most of its structure with **MB25**, excluding the replacement of the double bound near the ProDOT ring with a thiophene), showed only slightly lower initial gas production compared to **MB25**, but without recording a successive massive drop of activity. In fact, in its case the amount of evolved H_2 and TON resulted the highest among all the dyes.

Table 2.12 Photocatalytical performances in H_2 production.

Dye	H_2 amount [μmol g^{-1}][a]	TON[b]	LFE_{03}[c]	LFE_{20}[d]
D5	1884	397	0.065%	0.038%
DF15	2371	474	0.066%	0.050%
MB25	2846	569	0.127%	0.041%
AD418	4359	872	0.117%	0.121%

[a] Overall H_2 amount produced after 20h of irradiation per gram of catalyst; [b] TON = (2 × H_2 total amount after 20h of irradiation)/(dye loading); [c] Light-to-fuel efficiency calculated after 3h of irradiation; [d] Light-to-fuel efficiency calculated after 20h of irradiation.

In general, the results obtained for all dyes were quite remarkable due to the very little difference between their ground-state oxidation potential and the potential for one-electron oxidation of TEOA. In fact, all the compounds exhibit ground-state oxidation potentials ranging from +0.94 V to +1.09 V (Table 2.11), very close to the reported value for the TEOA redox potential (from +0.82 to +1.07 V, depending on the conditions used[48]). Despite that very little difference, the production of H_2 was possible with all the dyes, demonstrating that dye regeneration was always active, even in presence of a seemingly small overpotential, while no direct relationship could be identified between the amount of H_2 evolved and the E_{ox} value. This last observation clarifies how H_2 evolution activity depends on the delicate balance of various factor, not only limited to the optical and electrochemical properties of the dyes, but also related to the characteristics of the water/dye/TiO_2 interfaces that can be strongly influenced by the presence and the position of bulky hydrophobic groups.

The degradation process of **MB25** on the TiO_2 film during the photocatalytic activity was then analyzed. Already during its synthesis, this compound showed the tendency to degrade, possibly due to isomerization of its double bond, as testified by the fact that **AD418**, which does not have a double bond in its structure, did not show any particular degradation process.

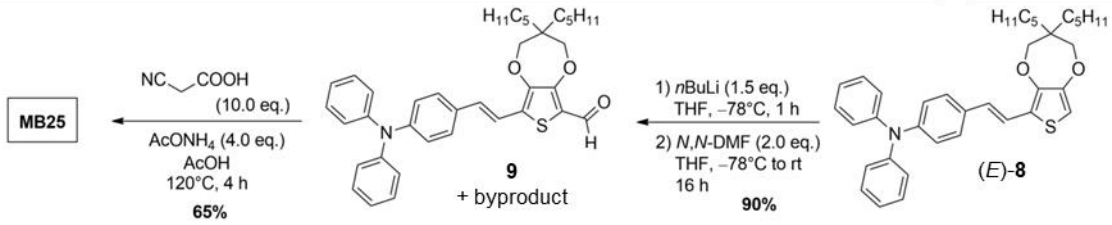

*Scheme 2.10 Synthesis of **MB25** starting from triarylamine derivative **8**.*

In Scheme 2.10 part of the synthetic pathway for the synthesis of **MB25** is shown. Aldehyde **9** was obtained in a 10:1 mixture with another similar aldehyde from metalation with *n*-BuLi, followed by quenching with *N*,*N*-DMF of the compound **8**, that was obtained as pure *E* isomer by Horner-Wadsworth-Emmons reaction. But, after purification of the compound **9** by flash column chromatography, surprisingly, the ratio of the two aldehydes changed, arriving close to 1:1, with the ESI-MS analysis showing only one mass value for the mixture. With these data, the possibility to

brought back the aldehydes ratio to the original 10:1 by treatment of the mixture with I_2 at r.t.[25] confirmed that the mixture was composed by the two *E*/*Z* isomers of the aldehyde **9** (the NMR was too crowded to be able to identify the peaks related to the protons on the double bond).

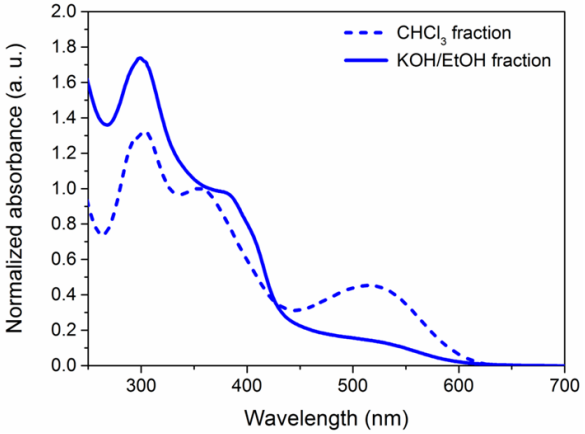

Figure 2.33 UV-Vis spectra of the $CHCl_3$ fraction and the KOH/EtOH fraction.

Regarding the H_2 production experiment, subsequent UV-Vis and ESI-MS analysis on the retrieved powder suggested that a reaction on the backbone of **MB25** took place. Two fractions were collected from the used powder, one retrieved after extraction with organic solvent ("$CHCl_3$ fraction") and the second by extraction in presence of a base ("KOH/EtOH fraction"). The UV-Vis spectra (Figure 2.33) of the two fractions showed a strong peak around 305 nm and a weaker one around 360 nm that could be related to the localized π → π* transition proper of the triarylamine moiety of this kind of D-π-A dyes,[49] suggesting that the donor group was still attached to the backbone. The spectrum of the $CHCl_3$ fraction showed the presence also of another peak around 513 nm, in correspondence of the λ_{max} of the pristine dye **MB25**: this can be explained with the presence on the powder surface of some compound either physisorbed (not directly linked with the carboxylic moiety) or aggregated by means of weak interactions (i.e. π-stacking) on the top of the monolayer of anchored dye, thus not participating on the electron injection process. This hypothesis was confirmed by the ESI-MS spectra of the $CHCl_3$ fraction that showed the presence of only one intense peak with *m/z* = 660, compatible with the unscathed structure of dye **MB25**. On the other hand, the nature of the main component present in the KOH/EtOH fraction (*m/z* = 766.23) could not be clearly assigned to any derivative of acid **MB25**. The presence of the ProDOT ring close to the double bond near the triarylamine, could have favored the protonation of the unsaturated moiety thanks to its electrondonating ability, followed by nucleophilic addition of water or TEOA derivatives.[50] We proposed that the hydrolysis of the already degraded compound **11** triggered the conjugated addition of ethanol to the former double bond leading to the formation of the product of decomposition **12** (Scheme 2.11). The addition of an ACN solution of formic acid to that of the sample to facilitate ionization, could have led to the formation of the protonated **12**·CH_3CN complex (*m/z* = 766.23), which perfectly matched the mass of the main peak observed in the ESI-MS spectrum. In order to confirm the hypothesis, the fragmentation of the compound related to this last peak was carried out and the obtained fragmentation peaks showed *m/z* equal to 725.55, 709.57 and 693.42. While the first one could be related to the protonated form of compound **12** and confirm the hypothesis, the explanation of the other two is more difficult and an hypothesis is given in Scheme 2.11 (the protonated form of the compounds **13** and **14** have to be considered). Unfortunately the ^{1}H-NMR analysis of the two fractions was impossible to the high dilution of the samples. In **AD418**, with the replacement of the double bond near the ProDOT with the thiophene ring, the dye degradation

was not observed, validating the hypothesis that the nucleophilic attack on that part of the backbone is the main responsible of the drop in activity of the compound **MB25**.

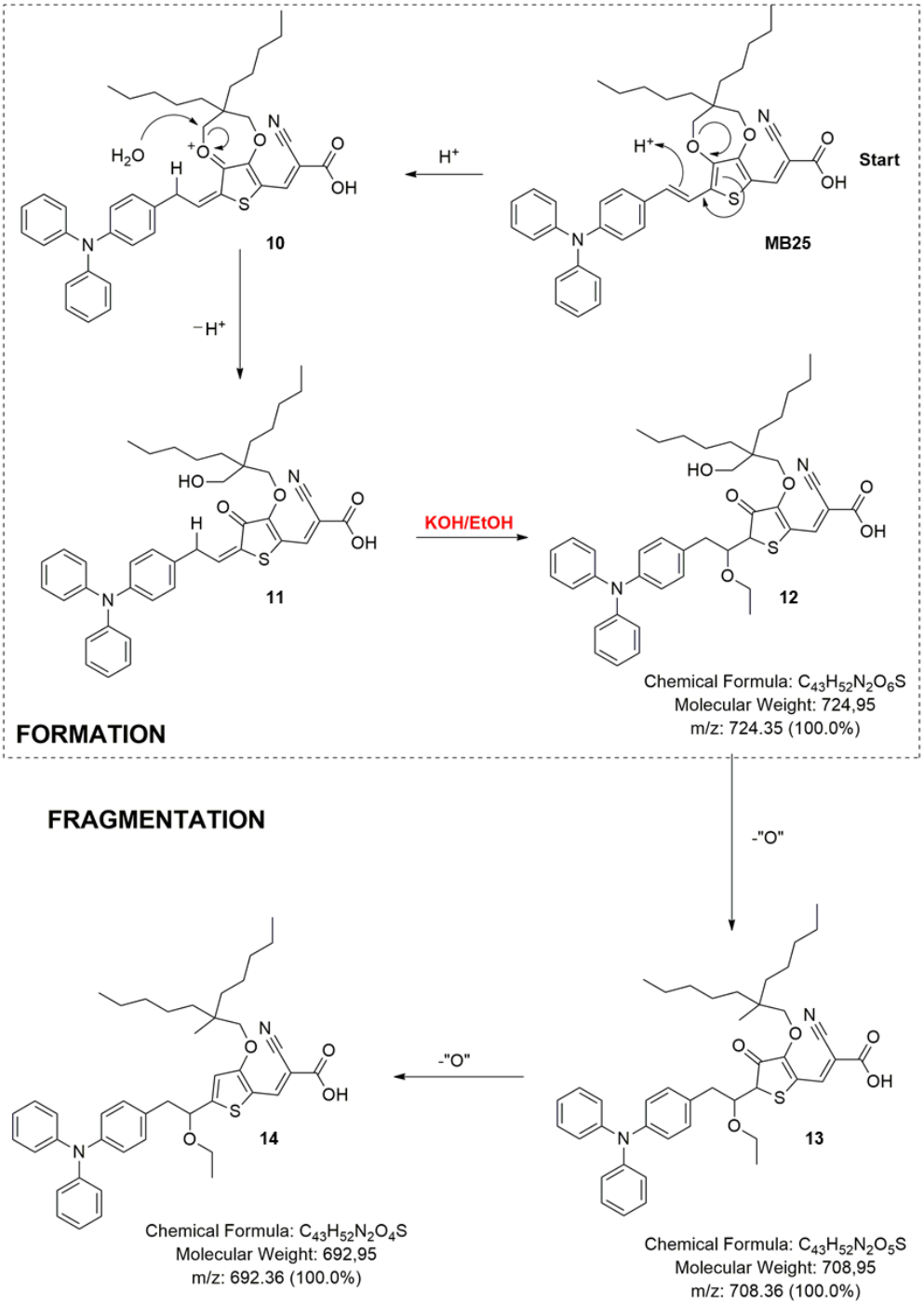

*Scheme 2.11 Proposed decomposition pathway for the dye **MB25** and proposed fragmentation process for the mass spectrum of the KOH/EtOH fraction.*

2.3. Conclusions

This chapter of the PhD work has been focused onto the application of metal-free organic dyes with a particular structure, called D-π-A dyes, in two different field of the photoactive technologies, the Dye-Sensitized Solar Cells and the photocatalytic hydrogen production. In both this kind of devices, the dyes acted as photosensitizers loaded on a TiO_2 film, capable to transfer electrons to the semiconductor itself. For these reasons, the research needed to focus on the search for structures characterized by good light-harvesting properties and great long-term stability.

In the first part of the work (Chapter 2.1), the employment of different silylated anchoring groups in DSSC was studied, along with their optic and electrochemical properties. The processes that happens onto the TiO_2 surface when trialkoxysilane are used as anchoring groups were analyzed and the obtained results were compared with the literature data and the performances recorded for complete solar cells build with these dyes. The study showed how the group can act as excellent anchoring moiety but only upon a proper and fine optimization of the device construction. Therefore, a new general way to introduce an alternative group showing similar properties was explored. The introduction of the new group, the silatrane, on the backbone of a series of cyanoacrylic acids was possible and resulted to be easier and more general than the insertion of the analogous trialkoxysilane group. Finally, the nature of the bond established from the silatrane dyes with the TiO_2 film was analyzed and compared to those of the analogous siloxane derivatives. Both the two groups showed the same stability towards the desorption and the recorded characterization of the behavior of the dyes upon the sensitization showed how the species that are created on the semiconductor surface are the same for both the two anchoring groups.

The second part of the work (Chapter 2.2) was focused onto the use of several cyanoacrylic acids for photocatalytic hydrogen production. The study was aimed to understand how some modifications on the molecular backbone of the above mentioned dyes can change the long-stability and the production rate of the final device. In particular, the effect of the presence and of the positioning of electrondonating moiety and bulky hydrophobic chains was studied. The H_2 evolution experiments showed how the introduction of electronrich group on the donor part of the molecule and the presence of long hydrophobic chains in the middle of the molecular backbone can greatly increase the hydrogen production rate. In particular, the presence of the alkyl chains on the π-spacer seemed to excellent shield the titania surface from the approach of species from the solution, increasing the performances. The unexpected results on the long-term stability recorded for **MB25** was studied and explained by the existence of a degradative pathway taking place on the double bond near the triarylamine group because of the coordinative properties of the ProDOT ring. Then, the replacement of the double bond with a thiophene ring (**AD418**) allows to maintain the same excellent H_2 production rate and to greatly increase the stability of the system, eliminating the degradation processes that was present for **MB25**.

2.4. Experimental Section

2.4.1. Synthetic Procedures

3-Aminophenyl silatrane (6)

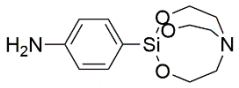

6

In a flame-dried round bottom flask under an atmosphere of nitrogen, 3-aminophenyltrimethoxysilane (300 mg, 1.41 mmol, 1.00 eq.) was dissolved in dry toluene (1 mL). To the solution was then added triethanolamine (190 µL, 1.43 mmol, 1.02 eq.) and a catalytic amount of sodium hydroxide (approximately 5% mol). The mixture was heated to reflux and left under vigorous stirring for 16h. After that, the resulting suspension was cooled and filtered to yield a grey solid, that was washed with cold dichlorometane (2 × 5 mL). A white solid was then collected and the crude product was used without further purification for the next step (340 mg, 1.28 mmol, 91% yield).

^{1}H-NMR ($CDCl_3$, 300 MHz): δ (ppm) 7.53 (d, *J* = 7.6 Hz, 2H), 6.64 (d, *J* = 7.8 Hz, 2H), 3.88 (t, *J* = 5.6 Hz, 6H), 2.89 (t, *J* = 5.6 Hz, 6H).

The spectroscopic data were in agreement with those reported in the literature.[30]

2.4.1.1. Preparation of Silatrane Dyes; General Procedure

The appropriate acid **DF15**, **MB25**, or **MK-2** (0.045 mmol, 1.00 eq.) was dissolved in anhydrous 1,2-dichloroethane (1 mL), then EDC-Cl (13 mg, 0.069 mmol, 1.5 eq.) was added. The solution was left under vigorous stirring for 30 min, during which it turned blue. 3-Aminophenyl silatrane (**6**; 19 mg, 0.069 mmol, 1.5 eq.) was then added, and the mixture was allowed to react at 50 °C for 16h. The solution was diluted with dichloromethane (10 mL) and washed with 0.3 M (aq) HCl (3 × 30 mL) and H_2O (2 × 30 mL). The organic phase was dried over Na_2SO_4 and the solvent was removed under reduced pressure. The crude product was then purified by silica gel flash column chromatography to give the pure silatrane product.

(*E*)-*N*-(4-(2,8,9-Trioxa-5-aza-1-silabicyclo[3.3.3]undecan-1-yl)phenyl)-3-(5-((*E*)-4-(*bis*(4-(hexyloxy)phenyl)amino)styryl)thiophen-2-yl)-2-cyanoacrylamide (MB96)

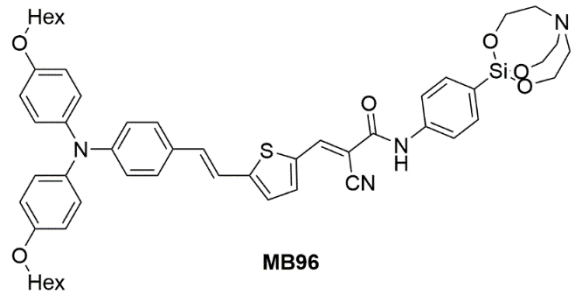

MB96

Prepared starting from dye **DF15** (29 mg). Purified by silica gel flash column chromatography (Tol/AcOEt 10:1 to Tol/AcOEt 2:1). Dark red amorphous solid (27 mg, 0.030 mmol; 66% yield).

IR (KBr): v = 3390, 2923, 2199, 1671, 1575, 1506, 1239 cm^{-1}.

^{1}H-NMR (C_6D_6, 400 MHz): δ (ppm) 8.38 (s, 1H), 8.22 (d, *J* = 8.3 Hz, 2H), 7.73 (bs, 1H), 7.60 (d, *J* = 8.4 Hz, 2H), 7.14-7.05 (m, 8H), 6.99 (d, *J* = 16.0 Hz, 1H), 6.93 (d, *J* = 3.9 Hz, 1H), 6.84-6.77 (m, 5H), 6.51 (d, *J* = 3.9 Hz, 1H), 3.65 (t, *J* = 6.4 Hz, 4H), 3.47 (t, *J* = 5.7 Hz, 6H), 1.99 (t, *J* = 5.7 Hz, 6H), 1.65-1.59 (m, 4H), 1.38-1.31 (m, 4H), 1.28-1.18 (m, 8H), 0.88 (t, *J* = 7.0 Hz, 6H).

^{13}C-NMR (C_6D_6, 100 MHz): δ (ppm) 158.4, 156.6, 152.5, 149.9, 144.3, 140.7, 140.3, 138.7, 137.5, 136.0, 134.8, 133.0, 128.6, 128.5, 127.5, 126.1, 120.1, 119.0, 118.3, 117.9, 115.9, 100.2, 68.2, 57.9, 50.8, 31.9, 29.7, 26.1, 23.0, 14.3.

HRMS: *m/z* = 896.3996 $[M^{\cdot}]^{+}$ (calculated *m/z* = 896.39973)

(*E*)-*N*-(4-(2,8,9-Trioxa-5-aza-1-silabicyclo[3.3.3]undecan-1-yl)phenyl)-2-cyano-3-(8-((*E*)-4-(diphenylamino)styryl)-3,3-dipentyl-3,4-dihydro-2*H*-thieno[3,4-*b*][1,4]dioxepin-6-yl)acrylamide (MB113)

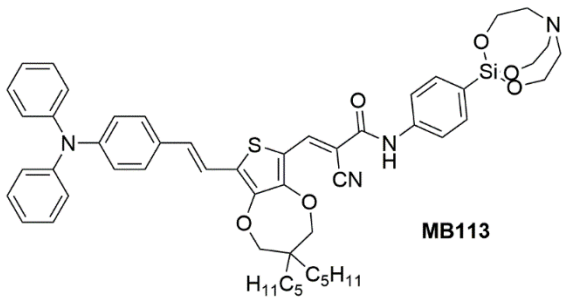

MB113

Prepared starting from dye **MB25** (30 mg). Purified by silica gel flash column chromatography (Tol/AcOEt 10:1 to Tol/AcOEt 2:1). Dark red amorphous solid (18 mg, 0.020 mmol; 43% yield).

IR (KBr): v = 3420, 2923, 2194, 1666, 1577, 1496, 1271 cm^{-1}.

^{1}H-NMR ($CDCl_3$, 400 MHz): δ (ppm) 8.56 (s, 1H), 7.76 (bs, 1H), 7.74 (d, *J* = 8.2 Hz, 2H), 7.53 (d, *J* = 8.2 Hz, 2H), 7.37 (d, *J* = 8.6 Hz, 2H), 7.30-7.28 (m, 2H), 7.14-6.99 (m, 12H), 4.03 (s, 2H), 3.97 (s, 2H), 3.91 (t, *J* = 5.7 Hz, 6H), 2.93 (t, *J* = 5.7 Hz, 6H), 1.37-1.29 (m, 16H), 0.91 (t, *J* = 6.8 Hz, 6H).

^{13}C-NMR ($CDCl_3$, 100 MHz): δ (ppm) 159.3, 155.9. 148.4, 147.4, 145.8, 141.0, 138.8, 137.1, 135.2, 132.1,

131.2, 130.2, 129.5, 128.1, 125.1, 123.6, 122.8, 119.0, 118.5, 115.6, 113.5, 95.1, 78.2, 77.9, 57.9, 51.2, 43.8, 32.7, 32.2, 29.8, 22.7, 14.2.

HRMS: *m/z* = 908.3999 $[M^{\cdot}]^{+}$ (calculated *m/z* = 908.39973)

(*E*)-*N*-(4-(2,8,9-Trioxa-5-aza-1-silabicyclo[3.3.3]undecan-1-yl)phenyl)-2-cyano-3-(5'''-(9-ethyl-9*H*-carbazol-3-yl)-3',3'',3''',4-tetrahexyl-[2,2':5',2'':5'',2'''-quaterthiophen]-5-yl)acrylamide (MB104)

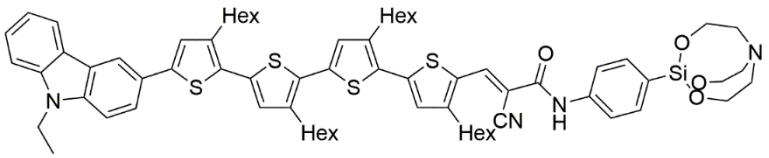

MB104

Prepared starting from dye **MK-2**, (43 mg). To promote its dissolution in the reaction mixture, **MK-2** was first dissolved in dry THF (0.5 mL) and then dry 1,2-dichloroethane was added. Purified by silica gel flash column chromatography (Tol/AcOEt 20:1 to Tol/AcOEt 2:1). Dark red amorphous solid (33 mg, 0.027 mmol; 61% yield).

IR (KBr): v = 3409, 2923, 2194, 1671, 1572, 1506, 1422, 1231 cm^{-1}.

^{1}H-NMR ($CDCl_3$, 300 MHz): δ (ppm) 8.57 (s, 1H), 8.31 (d, *J* = 1.2 Hz, 1H), 8.15 (d, *J* = 7.7 Hz, 1H), 7.87 (bs, 1H), 7.77-7.71 (m, 3H), 7.57-7.47 (m, 3H), 7.43 (d, *J* = 4.3 Hz, 1H), 7.40 (d, *J* = 4.9 Hz, 1H), 7.29-7.17 (m, 2H), 7.08 (s, 1H), 7.02 (s, 2H), 4.38 (q, *J* = 7.0 Hz, 2H), 3.92 (t, *J* = 5.7 Hz, 6H), 2.93 (t, *J* = 5.7 Hz, 6H) 2.87-2.80 (m, 8H), 1.78-1.64 (m, 8H), 1.46 (t, *J* = 7.1 Hz, 3H), 1.40-1.34 (m, 24H), 0.92-0.90 (m, 12H).

^{13}C-NMR ($CDCl_3$, 75 MHz): δ (ppm) 159.0, 155.0, 144.2, 143.6, 143.1, 142.3, 141.0, 140.8, 140.5, 139.7, 139.2, 137.0, 136.6, 135.3, 135.2, 130.1, 129.4, 129.0, 128.7, 128.4, 127.4, 126.2, 125.3, 125.2, 124.0, 123.5, 123.0, 120.7, 119.3, 119.0, 118.1, 117.6, 108.9, 108.8, 97.5, 57.9, 51.2, 37.8, 31.9, 31.8, 31.7, 31.4, 30.7, 30.5, 30.2, 29.9, 29.7, 29.5, 29.4, 29.2, 22.8, 22.7, 14.3, 14.0.

HRMS: *m/z* = 1202.5298 $[M^{\cdot}]^{+}$ (calculated *m/z* = 1202.52957)

2.4.2. Other Procedures Chapter 2.1.2

- **Spectroscopic measurements**

Sub-picosecond transient absorption spectroscopy (TAS) has been carried out with a system based on a Ti:sapphire regenerative amplifier laser system (BMI Alpha 1000) and a fs-laser oscillator (Spectra Physics Tsunami). The details of the experimental system have been described in previous works.[51] For the current measurements the pump wavelength has been fixed either at 400 nm, obtained by second harmonic generation of the fundamental laser radiation at 800 nm, or at 520 nm. Visible pulses have been obtained by mixing the output of commercial optical parametric generator and amplifier (TOPAS by Light Conversion, Vilnius, Lithuania) with the residual laser fundamental.[52,53] Excitation power was set at 100-150 nJ. The probe pulses have been obtained by focusing a portion of the 800 nm laser radiation on a 3 mm thick CaF_2 window. Both pump and probe were focused on the sample with a 150 mm parabolic mirror, the spot size of both

beams on the focus was about 100 µm. Transient spectra have been recorded for a time interval spanning between -5 and 1500 ps. The IRF of the system was about 150 fs. The sample was contained in a quartz cell with a 2 mm optical path, mounted on a movable stage in order to minimize photodegradation. Solid state samples were directly mounted on the same motorized stage used for solution samples. The OD of all analysed samples was between 0.2 and 0.5 at the excitation wavelength. Visible absorption spectra were recorded using a Perkin Elmer LAMBDA 950, while fluorescence was recorded using a Perkin Elmer LS55 fluorimeter.

- **Data analysis**

Femtosecond transient spectra have been analysed by global analysis, which consists in the simultaneous fitting of all the collected kinetic traces by means of exponential functions. The number of kinetic components has been identified by singular values decomposition (SVD).[54,55] Global analysis has been performed using the GLOTARAN software,[19,56] and employing a linear unidirectional kinetic scheme. Transient spectra were numerically corrected for the chirp of the white light pulse before global analysis, using a third order polynomial function.

- **Computational methods**

DFT and TDDFT calculations on compounds **DF15, MB25, MB56** and **MM62** have been performed using the Gaussian 09, Revision C.01 suite of programs.[57] Geometry optimization was carried out *in vacuo* using the B3LYP functional[58,59] and the standard 6-31G* basis set for all atoms. Methyl groups have been used in place of the alkyl chains to reduce the computational cost. The absorption maximum (λ^a_{max}), vertical excitation energy (E_{exc}) and oscillator strength (f) in solution were calculated on the minimum structures via time-dependent DFT (TD-DFT) at the CAM-B3LYP/6-31G*[60] and MPW1K/6-31G*[61] levels. Solvent effects have been included by using the polarizable continuum model (PCM).[62] Geometry optimizations of the dyes on TiO_2 was carried out using a $Ti_{16}O_{32}$ model which has been proven to be a suitable model for computing energies and molecular orbitals of organic dyes/TiO_2 systems.[63] The dyes were anchored on the semiconductor using a bidentate bridging mode and the optimizations of the dye/TiO_2 systems were performed using the B3LYP/6-311G(d,p) level, in which the standard LANL2DZ basis set was used for the Ti atom. The absorption maximum (λ^a_{max}), vertical excitation energy (E_{exc}) and oscillator strength (f) of dyes on TiO_2 were calculated on the optimized structures at the CAM-B3LYP/6-311G(d,p) level in which the standard LANL2DZ basis set was used for the Ti atom; for the sake of comparison, λ^a_{max}, E_{exc} and f for **DF15, MB25, MB56** and **MM62** dyes in CH_2Cl_2 was also computed at the CAM-B3LYP/6-311G(d,p) level of theory.

The total densities of states (TDOS) and partial densities of states (PDOS) for the optimized isolated dyes and dyes/TiO_2 structures were obtained using GaussSum 3.0.[64] DOS spectra were obtained by convoluting orbital contributions with Gaussian curves of full width at half maximum of 0.3 eV.

- **DSSC fabrication and photoelectrochemical measurements (Siloxane Series DF15, MM62, MB25, MB56)**

Transparent photoanodes for small-scale DSSCs were prepared by screen-printing a commercial TiO_2 paste (Dyesol 18NR-T) on a 8 Ω sq^{-1} conductive glass substrate (Pilkington), and by sintering the resulting electrodes at 520 °C for 30 minutes. After sintering, the thickness of the semiconductor layer was measured by means of a profiler (Dektak 150, Veeco) and determined to be 5.5 µm. In both cases, the electrode active area was 0.25 cm^2. Counter electrodes were obtained by screen printing a commercial platinum-containing paste (Chimet) on pre-drilled conductive glass plates and by heating at 420 °C for 15 minutes. TiO_2 photo-electrodes were sensitized by overnight immersion into the appropriate dye solution (1.0×10^{-4} M in Toluene), which took place at r.t. for the carboxylic acid dyes and at 70°C for the silicon-containing dyes. After

sensitization, the anodes were rinsed with EtOH and deionized water, and then dried. A TiO_2-sensitized photoanode and a Pt counter electrode were assembled into a sealed sandwich-type cell using a 25 μm hot-melt Surlyn® gasket (Solaronix). A drop of the I^-/I_3^- containing commercial HPE electrolyte solution (Dyesol) was placed on the drilled hole on the back of the counter electrode and was driven into the cell by vacuum backfilling. The hole was finally sealed by using additional sealing film and a small glass cover. Fabrication of strip cells (3.6 cm^2 active area) was carried out following the same procedure. The measurements were performed with a power of incoming radiation of 100 mW cm^{-2}. J/V curves were obtained by applying an external bias to the cell and measuring the generated photocurrent with a Keithley model 2400 digital source-meter, under the control of dedicated LabTracer 2.0 software. A black shading mask was used to avoid overestimation of the measured parameters. IPCE spectra were measured with a dedicated apparatus built with the following components: Newport model 70612 Xenon lamp (150 W), Cornerstone 130 1/8 m monochromator and Keithley model 2400 digital source-meter.

- **Optical and electrochemical measurements**

UV-Vis absorption spectra were recorded on diluted solutions of the compounds (approx. 10^{-5} M in the solvents specified in the text). DRS spectra were recorded on sensitized Pt/TiO_2 catalyst powders in the reflectance mode using an integrating sphere (with Ba_2SO_4 as a reference standard), and were converted to the corresponding absorption spectra using the Kubelka-Munk equation. Cyclic voltammetry experiments were conducted in dichloromethane solution employing a three-electrode cell having a glassy carbon working electrode, a platinum counter-electrode and an aqueous Ag/AgCl (sat. KCl) reference electrode. The supporting electrolyte was electrochemical-grade $[N(Bu)_4]PF_6$. Under these experimental conditions, the one-electron oxidation of ferrocene occurs at $E^{o\prime}$ = 0.62 V.

2.4.3. Other Procedures Chapter 2.1.3

- **Preparation of TiO_2 functionalized films**

The titania paste (Dyesol 18NR-T) was screen-printed on a 2 cm × 2 cm sodalime glass substrate, and the resulting films (active area: 1.44 cm^2) were sintered at 520 °C for 30 min. After sintering, the titania films were sensitized by overnight immersion into the appropriate dye solution (1.0×10^{-4} M in Tol), which took place at r.t. for the carboxylic acid dyes and at 70°C for the silicon-containing dyes. After sensitization, the films were rinsed with EtOH and deionized water, and dried.

- **Preparation of TiO_2 functionalized powders**

Nc-TiO_2 powder (Sigma-Aldrich, 50 mg) was sensitized by overnight immersion into a 2.0×10^{-3} M solution in Tol of the dyes (once again at r.t. for **DF15**, and at 70°C for **MM62** and **MB96**). After sensitization, the coloured powder was filtered, rinsed with petroleum ether and dried.

- **Measurement of density of adsorbed dye molecules on TiO_2**

The TiO_2 films, sensitized with **MM62** and **MB96** according to the procedure described above, were placed in flasks containing 15 mL of a 0.1 M solution of KOH in EtOH/THF 9:1. After 3 days at r.t. followed by 4 days at 50°C under gyroscopic stirring, full decoloration of the films was observed. The absorbance of the resulting solutions was measured by UV-Vis spectroscopy and compared to that of a standard 2.5×10^{-5} M solution of the compounds in the same solvent/base mixture. The amount of dye present in the unknown solution was calculated and divided by the film surface area, yielding density values in the 1.0-0.5 × 10^{-7} mol cm^{-2} range.

- **Dye desorption kinetics**

The TiO_2 sensitized films were placed in 50 mL flasks containing 20 mL of a ACN/H_2O 1:1 mixture (v/v), which was then heated at 60°C. At specific times (after 5, 15, 30, 60 and 120 min. of immersion), the films were removed from the solvent mixture, rinsed with EtOH and dried, and the absorbance of the films at the dye λ_{max} was registered using a UV-Vis spectrometer. After the measurement, the films were placed back in the solution and the desorption reaction was continued for a total of 3h.

2.4.4. Other Procedures Chapter 2.2

- **Preparation of Pt/TiO_2 nanopowder**

Pt was photodeposited on TiO_2 Degussa P25 following a previously reported procedure.[40a,65] Briefly, 2 g of TiO_2 Degussa P25 were suspended in 400 mL $Pt(NO_3)_2$ aqueous solution (EtOH 50 % v/v), in order to reach a final Pt loading of 1.0 wt%. After stirring for 1h in the dark, the suspension was irradiated with a 450 W medium pressure Hg lamp for 4h. Nanopowders were recovered through centrifugation, washed with EtOH 3 times, and dried under vacuum at 50 °C overnight.

- **Dyes adsorption on Pt/TiO_2**

200 mg of Pt/TiO_2 nanopowder was suspended in 20 mL of dye solution (0.1 mM in ethanol) for 24h in the dark. Then, the nanopowder was separated through centrifugation, washed twice with ethanol, and dried under vacuum at room temperature overnight. After staining, the concentration of the dyes in the solution was measured by UV-vis spectroscopy. More than 95% of the dye was adsorbed on the Pt/TiO_2 material in all cases.

- **Hydrogen production through photoreforming**

The dye-sensitized Pt/TiO_2 nanomaterials have been tested for H_2 production using TEOA as sacrificial electron donor, following or slightly modifying a previously described procedure.[38b] Briefly, 60 mg of the dye-sensitized Pt/TiO_2 catalyst was suspended into 60 mL of 10 % v/v aqueous solution of TEOA previously neutralized with HCl. After purging with Ar (15 mL min^{-1}) for 30min, the suspension was irradiated using a 150 W Xe lamp with a cut-off filter at 420 nm. Irradiance was ~ 6 × 10^{-3} W m^{-2} in the UV-A range and ~ 1080 W m^{-2} in the visible and near-IR range (400 – 1000 nm). The concentration of H_2 in gas stream coming from the reactor has been quantified using a Agilent 7890 gaschromatograph equipped with a TCD detector, connected to a Carboxen 1010 column (Supelco, 30 m × 0.53 mm ID, 30 µm film) using Ar as carrier. Blank experiments on Pt/TiO_2 in the absence of dyes showed no H_2 evolution under any of the experimental conditions used in this work.

The performances of the sensitized photocatalysts have been reported in terms of H_2 production rate and overall H_2 productivity. Turn-Over Numbers (TON) were calculated from the total amount of H_2 produced in 20h of irradiation as:

$$\mathrm{TON} = \frac{2 \text{ x overall } \mathrm{H_2} \text{ amount } (\mu\mathrm{mol\ g^{-1}})}{2 \text{ x dye loading } (\mu\mathrm{mol\ g^{-1}})}$$

Light-to-Fuel Efficiency (LFE) was calculated as:

$$\mathrm{LFE} = \frac{\mathrm{F_{H_2}}\ \Delta \mathrm{H^0_{H_2}}}{\mathrm{S}\ \mathrm{A_{irr}}}$$

where F_{H2} is the flow of H_2 produced (expressed in mol s^{-1}), ΔH^0_{H2} is the enthalpy associated with H_2 combustion (285.8 kJ mol^{-1}), S is the total incident light irradiance, as measured by adequate radiometers in 400 – 1000 nm range (expressed in W cm^{-2}) and A_{irr} is the irradiated area (expressed in cm^2). UV-Vis spectra of the aqueous solutions recovered at the end of the photocatalytic runs highlighted that no desorption of the dyes took place during the experiments.

- **Analysis of the species derived from dye MB25 after the photocatalytic H_2 evolution experiment**

After completion of the photocatalytic experiment (carried out as described above), catalyst suspension was first filtered and washed with EtOH: after filtration the supernatant aqueous solution was colorless, indicating that simple sensitizer leaching was not the cause of the decrease in catalytic performances. The catalyst was then suspended in chloroform at reflux for 2h in order to extract the species loosely attached to the semiconductor ("$CHCl_3$ fraction"). Finally, it was subjected to base-promoted desorption (using KOH 0.025 M in EtOH), to extract also the species still attached via the carboxylate-titanium linkage ("KOH/EtOH fraction"), followed by neutralization with diluted HCl.

2.5. References

1 Lin, L.-Y.; Lee, C.-P.; Vittal, R.; Ho, K.-C. *J. Power Sources* **2011**, *196*, 1671.

2 Kitamura, T.; Okada, K.; Matsui, H.; Tanabe, N. *J. Sol. Energ.-T ASME* **2010**, *132*, 021105-1.

3 Chen, C.; Yang, X.; Cheng, M.; Zhang, F.; Sun, L. *ChemSusChem* **2013**, *6*, 1270.

4 Zhang, L.; Cole, J. M. *ACS Appl. Mater. Interfaces* **2015**, *7*, 3427.

5 (a) Metwalli, E.; Haines, D.; Becker, O.; Conzone, S.; Pantano, C. G. *J. Colloid Interf. Sci.* **2006**, *298*, 825; (b) Fukaya, N.; Haga, H.; Tsuchimoto, T.; Onozawa, S.; Sakakura, T.; Yasuda, H. *J. Organomet. Chem.* **2010**, *695*, 2540.

6 (a) Mittal, K. L. *Silanes and Other Coupling Agents, Utrecht*; **2000**; p Vol. 4; (b) Naik, V.V.; Crobu, M.; Venkataraman, N.V.; Spencer, N.D. *J. Phys. Chem. Lett.* **2013**, *4*, 2745.

7 (a) Kakiage, K.; Yamamura, M.; Fujimura, E.; Kyomen, T.; Unno, M.; Hanaya, M. *Chem. Lett.* **2010**, *39*, 260; (b) Kakiage, K.; Tokutome, T.; Iwamoto, S.; Kyomen, T.; Hanaya, M. *Chem. Commun.* **2013**, *49*, 179; (c) Kakiage, K.; Aoyama, Y.; Yamamura, M.; Yano, T.; Unno, M.; Kyomen, T.; Hanaya, M. *Silicon* **2014**, *6*, 123.

8 Barozzino Consiglio, G.; Pedna, F.; Fornaciari, C.; Fabrizi de Biani, F.; Marotta, G.; Salvatori, P.; Basosi, R.; De Angelis, F.; Mordini, A.; Parisi, M.L.; Peruzzini, M.; Reginato, G.; Taddei, M.; Zani, L. *J. Organomet. Chem.* **2013**, *723*, 198.

9 Kakiage, K.; Aoyama, Y.; Yano, T.; Oya, K.; Fujisawa, J.-I.; Hanaya, M. *Chem. Commun.* **2015**, *51*, 15894.

10 (a) Kakiage, K.; Aoyama, Y.; Yano, T.; Otsuka, T.; Kyomen, T.; Unno, M.; Hanaya, M. *Chem. Commun.* **2014**, *50*, 6379; (b) Kakiage, K.; Aoyama, Y.; Yano, T.; Oya, K.; Kyomen, T.; Hanaya, M. *Chem. Commun.* **2015**, *51*, 6315; (c) Kakiage, K.; Osada, H.; Aoyama, Y.; Yano, T.; Oya, K.; Iwamoto, S.; Fujisawa, J.-I.; Hanaya, M. *Sci Rep.* **2016**, *6*, 35888.

11 (a) Koumura, N.; Wang, Z-S.; Mori, S.; Miyashita, M.; Suzuki, E.; Hara, K. *J. Am. Chem. Soc.* **2006**, *128*, 14256; (b) Wang, Z-S.; Koumura, N.; Cui, Y.; Takahashi, M.; Sekiguchi, H.; Mori, A.; Kubo, T.; Furube, A.; Hara, K. *Chem. Mater.* **2008**, *20*, 3993.

12 Bessi, M.; Monini, M.; Calamante, M.; Mordini, A.; Sinicropi, A.; Di Donato, M.; Iagatti, A.; Foggi, P.; Zani, L.; Reginato, G. *Synthesis* **2017**, *49*, 3975.

13 Frye, C.L.; Vincent, G.A.; Finzel, W.A., *J. Am. Chem. Soc.* **1971,** *93*, 6805.

14 Brennan, B. J.; Keirstead, A. E.; Liddell, P. A.; Vail, S. A.; Moore, T. A.; Moore, A. L.; Gust, D. *Nanotechnology* **2009**, *20*, 505203.

15 Materna, K.L.; Rudshteyn, B.; Brennan, B.J.; Kane, M.H.; Aaron J. Bloomfield; Huang, D.L.; Shopov, D.Y.; Batista, V.S.; Crabtree, R.H.; Brudvig, G.W., *ACS Catal.* **2016,** *6*, 5371.

16 Brennan, B.J.; Llansola Portoles, M.J.; Liddell, P.A.; Moore, T.A.; Moore, A.L.; Gust, D., *Phys. Chem. Chem. Phys.* **2013,** *15*, 16605.

17 (a) Martın, C.; Ziolek, M.; Douhal, A. *J. Photochem. Photobiol. C* **2016**, *26*, 1; (b) Sobus, J.; Karolczak, J.; Komar, D.; Anta, J.A.; Ziolek, M. *Dyes Pigments* **2015**, *113*, 692; (c) de Miguel, G.; Marchena, M.; Ziolek, M.; Pandey, S.S.; Hayase, S.; Douhal, A. *J. Phys. Chem. C* **2012**, *116*, 12137.

18 Boschloo, G.; Hagfeldt, A. *Acc. Chem. Res.* **2009**, *42*, 1819.

19 Van Stokkum, I.H.M.; Larsen, D.S.; Van Grondelle, R. *Biochim. Biophys. Acta* **2004**, *1657*, 82.

20 (a) Ragnoni, E.; Di Donato, M.; Iagatti, A.; Lapini, A.; Righini, R. *J. Phys. Chem. B* **2014**, *119*, 420; (b) Wurthner, F.; Archetti, G.; Schmidt, R.; Kuball, H-.G. *Angew. Chem. Int. Ed.* **2008**, *47*, 4529; (c) Seo, J.; Kim, S.; Park, S.Y. *J. Am. Chem. Soc.* **2004**, *126*, 11154.

21 (a) Wiberg, J.; Marinado, T.; Hagberg, D.P.; Sun, L.; Hagfeldt, A.; Albinsson, B. *J. Phys. Chem. C* **2009**, *113*, 3881; (b) Sobus, J.; Gierczyk, B.; Burdzinski, G.; Jancelewicz, M.; Polanski, E.; Hagfeldt, A.; Ziołek, M. *Chem. Eur. J.* **2016**, *22*, 15807; (c) Sobus, J.; Kubicki, J.; Burdzinski, G.; Ziołek, M. *ChemSusChem* **2015**, *8*, 3118.

22 Wiberg, J.; Marinado, T.; Hagberg, D.P.; Sun, L.; Hagfeldt, A.; Albinsson, B. *J. Phys. Chem. B* **2010**, *114*, 14358.

23 Ye, S.; Kathiravan, A.; Hayashi, H.; Tong, Y.; Infahsaeng, Y.; Chabera, P.; Pascher, T.R.; Yartsev, A.P.; Isoda, S.; Imahori, H.; Sundstrom, V. *J. Phys. Chem. C* **2013**, *117*, 6066.

24 (a) Piatkowski, P.; Martin, C.; di Nunzio, M.R.; Cohen, B.; Pandey, S.; Hayse, S.; Douhal, A. *J. Phys. Chem. C* **2014**, *118*, 29674; (b) Kim, B-.G.; Chung, K.; Kim, J. *Chem. Eur. J.* **2013**, *19*, 5220; (c) Debnath, T.; Maity, P.; Lobo, H.; Singh, B.; Shankarling, G.S.; Ghosh, H.N. *Chem. Eur. J.* **2014**, *20*, 3510.

25 Franchi, D.; Calamante, M.; Reginato, G.; Zani, L.; Peruzzini, M.; Taddei, M.; Fabrizi De Biani, F.; Basosi, R.; Sinicropi, A.; Colonna, D.; Di Carlo, A.; Mordini, A. *Tetrahedron* **2014**, *70*, 6285.

26 Marotta, G.; Lobello, M.G.; Anselmi, C.; Barozzino Consiglio, G.; Calamante, M.; Mordini, A.; Pastore, M.; De Angelis, F. *ChemPhysChem*. **2014**, *15*, 1116.

27 (a) Wang, P.; Zakeeruddin, S.M.; Moser, J.E.; Nazeeruddin, M.K.; Sekiguchi, T.; Grätzel, M. *Nat. Mater.* **2003**, *2*, 402; (b) Heiniger, L.-P.; O'Brien, P.G.; Soheilnia, N.; Yang, Y.; Kherani, N.P.; Grätzel, M.; Ozin, G.A.; Tétrault, N. *Adv. Mater.* **2013**, *25*, 5734.

28 Bessi, M.; Monini, M.; Calamante, M.; Mordini, A.; Sinicropi, A.; Di Donato, M.; Iagatti, A.; Foggi, P.; Zani, L.; Reginato, G. *Synthesis* **2017**, *49*, 3975.

29 Kunai, A.; Sakurai, T.; Toyoda, E.; Ishikawa, M.; Yamamoto, Y. *Organometallics* **1994**, *13*, 3233.

30 Brennan, J.B.; Gust, D.; Brudvig, D.W. *Tetrahedron Lett.* **2014**, *55*, 1062.

31 Frye, C.L.; Vogel, G.E.; Hall, J.A. *J. Am. Chem. Soc.* **1961**, *83*, 996.

32 Zhang, X.; Peng, B.; Zhang, S.; Peng, T. *ACS Sust. Chem. Eng.* **2015**, *3*, 1501.

33 (a) Cecconi, B.; Manfredi, N.; Montini, T.; Fornasiero, P.; Abbotto, A. *Eur. J. Org. Chem.* **2016**, *31*, 5194; (b) Zhang, X.; Peng, T.; Song, S. *J. Mater. Chem. A* **2016**, *4*, 2365.

34 Choi, S.K.; Yang, H.S.; Kim, J.H.; Park, H. *Appl. Catal., B* **2012**, *121*, 206.

35 Lee, J.; Kwak, J.; Ko, K.C.; Park, J.H.; Ko, J.H.; Park, N.; Kim, E.; Ryu, H.; Ahn, K.T.; Lee, J.Y.; Son, S.U. *Chem. Commun.*, **2012**, *48*, 11431.

36 Tiwari, A.; Mondal, I.; Pal, U. *RSC Adv.* **2015**, *5*, 31415.

37 (a) Watanabe, M.; Hagiwara, H.; Iribe, A.; Ogata, Y.; Shiomi, K.; Staykov, A.; Ida, S.; Tanaka, K.; Ishihara, T. *J. Mater. Chem. A* **2014**, *2*, 12952; (b) Kumari, A.; Mondal, I.; Pal, U. *New J. Chem.* **2015**, *39*, 713.

38 (a) Tiwari, A.; Pal, U. *Int. J. Hydr. En.* **2015**, *40*, 9069; (b) Cecconi, B.; Manfredi, N.; Ruffo, R.; Montini, T.; Romero-Ocana, I.; Fornasiero, P.; Abbotto, A. *ChemSusChem* **2015**, *8*, 4216.

39 Li, X.; Cui, S.; Wang, D.; Zhou, Y.; Zhou, H.; Hu, Y.; Liu, J-.G.; Long, Y.; Wu, W.; Hua, J.; Tian, H.; *ChemSusChem* **2014**, *7*, 2879.

40 (a) Lee, S.H.; Park, Y.; Wee, K.R.; Son, H.J.; Cho, D.W.; Pac, C.; Choi, W.; Kang, S.O. *Org. Lett.* **2010**, *12*, 460; (b) Han, W-.S.; Wee, K-:R.; Kim, H-.Y.; Pac, C.; Nabetani, Y.; Yamamoto, D.; Shimada, T.; Inoue, H.; Choi, H.; Cho, K.; Kang, S.O. *Chem. Eur. J.* **2012**, *18*, 15368; (c) Lin, R.Y-.Y; Wu, F-.L.; Li, C-.T.; Chen, P-.Y.; Ho, K-.C.; Lin, J.T. *ChemSusChem* **2015**, *8*, 2503.

41 Manfredi, N.; Cecconi, B.; Calabrese, V.; Minotti, A.; Peri, F.; Ruffo, R.; Monai, M.; Romero-Ocana, I.; Montini, T.; Fornasiero, P.; Abbotto, A. *Chem. Commun.* **2016**, *52*, 6977.

42 Narayanaswamy, K.; Tiwari, A.; Mondal, I.; Pal, U.; Niveditha, S.; Bhanuprakash, K.; Singh, S.P. *Phys. Chem. Chem. Phys.* **2015**, *17*, 13710.

43 Hagberg, D.P.; Edvinsson, T.; Marinado, T.; Boschloo, G.; Hagfeldt, A.; Sun, L. *Chem. Commun.* **2006**, 2245.

44 Dessì, A.; Calamante, M.; Mordini, A.; Peruzzini, M.; Sinicropi, A.; Basosi, R.; Fabrizi de Biani, F.; Taddei, M.; Colonna, D.; Di Carlo, A.; Reginato, G.; Zani, L. *Chem. Commun.* **2014**, *50*, 13952.

45 Bockris, J.O.M.; Khan, S.U.M. *Surface Electrochemistry - A Molecular Level Approach*, Springer US, New York, **1993**.

46 Tian, H.; Yang, X.; Cong, J.; Chen, R.; Teng, C.; Liu, J.; Hao, Y.; Wang, L.; Sun, L. *Dyes Pigments* **2010**, *84*, 62.

47 (a) Tauc, J. *Mater. Res. Bull.* **1968**, *3*, 37; (b) Coluccini, C.; Manfredi, N.; Salamone, M.M.; Ruffo, R.; Lobello, G.M.; De Angelis, F.; Abbotto, A. *J. Org. Chem.* **2012**, *77*, 7945.

48 (a) Kalyanasundaram, K.; Kiwi, J.; Grätzel, M. *Helv. Chim. Acta* **1978**, *61*, 2720; (b) Manke, A-.M.; Geisel, K.; Fetzer, A.; Kurz, P. *Phys. Chem. Chem. Phys.* **2014**, *16*, 12029.

49 Zhang, X.; Gan, X.; Yao, S.; Zhu, W.; Yu, J.; Wu, Z.; Zhou, H.; Tian, Y.; Wu, J. *RSC Adv.* **2016**, *6*, 60022.

50 (a) Abe, R.; Hara, K.; Sayama, K.; Domen, K.; Arakawa, H. *J. Photochem. Photobiol. A* **2000**, *137*, 63; (b) Li, Q.; Che, Y.; Ji, H.; Chen, C.; Zhu, H.; Ma, W.; Zhao, J. *Phys. Chem. Chem. Phys.* **2014**, *16*, 6550.

51 Gentili, P.L.; Mugnai, M.; Bussotti, L.; Righini, R.; Foggi, P.; Cicchi, S.; Ghini, G.; Viviani S.; Brandi, A. *J. Photochem. Photobiol. A* **2007**, *187*, 209.

52 Bayanov, I.M.; Danielius, R.; Heinz, P; Seilmeier A. *Opt. Commun.* **1994**, *113*, 99.

53 Danielius, R.; Piskarskas, A.; Di Trapani, P.; Andreoni, A.; Solcia, C.; Foggi, P. *Appl. Optics* **1996**, *35*, 5336.

54 Henry, E.R. *Biophys. J.* **1997**, *72*, 652.

55 Henry, E.R.; Hofrichter, J. in "*Methods in Enzymology*", ed. Ludwig Brand, M.L.J., Academic Press, **1992**, vol. *210*, pp. 129.

56 Snellenburg, J.J.; Laptenok, S.; Seger, R.; Mullen, M.K.; Van Stokkum, I.H.M. *J. Stat. Softw.* **2012**, *49*, 1.

57 Frisch, M.J.; Trucks, G.W.; Schlegel, H.B.; Scuseria, G.E.; Robb, M.A.; Cheeseman, J.R.; Scalmani, G.; Barone, V.; Mennucci, B.; Petersson, G.A.; Nakatsuji, H.; Caricato, M.; Li, X.; Hratchian, H.P.; Izmaylov, A.F.; Bloino, J.; Zheng, G.; Sonnenberg, J.L.; Hada, M.; Ehara, M.; Toyota, K.; Fukuda, R.; Hasegawa, J.; Ishida, M.; Nakajima, T.; Honda, Y.; Kitao, O.; Nakai, H.; Vreven, T.; Montgomery, J. A., Jr.; Peralta, J.E.; Ogliaro, F.; Bearpark, M.; Heyd, J.J.; Brothers, E.; Kudin, K.N.; Staroverov, V.N.; Keith, T.; Kobayashi, R.; Normand, J.; Raghavachari, K.; Rendell, A.; Burant, J.C.; Iyengar, S.S.; Tomasi, J.; Cossi, M.; Rega, N.; Millam, J.M.; Klene, M.; Knox, J.E.; Cross, J. B.; Bakken, V.; Adamo, C.; Jaramillo, J.; Gomperts, R.; Stratmann, R.E.; Yazyev, O.; Austin, A.J.; Cammi, R.; Pomelli, C.; Ochterski, J.W.; Martin, R.L.; Morokuma, K.; Zakrzewski, V.G.; Voth, G.A.; Salvador, P.; Dannenberg, J.J.; Dapprich, S.; Daniels, A.D.; Farkas, O.; Foresman, J.B.; Ortiz, J.V.; Cioslowski, J.; Fox, D.J., Gaussian 09. In *Revision C.01*, Gaussian, Inc. ed.; Wallingford, CT, **2010**.

58 Becke, A.D. *J. Chem. Phys.* **1993**, *98*, 5648.

59 Lee, C.; Yang, W.; Parr, R.G. *Phys. Rev. B* **1988**, *37*, 785.

60 Yanai, T.; Tew, D.P.; Handy, N.C. *Chem. Phys. Lett.* **2004**, *393*, 51.

61 Lynch, B.J.; Fast, P.L.; Harris, M.; Truhlar, D.G. *J. Phys. Chem. A* **2000**, *104*, 4811.

62 Tomasi, J.; Mennucci, B.; Cammi, R. *Chem. Rev.* **2005**, *105*, 2999.

63 (a) Paramasivam, M.; Chitumalla, R.K.; Singh, S.P.; Islam, A.; Han, L.; Jayathirtha Rao, V.; Bhanuprakash, K. *J. Phys. Chem. C* **2015**, *119*, 17053; (b) Guo, M.; He, R.; Dai, Y.; Shen, W.; Li, M.; Zhu, C.; Lin, S.H. *J. Phys. Chem. C* **2012**,

116, 9166; (c) Wang, J.; Li, M.; Qi, D.; Shen, W.; He, R.; Lin, S.H. *RSC Adv.* **2014**, *4*, 53927; (d) Lundqvist, M.J.; Nilsing, M.; Persson, P.; Lunell, S. *Int. J. Quantum Chem.* **2006**, *106*, 3214.

64 O'Boyle, N.M.; Tenderholt, A.L.; Langner, K.M. *J. Comput. Chem.* **2008**, *29*, 839.

65 Romero Ocaña, I.; Beltram, A.; Delgado Jaén, J.J.; Adami, G.; Montini, T.; Fornasiero, P. *Inorg. Chim. Acta* **2015**, *431*, 197.

Development of Polyamidoamine Hydrogels: Towards New Stimuli-Responsive Materials

Chapter 3

Introduction and Aim of the Work

3.1. What Are Hydrogels?

Hydrogels are three-dimensional networks of crosslinked hydrophilic macromolecules or polymers that can swell in water without dissolution and entrap large amounts of solvent, up to thousand times of their dry weight, through surface tension effects[1] (Figure 3.1). Since the first pioneering work of Wichterle and Lim in 1960,[2] due to their hydrophilic characteristics and potential biocompatibility, hydrogels have been a topic of great interest in materials science. Even though the first hydrogels being tested were based on natural polymers, the employment of total synthetic structures started almost immediately,[3] leading to the first significant differentiation inside this class of materials. The first application found for these novel materials was in the biomedical area, both focusing on the encapsulation and growth of cells inside the hydrogel network[4] and on the synthesis of tissue-like systems, due to the possibility to mimic the viscoelastic properties of the human tissue.[5]

Figure 3.1 Example of polyacrylates hydrogels swelling behavior.

3.1.1. General Structural Properties

The aspect of a common hydrogel is that of a porous elastic network whose interstitial space can be completely filled by water and that usually can undergo a reversible cycle between the swollen and dry states (Figure 3.2). This structure can be taken after equilibration in aqueous medium, resulting from the balance between the solvation forces acting on the repeating units of the macromolecular chains, which lead to an expansion of the network, and the elastic force of the cross-linked structure.[6] Hydrogels can be synthetized in different shapes, depending on the reactor employed during the gelation process and can also easily change their size and shape in response to environmental stimuli, for example by expelling or imbibing water from the outside solution. In addition, during the swelling process other species (for example endowed with reactive and even potentially polymerizable functional groups) can also be introduced inside the network, occupying the void volume and interacting with its chain segments or pendant moieties.

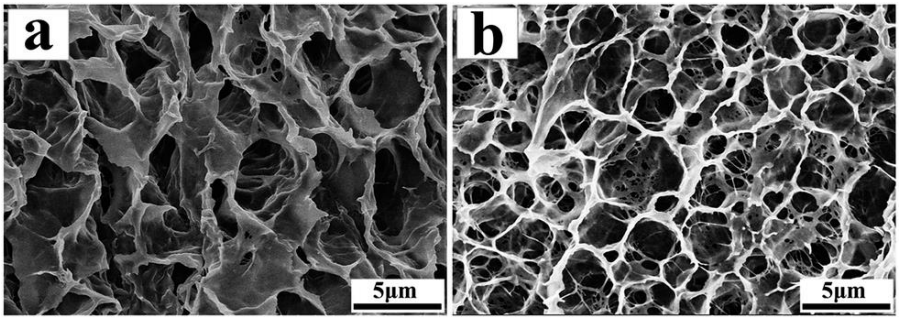

Figure 3.2 SEM pictures of hydrogels obtained with polyethyleneglycole of different weight.[7]

The hydrogels properties of being soft elastomeric materials with a low interfacial tension and high swelling capability, makes them a perfect candidate for biological applications: the first property in fact can reduce the mechanical and frictional irritation to the tissue bed, while the other two can increase the permeability of drug molecules and metabolites, promoting cell adhesion and proliferation.[8] In particular, the possibility to immobilize and stabilize enzymes[9] allows their use also as micro-bioreactors, by hosting biological molecules and providing a suitable environment for their reactions.[10]

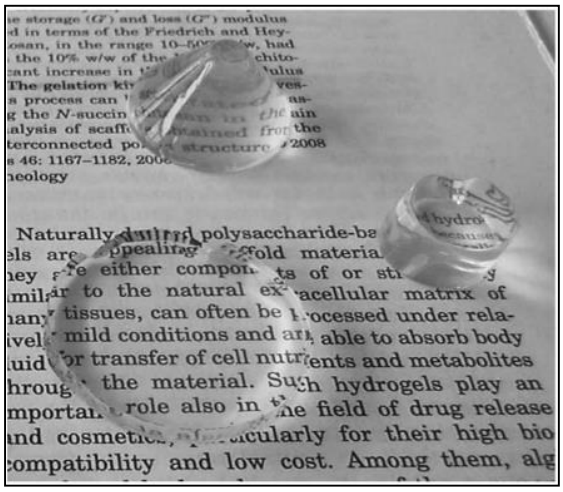

Figure 3.3 Examples of different shaped hydrogels.[11]

All hydrogels specific characteristics, be they physical (even their mass transport properties[12]), chemical or biological (i.e. biocompatibility[13] or biodegradability[14]), are strongly dependent from the nature of the network, the gelation conditions and crosslinking properties. For this reason, hydrogels are classified in several ways depending on the nature of the reactant employed, of the crosslinking established between the different components and their structural characteristics.[1b,15]

3.2. Classifications

Hydrogels can be classified in various ways,[16] based on their original source (natural *vs* synthetic systems), their network structure (inter-penetrating, copolymeric, homopolymeric or double), the crosslinking method (chemical or physical), their charge (anionic, cationic, amphoteric, and non-ionic) or their biodegradability (if they are degradable or not). Each class exhibits particular advantages and disadvantages which influence also the possible final application of the material. However, the most useful classifications are those based on the nature of the hydrogel network, on the crosslinking used and on the network structure; they will be briefly described below.

3.2.1. Natural *vs* Synthetic Components

There are many studies about the employment of natural compounds (both polymers or small molecules) in hydrogels synthesis, motivated by the low toxicity, biodegradability and cell-interactive properties of such systems.[17] Two main classes of biological compounds have been used for this application, proteins and polysaccharides. Collagen,[18] gelatin,[19] fibrin[20] and heparin[21] are the most employed proteins, while chitosan,[22] hyaluronic acid,[23] agarose[24] and alginate[25] are the polysaccharides that recorded the best results for the synthesis of hydrogels. In particular, collagen and hyaluronic acid (Figure 3.4) have been extensively studied, the former for its elasticity and high biodegradability, while the latter for its high biological activity and capability to take part in more complex networks;[26] indeed, in recent years hyaluronic acid has been more and more employed not only in the hydrogel field,[27] but also in the general area of biomedical sciences.[28] The major drawbacks in the application of polysaccharides for hydrogel preparation are their lack of adequate physical properties (which are difficult to improve by structural modifications),[29] and the limited control of their degradability, possibly leading to potential immunogenic responses, which would compromise their activity.[30] Finally, some natural biomolecules (such as nucleotides or folic acid) have also been used for the preparation of physically crosslinked hydrogels based onto hydrogen bond and π-stacking interactions, still showing excellent biocompatibility and cell proliferation properties.[31]

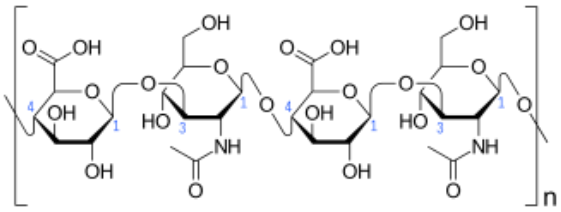

Figure 3.4 Hyaluronic acid structure.

On the other hand, synthetic polymers emerged as a valid alternative to natural compounds,[1a,32] due to their controllable degradation rates (for example by inclusion of photodegradable linkers[33] as well as other variously tunable molecular and micro structures).[34] In particular, their highly reproducible syntheses and easy functionalization allow the incorporation of tailored functionalities,[35] biological molecules[36] or inorganic nanocomposites, which can be even covalently bound to the polymer structure.[34b] For example, enzymes or amino acids sequences have been widely employed for enhancing the cell-adhesion of synthetic polymers.[37] However, also this class of hydrogels exhibits some drawbacks, principally related to its inherent lack of biological compatibility if not properly functionalized,[17a,38] limiting its ability to promote differentiation and proliferation of cells and tissue regeneration.[39] For this reason, combinations of natural and synthetic polymers have also been widely investigated for various biological and biomedical applications.[40]

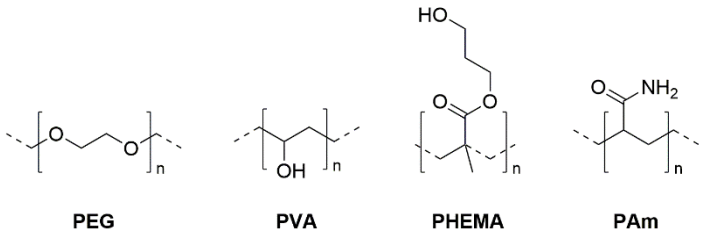

Figure 3.5 Structure of the most used synthetic polymers for hydrogel synthesis.

The principal synthetic polymers employed for the synthesis of novel hydrogels are poly(ethylene glycol) (PEG), poly(vinyl alcohol) (PVA), poly(hydroxyethyl methacrylate) (PHEMA) and poly(acrylamide) (PAm), whose structures are reported in Figure 3.5, even though polypeptides are widely used as well.[39] PEG and PHEMA hydrogels are probably the most widely employed networks in the field. In the case of PEG, this is due to its low toxicity and immunogenity properties, thanks to which it was approved also from the U.S. Food and Drug Administration for various clinical uses.[41] PHEMA on the other hand has been employed in several biomedical devices, even in contact lenses.[42] Both polymers can be easily modified and even photopolymerized using various diacrylates as crosslinkers.[43] PVA has characteristics extremely similar to those of PEG, mostly the high hydrophilicity. It possesses a high elasticity and can be polymerized using several methods, both without (by freezing/thaw methodologies)[44] or with crosslinker (e.g. glutaraldehyde[45]). PAm hydrogels are more similar in structure to PHEMA but they found more often use in "technological" applications instead of biomedical ones, especially due to the high toxicity of the starting materials. A particular property common to several PAm hydrogels is their thermosensitivity,[46] a characteristic which allows their use in the field of sensors.[47]

3.2.2. Crosslinking Differentiation

The crosslinking of the different hydrogel components into a more complex polymeric network is the main process occurring during the gelation.[48] For this reason, the type and degree of crosslinking can influence many of the material properties, such as the degree of swelling, the elastic modulus and the transport of molecules.[49] The presence of a physical (non-covalent) or chemical (covalent) crosslinking (Figure 3.6) can lead to two major classes of hydrogels which exhibit different properties and thus have a different application scope. Historically, hydrogel research mainly focused on chemically crosslinked systems, although in recent years physical crosslinking acquired some popularity due to the possibility to avoid the use of the crosslinker itself, which can be toxic and whose excess usually has to be removed from the final material.[15]

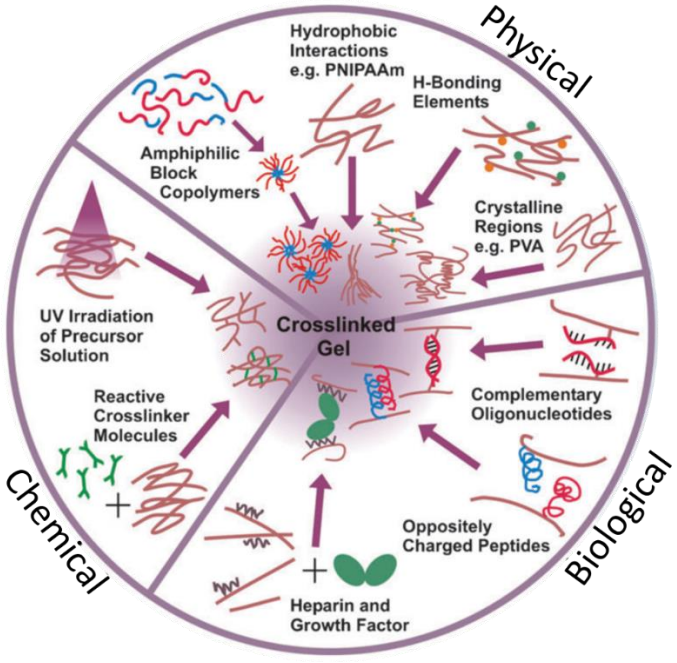

Figure 3.6 Different kinds of hydrogel crosslinking.[34b]

Chemically cross-linked hydrogels (Figure 3.7a) are materials which can form a novel polymeric network by establishing covalent bonds through chemical reactions. During the process, small molecules or even living cells can be entrapped in the forming network. They are permanent systems[50] which cannot be dissolved anymore without the disruption of the covalent network. These stable materials can be obtained using various reactions on fairly concentrated aqueous solution.[51] The main synthetic tools for making a chemically crosslinked hydrogel are radical polymerization,[52] click chemistry,[53] Michael reactions,[54] Schiff's base formation,[55] enzymatic reactions,[56] or disulfide-forming reactions.[57] Radical and photo polymerizations are initiated by free radicals produced by peroxides and other radical generators, or by decomposition of a photoinitiator upon visible or UV light exposure. The free radicals then react with the monomers, typically acrylate moieties, to form the hydrogel network.[58] As far as click chemistry is concerned, one of the most representative reaction is the CuAAC reaction,[59] which has been widely used for the synthesis of hydrogels, due to the mild conditions, the compatibility with aqueous environment and the high tolerance for functional groups, which allows its use also in the presence of proteins and peptides.[60] To be performed, the reaction requires the previous functionalization of the different hydrogel components with an alkyne and an azide, which can be present either on the main monomer or the crosslinker depending on the particular needs, and a Cu salt to catalyze the process, even though catalyst-free versions of the reaction have also been successfully employed.[61] Michael-type additions between both thiols or amines and acrylates have been employed and , unlike other addition reactions, exhibit the major advantage to be applicable in aqueous medium, at room temperature and at physiological pH, without the need of adding any other reactant.[62] Another process that does not require any additional initiator is Schiff's base formation, in which amines and aldehyde groups react to form carbon–nitrogen double bonds. Moreover, the aldehyde groups present in polymer chains can even react with amino groups of natural tissues, promoting integration of the hydrogel into the surrounding environment.[63] Enzymatic processes have received also remarkable attention for their cell-friendly reaction conditions, such as a neutral pH, aqueous environment and mild temperature. They present also another significant advantage, the substrate specificity of the enzyme, which can prevent toxicity caused by side reactions and lead to a great control of the process outcome.[64] However this last property is also one of the principal drawbacks, because it also limits the number of reagents that can be employed for the hydrogel synthesis. Chemically crosslinked hydrogels usually possess greater stability and better mechanical properties if compared to their physically crosslinked counterparts, but the permanent crosslinking can make the material rather fragile and unable to self-heal once the network is broken.[65] For this reason, chemical hydrogels including transient junctions, such as polymer chain entanglements or hydrogen bonds, present more advantages, while the fine tuning of the cross-linker allows to obtain hydrogels with different mechanical properties.[66] Another alternative is the so called "dynamic covalent polymer networks" in which reversible covalent bonds, such as those needed to form acylhydrazones, allow construction of an hydrogel capable to show the self-healing reversibility characteristics of physically bonded network, while maintaining the good mechanical properties and stability typical of the chemically crosslinked hydrogels.[67] Chemical hydrogels present also another important drawback, which is that the residual chemical crosslinkers, organic solvents, and photoinitiator which did not react or were not removed from the material may cause cytotoxicity.

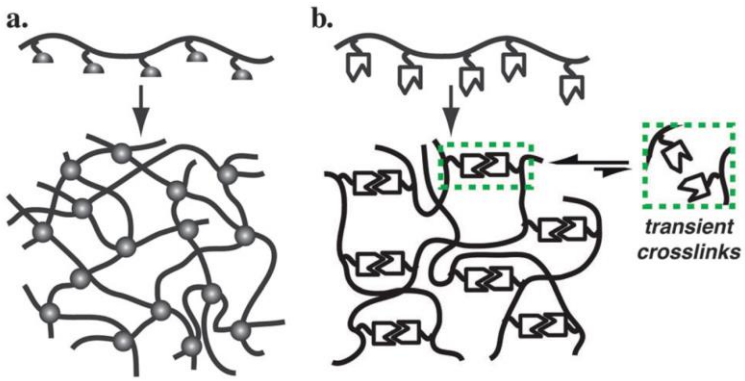

Figure 3.7 Schematic representation of hydrogels with (a) chemical and (b) physical crosslinking.[68]

Different from chemically crosslinked networks, physically crosslinked hydrogels (Figure 3.7b) achieve a gel state by establishing intermolecular weak forces such as hydrogen bonding (e.g. using natural polysaccharides[69]), hydrophobic interactions,[70] metal-ligand complexation,[71] electrostatic ionic forces (e.g. with polyelectrolites[72]) or intermolecular assemblies such as guest–host inclusion (e.g. with cyclodextrins[73]), stereo-complexation[74] and complementary binding.[68] These interactions can be achieved by internal arrangement of the reagents themselves or can be induced by external stimuli such as heat, pH, ionic strength electric fields, light, pressure, sound or the presence of specific molecules.[75] Due to the non-covalent characteristic of the bonds, the process produces reversible hydrogels in mild conditions and aqueous solution in the absence of chemical crosslinkers,[76] providing simple and safe approaches to preparing biocompatible hydrogels, even if these good characteristics are often associated to unsatisfactory mechanical properties and to an increased sensitivity to the environmental conditions.[68]

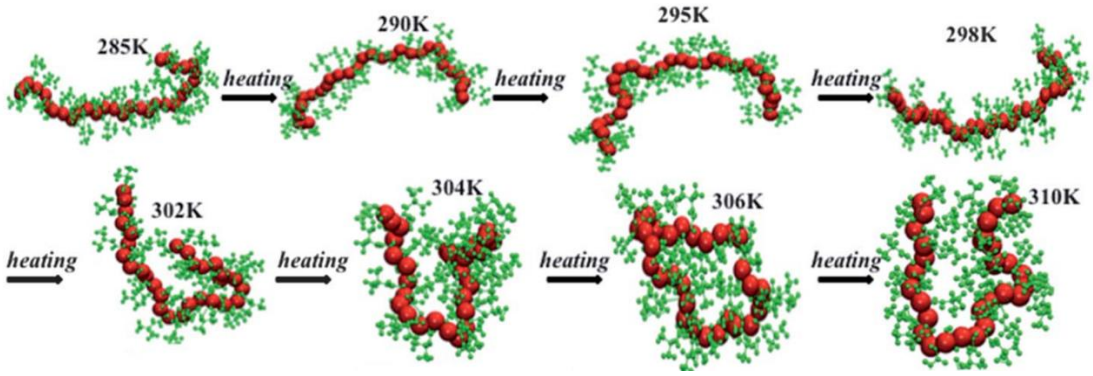

Figure 3.8 Snapshots showing conformations of a 30-mer poly(N-isopropylacrylamide) during a ultrafast heating process. Backbone atoms of the polymer are shown in red, while atoms in the side-chain are shown in green.[77]

As examples, poly(*N*-isopropylacrylamide) and agarose are two of the most studied physically crosslinked hydrogels due to their thermoresponsive properties, arising directly from their crosslinking nature. Poly(*N*-isopropylacrylamide) undergoes a coil-to globule transition by warming it above its lower critical solution temperature of 32°C (Figure 3.8), releasing the water molecules bound to the isopropyl side groups, which results in an increase of the intra- and inter- molecular hydrophobic interactions between these groups.[78] On the other hand, in agarose the cross-linking is driven by the formation and aggregation of double helical structures, when the temperature decreases from the melting point (≈ 85°C).[79] All the interactions mentioned above can also take place simultaneously in order to enhance the final properties of the material and realize more complicated structures (Figure 3.9). This, for example, can happen with already relatively complex short peptides, in which the mix of hydrophobic,

H-bond and ionic interactions between the side chains could lead to the spontaneously organization in nanofibers that aggregate to form the hydrogel,[80] or also with particular small molecules capable to give both hydrophobic and hydrophilic interactions, which can self-assembly in ordered macro-aggregates and then in the final hydrogel network[31] (Figure 3.9).

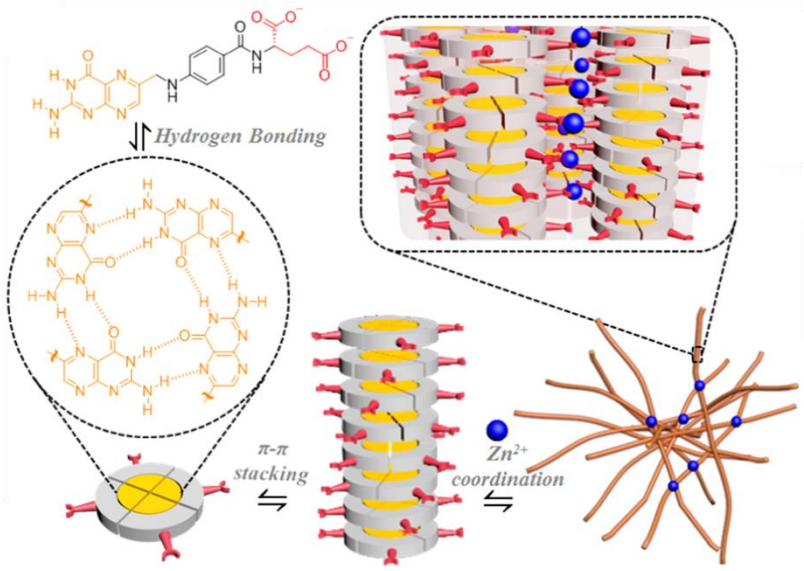

Figure 3.9 Example of self-assembly of a small molecule (folate salt) into a supramolecular hydrogel using several weak interactions.[31]

3.2.3. Network Structure

This classification is based on the nature of the hydrogel network, which is another factor which can be modified when looking at a specific application for the material. In particular, homopolymeric, copolymeric and multipolymer interpenetrating network (IPN) hydrogels can be distinguished.

Homopolymeric hydrogels are networks derived from the polymerization of a single species of monomer, which represent the basic repeating unit of the system.[81] They are the easiest form of hydrogels to be synthetized and their properties mostly depend on the degree of crosslinking and on the polymerization technique used. One of the most common examples of homopolymeric hydrogels are PHEMA networks, which are usually crosslinked using diacrylates.

On the other hand, copolymeric networks are synthetized using two or more different monomer species, in which at least one is an hydrophilic component. The repeating unit of the system is variable because it depends on the polymerization conditions and the type of control exerted on the process, so that the monomers can be arranged in blocks or in an alternating configuration or even randomly.[82] An example of copolymeric networks are hydrogels obtained by Aza-Michael reaction, in which usually more than one monomer is employed in order to better tune the final properties of the material.[83]

IPN are more complex systems composed by two different interpenetrating networks, which could be either natural or synthetic and either physically or chemically crosslinked.[84] If only one of the polymers is crosslinked, the material is called “semi-IPN”, while if both are crossliked (not necessarily together), the material is a proper IPN.[85] IPN are an important class of hydrogels because their double nature structure confers them better mechanical properties and stability, which can also be better controlled compared to “classic” hydrogels. Such properties are attributed to their unique contrasting network

structure and strong network entanglement[86] (Figure 3.10). For these reasons, from their first synthesis in 2003,[87] many efforts have been devoted to the optimization of their synthesis and properties. Gong *et al.*[86b] have summarized the principles for preparation of tough chemically linked IPN hydrogels: (i) rigid and brittle polymeric chains serves as the first network, while soft and ductile neutral polymer serves as the second network; (ii) the molar concentration of the second network is 20–30 times that of the first network; (iii) the first network is tightly while the second network is loosely crosslinked to achieve a strong asymmetric gel structure.[88] Based on these design concepts, several synthetic methodologies have been developed and led to the production of different tough IPN hydrogels, including microgel-reinforced,[89] void,[90] inverse,[91] jellyfish,[92] liquid crystalline,[93] and lamellar bilayer IPN hydrogels.[94] The typical synthetic procedure is a so called "two-step procedure" in which, usually, the first step consists in the formation of a tightly cross-linked network gel of polyelectrolyte, followed by its immersion in an aqueous solution of a second monomer with a low ratio of cross-linking agent. Then, the second step is performed by carrying out the polymerization of the second component in the first network.[87] Owing to its polyelectrolyte nature, the first network synthetized highly swells in the second monomer solution and, as result, the first gel network is highly diffuse in the final product and, at the same time, the amount of the second network in the final material is in large excess to that of the first network. Other methodologies have been employed for the synthesis of IPN hydrogels, such as molecular stent,[95] one-pot,[96] extrusion 3D-printing,[97] and free-shapeable methods.[98]

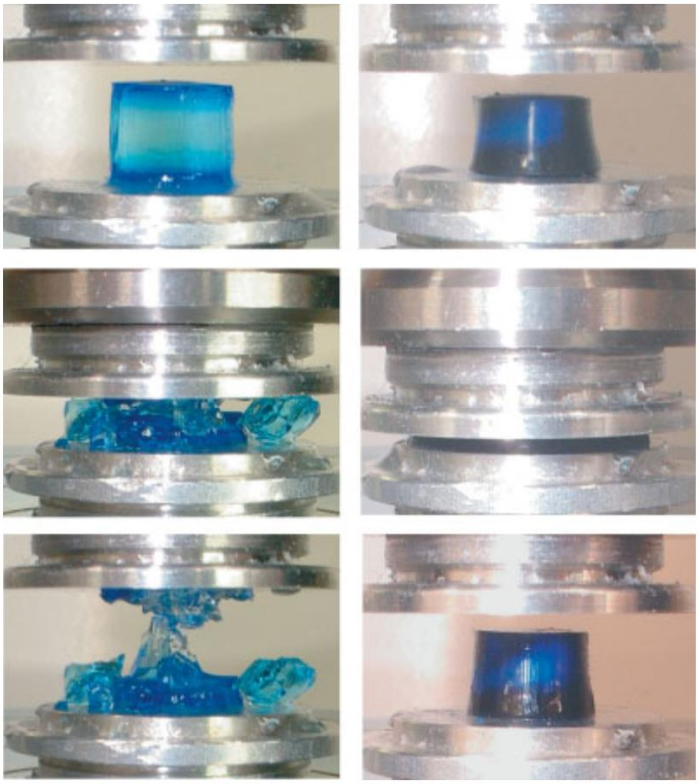

Figure 3.10 Different behavior under high compression between (a) "classical" homopolymeric and (b) IPN hydrogels.

The strong chain entanglement between two different networks present in IPN gels is the origin of their particular toughness and strength, and increases when the molar ratio of the second network to the first one increases.[99] The reason behind the influence of such strong interaction on the mechanical properties of the material derives from a dual stress-loading transfer between the two networks, possible due to the inter-network topological entanglement of these interactions. The density ratio of elastically effective polymer chains of the two networks, in fact, ensures that the propagation of the

micro-cracks in the brittle first network is prevented by the ductile second network. On the other hand, the second network will transfer the stress back to the brittle first network, causing further internal fracture of the latter, but without causing its collapse.[84] The inter-network interactions present can be either covalent or noncovalent, with or without chemical crosslinkers: by adjusting them and the structural parameters of the two networks, a wide range of mechanical performances can be reached, according to the designed application.[100]

3.3. Gel Network Engineering

The extreme flexibility of hydrogel networks allowed the development of more complex materials containing also other components, and to their successive applications in several new fields. Accordingly, several new categories of hydrogels were introduced over the years, each one having particular characteristics. Some of the most famous and used hydrogel materials will be briefly presented in the next sections.

- **Nanocomposite Hydrogels**

Nanocomposite hydrogels are soft materials whose polymer network incorporates nanoparticles or nanostructures, both physically or by covalent attachment, capable to enhance the properties of the material.[101] Traditionally, the addition of nanocomposites has been employed to improve the mechanical properties of hydrogels, and reinforcing materials have been typically limited to organic/polymeric nanoparticles. The first attempts in this direction were made with inorganic nanoparticles;[102] since then, various kinds of nanoparticles (carbon-based, inorganic, metal-based or even polymeric) have been used to obtain nanocomposite hydrogels, as well as other nanostructures like nanotubes or graphene (Figure 3.11).[103] One of the main reasons behind the use of nanoparticles is the large surface-to-volume ratio, which can increase the particles–matrix interactions and enhance the nanoparticles effect on the overall material. The main challenges in the use of nanoparticles is to achieve a both a homogeneous dispersion and a good adhesion to the polymeric matrix , but many studies have been focused on the resolution of this problem.[104] For this last issue in particular, methods centered onto the functionalization of the nanoparticle surface have been widely developed and employed.[105] These procedures led also to the design of novel hydrogels with tailored functionalities,[106] thanks to the fact that nanomaterials often possess specialized and tunable functions that are not found in the polymers matrices. Nanocomposite hydrogels exhibiting enhanced properties such as mechanical strength and swelling,[72a,107] stimuli-responsive behavior induced via magnetic,[108] optical,[109] or thermal changes[110] have also been synthetized and widely applied, especially in the biomedical field for drug release devices.[103]

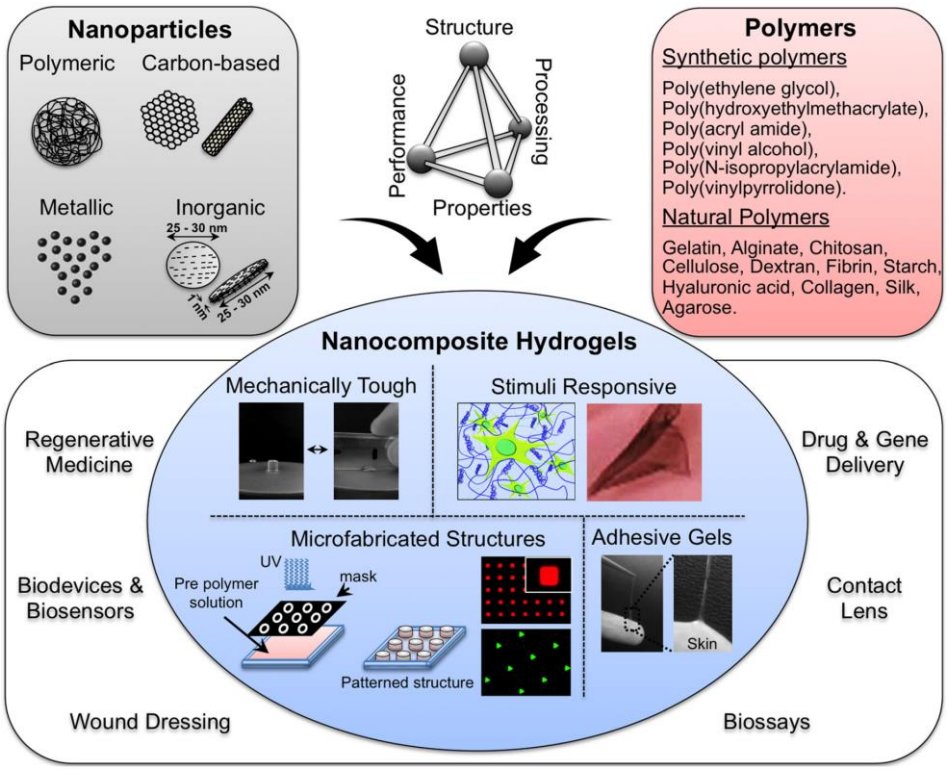

Figure 3.11 Examples of the extreme variety of nanocomposites employed for the synthesis of functionalized hydrogels and of the applications of the final materials.[101a]

- **Biodegradable Hydrogels**

Many biomedical applications require hydrogels that can be easily degraded in physiological conditions, in order to be eliminated from the organism after the exploitation of their activity without the need to remove the implant. The main challenge is to design the material with a precise degradation rate capable to match the entire duration of the clinical application.[111] While this parameter can be difficult to control when natural hydrogels are used,[33] synthetic hydrogel networks can be tuned by fine tailoring of the polymer structure, the cross-linking density and the amount of incorporated degradable moieties. Many approaches have been developed in the last years to synthetize efficient biodegradable hydrogels[17a] and the most effective strategy appear the intercalation in the hydrogel network of particular linkers that can be degraded by specific agents, for example *via* ester hydrolysis, enzymatic degradation, photolytic cleavage or reversible click reactions. There are two principal methods to introduce those degradable linkers, either by the formation of degradable bonds during the synthesis of the hydrogel network, or by using specific crosslinkers containing suitable cleavable bonds. The degradation of the cleavable bond then leads to the disruption of the connections within the hydrogel network, causing dissolution of the initially insoluble material. Particularly interesting are hydrogel scaffolds containing cell-cleavable bonds, which are degraded upon interaction with living cells as an effect of interaction with cell-secreted molecules.[112] For example, this can be achieved by incorporation into the hydrogel network of protease-cleavable moieties as crosslinkers, due to the high concentration of these enzymes into living cells,[113] or with the introduction of disulfide bonds, since the cleavage of this moiety is easily controllable under physiological conditions by altering the concentration of reductants, such as glutathione, which are typical cell metabolites.[114] As a consequence, the latter degradation strategy is considered very promising in the field of the tissue engineering and drug delivery.

- **Injectable Hydrogels**

This kind of hydrogels was designed for biomedical applications, with the aim to overcome some of the most common problems regarding the use of invasive procedures during patient therapy. Injectable hydrogels, in fact, can be directly delivered *in vivo* in a minimally invasive manner, and then rapidly solidify inside the body, without the need of any surgical operation.[17] Moreover, these hydrogels can be formed directly *in situ*, under physiological conditions, and can be also loaded with bioactive compounds prior to the injection and successive gelation.[115] The three most common methods generally used to develop injectable hydrogels are photo-gelation, thermal gelation and chemical gelation. Photo-gelation methods are based on the exposure to visible or near UV radiation of water soluble components having photolabile groups on their chemical structure, in the presence of appropriated photo-initiators. Instead, thermal-gelation takes advantage of the phase transition properties near physiological temperature of particular polymers, thus achieving hydrogels formation through small temperature changes after injection.[116] However, both these methods present some inconveniences: use of the UV light can be challenging in areas difficult to reach, while thermoresponsive materials can lose mechanical integrity due to the diluting environment of the body.[117] On the other hand, chemical gelation does not show any of these drawbacks: according to this approach, hydrogels are formed by reaction of monomers and crosslinkers with complementary functional groups in physiological conditions and do not require any other input to be formed. For this reason, several different chemical processes have been employed for this purpose, such as Michael addition reactions[118] or Schiff base and disulfide bond formation,[17a,119] taking always care not to use toxic components.

3.3.1. Stimuli Responsive Hydrogels

Stimuli responsive hydrogels are a particular class of materials whose peculiar trait is to respond to environmental stimuli (both physical or chemical) by exhibiting unexpected changes in their properties: these can include dimensions, network structure, mechanical strength and permeability; for this reason, such materials are also called environmentally sensitive or smart hydrogels.[120] The most commonly employed physical stimuli include light, pressure, temperature, electric fields, magnetic fields and mechanical stress, while chemical stimuli include pH, ionic factors and chemical agents. The effect induced by the external stimulus in the hydrogel network can be often observed also on the macroscopic scale in different forms, but the most common is a change in shape and size, which also influences their water uptake capability[121] (Figure 3.12).

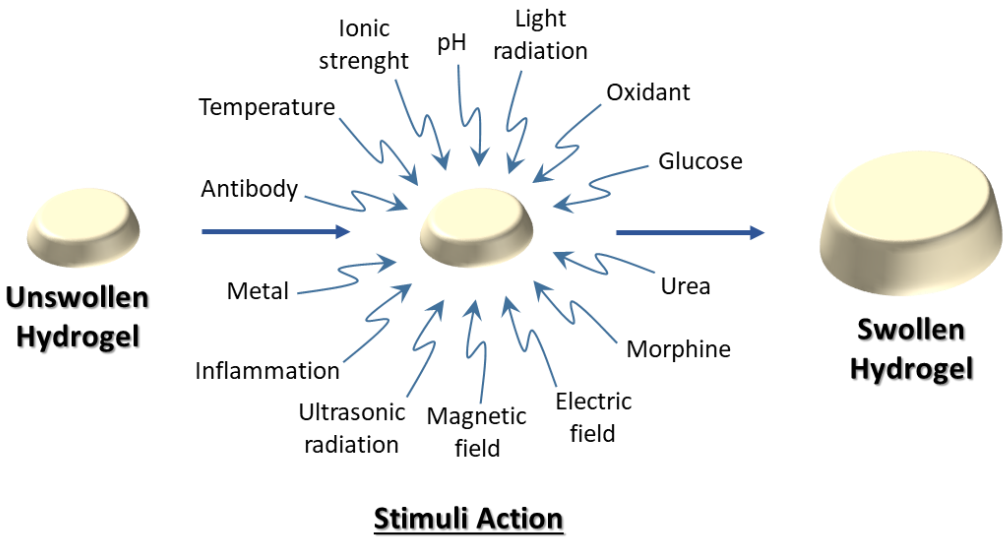

Figure 3.12 Representation of the typical stimuli-responsive hydrogel behavior.

This kind of hydrogels are often classified depending on the stimulus to which they respond, since a huge variety of chemical structures can be employed in each case. For example, a particular class, called "dual responsive hydrogels", is defined by the reaction to a combination of two stimuli responsive mechanisms in the same hydrogel system, and is mostly composed by particular IPN system. The most studied stimuli for this application are, without doubt, pH, temperature, light and electricity.[16,122] The first two systems will be briefly described in the next sections, while the other two will be analyzed more in detail in the next chapters of this PhD thesis (respectively in Chapter 4 and Chapter 5).

- **pH Responsive Hydrogels**

pH responsive hydrogels are systems possessing a large number of ionic pendant groups that can accept or donate protons in response to an environmental pH change, dramatically altering the degree of ionization of the matrix.[123] This change strongly depends on the amount of such functional groups and their pK_a or pK_b values, and usually the modification in the net charge of the ionized pendant groups causes a sudden volume transition due to the generation of electrostatic repulsive forces between them, creating a large osmotic swelling force. Depending on the ionic groups employed, there are two types of pH responsive hydrogels: anionic and cationic systems. Anionic hydrogels are networks in which the ionization process leads to the formation of anions: accordingly, pendent groups such as carboxylic or sulfonic acids are employed. With this kind of groups deprotonation is the process responsible for the increment of the swelling capacity of the system, and it occurs when the environmental pH is above the pK_a.[124] On the other hand, cationic hydrogels contain pendent groups such as amines, capable to be protonated, and thus ionized, when the surrounding pH is below the pK_b, increasing the swelling due to the increased electrostatic repulsions.[125]

- **Temperature Responsive Hydrogels**

Temperature sensitive hydrogels are defined by their ability to change their volume when they detect a variation of the surrounding temperature.[126] These networks can be classified as positive or negative temperature responsive systems, depending on their change in volume in response to a drop of the environmental temperature.[46] A network is defined a positive temperature responsive hydrogel when it possess a upper critical solution temperature (UCST) and then it shrinks, releasing solvents or fluid from the matrix, when the temperature is below the UCST.[127] Instead, at higher temperatures than the

UCST, swelling takes place. The reason behind the shrinking at low temperatures relies in the formation of a complex structure of hydrogen bonds among the polymeric chains of the network, which dissociates at a higher temperatures (above the UCST), allowing the hydrogel to swell to the maximum possible extent. On the other hand, negative temperature responsive hydrogels have an opposite parameter called low critical solution temperature (LCST); accordingly, they shrink when the temperature increases above the LCST and swell when it is lower than the LCST. The LCST can be altered in different ways, such as by mixing a small amount of ionic copolymer in the gels or by changing the solvent composition, and in general shifts to lower values by employing polymers with more hydrophobic constituents.[128] These kind of networks possess two distinct parts, a hydrophobic and a hydrophilic one:[129] at temperatures lower than the LCST, the solvent establishes hydrogen bonds with the hydrophilic part, improving the swelling capability of the network, which could even result into the transition to the solution state of the hydrogel (Figure 3.13); as the temperature increases and surpasses the LCST, the hydrophobic interaction within the hydrophobic part becomes stronger, while at same time, the hydrogen bonds will progressively dissociate, resulting in a global shrinking of sample with a release of the trapped fluids.[130]

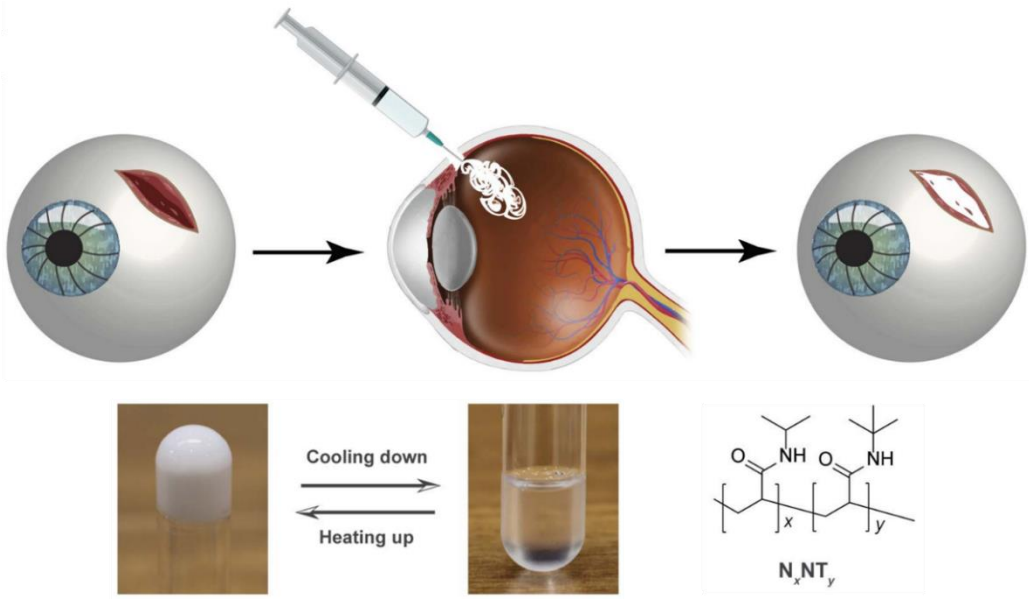

Figure 3.13 Example of the use of a thermoresponsive hydrogel in regenerative medicine. The polymeric network can be injected as liquid at low temperatures and when raised to body temperature, a heat-induced gelation converts the hydrogel into a solidified occlusion. The sealant can be then repositioned or removed without causing additional trauma via exposure to cold water.[131]

3.4. General Hydrogels Characterization

The characterization of such complex systems is not easy and can require several different techniques and methodologies. For this reason, usually, the final protocol adopted strongly depends on the final application of the material, in turn dictating the most interesting properties to be determined. Even with that premise, a specific experiment, the determination of the equilibrium degree of swelling (EDS), is always carried out because it defines the principal characteristic of an hydrogel, its water uptake capability. Other experiments that are almost always carried out are the rheological characterization, which provides information on the mechanical properties of the network (i.e. the elasticity), biocompatibility tests, differential scanning calorimetry (DSC), as well as thermogravimetric (TGA), FT-IR and SEM analyses.[48,132]

3.4.1. Equilibrium Degree of Swelling

Good hydrogel biocompatibility arises from their higher water content, which causes also them to become softer and to assume elastic properties. Their ability to swell and de-swell in a particular medium depends on many factors, such as crosslinking density, hydrophilicity of polymer chains, and the solvent nature. Moreover, the amount of water uptaken into the network regulates also the absorption and diffusion of solutes throughout the scaffold.[133] Hydrogels swelling and shrinking processes, due to the changes in volume they involve (Figure 3.14), are currently among the most employed characteristics in various applications including control of microfluidic flow, muscle-like actuators and drug delivery.[134] When a dry hydrogel begins to absorb water, solvent molecules start to hydrate the most polar hydrophilic groups present in the polymer chains; then, as a result of polar groups hydration, the network begins to swell and to expose the hydrophobic groups, leading to the incorporation of hydrophobically-bound water.[135] Finally, the network imbibes additional water filling the free interstitial spaces present, due to the osmotic driving force of the network chains towards infinite dilution.[78] The swelling process, which distends the network, is opposed by the elastic contractibility of the stretched polymer network and an hydrogel reaches its EDS when a balance occurs between these two forces. This parameter can be then calculated by gravimetric measurements using Equation 1:

$$\mathrm{EDS} = \frac{W_{wet} - W_{dry}}{W_{dry}} \times 100 \qquad \text{Eq. (1)}$$

where W_{wet} and W_{dry} are, respectively, the measured weight of the swollen and lyophilized hydrogel. The EDS value reached by each network mainly depends on the hydrogel crosslinking characteristics and density,[79] but also on the pH value of the surrounding medium, which could cause the ionization of pendent groups on the polymer chains and thus increase the swelling properties of the system. These values are usually comprised between 100% and 1000%, although even higher values have been recorded.[80]

Figure 3.14 Schematic representation of the swelling process.

3.4.2. Rheological Characterization

The rheological characteristics of hydrogels are key parameters to understand their structure and consequently their application scope. Measurements can be performed at different swelling states of the material and can give different results due to the influence of water on the hydrogel physical properties; the most common case is to characterize the hydrogel in its saturated swelling conditions, in order to mimic its physical conditions in the biological environment. Oscillatory rheology is a powerful tool to understand both the structural and dynamic characteristics of the system because it allows to quantify both its elastic and viscous-like properties by measuring two dynamic moduli: the storage

modulus, G', which describes the elastic response, and the loss modulus, G'', which is related to the viscous behavior. The relation between these two values is often used also to monitor the gelation process of the hydrogel: in fact while for a not-crosslinked polymer solution G'' is much higher than G' (for the predominance of the viscous property if compared to the elastics), for partially crosslinked polymers G' increases and becomes higher than G''; finally, when the hydrogel gelation process finishes, the highly crosslinked network exhibits a solid-like mechanical spectrum with both very high G' and G'' values, still showing the relation G' > G''.[136] Furthermore, a high separation between the two values suggest the formation of a mechanically strong network.[137] From the graph of G' and G'' vs. time (an example is shown in Figure 3.15) it is also possible to evaluate the gelation time, which correspond to the sol-gel transition of the system and correspond at the time when the crossover between the curves of G' and G'' occurs.

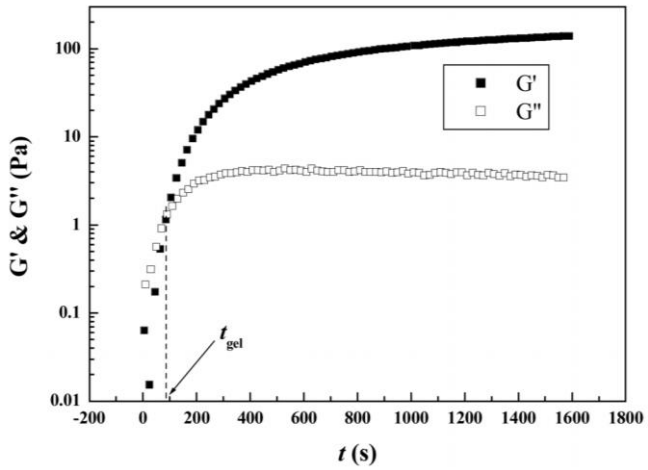

Figure 3.15 Example of time evolution of the two Young moduli during the gelation process.[138]

Usually, oscillatory shear measurements are performed in the linear viscoelastic regime, in order to let G' and G'' be independent from the strain amplitude. The viscoelastic zone can be evaluated by a stress strain-sweep analysis in which the samples are subjected to a stress and deformed at different shear strains (γ) at fixed frequency (an example is showed in Figure 3.16a). From that graph is then possible to determine the value of shear strain γ to be employed for the determination of the two Young moduli.

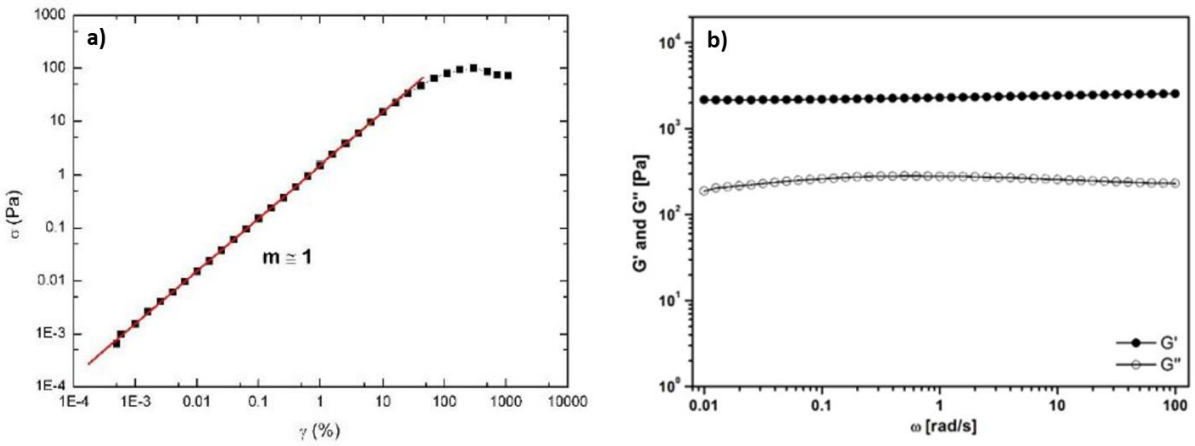

Figure 3.16 Examples of (a) stress-strain curve and (b) G' and G'' graph as function of the oscillation frequency.[83]

The last experiment which is usually performed is the evaluation of the stability of G' and G'' over a range of frequencies with a frequency sweep analysis. The strain determined within the viscoelastic regime is then applied to the hydrogel samples in a particular chosen range of frequencies and the samples response is recorded, generating a graph showing the dependence of the two Young moduli *vs* the frequency (an example is showed in Figure 3.16b). In this case, a frequency-independent behavior of both G' and G'' indicate the formation of a well-developed, cross-linked, and robust network.[139]

3.4.3. Other Characterization techniques

As pointed out above, depending from the final application of the material there are various other analysis that can performed on hydrogels systems. Among them, there are few experiments which provide useful information based on comparisons with other similar systems or starting materials (i.e. SEM, FT-IR) or others which can give complementary data to those already obtained (i.e. DSC or TGA). Remarkable are also the biocompatibility tests, in which the toxicity of the material and its components is evaluated.

- **FT-IR and SEM**

FT-IR (Fourier transform infrared) spectroscopy is a useful technique for identifying functional groups present on both small molecules and polymers. The technique is extremely flexible in term of sampling methods,[140] which can be chosen according to the sample physical state. The most common methods used include transmission (for singular substances or semi-thin films), external reflection (for thin films loaded onto a reflecting substrate), reflection-absorption (extremely-thin films loaded onto a metal substrate), internal reflection (thick and soft materials or for "wet" measurements) and diffuse reflection (on powders). The obtained spectrum represents the fingerprint of the material and, for polymers, can be compared to those of the starting materials in order to identify their presence and their contribution to the polymer structure, along with the new signals related to the newly formed bonds.

Scanning electron microscopy (SEM) can be used to provide information about the sample surface topography,[141] composition, and other properties such as electrical conductivity. Due to the usual low conductivity of hydrogels, the samples have to be covered with a thin layer of conducting material (typically gold or silver, but other choices are possible depending on the wanted magnification of the images) before the analysis. Magnification in SEM can be controlled over a range of up to 6 orders of magnitude from about 10 to 500,000 times. This is a powerful technique widely used to capture the 3D aspect of the hydrogels network, although, due to the high vacuum conditions needed for the experiments, the structure recorded is that of the collapsed state of the gel, not that of its swollen state.[132]

- **DSC and TGA**

These two techniques allow to obtain additional information about the network physical properties. DSC is a sensitive method to measure the polymers phase transitions as a function of temperature through the changes in heat capacity, allowing to identify the glass transition temperature, crystal structure and crystal transition temperature. In general this technique can be used to investigate the crystalline nature of the hydrogels and if different domains exist within the network, especially for those prepared by freezing-thawing processes, providing information also on the evolution of the system during the

swelling process.[142] TGA is a useful tool to evaluate the thermal stability of the system and its composition. The samples are usually heated to high temperature and then burned both in the presence or in the absence of oxygen, while the change in weight of the material is recorded. The shape of the graph and the presence of unburned residues allow to identify the presence and the amount of components different from the polymeric matrix (i.e. nanocomposites material) and the range of temperature for the application of the hydrogel.[143]

- **Biocompatibility Tests**

Hydrogels must be biocompatible and non-toxic in order to find application in the biomedical sector. A good parameter to first assess the biocompatibility of the material is its hydrophilicity (which can be determined by measuring the contact angle of the material with water), since usually higher levels of hydrophilicity are associated to greater levels of cells attachment[144] and better blood compatibility.[145] However, most of the polymers must also pass cytotoxicity and in-vivo toxicity tests before finding real application.[146] Biocompatibility tests consist in the evaluation of two different parameters, namely biosafety (the ability to induce an appropriate host response after the exposure to the material, not only systemic but also local, with absence of cytotoxicity, mutagenesis, and/or carcinogenesis of the natural tissue) and biofunctionality (defined as the ability of the material to perform the specific task for which it is intended, e.g. allow cells proliferation or migration). Evaluation of these two properties is usually performed on the final material, without taking into account the toxicity of the starting components; for this reason, various purification processes should be performed on the hydrogel, such as solvent washing or dialysis, in order to remove all residues of hazardous chemicals deriving from its synthesis. Indeed, most of the toxicity issues associated with hydrogels are actually related to the presence of unreacted monomers, oligomers and initiators that leach out during application.

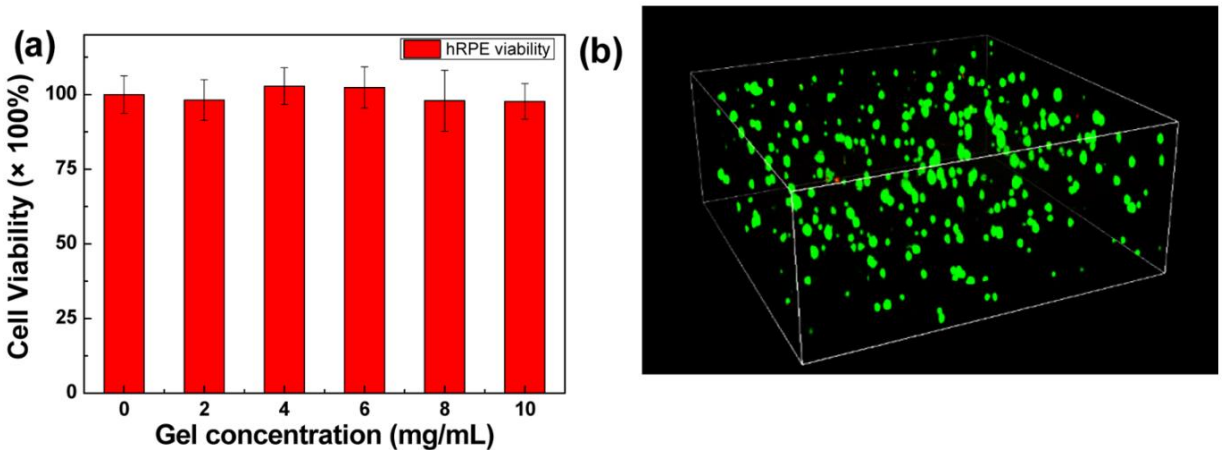

Figure 3.17 Examples of (a) cell viability test, printed in hydrogel after 48h incubation; (b) live/dead assay of cells embedded into the same matrix after 48h incubation, recorded with three-dimensional stacking confocal laser scanning microscopy (in green living cells, in red dead cells).[31]

In vitro tests (Figure 3.17) are the most common tool to carry out the initial biocompatibility test and to evaluate the cytotoxicity aspects of the material in the presence of living host cells. This kind of tests can be usually performed following two different procedures.[136b] The first method is a direct determination, in which the material whose biocompatibility has to be determined is placed in contact with the chosen host cells and then it is incubated for a determined period of time at fixed temperature. The subsequent determination of the cytotoxicity is carried out on the cells detached from the material. The second method is based on an indirect determination. The sample is kept in a suitable physiological solution (e.g. phosphonate buffer) and is then incubated for a fixed amount of time to allow the release

of any component from the material itself. The collected leachates are subsequently employed in the biocompatibility tests in the presence of the cells. Usually, cell viability and proliferation are determined from this kind of cytotoxicity tests. The procedure of a typical experiment requires the sterilization of the hydrogel before the start, followed by the seeding with the host cells. The material is then incubated for ≈ 1h to allow the first cell adhesion and, after that, the proper incubation begins with the addition of the culture media and the transfer of the systems into an incubator at a fixed temperature (usually 37°C). After the chosen amount of time, the cells are detached from the substrate and the cell viability and proliferation is visualized by microscopy or by carrying out specific colorimetric assay.[147] However, even if *in vitro* tests provide useful information about the biocompatibility and cytotoxicity of the material, the behavior of the system once moved from the simple interaction with cells to a real tissue can be strongly different. For this reason, *in vivo* tests in animals are always necessary when looking for an application on humans.

3.5. Aim of the work

As already discussed, stimuli-responsive hydrogels are very interesting systems with various potential applications. Depending on the stimulus employed, in fact, they have been used in many different sectors, from the biomedical area to the field of energy storage materials. Therefore, this entire field of research is extremely open to the development of more advanced systems, able to optimize efficiency or resolve practical problems compared to the existing options. We decided to focus on the development of hydrogels able to respond to two of the most fundamental and easy-to-apply stimuli, namely electricity and light.

The first part was focused onto the optimization of the introduction of several conductive polymers inside a particular hydrogel matrix which was never made conductive before. This hydrogel network can be synthetized by Aza-Michael reaction without the need of any other initiator and in mild reaction conditions, giving rise to an extremely versatile material due to its good tolerance towards other functional groups and easy exchangeability of its components. Investigating the possibility of introducing a conductive moiety inside this network could then broaden the use of this flexible matrix in the field of the stimuli-responsive hydrogels.

The second part regarded the development of a novel light-responsive hydrogel characterized by a tandem responsive system. Light is probably the most interesting stimulus due to its easy application and control over time and space. For this reason, this kind of systems have always attracted much attention due to the various application they can find. We decided to develop a particular system in which the light-responsiveness is granted by a chain effect between a photosensitive molecule and an oxidisable compound, which can lead to a change of its physical properties. We anticipated that carrying out this tandem process on a flexible hydrogel matrix could allow a simple and precise tuning of the network properties, opening the way to potential practical applications.

3.6. References

[1] (a) Seliktar, D. *Science* **2012**, *336*, 1124; (b) Buenger, D.; Topuz, F.; Groll, J. *Prog. Polym. Sci.* **2012**, *37*, 1678; (c) Lee, K.Y.; Mooney, D.J. *Chem. Rev.* **2001**, *101*, 1869.

[2] Wichterle, O.; Lim, D. *Nature* **1960**, *185*, 117.

[3] Ratner, B.D.; Hoffman, A.S. "*Synthetic hydrogels for biomedical applications*" in "*Hydrogels for Medical and Related Applications*", ACS Symposium Series, Vol. 31, **1976**.

[4] Lim, F.; Sun, A.M. *Science* **1980**, *210*, 908.

[5] Yannas, I.V.; Lee, E. *Proc. Natl. Acad. Sci. USA* **1989**, *86*, 933.

[6] Trigo, R.; Blanco, M.; Huerta, P.; Olmo, R.; Teijon, J. *Polym. Bull.* **1993**, *31*, 577.

[7] Xu, Z.; Li, J.; Zhou, H.; Jiang, X.; Yang, C.; Wang, F.; Pan, Y.; Li, N.; Li, X.; Shi, L.; Shi, X. *RSC Adv.* **2016**, *6*, 43626.

[8] Li, H.; Wang, D.Q.; Liu, B.L.; Gao, L.Z. *Colloids Surf. B Biointerfaces* **2004**, *33*, 85.

[9] (a) Arica, M.Y.; Bayramoglu, G. *Biochem. Eng. J.* **2004**, *20*, 73; (b) Jimenez, C.; Bartrol, J.; de Rooij, N.F.; Koudelka-Hep, M. *Anal. Chim. Acta* **1997**, *351*, 169.

[10] Ulijn, R.V. *J. Mater. Chem.* **2006**, *16*, 2217.

[11] Straccia, M.C.; Gomez d'Ayala, G.; Romano, I.; Laurienzo, P. *Carbohyd. Polym.* **2015**, *125*, 103.

[12] Pishko, M.V.; Revzin, A.; Simonian, A.L. *Sensors* **2002**, *2*, 79.

[13] Luo, Y.; Kirker, K.R.; Prestwich, G.D. *J. Control. Release* **2000**, *69*, 169.

[14] Poon, Y.F.; Cao, Y.; Zhu, Y.; Judeh, Z.M.; Chan-Park, M.B. *Biomacromolecules* **2009**, *10*, 2043.

[15] Hennink W.E.; van Nostrum, C.F. *Adv. Drug Deliv. Rev.* **2002**, *54*, 13.

[16] Ullah, F.; Bisyrul, M.; Othman, H.; Javed, F.; Ahmad, Z.; Akil, H. *Mat. Sci. Eng. C* **2015**, *57*, 414.

[17] (a) Li, Y.; Rodrigues, J.; Tomas, H. *Chem. Soc. Rev.* **2012**, *41*, 2193; (b) Yamaguchi, N.; Zhang, L.; Chae, B.S.; Palla, C.S.; Furst, E.M.; Kiick, K.L. *J. Am. Chem. Soc.* **2007**, *129*, 3040.

[18] Glowacki, J.; Mizuno, S. *Biopolymers* **2008**, *89*, 33.

[19] Sakai, S.; Hirose, K.; Taguchi, K.; Ogushi, Y.; Kawakami, K. *Biomaterials* **2009**, *30*, 3371.

[20] Sperinde, J.J.; Griffith, L.G. *Macromolecules* **2000**, *33*, 5476.

[21] Tae, G.; Kim, Y.J.; Choi, W.I.; Kim, M.; Stayton, P.S.; Hoffman, A.S. *Biomacromolecules* **2007**, *8*, 1979.

[22] Bhattarai, N.; Gunn, J.; Zhang, M.Q. *Adv. Drug Deliv. Rev.* **2010**, *62*, 83.

[23] Tan, H.P.; Ramirez, C.M.; Miljkovic, N.; Li, H.; Rubin, J.P.; Marra, K.G: *Biomaterials* **2009**, *30*, 6844.

[24] Jin, N.; Morin, E.A.; Henn, D.M.; Cao, Y.; Woodcock, J.W.; Tang, S.; He, W.; Zhao, B. *Biomacromolecules* **2013**, *14*, 2713.

[25] Gumera, C.; Rauck, B.; Wang, Y. *J. Mater. Chem.* **2011**, *21*, 7033.

[26] (a) Burdick, J.A.; Prestwich, G.D. *Adv. Mater.* **2011**, *23*, H41; (b) Xu, X.; Jha, A.K.; Harrington, D.A.; Farach-Carson, M.C.; Jia, X. *Soft Matter* **2012**, *8*, 3280.

[27] Sepideh, M.; Dashtebayaz, S.; Nourbakhsh, M.S. *Int. J. Polym. Mater.* PO **2018**, DOI: 10.1080/00914037.2018.1455680.

[28] (a) Fakhari, A.; Berkland, C. *Acta Biomater.* **2013**, *9*, 7081; (b) Price, R.D.; Berry, M.G.; Navsari, H.A. *J. Plast. Reconstr. AES* **2007**, *60*, 1110.

[29] Nuttelman, C.R.; Rice, M.A.; Rydholm, A.E.; Salinas, C.N.; Shah, D.N.; Anseth, K.S. *Prog. Polym. Sci.* **2008**, *33*, 167.

[30] Zhu, J.M. *Biomaterials* **2010**, *31*, 4639.

[31] Liu, K.; Zang, S.; Xue, R.; Yang, J.; Wang, L.; Huang, J.; Yan, Y. *ACS Appl. Mater. Interfaces* **2018**, *10*, 4530.

[32] Lutolf, M.P.; Hubbell, J.A. *Nat. Biotechnol.* **2005**, *23*, 47.

[33] Nicodemus, G.D.; Bryant, S.J. *Tissue Eng. Pt B-Rev.* **2008**, *14*, 149.

[34] (a) Drury, J.L.; Mooney, D.J. *Biomaterials* **2003**, *24*, 4337; (b) Place, E.S.; George, J.H.; Williams, C.K.; Stevens, M.M: *Chem. Soc. Rev.* **2009**, *38*, 1139.

[35] Malkoch, M.; Vestberg, R.; Gupta, N.; Mespouille, L.; Dubois, P.; Mason, A.F.; Hedrick, J.L.; Liao, Q.; Frank, C.W.; Kingsbury, K.; Hawker, C.J. *Chem. Commun.* **2006**, 2774.

[36] Lowe, S.B.; Tan, V.T.G.; Soeriyadi, A.H.; Davis, T.P.; Gooding, J.J: *Bioconjugate Chem.* **2014**, *25*, 1581.

[37] (a) Liu, S.Q.; Tian, Q.; Wang, L.; Hedrick, J.L.; Hui, J.H.; Yang, Y.Y.; Ee, P.L. *Macromol. Rapid Commun.* **2010**, *31*, 1148; (b) Yang, F.; Williams, C.G.; Wang, D.A.; Lee, H.; Manson, P.N.; Elisseeff, J. *Biomaterials* **2005**, *26*, 5991.

[38] Annabi, N.; Nichol, J.W.; Zhong, X.; Ji, C.; Koshy, S.; Khademhosseini, A.; Dehghani, F. *Tissue Eng. Pt B-Rev.* **2010**, *16*, 371

[39] Mart, R.J.; Osborne, R.D.; Stevens, M.M.; Ulijn, R.V. *Soft Matter* **2006**, *2*, 822.

[40] (a) Hoffman, A.S. *Adv. Drug Del. Rev.* **2002**, *54*, 3; (b) Perez, R.A.; Won, J-.E.; Knowles, J.C.; Kim, H-.W. *Adv. Drug Del. Rev.* **2013**, *65*, 471.

[41] Brocchini, S.; Godwin, A.; Balan, S.; Choi, J-.W.; Zloh, M.; Shaunak, S. *Adv. Drug Del. Rev.* **2008**, *60*, 3.

[42] Kidane, A.; Szabocsik, J.M.; Park, K. *Biomaterials* **1998**, *19*, 2051.

[43] (a) He, L.; Read, E.S.; Armes, S.P.; Adams, D.J. *Macromolecules* **2007**, *40*, 4429; (b) Ayhan, F.; Ozkan, S. *Drug Deliv.* **2007**, *14*, 433.

44 Jensen, B.E.B.; Dávila, I.; Zelikin, A.N. *J. Phys. Chem. B* **2016**, *120*, 5916.
45 Kamoun, E.A.; Chen, X.; Mohy Eldin, M.S.; Kenawy, E.R-.S. *Arab. J. Chem.* **2015**, *8*, 1.
46 Laftah, W.A.; Hashim, S.; Ibrahim, A.N. *Polym.-Plast. Technol.* **2011**, *50*, 1475.
47 Shi, Y.; Ma, C.; Peng, L.; Yu, G. *Adv. Funct. Mater.* **2015**, *25*, 1219.
48 Gulrez, S.K.H.; Al-Assaf, S.; Phillips, G.O. "Hydrogels: Methods of Preparation, Characterisation and Applications" in "Progress in Molecular and Environmental Bioengineering", IntechOpen, **2011**.
49 (a) Kuo, C.K.; Ma, P.X. *Biomaterials* **2001**, *22*, 511; (b) Maitra, J.; Shukla, V.K. *Am. J. Polym. Sci.* **2014**, *4*, 25.
50 a) Topuz, F.; Okay, O. *Biomacromolecules* **2009**, *10*, 2652; b) Trabbic-Carlson, K.; Setton, L.A.; Chilkoti, A. *Biomacromolecules* **2003**, *4*, 572.
51 Jagur-Grodzinski, J. *Polym. Adv. Technol.* **2010**, *21*, 27.
52 (a) Nguyen, K.T.; West, J.L. *Biomaterials* **2002**, *23*, 4307; (b) Jeon, O.; Powell, C.; Solorio, L.D.; Krebs, M.D.; Isberg, E. *J. Control. Release* **2011**, *154*, 258.
53 (a) Ossipov, D.A.; Hilborn, J. *Macromolecules* **2006**, *39*, 1709; (b) Xu, J.; Filion, T.M.; Prifti, F.; Song, J. *Chem. Asian J.* **2011**, *6*, 2730.
54 (a) Cai, S.; Liu, Y.; Shu, X.Z.; Prestwich, G.D. *Biomaterials* **2005**, *26*, 6054; (b) Pritchard, C.D.; O'Shea, T.M.; Siegwart, D.J.; Calo, E.; Anderson, D.G.; Reynolds, F.M.; Thomas, J.A.; Slotkin, J.R.; Woodard, E.J.; Langer, R. *Biomaterials* **2011**, *32*, 587.
55 Koutroumanis, K.P.; Avgoustakis, K.; Bikiaris, D. *Carbohydr. Polym.* **2010**, *82*, 181.
56 (a) Jin, R.; Hiemstra, C.; Zhong, Z.; Feijen, J. *Biomaterials* **2007**, *28*, 2791; (b) Bae, J.W.; Choi, J.H.; Lee, Y.; Park, K.D. *J. Tissue Eng. Regen. Med.* **2015**, *9*, 1225.
57 Sakloetsakun, D.; Hombach, J.M.R.; Bernkop-Schnurch, A. *Biomaterials* **2009**, *30*, 6151.
58 Hunt, J.A.; Chen, R.; van Veen, T.; Bryan, N. *J. Mater. Chem. B* **2014**, *2*, 5319.
59 Lutz, J.F.; Zarafshani, Z. *Adv. Drug. Del. Rev.* **2008**, *60*, 958.
60 Nguyen, Q.V.; Huynh, D.P.; Park, J.H.; Lee, D.S. *Eur. Polym. J.* **2015**, *72*, 602.
61 (a) Clark, M.; Kiser, P. *Polym. Int.* **2009**, *58*, 1190; (b) Agard, N.J.; Prescher, J.A.; Bertozzi, C.R. *J. Am .Chem. Soc.* **2004**, *126*, 15046.
62 Ferruti, P.; Bianchi, S.; Ranucci, E.; Chiellini, F.; Caruso, V. *Macromol. Biosci.* **2005**, 613.
63 Yu, F.; Cao, X.; Du, J.; Wang, G.; Chen, X. *ACS Appl. Mater. Inter.* **2015**, *7*, 24023.
64 Teixeira, L.S.M.; Feijen, J.; van Blitterswijk, C.A.; Dijkstra, P.J.; Karperien, M. *Biomaterials* **2012**, *33*, 1281.
65 Kolb, H.C.; Finn, M.G.; Sharpless, K.B. *Angew. Chem. Int. Ed* **2001**, *40*, 2004.
66 Jiang, Y.; Chen, J.; Deng, C.; Suuronen, E.J.; Zhong, Z. *Biomaterials* **2014**, *35*, 4969.
67 Apostolides, D.E.; Patrickios, C.S. *Polym. Int.* **2018**, *67*, 627.
68 Appel, E.A.; del Barrio, J.; Loh, X.J.; Scherman, O.A. *Chem. Soc. Rev.* **2012**, *41*, 6195.
69 Habibi, Y.; Lucia, L.A.; Rojas, O.J. *Chem. Rev.* **2010**, *110*, 3479.
70 Zhao, Y.-L.; Stoddart, J.F. *Langmuir* **2009**, *25*, 8442.
71 (a) Kumpfer, J.R.; Rowan, S.J. *J. Am. Chem. Soc.* **2011**, *133*, 12866; (b) Beck, B.J.; Rowan, S.J. *J. Am. Chem. Soc.* **2003**, *46*, 13922.
72 (a) Wang, Q.; Mynar, J.L.; Yoshida, M.; Lee, E.; Lee, M.; Okuro, K.; Kinbara, K.; Aida, T. *Nature* **2010**, *463*, 339; (b) Mynar, J.L.; Aida, T. *Nature* **2008**, *451*, 895.
73 (a) Reinhoudt, D.; Atwood, J.; Lehn, J-.M. "*Comprehensive Supramolecular Chemistry*", Pergamon Press, Oxford, **1996**; (b) Seiffert, S.; Sprakel, J. *Chem. Soc. Rev.* **2012**, *41*, 909.
74 Chung, H.J.; Lee, Y.; Park, T.G. *J. Control. Release* **2008**, *127*, 22.
75 Qiu, Y.; Park, K. *Adv. Drug. Del. Rev.* **2001**, *53*, 321.
76 Hennink, W.E.; van Nostrum, C.F. *Adv. Drug Del. Rev.* **2012**, *64*, 223.
77 Deshmukh, S.A.; Kamath, G.; Suthar, K.J.; Mancini, D.C.; Sankaranarayanan, S.K.R.S. *Soft Matter* **2014**, *10*, 1462.
78 Zhang, X.-Z.; Chu, C.-C. *Chem. Commun.* **2004**, 350.
79 Fatin-Rouge, N.; Milon, A.; Buffle, J.; Goulet, R.R.; Tessier, A. *J. Phys. Chem. B* **2003**, *107*, 12126.
80 (a) Loo, Y.; Zhang, S.; Hauser, C.A.E. *Biotechnol. Adv.* **2012**, *30*, 593; (b) Xu, C.; Kopeček, J. *Polym. Bull.* **2007**, *58*, 53.
81 Ahmed, E.M. *J. Adv. Res.* **2015**, *6*, 105.
82 Yang, L.; Chu, J.S.; Fix, J.A. *Int. J. Pharm.* **2002**, *235*, 1.
83 Fiorini, F.; Prasetyanto, E.A.; Taraballi, F.; Pandolfi, L.; Monroy, F.; López-Montero, I.; Tasciotti, E.; De Cola, L. *Small* **2016**, *12*, 4881.
84 Chen, Q.; Chen, H.; Zhua, L.; Zheng, J. *J. Mater. Chem. B* **2015**, *3*, 3654.
85 (a) Maolin, Z.; Jun, L.; Min, Y.; Hongfei, H. *Radiat. Phys. Chem.* **2000**, *58*, 397; (b) Hacker, M.C.; Mikos, A.G. "*Synthetic polymers, principles of regenerative medicine*" 2nd ed., **2011**, pp. 587–622.
86 (a) Lin, Z.; Qiang, C.; Kun, X. *Prog. Chem.* **2014**, *26*, 1032; (b) Gong, J.P. *Soft Matter* **2010**, *6*, 2583.
87 Gong, J.P.; Katsuyama, Y.; Kurokawa, T.; Osada, Y. *Adv. Mater.* **2003**, *15*, 1155.
88 (a) Simha, N.; Carlson, C.; Lewis, J. *J. Mater. Sci.-Mater. M.* **2004**, *15*, 631; (b) Chen, Y.; Dong, K.; Liu, Z.; Xu, F. *Sci. China Technol. Sc.* **2012**, *55*, 2241.
89 Hu, J.; Hiwatashi, K.; Kurokawa, T.; Liang, S.M.; Wu, Z.L.; Gong, J.P. *Macromolecules* **2011**, *44*, 7775.

90 Nakajima, T.; Furukawa, H.; Tanaka, Y.; Kurokawa, T.; Gong, J.P. *J. Polym. Sci. Pol. Phys.* **2011**, *49*, 1246.

91 Waters, D.J.; Engberg, K.; Parke-Houben, R.; Ta, C.N.; Jackson, A.J.; Toney, M.F.; Frank, C.W. *Macromolecules* **2011**, *44*, 5776.

92 Wang, X.; Wang, H.; Brown, H.R. *Soft Matter* **2011**, *7*, 211.

93 Yang, W.; Furukawa, H.; Gong, J.P. *Adv. Mater.* **2008**, *20*, 4499.

94 Haque, A.; Kurokawa, T.; Kamita, G.; Gong, J.P. *Macromolecules*, **2011**, *44*, 8916.

95 (a) Nakajima, T.; Sato, H.; Zhao, Y.; Kawahara, S.; Kurokawa, T.; Sugahara, K.; Gong, J.P. *Adv. Funct. Mater.* **2012**, *22*, 4426; (b) Nakajima, T.; Fukuda, Y.; Kurokawa, T.; Sakai, T.; Chung, U-.I.; Gong, J.P. *ACS Macro Lett.* **2013**, *2*, 518.

96 Chen, Q.; Zhu, L.; Zhao, C.; Wang, Q.; Zheng, J. *Adv. Mater.* **2013**, *25*, 4171.

97 Muroi, H.; Hidema, R.; Gong, J.P.; Furukawa, H. *JSME Int. J. A-Solid M.* **2013**, *7*, 163.

98 Nakajima, T.; Takedomi, N.; Kurokawa, T.; Furukawa, H.; Gong, J.P. *Polym. Chem.* **2010**, *1*, 693.

99 (a) Tsukeshiba, H.; Huang, M.; Na, Y-.H.; Kurokawa, T.; Kuwabara, R.; Tanaka, T.; Furukawa, H.; Osada, Y.; Gong, J.P. *J. Phys. Chem. B* **2005**, *109*, 16304; (b) Ahmed, S.; Nakajima, T.; Kurokawa, T.; Anamul Haque, M.; Gong, J.P. *Polymer* **2014**, *55*, 914.

100 Nakajima, T.; Tanaka, Y.; Furukawa, H.; Kurokawa, T.; Gong, J.P. *Kobunshi Ronbunshu* **2008**, *65*, 707.

101 (a) Gaharwar, A.K.; Peppas, N.A.; Khademhosseini, A. *Biotechnol. Bioeng.* **2014**, *111*, 441; (b) F. Song, X. Li, Q. Wang, L. Liao, C. Zhang, J. Biomed. Nanotechnol. 2015, 11, 40

102 H. Sato, H. Ohtani, R. Harada, S. Tsuge, M. Kato, A. Usuki, Polym. J 2006, 38, 171

103 Merino, S.; Martín, C.; Kostarelos, K.; Prato, M.; Vázquez, E. *ACS Nano* **2015**, *9*, 4686.

104 Oliveira, M.; Machado, A.V. "*Nanocomposites: Synthesis, Characterization and Applications",* N. Publishers, **2013**.

105 (a) Supová, M.; Martynková, G.; Barabaszová, K. *Sci. Adv. Mater.* **2011**, *3*, 1; (b) Rong, M.Z.; Zhang, M.Q.; Ruan, W.H. *Mater. Sci. Technol.* **2006**, *22*, 787.

106 Peppas, N.A.; Hilt, J.Z.; Thomas, J.B. "*Nanotechnology in Therapeutics: Current Technology and Applications"*, Horizon Bioscience, **2007**.

107 Paranhos, C.M.; Soares, B.G.; Oliveira, R.N.; Pessan, L.A. *Macromol. Mater. Eng.* **2007**, *292*, 620.

108 Satarkar, N.S.; Hilt, J.Z. *J. Control. Release* **2008**, *130*, 246.

109 Tokarev, I.; Tokareva, I.; Minko, S. *Adv. Mater.* **2008**, *20*, 2730.

110 Wang, C.; Flynn, N.T.; Langer, R. *Adv. Mater.* **2004**, *16*, 1074.

111 Ko, D.Y.; Shinde, U.P.; Yeon, B.; Jeong, B. *Prog. Polym. Sci.* **2013**, *38,* 672.

112 Daley, W.P.; Peters, S.B.; Larsen, M. *J. Cell Sci.* **2008**, *121*, 255.

113 Lutolf, M.P.; Lauer-Fields, J.L.; Schmoekel, H.G.; Metters, A.T.; Weber, F.E.; Fields, G.B.; Hubbell, J.A. *Proc. Natl. Acad. Sci.* USA **2003**, *100*, 5413.

114 (a) Bromberg, L.; Temchenko, M.; Alakhov, V.; Hatton, T.A. *Langmuir* **2005**, *21*, 1590; (b) Zhang, J.; Skardal, A.; Prestwich, G.D. *Biomaterials* **2008**, *29*, 4521.

115 Choi, B.; Loh, X.J.; Tan, A.; Loh, C.K.; Ye, E.; Joo, M.K.; Jeong, B. "*In-Situ Gelling Polymers: For Biomedical Applications*", Springer Singapore, **2015**.

116 Singh, H.; Nair, L.S. "*Integrated Biomaterials for Biomedical Technology*", John Wiley & Sons, **2012**.

117 Patenaude, M.; Smeets, N.M.B.; Hoare, T. *Macromol. Rapid Comm.* **2014**, *35*, 598.

118 Nguyen, M.K.; Lee, D.S. *Macromol. Biosci.* **2010**, *10*, 563.

119 Annabi, N.; Tamayol, A.; Uquillas, J.A.; Akbari, M.; Bertassoni, L.E.; Cha, C.; Camci-Unal, G.; Dokmeci, M.R.; Peppas, N.A.; Khademhosseini, A. *Adv. Mater.* **2014**, *26*, 85

120 (a) Peppas, N.; Bures, P.; Leobandung, W.; Ichikawa, H. *Eur. J. Pharm. Biopharm.* **2000**, *50*; 27; (b) Gil, S.; Hudson, S.M. *Prog. Polym. Sci.* **2004**, *29*, 1173.

121 (a) Koettinga, M.C.; Petersa, J.T.; Steichenb, S.D.; Peppas, N.A. *Mater. Sci. Eng. R* **2015**, *93*, 1; (b) Echeverria, C.; Fernandes, S.N.; Godinho, M.H.; Borges, J.P.; Soares, P.I.P. *Gels* **2018**, *4*, 54.

122 Sood, N.; Bhardwaj, A.; Mehta, S.; Mehta, A. *Drug. Deliv.* **2016**, *23*, 748.

123 Patel, A.; Mequanint, K. "*Hydrogel biomaterials, Biomedical Engineering - Frontiers and Challenges",* InTech, **2011**.

124 (a) Jianqi, F.; Lixia, G. *Eur. Polym. J.* **2002**, *38*, 1653; (b) Li, J.; Li, X.; Ni, X.; Wang, X.; Li, H.; Leong, K.W. *Biomaterials* **2006**, *27*, 4132.

125 (a) Gupta, P.; Vermani, K.; Garg, S. *Drug Discov. Today* **2002**, *7*, 569; (b) Baker, J.P.; Stephens, D.R.; Blanch, H.W.; Prausnitz, J.M. *Macromolecules* **1992**, *25*, 1955.

126 Richter, A. "*Hydrogels for actuators*" in "*Hydrogel Sensors and Actuators*", Springer, **2010**.

127 Serra, L.; Doménech, J.; Peppas, N.A. *Biomaterials* **2006**, *27*, 5440.

128 Behl, M.; Zotzmann, J.; Lendlein, A. "*Shape-memory polymers and shape-changing polymers*" in "*Shape-Memory Polymers*", Springer, **2010**.

129 Wang, Y.; Xu, S.; Chen, T.; Guo, H.; Liu, Q.; Ye, B.; Zhang, Z.; He, Z.; Cao, S. *Polym. Chem.* **2010**, *1*, 1048.

130 Qiu, Y.; Park, K. *Adv. Drug Deliv. Rev.* **2012**, *64*, 49.

131 Bayat, N.; Zhang, Y.; Falabella, P.; Menefee, R.; Whalen III, J.J.; Humayun, M.S.; Thompson, M.E. *Sci. Transl. Med.* **2017**, *9*, eaan3879.

132 (a) Sirousazar, M.; Forough, M.; Farhadi, K.; Shaabani, Y.; Molaei, R. "*Hydrogels: Properties, Preparation, Characterization and Biomedical, Applications in Tissue Engineering, Drug, Delivery and Wound Care*" in "*Advanced Healthcare Materials*", Scrivener Publishing, **2014**; (b) Shetye, S.P.; Godbole, A.; Bhilegaokar, S.; Gajare, P. *Ijrm Human*, **2015**, *1*, 47.

133 (a) Amsden, B. *Macromolecules* **1998**, *31*, 8382; (b) McNeill, M.E.; Graham, N.B. *J. Biomater. Sci. Polym.* **1993**, *4*, 305.

134 De, S.K.; Aluru, N.R.; Johnson, B.; Crone, W.C.; Beebe, D.J.; Moore, J. *J. Microelectromech S.* **2002**, *11*, 544.

135 Cho, E.C.; Lee, J.; Cho, K. *Macromolecules* **2003**, *36*, 9929.

136 (a) Barth, H.G.; Pasch, H. "*Rheology Essentials of Foods and Cosmetics*", Springer, Berlin, **2005**, pp. 125; (b) Pal, K.; Banthia A.K.; Majumdar, D.K. *Des. Monomers Polym.* **2009**, *12*, 197.

137 (a) Yang, S.; Leong, K.F.; Du, Z.; Chua, C.K. *Tissue Eng.* **2001**, *7*, 679; (b) Al-Abboodi, A.; Fu, J.; Doran, P.M.; Tan, T.T.Y.; Chan, P.P.Y. *Adv. Healthc. Mater.* **2014**, *3*, 725; (c) Reisch, A.; Tirado, P.; Roger, E.; Boulmedais, F.; Collin, D.; Voegel, J-.C.; Frisch, B.; Schaaf, P.; Schlenoff, J.B. *Adv. Funct. Mater.* **2013**, *23*, 673.

138 Weng, L.; Chen, X.; Chen, W. *Biomacromolecules* **2007**, *8*, 1109.

139 (a) Gupta, N.V.; Shivakumar, H.G. Iran. J. Pharm. Res. **2012**, *11*, 481; (b) Feng, D.; Bai, B.; Wang, H.; Suo, Y.; *New J. Chem.* **2016**, *40*, 3350.

140 Chalmers, J.M.; Grifths, P.R. "*Handbook of vibrational spectroscopy*" Vol. 2, John Wiley & Sons, Chichester, **2002.**

141 Pourjavadi, A.; Kurdtabar, M. *Eur. Polym. J.* **2007**, *43*, 877.

142 (a) Hassan, C.M.; Peppas, N.A. *Macromolecules* **2000**, *33*, 2472; (b) Castelli, F.; Sarpietro, M.G.; Micieli, D.; Ottimo, S.; Pitarresi, G.; Tripodo, G.; Carlisi, B.; Giammona, G. *Eur. J. Pharm. Sci.* **2008**, *35*, 76.

143 Rusu, A.G.; Popa, M.I.; Lisa, G.; Vereştiu, L. *Thermochim. Acta* **2015**, *613*, 28.

144 van Wachem, P.B.; Hogt, A.H.; Beugeling, T.; Feyen, J.; Bantjies, A.; Detmers, J.P.; van Aken, A.W.G. *Biomaterials* **1987**, *8*, 323.

145 Hench , L.L.; Jones, J.R. "*Biomaterials, Artificial Organs and Tissue Engineering*", Woodhead, Cambridge **2005**.

146 Das, N. *Int. J. Pharm. Pharm. Sci.* **2013**, *5*, 112.

147 Danielsson, D.; Ruault, S.; Simonet, M.; Neuenschwander, P.; Freya, P. *Biomaterials* **2006**, *27*, 1410.

Chapter 4

Conductive Hydrogels

4.1. Background

In this chapter the studies carried out for developing new conductive hydrogels will be reported. Electroconductive hydrogels are a class of stimuli-responsive hydrogels which bring together the redox switching and electrical properties of the inherently conductive electroactive component with the facile small molecule transport, high hydration levels, tunable physical properties and biocompatibility of cross-linked hydrogels.[1] In recent year these hybrid materials became very popular in the field of material sciences, due to the wide range of possible applications derived from the features of both class of materials they are derived. For instance, as it happens for non-conductive hydrogels they can be employed in the field of the energy storage devices or as electrodes in novel sensors development, while as conductive materials could be easily used for biological applications providing to solve the issue of their inherent toxicity. Conductive hydrogels are generally constituted by two different parts, an hydrogel matrix, either chemically or physically crosslinked, and a conductive material, which could be represented by conductive polymers, carbon nanotubes[2], graphene or graphene oxide[3] and metal nanoparticles.[4] Of course the final properties of the hybrid material depend from the characteristics of starting systems employed, from how they are synthetized and from the interactions they could establish between themselves, thus, also the choice of the electroconductive system used greatly change the properties of the final material. Some particular features can be controlled, i.e. magnetic[5] and antibacterial properties[6] can be implemented by incorporation of metal nanoparticles or high capacitance and electrochemical stability can be obtained by using graphene.[7] Another interesting feature of conductive polymers is that to allow altering of their optical and electronic properties by chemical modification of their backbone or by changes into their polymerization process.

4.1.1. Conductive Polymers

Conductive polymers are a family of highly conjugated polymers possessing spatially extended π-bonding that confers the feature to merge the positive properties of metals and conventional polymers (the ability to conduct charge, great electrical and optical properties) with flexibility in processing and ease of synthesis.[8] These materials display also a controllable switching of their electrical and optical properties and the possibility to have these properties altered by change of variables such as temperature, humidity, gas/vapor composition, medium ionic strength, pH. These factor in fact could alter the conjugated π-system of the polymer, which is the base of their conductive properties due to the possible delocalization of the electrons along the entire polymeric chain.[9] It is also possible to further enhance their electronic properties by performing a particular process called “doping”, which is able to increase the charge carriers amount along the entire length of the polymer. This process was accomplished for the first time performing the oxidation of polyacetilene with iodine vapor (Figure 4.1), leading to an increment of 10-million fold of the conductivity of the material.[10]

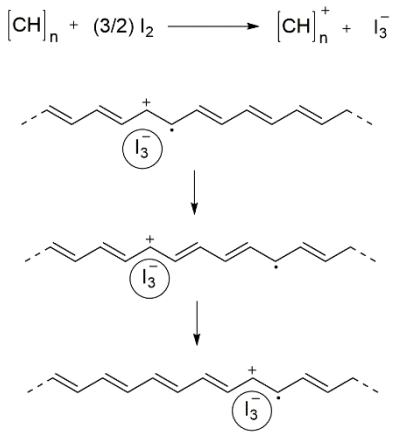

Figure 4.1 Doping process on polyacetilene.

This objective could be achieved in different ways: indeed, depending from the nature of the material, in analogy to the semiconductors, "n-type" (reduction) and "p-type" (oxidation) doping could be accomplished.[11] In the case of the n-type doping, an electron is introduced in the polymeric network and acts as charge carrier, while in the p-type doping is the vacancy created by the removal of an electron to undertake the role. These kind of modifications create local distortions of the crystal lattice of the network, disrupting the stable backbone and allowing the freely move of the above-mentioned charge carriers upon the application of an external field[12] (Figure 4.2). The conductivity is then strongly dependent from the mobility of these charge carriers and it could occur both intra and inter chain.[11a] On the other hand, as can be explained in Figure 4.2, the presence of structural disorder in the conjugated network, along with the packing of the polymeric chains, could strongly reduce the overall conductivity value due to the possibility of charge carriers hoping between the different chains.

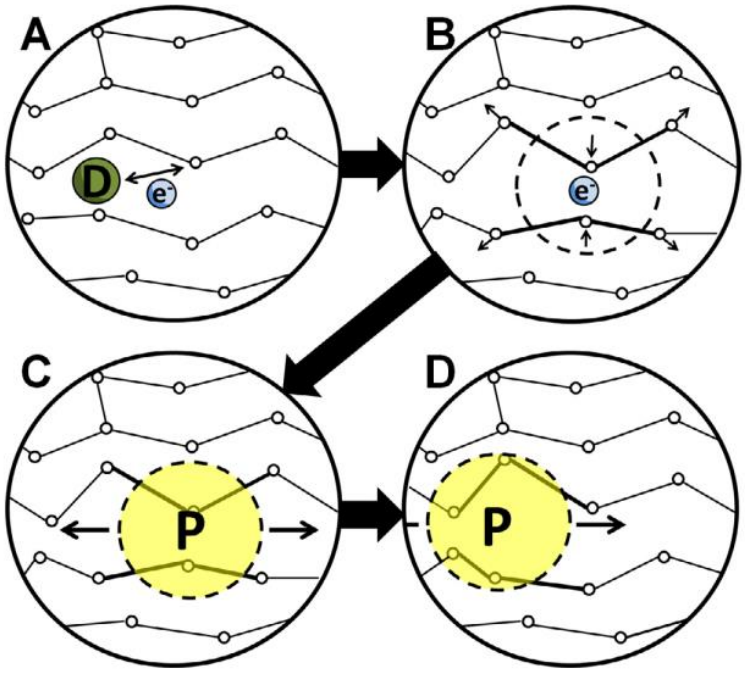

Figure 4.2 Simplified explanation of the electrical conductivity in conductive polymers. (a) The dopant create the charge carrier by removing/adding an electron; (b) the crystal lattice distortion is created as the most energetically favorable situation to stabilize the charge carrier; (c) a charge surrounded by a distortion is known as polaron and (d) it is able to travel along the polymer chain, allowing the electrical conduction.[13]

The doping process can be carried out using different procedures, both chemically or electrochemically or *via* photodoping.[14] In all the cases it is a reversible process: if an electric potential is applied through the polymer, it will cause the dopant to leave or re-enter into the polymer network, switching between its two different redox states, conductive and insulating.[14b,15] Dopants could be separated in two different categories depending from their size: small (i.e. Cl^-) and large (i.e. polystirenesulfonate, PSS) dopants, which then could differently affect the polymer structural and electrochemical properties.[14a,16] For example, while large dopants are more integrated into the polymer network and rarely leaking out, leading to an increased electrochemical stability,[16b,17] small dopants can easily leave and re-enter into the material with electrical stimulation, the latter property forming the base for drug release devices.[14a,18]

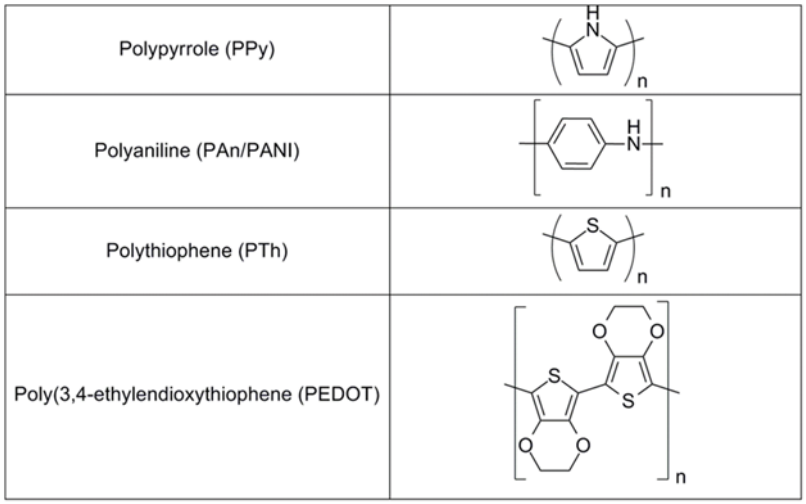

Figure 4.3 Most common polymeric materials employed in conductive hydrogels.

The possibility to modify the monomers by introduction of some functional groups is another interesting feature of this kind of materials. This can be an easy approach to allow direct covalent bond formation between the polymer and some interesting molecule[1] (such as a compound to be released) or a support.[19] For these reason, along with their good stability and high conductance, polyheterocycles have emerged as one of the most promising "families" of conductive polymers (Figure 4.3).

- **Polypyrrole (PPy)**

Polypirrole is probably the most studied conductive polymer because of a range of excellent qualities and stimuli-responsive properties,[20] such as good biocompatibility,[21] good chemical stability in air and water[22] and reasonably high conductivity in physiological conditions.[21,23] Polypirrole can be easily and flexibly synthesized at room temperature in a wide range of solvents, including water, with a large surface area, different porosities[21,23] and shapes[24] (i.e. fibers or nanotubes); furthermore, it can be easily modified to be more suitable for specific applications.[25] PPy is also a stimulus responsive material, allowing the dynamic control of its properties by the application of an electrical potential.[20b] The principal drawbacks of such material are that it cannot be processed further once synthetized,[16a] it has a non-thermoplastic behavior,[22] poor mechanical properties[26] (rigid, brittle) and it is completely insoluble. Nowadays it is employed in various field, from the electronic engineering[24] to the biomedical area,[16a] passing through specific applications as biomaterial.[27]

- **Polyaniline (PAn)**

The second most promising conductive polymer after PPy is polyaniline (PAn).[28] Such material exhibit many advantages, such as an easy synthesis, a low cost, a good environmental stability, and the ability to be electrically switched between its conductive and resistive states.[29] It can be found in one of three idealized oxidation states, depending from the polymerization conditions, which affect its conductivity: the fully oxidized pernigraniline base, half-oxidized emeraldine base and fully reduced leucoemeraldine base (Figure 4.4).[16a,28] The partially oxidized structure, the emeraldine, is in the most stable and conductive of the three states of the physical mixture used to obtain PAn. The other two states exhibit low conductivity values, however it can represent an advantage due to the ability to be electrically switched between its conductive and resistive states.[29b] Polymerization of PAn is not easy to perform and requires a stoichiometric amount of oxidant and acidic conditions to be able to achieve the synthesis in its most conductive form.

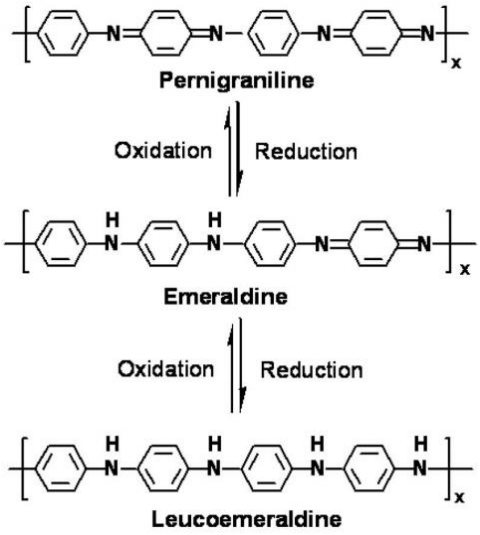

Figure 4.4 PAn molecular structure in its different oxidation states.[30]

PAn is also the only conductive polymer with electronic properties which can be regulated by protonation or charge transfer doping. Then, the control of the magnetic,[31] electrical[32] and physical[33] properties achievable for this polymer, makes PAn suitable to be employed on different applications, such as pH switching electrical conducting biomaterials,[34] electrically active redox biopolymers and matrixes for nanocomposite conductive polymers preparation.[35,36] Unfortunately, its low processability, lack of flexibility and non-biodegradability, along with the tendency to cause chronic inflammation once implanted,[15,29b] limit its use for biological applications.

- **Polythiophene Derivatives (PTh and PEDOT)**

The third class of interesting conductive polymers is mainly composed by polythiophene (PTh) and poly(3,4-ethylenedioxythiophene) (PEDOT). PTh is characterized by electronic stability and high electrical conductivity (it can reach ≈ 100 S cm^{-1}), which can be modified by the kind of dopant employed and the polymerization procedure used.[37] For these reasons, it has been intensively studied. For example, the effect of the length of the conjugated sequences on conductivity was evaluated and showing that oligomers consisting of 11 thiophene units have conductivity similar to that of higher molecular weight polythiophene.[38] Compared to PTh, PEDOT has another heterocyclic ring fused onto the position 3- and 4- of each thiophene ring (Figure 4.3), which greatly improve its electronic properties by lowering its band gap, its reduction and oxidation potential[39] and grant a good electrical, chemical

and environmental stability.[40] Furthermore, this substitution also confer to PEDOT better conductivity and thermal stability than PPy.[28,40] Another interesting characteristic of PEDOT is its ability to establish an electronic interaction with neurons on their surface and for this reason it finds applications in biosensing and bioengineering applications,[41] despite it lacks chemical functionalities able to covalently bind biological molecules. PTh and PEDOT can be synthetized both electrochemically and chemically. In particular, the electrochemical polymerization occurs with the deposition of a film of polymer on an electrode, resulting in the possibility to obtain also thin layer of conducting material. In both cases, after the synthesis any isolation of purification is required, even if side decomposition processes can always occur.

4.1.2. Conductive Hydrogels Synthesis

Many routes have been proposed for the synthesis of conductive hydrogels, but usually these materials have been produced as combinations of two separated phases created by each component. The most common procedures are depicted in Scheme 4.1 and are defined by their fabrication routes:

- Templated conductive hydrogels (Scheme 4.1a)
- Deposition of conductive polymers inside a pre-existing hydrogel matrix (Scheme 4.1b)
- Pre-mixing of all the precursors and then synthesis of the conductive hydrogel either with one or two polymerization steps (Scheme 4.1c)

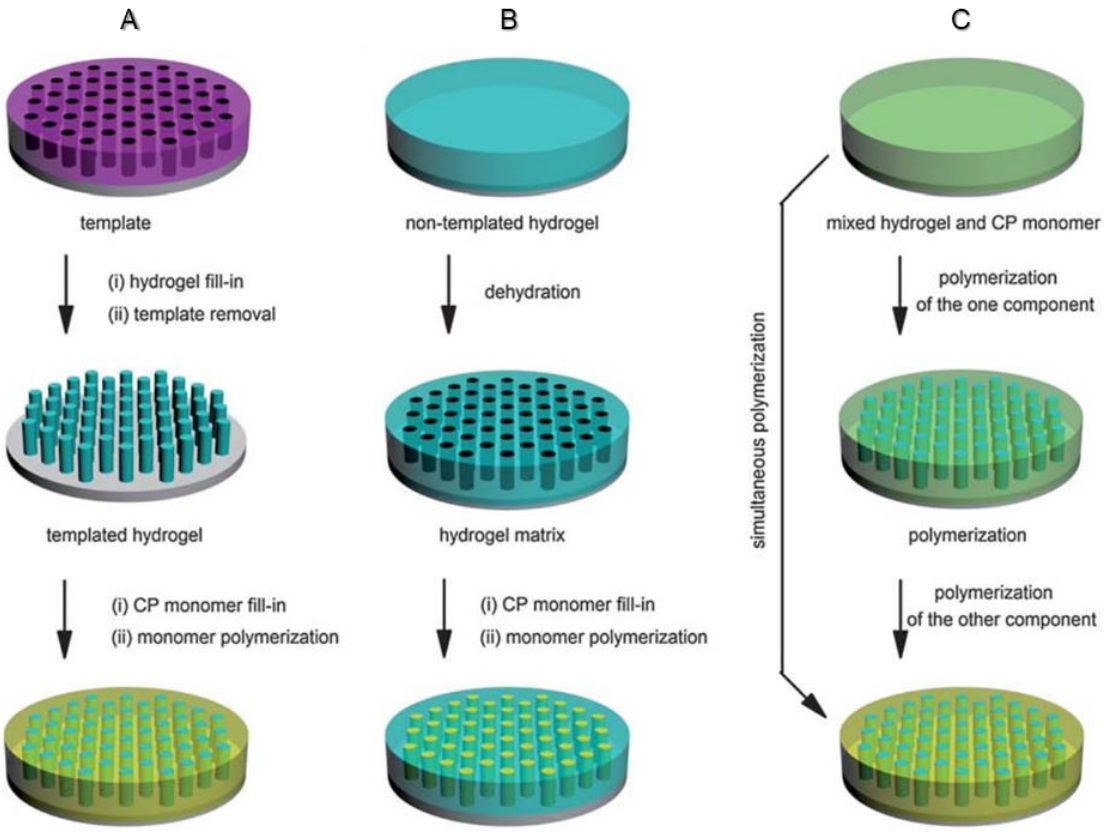

Scheme 4.1 Representation of the most common procedures for the synthesis of conductive hydrogels: (a) templated conductive hydrogel, (b) conductive polymer deposed within a pre-existing hydrogel matrix and (c) conductive hydrogel formed from mixed precursors, either simultaneously or in a two-step process.[42]

The first two routes (Scheme 4.1a and b) are extremely similar and differ only for the inherent structure of the hydrogel matrix employed. The electronic properties of conductive polymers usually improve by increasing surface area. Then, fabrication using a micro or nanostructured template gel matrix can have a great influence on the conductive of the material because with these procedures the surface area of conductive polymer synthetized inside the matrix can be significantly increased. Nonetheless, the polymerization of the conductive moiety within the confined area of a nanostructured template can also provide a huge control over the structure and the morphology of the network.[43] In both cases the dry hydrogel matrixes are swelled again into a solution of the conductive polymer monomer and, when the absorption reached its maximum value, the polymerization of the conductive moiety take place. Another alternative, even if less common if compared to the other two procedures already described, is the fabrication of the conductive hydrogels from a mixed precursors (Scheme 4.1c). In this method, the hydrogel and conductive polymer precursors are placed in the same vessel and then polymerized either together or in two different moments. The advantage of this procedure is the possibility to establish a better interaction between the two different network. It is particularly efficient when the two polymers could be synthetized using the same conditions.[44]

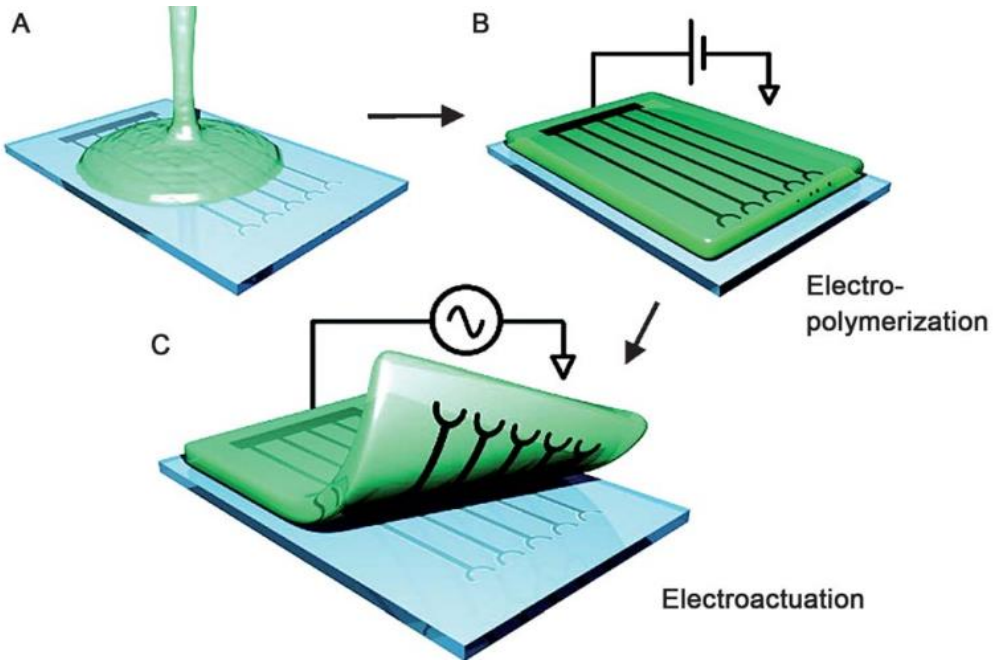

Figure 4.5 Example of the procedure for obtaining micropatterned electrodes from the electropolymerization of PEDOT.[47]

Finally, the polymerization of the conductive part can be carried out both by application of electrical charge or by exposition to a oxidizing agent. Even if the chemical method would be preferred, being more general and viable for almost all the conductive polymers, unfortunately the conductivities obtained using this procedure have always been lower than that recorded for materials obtained with the electrochemical method.[45] Additionally, the conductivity of the polymers created by chemical oxidation is known to be extremely dependent from the choice and purity of the solvent, the oxidant, the relative concentration of the reagents, reaction time, temperature, etc., and that make the synthesis difficult to reproduce.[45,46] On the contrary, the electrochemical synthesis allows the complete control of the polymerization process, making possible also to obtain micropatterned highly conductive hydrogels.[47]

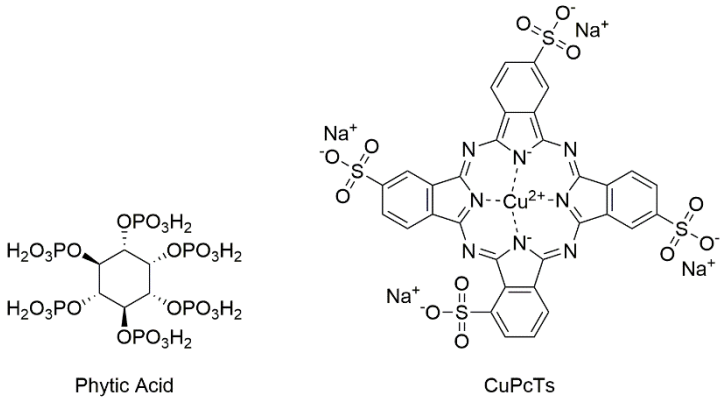

Figure 4.6 Novel crosslinkers employed in the synthesis of highly conductive hydrogels.

The main drawback of this method is that it usually result in gel composites that consist of both conductive and nonconductive components, reducing the overall conductivity of the resulting hydrogels. Recently an alternative procedure has been developed which allows to obtain conductive hydrogels composed only by a singular conductive network, without insulating part. Molecules with multiple functional groups, such as phytic acid and copper phthalocyanine-3,4',4",4‴-tetrasulfonic acid tetrasodium salt (CuPcTs, both in Figure 4.6), can in fact cross-link the conductive polymer chains without the need of any other support matrix, directly leading to the formation of a conductive hydrogel.[48] Basically, each of the crosslinker molecules can react with more than one conductive polymer chain by protonation of the nitrogen moieties and through electrostatic interactions, thus acting both as cross-linkers and dopant compounds. Nevertheless, these crosslinker molecules provide also the hydrophilicity which would be extremely reduced in a network only composed by conductive polymer chains. The conductive hydrogels synthetized with this procedure exhibit high electrical and ionic conductivities, due to the construction of a heavily doped and interconnected polymer network suitable for electron transport and a hierarchically porous structure suitable for ion diffusion (Figure 4.7a). Furthermore, their chemical and physical properties can be easily tuned by changing the cross-linker used in the synthesis and the reaction conditions. For example, in Figure 4.7b is reported PPy-hydrogel with an interconnected fiber structure, synthesized using CuPcTs as crosslinker,[49] while in Figure 4.7c is reported an hollow-sphere microstructured PPy-hydrogel obtained by interfacial synthesis still using phytic acid, and adjusting the ratio between crosslinker and polymer monomers.[50]

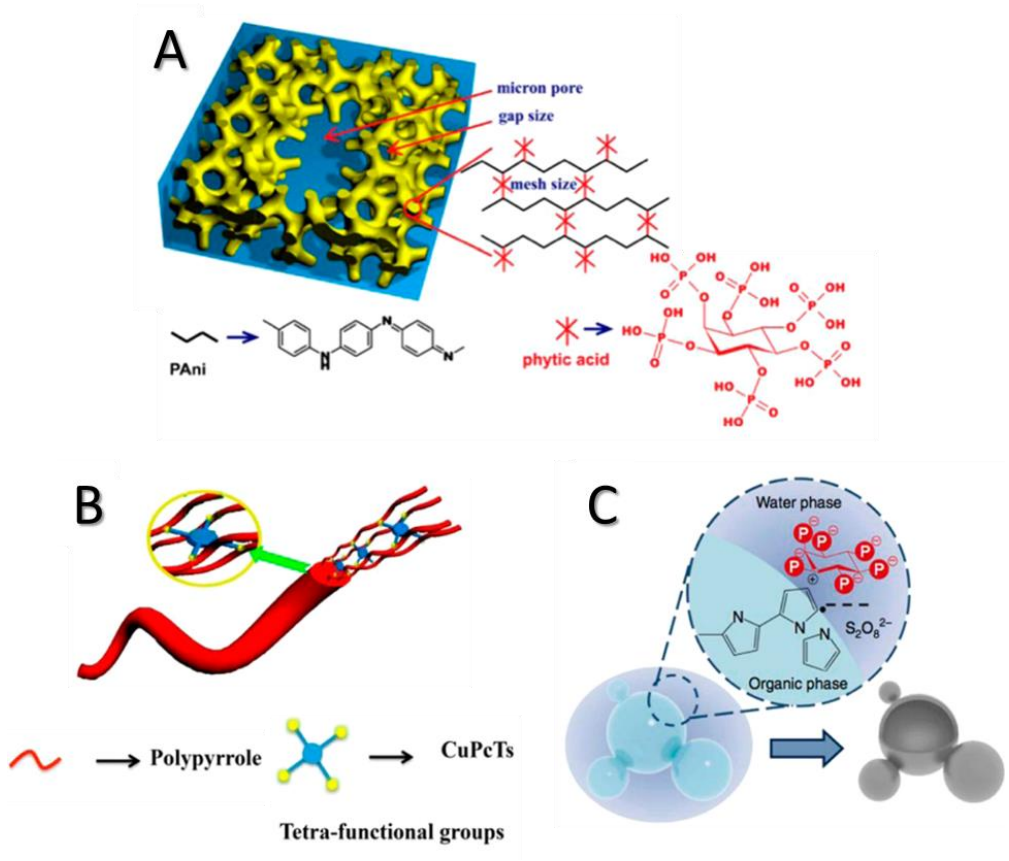

Figure 4.7 (a) Schematic and photograph of the 3D network structured PAn gel using phytic acid as the dopant and cross-linker;[48] (b) illustration of the supramolecular self-sorting mechanism that aligns the PPy chains to form the 1D nanostructure;[49] (c) schematic of interfacial synthesis of the hollow-sphere-structured PPy.[50]

4.1.3. Main Applications

Some of the most interesting application fields of these materials are reported in Figure 4.8 and will be discussed in the next paragraphs.

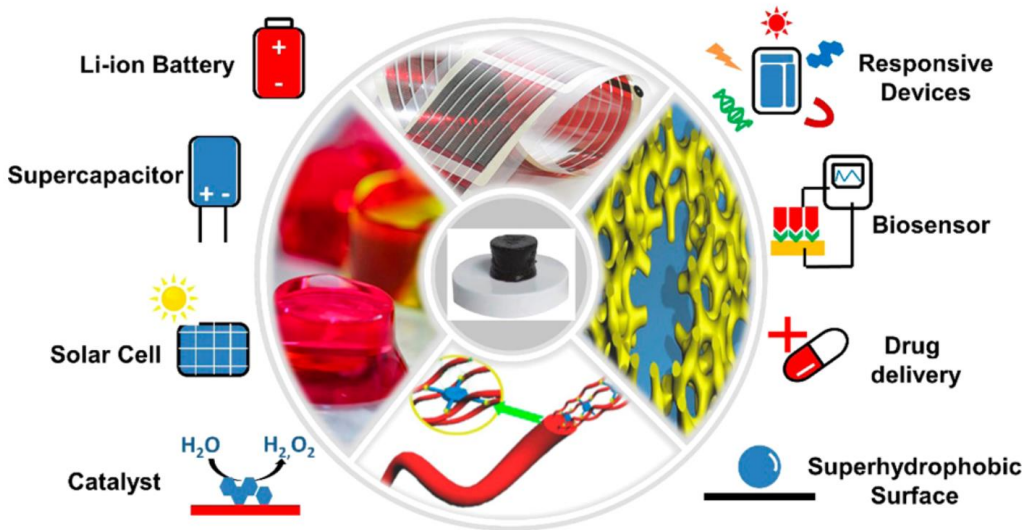

Figure 4.8 Examples of the application fields of the conductive hydrogels.[51]

- **Sensors & Biosensors**

It is one of the most common application of these materials, through the binding (covalent or not) of compounds able to give a specific response to an analyte (i.e. GO enzymes). The conductive part has to be designed in order to have a regular response to electrical signals which could be generated upon a specific interaction between the active moiety of the conductive polymer and the analyte[52] (Figure 4.9). For example, biomolecules could be easily used because their bioactivity is not altered by the material, due its biocompatibility.[42,53] This last property allows their use also in implantable biosensors for continuous measures of particular parameters (i.e. glucose) or for electrode coating; in this last case, the purpose behind their employment is to inhibit the inflammatory process, while still enhancing the current response.[1]

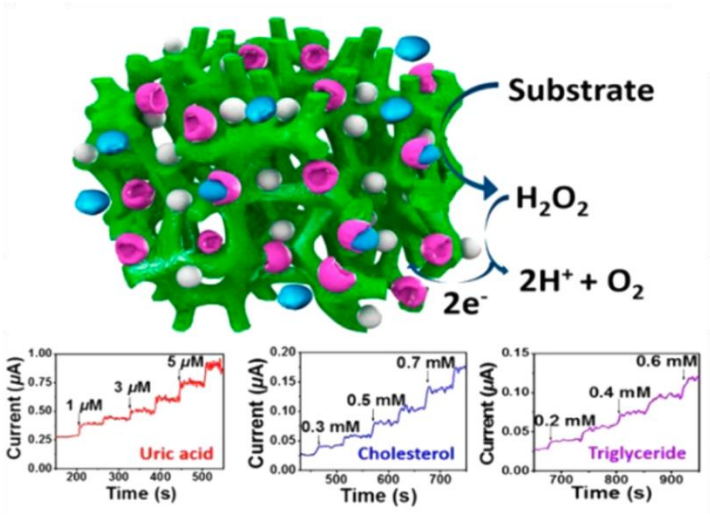

Figure 4.9 Schematic of the sensing mechanism of a conductive hydrogel-based electrode platform and its instant current−time response curves after the addition of different metabolites.[54]

In addition, the particular property of changing the conductivity value depending from the environmental conditions, open to the employment as sensor for temperature, pH or humidity measurements.[2] The presence of the hydrogel matrix allow a better processability of the material, due to the better physical properties and the possibility to be modelled in different shapes. In other cases, the conductivity is employed only to transmit a signal, while the proper stimuli-responsiveness is exploited by the hydrogel matrix. Noteworthy are two particular examples, for a temperature[55] and pressure sensors.[50] The first system is based on a soft hollow shaped conductive network: when even a small pressure is applied, the compression of the bubbles is translated into an increment of the conductivity of the material (Figure 4.10a). In the second system, instead, the thermosensitive hydrogel matrix exhibit a change in volume of the material depending from the temperature, allowing or not the contact between two electrodes (Figure 4.10b).

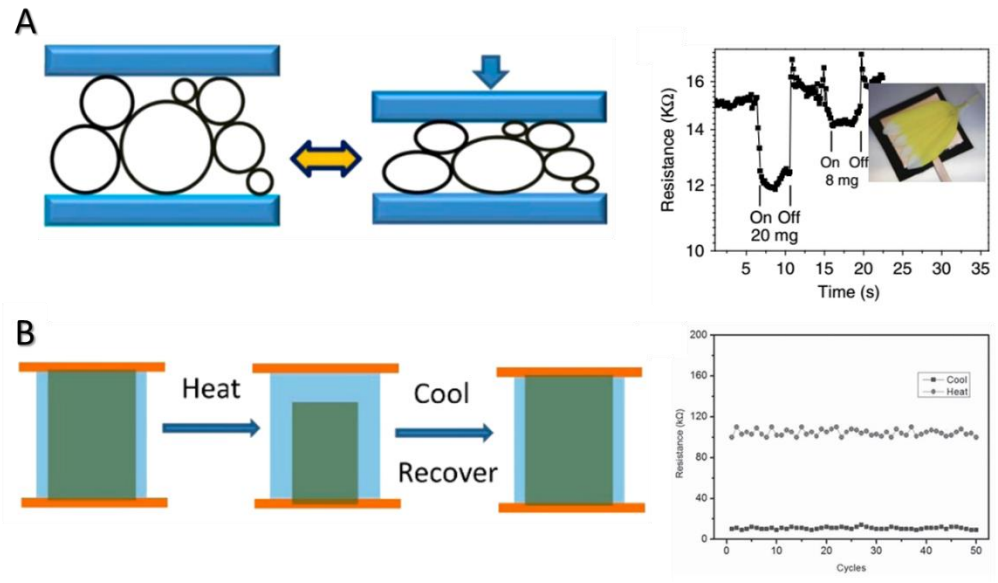

Figure 4.10 Working representation of temperature (a) and pressure (b) sensors realized employing conductive hydrogels, along with their electrical response to the applied stimuli.[50,55]

- **Neural Prosthesis**

Neural prosthesis are engineered assistive devices that present a solution to restoring function lost to neural damage, relying on an effective electrical communication between the implanted device and the central nervous system. In this context, electroconductive hydrogels may be useful in providing an electrically conductive, low-impedance and non-cytotoxic interface for long term, implantable neural prosthetic devices. Incorporation of a conductive polymer into a hydrogel network offers major advantages over its use on its own, due the superior mechanical properties (i.e. flexibility and biocompatibility) and the better interaction with the body environment that the gel could ensure.[56] Nevertheless, the hydrogel matrix can arrive to mimic the strength and flexibility of the natural tissue, due to its particular structure and even allow the proliferation of cellules on its surface, while the conductive part could be tuned in order to have similar resistance as the natural neuron, leading to the design of an ideal tissue-like prosthesis[57] (Figure 4.11).

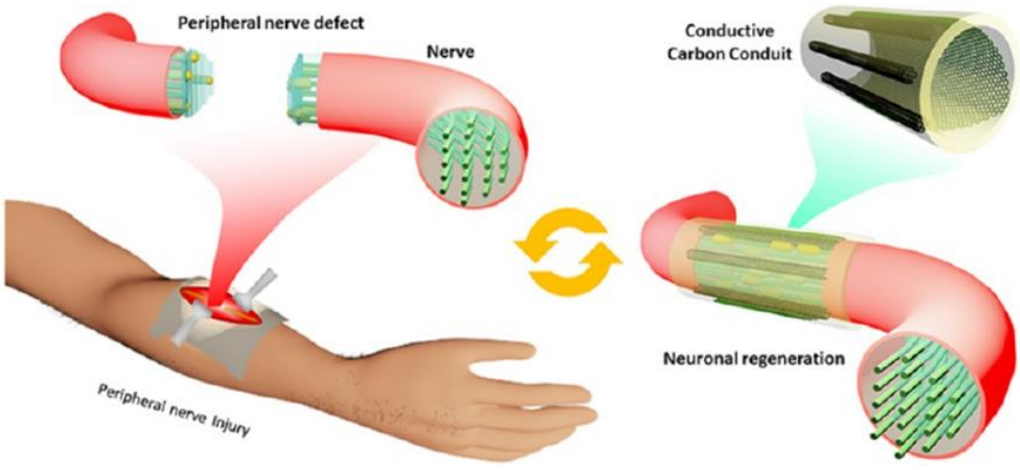

Figure 4.11 Ideal application of a conductive hydrogel as neural prosthesis.[57]

- **Drug Release Devices**

Drug delivery is the process of transferring a drug into the body over a period of time and at specific rate, in order to maintain a stable drug concentration for effective therapy. Electro-stimulated drug release devices are engineered devices that produce a programmed drug release profile influenced by the application of a predetermined voltage or current. Conductive electroactive polymers could be a good option for this purpose, since they possess substantial porosity and delocalized charge centers to allow counter-ion diffusion and electromigration inside the polymeric electrode body in response to oxidation or reduction. Also in this case the principal drawbacks of the pristine conductive polymers, such as low drug loading levels, poor control and unpredictability of the binding and release kinetics, and finally low diffusion coefficients of the released drug through the dense semi-crystalline polymer fibrils, could overcome by their employment in tandem with an hydrogel matrix which would be then responsible for all the process described before, even speeding up the on-off response of the material.[1] According to these premises, conductive hydrogels have been widely developed for the release of both ions and molecules of biological interest, due to their high void volumes and high diffusion coefficients.[58] The flexibility of the hydrogel matrix also allows the use of novel release mechanism, as for instance the cyclic change of the gel volume due to an electrochemical reaction (following a change in redox state) of the conductive part.[59] In this context, CNT-hydrogels have been widely employed due to their exceptionally high electron conductivity, that could also aid the synthesis of well-dispersed co-networks of electroactive polymers for a better tuning of electrochemical properties[60] (Figure 4.12).

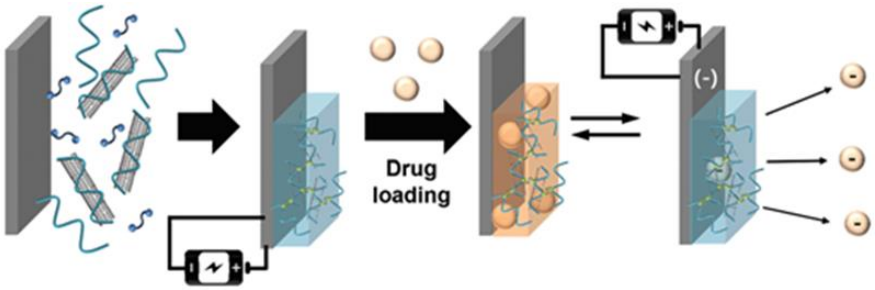

Figure 4.12 Example of working mechanism of a drug release device based on a CNT-conductive hydrogel.[60]

- **Electrochemical Capacitators**

Designed to take advantage of the near-surface charge storage mechanism, electrochemical capacitors show high power density and can store and release the energy within the time frame of a few seconds. The 3D nanostructured conductive hydrogels, besides possessing a good electrochemical stability, have a highly porous microstructure, a large surface area, excellent compatibility with other hydrophilic molecules (i.e. electrolyte solution), and tunable mechanical properties originated from the crosslinking structure and swelling nature, thus becoming a promising material for this application (Figure 4.13). In particular, their 3D hierarchical nanostructure can provide an excellent interface for electrolyte ions to access their electroactive surface, while the intrinsically conducting and robust framework could promote the charge/mass transport, thus improving the electrochemical usage of active material.[42,61]

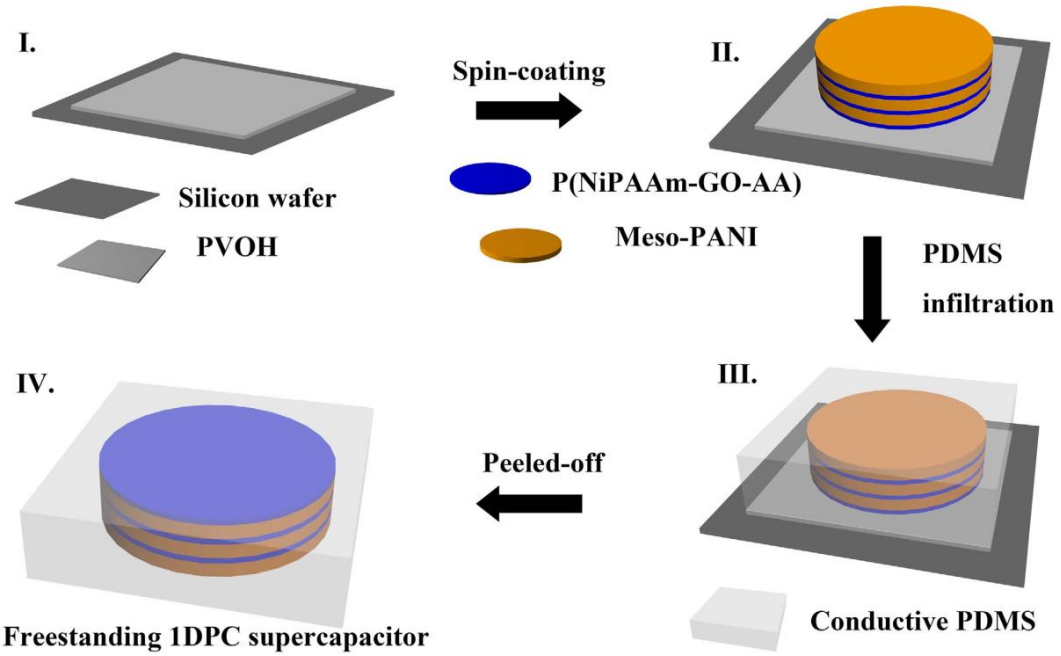

Figure 4.13 Schematic representation for the construction of a conductive hydrogel-based supercapacitor.[62]

4.2. Results and Discussion

This part of the PhD work will be focused onto the development of novel electroconductive materials based on a hydrogel matrix recently developed and never made conductive before. A study centered on the polymerization conditions and on the introduction of modifications into the hydrogel structure in order to maximize the electronic properties of the final hybrid materials will be carried out and discussed.

4.2.1. Preliminary Studies

4.2.1.1. Constructing a New Hydrogel

Initially, to start the study of these materials, the synthesis of polyacrylamide-based hydrogels obtained by radical polymerization was carried out, employing different amounts of crosslinker and different reaction times to obtain self-standing materials capable to swell in water. The chosen system was based on the use of acrylamide (Acr) as main monomer, an oligomer of ethylene glycol as crosslinker and an initiator system composed by tetramethylethylendiamine (TMEDA) and ammonium persulfate (APS), a matrix that is well known for its simple synthesis and its hydrophilicity (Figure 4.14).[63]

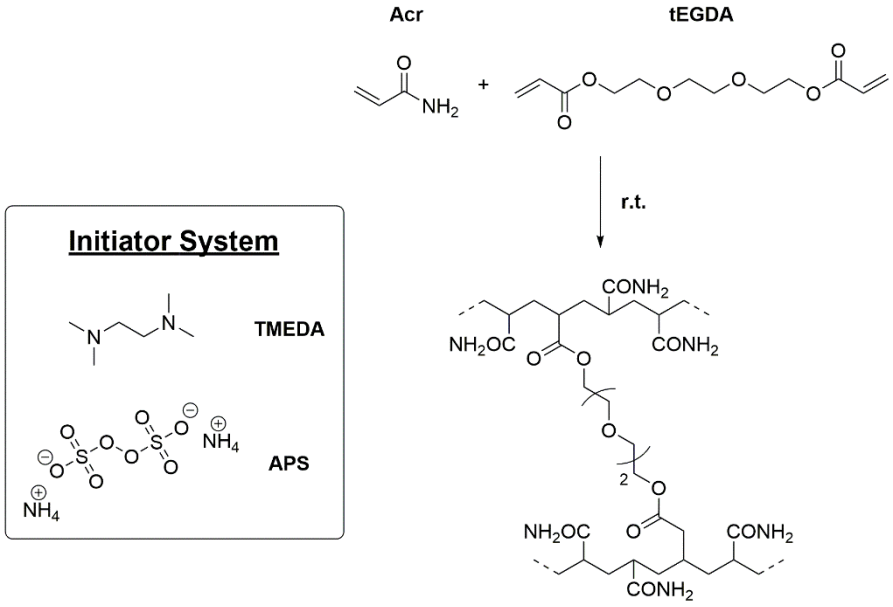

Figure 4.14 Representation of the first gel matrix used.

As crosslinker, triethylene glycol diacrylate (**tEGDA**) was used, which could be obtained by a standard acrylation of triethylene glycol (**15**) with acryloyl chloride (**16**) in the presence of an organic base (Scheme 4.2).[64]

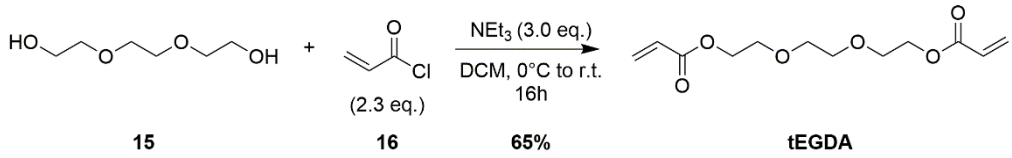

*Scheme 4.2 Synthesis of the crosslinker **tEGDA**.*

After chromatographic purification, it was possible to isolate the desired product with an acceptable yield. Once the crosslinker had been obtained, it was tested in the preparation of the chosen hydrogel matrix. In a typical synthesis, **tEGDA** was dissolved in water (with initial heating to facilitate its dissolution); subsequently, acrylamide and the initiator system were added in this order under stirring. When all the solids were dissolved, stirring was stopped and the solution was allowed to react for the desired time at room temperature (see Table 4.1). To stop the polymerization process, the hydrogels were removed from the reactor and put in distilled water in order to release all the unreacted starting materials. After 3h the water was changed and the gels cut in pieces and used for different experiments. Initially, the hydrogel was prepared applying the same components ratio and reaction time used in literature for a similar system[63] in which the crosslinker was tetraethylene glycol diacrylate (Entry 1, Table 4.1). Then, the amount of crosslinker was increased[65] in order to observe the change in physical aspect and behavior after the diminution of the degree of freedom of the polymer chains inside the hydrogel. The conditions applied and the results obtained for the different gel matrix are reported in Tab 4.1 and will be discussed in the next chapter.

4.2.1.2. Characterization of the Matrix

In all the cases, the gelation process occurs without problems and solid hydrogels were obtained, appearing transparent and homogeneous without any sign of phase separation. The hydrogels became slightly yellowish as the crosslinker amount was increased. The inverted vial test (the easiest way to confirm gelation) was performed and all the samples were self-standing, showing that the matter withstood gravitation without falling out when the tube was inverted (Figure 4.15).

Figure 4.15 Inverted vial test for one the synthetized hydrogels.

The main characterization was then performed by comparing the equilibrium degree of swelling (EDS) of the different gels, calculated as already described (see Chapter 3.4.1). The samples used to determine the EDS, after being washed after their synthesis, were put again in water and left there until a constant weight was reached (the water bath was changed every 6h). To determine the EDS, the swollen weight was measured by weighting the gels after removing the external water with a paper tissue, while the dry weight was measured after gel lyophilization. All the hydrogels proved to be reversible, so they were able to undergo wetting-drying cycles in 16h, which involved a swell/collapse behavior, without losing their properties.

Table 4.1 Different formulations tested for the new gel matrix.

Formulation	**tEGDA (%)**	**Acr (M)**	**tEGDA (mM)**	**TMEDA (mM)**	**APS (mM)**	**H_2O (mL)**	**Time (min.)**	**EDS (%)**
1	0.6%	1.69	2.3	13.1	3.1	10	10	-
2	0.6%		2.3				30	-
3	1.2%		5.6				10	10900
4	1.2%		5.6				30	3700
5	1.2%		5.6				60	4400
6	2.4%		11.2				10	4700
7	2.4%		11.2				30	3200
8	2.4%		11.2				60	4000

In Table 4.1 the EDS for all the formulation tested are reported. For Entry 1 and 2 it was not possible to calculate the EDS value because after one night spent in water the hydrogel samples were completely unraveled and it was impossible to retrieve any solid material from the solution. Probably

the amount of crosslinking present inside the network was too low to keep the linear polymer chains together once the material was put in a huge amount of solvent. In both cases, after evaporation of the solvent, it was possible to recover a white powder, but it resulted to be totally insoluble in all common solvents ($CHCl_3$, DCM, Tol, MeOH, THF, acetone, ACN and DMSO), making an NMR analysis impossible. Analyzing the other samples data, it can be seen how a particular trend was present for both the series (ratio 1.2% w/w, Entry 3 to 5 and ratio 2.4% w/w Entry 6 to 8): as far as the gelation time was considered, the EDS value increased in the order 30min<60min<10min. These results were quite unexpected, since longer reaction times were supposed to produce materials with a higher crosslinking degree, leading to a different order, namely 60min<30min<10min. The abnormal results of the comparison of EDS values between 30 and 60min could be explained by considering that, since the amount of crosslinker was quite low if compared to the main monomer (Acr), probably after 30min it was completely consumed, leading to the exclusive linear chains elongation in the remaining 30min of reaction. Such phenomenon could lead to an overall decrease of the network crosslinking degree, explaining the higher water uptake capability. On the other hand, as expected, the EDS value diminished when the amount of crosslinker was increased.

Table 4.2 Hydrogels behavior at different pH.

Formulation	Ratio tEGDA/Acr (w/w)	Time (min.)	EDS pH 4.7	EDS pH 7.0	EDS pH 9.3
4	1.2%	30	1300%	3700%	-
5	1.2%	60	1400%	4400%	-

The behavior of the hydrogels at different pH was then tested. Washed samples of the gels were put in aqueous solution at different pH values for several days and, once they reached a stable swollen weight, their EDS was evaluated. A buffer composed by the couple acetic acid/sodium acetate (equimolar solution, pH = 4.7) was used to test the behavior in acidic conditions, while an equimolar solution of ammonium hydroxide/ammonium chloride (pH = 9.3) was employed for the basic pH. As can be seen in Table 4.2, hydrogels in acidic solution exhibited a smaller EDS if compared to those swollen in pure water, while it was impossible to record a value in basic solution due to degradation of the gel network. This behavior could be easily explained after taking a look at the gel structure (Figure 4.14): in an acidic solution, the high proton concentration can enhance the formation of hydrogen bonds between the linear chains of the gel network, leading to a more collapsed structure; on the other hand, at basic pH, hydrolysis of the crosslinker ester bonds can occur, destroying the whole structure.

Table 4.3 Formulations tested after changing the hydrogels dimension.

Formulation	Ratio tEGDA/Acr (w/w)	Acr (M)	tEGDA (mM)	TMEDA (mM)	APS (mM)	H_2O (mL)	Time (min.)	EDS (%)
7	2.4%	1.69	11.2	13.1	3.1	0.3	30	-
9	4.8%		22.4					6200
10	9.6%		44.8					4100
11	23.2%		108.4					1100

Next, we tried to find condition suitable to control the dimensions of the hydrogels, in particular to reduce them in order to uniform the shape of the samples without the need to cut them for performing special experiments (i.e. the resistivity of the conductive hydrogel is strongly dependent from the

sample dimensions). To do that, the polymerization reaction was carried out in the same conditions already experimented but, once the stirring bar was removed, the solution was transferred in smaller container of *ca.* 0.3 mL volume, where the gelation process was completed. After 30 min., the samples were removed and put in water for further 3h. For each formulation, 7 samples were prepared. Formulation 7 (Table 4.3) was chosen as a reference because it gave the lowest EDS value producing a gel whose shape and softness did not increase too much. Unexpectedly, once the polymerization was carried out with this method, the corresponding gels unraveled after one night in water. For this reason, we decided to test formulations with higher amounts of crosslinker. Among them, the formulation that granted the better toughness, even without becoming too brittle, was formulation 11, that showed an EDS value of 1100%.

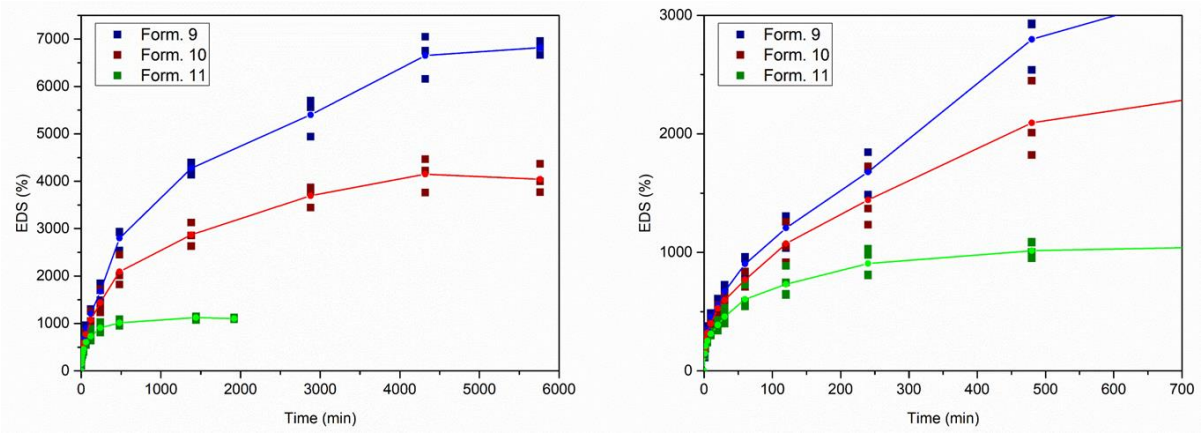

Figure 4.16 Kinetic study on the evolution of the EDS value overtime (left); zoom on the initial part of the kinetics (right). The line only connects the mean value of each set of points.

A study on time evolution of EDS was also performed. In this case, the dry hydrogels were immersed in distilled water, removed after precise intervals of time and their weight was recorded, having care to remove only superficial water before the measurement. As can be seen in Figure 4.16, there was not a linear dependence for the evolution of the EDS over time, but for all samples, after an initial rapid increase of the value, the EDS slowly reached a stable value. The zoom highlights how, while formulations 9 and 10 followed a similar evolution over time, reaching the maximum degree of swelling only after *ca.* 3 days, formulation 11 reached a stable weight already after *ca.* 8h, showing that the gel network obtained with this composition was much more compact than the others.

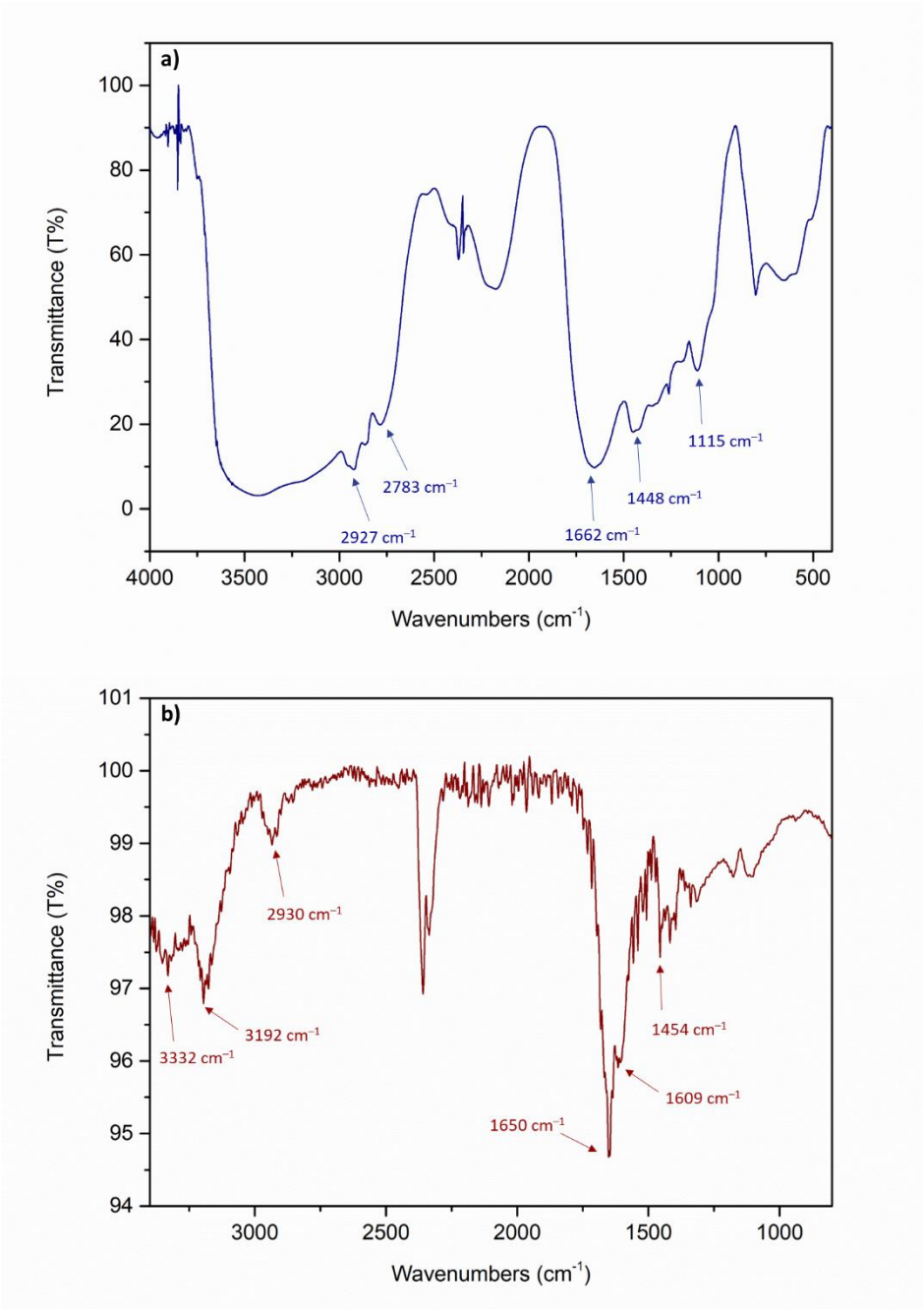

Figure 4.17 Hydrogels (form. 11) FT- IR (a) and ATR-IR (b) spectra.

Finally, the gel matrix was characterized by infrared spectroscopy. The FT-IR spectrum (Figure 4.17a) was recorded on KBr after grinding the dry hydrogel, while the ATR-IR spectrum was obtained directly from small pieces of dry gel (Figure 4.17b). In Table 4.4 the most significant peaks that can be recognized in the two different spectra are reported.[66]

Table 4.4 Diagnostic peaks in the recorded IR and ATR-IR spectra of the hydrogel matrix.

IR spectrum ν (cm^{-1})	**ATR-IR spectrum** ν (cm^{-1})	**Comment**
-	3332 3192	N-H stretching
2927 2783	2930	C-H stretching
1662	1650	C=O stretching
-	1609	N-H in plane bending
1448	1454	C-N stretching
1115	-	C-O stretching

The shape of the spectra resulted similar in the two different conditions, even if in the case of ATR-IR more signals could be detected. Indeed, the presence of the crosslinking could be detected in the IR spectrum by the signal at 1115 cm^{-1}, while in the ATR-IR spectrum, the two peaks present in that region could not be assigned due to the low intensity observed.

4.2.1.3. Development and Characterization of Conductive Hydrogels

To study the way of introduction of a conductive moiety inside the gel matrix, we chose to start testing one of the most common conductive polymers used in this field, namely polyaniline (PAn), that can be obtained from radical polymerization of aniline with ammonium persulfate (APS) in acidic conditions. To let the polymerization to occur inside the hydrogel, a typical two step procedure was adopted.[1,67] First, the gels were immersed for 18h in a solution of either the monomer of the conductive polymer or the radical initiator, in order to let the matrix absorb the component; then, the gels were removed from the solution, washed and finally immersed for additional few hours in a solution of the other component necessary for the polymerization (see Scheme 4.3). The obtained conductive hydrogels were then put in water for 2 days to remove all the residual unreacted reagents present inside the matrix.

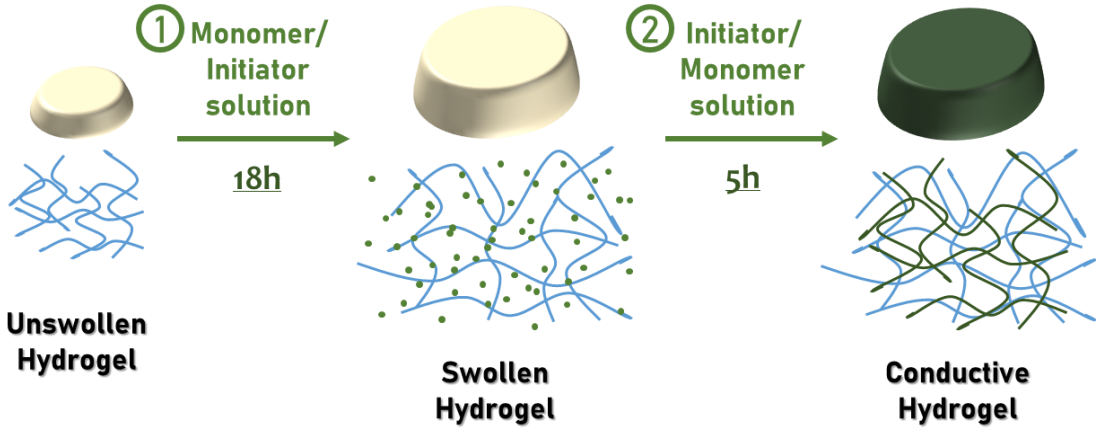

Scheme 4.3 Representation of the two step procedure adopted for the introduction of the conductive polymer inside the hydrogel matrix.

Two different protocols were tested and are summarized in Table 4.5. The first one reproduces a classical process,[68] with a first step (the long one) performed in a solution of aniline in aq. HCl (in order to maximize the amount of monomer encapsulated inside the matrix) and a second one where the gels were put in a solution of APS in water. A drawback of this method is that during the second step some aniline can diffuse in the water solution and polymerize there, reducing the loading of conductive polymer in the gel matrix. For this reason, a second protocol was developed[66b] to ensure that formation of the conductive polymer would take place only inside the hydrogel. In this case, the first step was performed in an acidic aqueous solution of APS, while the second one in a solution of aniline in hexane: with these conditions, the adsorbed APS will not be released in the solution outside the gel (the salt is not soluble in the organic solvent), whereas aniline can still diffuse inside the hydrophilic environment of the matrix because is also soluble in water. In both procedures, one step was always performed in acidic conditions to allow the polymerization process to occur at the correct pH. A special care need to be paid to the amount of APS used during aniline polymerization: it is important that an equimolar solution of aniline and APS is used in both procedures. In fact, since the process is stoichiometric, use of sub-molar quantities of APS will not produce enough polymer to obtain a conductive PAn network and, on the other hand, use of an excess of the persulfate can lead to overoxidation of the conductive polymer, decreasing its conductibility.[69]

Table 4.5 Summary of the conditions tested for the introduction of the conductive moiety inside the hydrogels.

	Procedure 1	**Procedure 2**
1st step (18h)	Aniline (0.1 M) in $HCl_{(aq.)}$ 1 M	APS (0.1 M) in $HCl_{(aq.)}$ 1 M
2nd step (5h)	APS (0.1 M) in H_2O	Aniline (0.1 M) in hexane

In summary, we can say that both methods induced the polymerization of the conductive moiety inside the hydrogels, with the expected difference that while with the first procedure the polymerization occurred also outside the gel (Figure 4.18), with the second one the process was forced to occur only inside the matrix. In the latter case the solution was only light yellow colored. The hydrogels obtained were all black (see Figure 4.18) and appeared more rigid than the pristine hydrogel, without becoming too brittle. They were, in fact, still able to gain again their shape after compression without breaking.

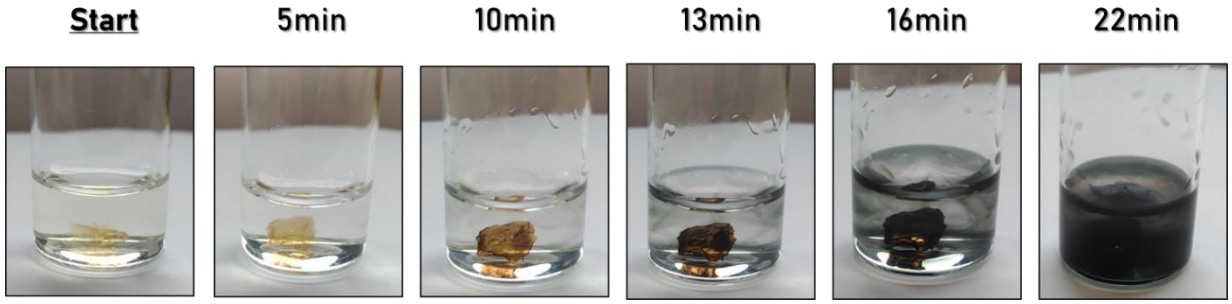

Figure 4.18 Evolution of the polymerization process following the procedure 1.

The hydrogels used in these experiments were obtained either with the formulation 9 or 10, to monitor the impact of the different crosslinking degree on the polymerization of the conductive part. To assess the best conditions for aniline polymerization, the process was carried out both on dry and rehydrated (after the maximum EDS was reached) hydrogels. After the polymerization of the conductive part, the hydrogels were left for 1 day in pure water (changed every hour for the first 10h) to remove all the unreacted compounds from the gel matrix and weighted again. By comparison of the weight before and

after the polymerization process, it was possible to determine the percentage of conductive polymer present in the final material (Eq. 1).

$$CP(\%) = \frac{W_{CH} - W_{PH}}{W_{CH}} \times 100 \qquad \text{Eq.(1)}$$

In Equation 1, CP% is the percentage of conductive polymer present, W_{CH} the dry weight of the conductive hydrogel and W_{PH} the dry weight of the pristine hydrogel. The CP% value was determined for all the samples, the values we found are shown in Table 4.6.

Table 4.6 Percentage of conductive polymer incorporated using the different polymerization conditions used.

Formulation	Initial gels	Procedure	CP%
9	Dried	1	57%
		2	64%
	Swollen	1	55%
		2	73%
10	Dried	1	48%
		2	56%
	Swollen	1	48%
		2	66%

As it can be seen, the best result in terms of CP% (73%) was obtained with formulation 9, using the second procedure and starting from an already swollen sample. By comparison, as expected, the results obtained for formulation 10 (with more crosslinking, and so capable to absorb less water) were always inferior. The second procedure always led to an higher amount of conductive polymer being incorporated, probably due to the fact that the polymerization process took place only inside the matrix and not in the outside solution. The fact that it was possible to incorporate more conductive polymer starting from a swollen gel than a dry one can be explained by the not complete recovery of the swollen state by the dry hydrogels during the re-hydration procedure.

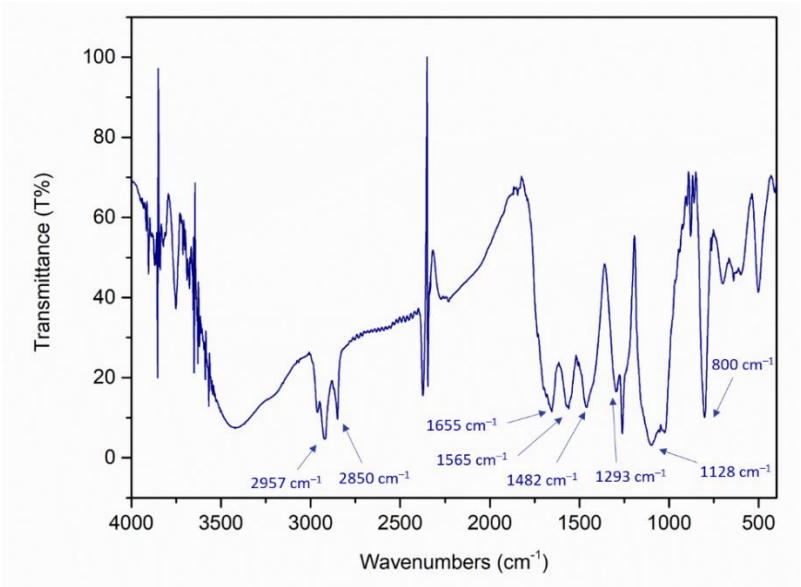

Figure 4.19 IR spectrum of a PAn-conductive hydrogel.

The IR analysis of the samples were then carried out. In Figure 4.19 one of the spectra recorded on KBr is reported, while in Table 4.7 the most significant peaks are listed.[65,66a]

Table 4.7 Diagnostic peaks recognizable in the IR spectrum of the conductive hydrogel

IR spectrum ν (cm^{-1})	**Comment**
2957 2850	C-H stretching Hy matrix
1655	C=O stretching Hy matrix
1565	C=N stretching PAn
1482	C=C stretching PAn
1293	C-N stretching, aromatic secondary amine PAn
1128	NH^{+}=C stretching PAn
800	C-H bending, aromatic PAn

Clearly it is evident the presence of new signals which can be assigned to the polymer now present inside the hydrogel. Particularly interesting are the two signals at 1565 and 1482 cm^{-1}, which are referred to the C=C and C=N stretching of the aromatic ring of polyaniline (see Figure 4.4 for the structure). This is confirmed in Figure 4.20, where the comparison between the spectra of the conductive hydrogel, of pure polyaniline (PAn) and of the pristine gel matrix is shown. As can be noticed, the spectrum of the final conductive hydrogel is close to the "sum" of the spectra of the two isolated components (the hydrogel and the conductor) suggesting that incorporation took place to a reasonable extent.

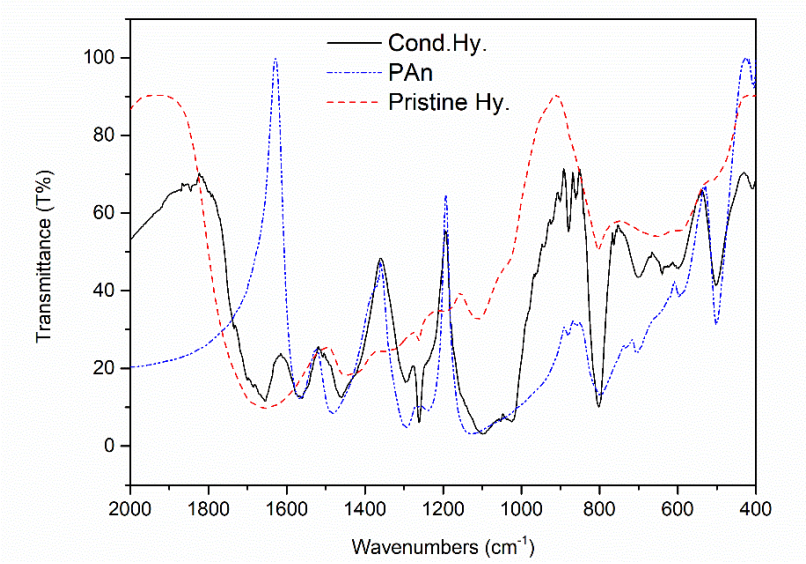

Figure 4.20 Comparison between the IR spectra of the conductive hydrogel (black line), the pure polyaniline (dotted blue line) and the pristine gel matrix (dashed red line).

Finally, the morphological characterization of the hydrogels obtained was carried out by means of environmental scanning electron microscopy (ESEM). This technique was chosen instead the classic SEM because of its instrumental setup (in terms of pumping process, electron beam used and signal detection) which allow to use a lower vacuum degree and to avoid any pretreatment of the sample (i.e. metal sputtering to make the material conductive) in case it is inherently conductive. For these reasons, conductive hydrogels are perfect sample for this analysis and the pictures obtained are a more close representation of how they look like once in the swollen state (in fact, the acquisition is made on a partially swollen hydrogel, not on the dry one). Inspecting the recorded pictures (Figure 4.21), it can be seen that the gels showed their typical porous structure with holes of two different average dimensions, which were evaluated to be of ca. 3-10 μm for the smaller ones and comprised between 28 and 40 μm for the larger pores.

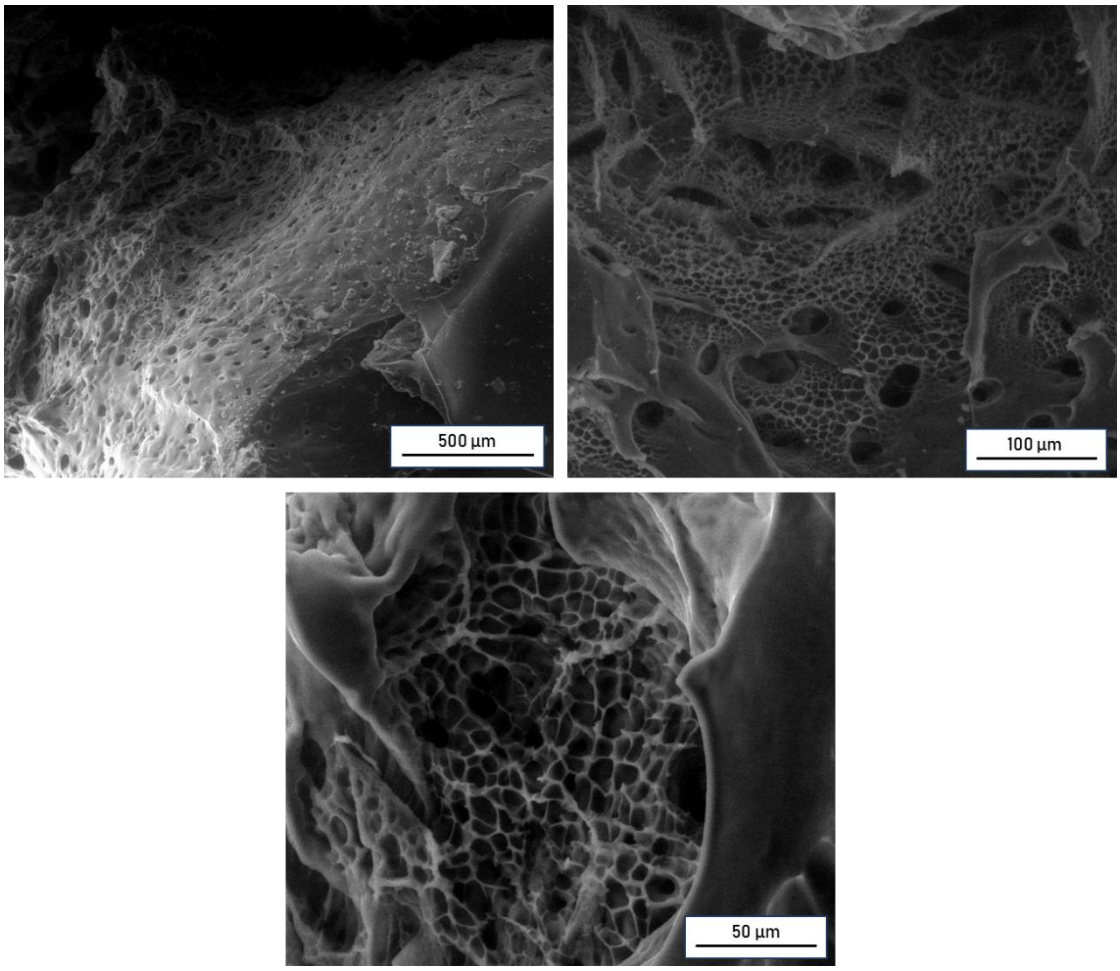

Figure 4.21 ESEM morphological characterization of the conductive hydrogel obtained with formulation 9 at different zoom resolutions.

4.2.1.4. Electrochemical Characterization*

The evaluation of the hydrogels electrochemical properties was carried out on samples obtained from formulation 11 (see Table 4.3), before and after doping of the conductive part. As already described in Chapter 4.1.1, conductive polymers can be doped in order to enhance their electronic properties; the process is compatible with the incorporation of the conductor inside a neutral matrix and, in the case of polyaniline, can be easily performed. Polyaniline doping consists only in protonating the polymer nitrogens: protonation in fact allows to expand the conjugation of the system and, by consequence, to enhance the conductivity of the polymer (Scheme 4.4). In addition, it also increases the ionic conductivity of the hydrogel, due to the increment of ionic groups inside the material. To perform the doping, the swollen conductive hydrogel samples obtained from aniline polymerization were first put in water for two days to remove all the unreacted components and then immersed in a HCl 1 M solution. Subsequently, the doped hydrogels were extracted from the solutions and dried with a paper tissue to remove the external water. The electrochemical properties of the two conductive hydrogels before and after doping were analyzed by means of cyclic voltammetry (CV) and electrochemical impedance spectroscopy (EIS) to determine their electrochemical redox potential and conductivity, respectively.

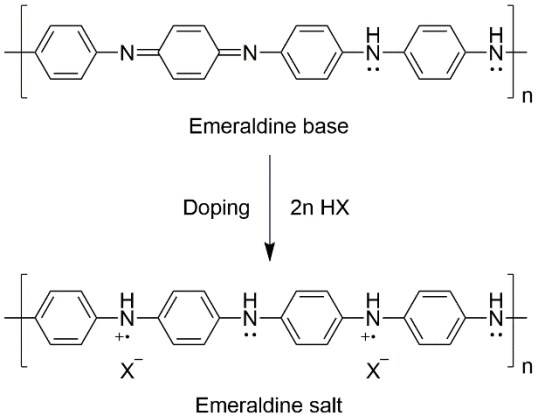

Scheme 4.4 Structural differences after doping in polyaniline.

In particular, EIS is an electrochemical technique used to determine the impedance of a system over a range of frequencies and to distinguish the different contributions of its distinct components (such as resistor and capacitor elements) by measuring the opposition to the flow of alternating current that is generated. The data obtained from the measurement can be plotted in different ways to help determine the electronic parameters of the system. One of the most used graphical representations is the Nyquist plot, in which the correlation between the real and the imaginary part of the impedance is reported. This graph is particularly important because from its analysis is possible to determine the resistance of the system (that is the real part of the impedance).

EIS measurements were performed on the swollen conductive hydrogels by placing them between two gold contacts (placing particular care in letting all the surface of the samples being in contact with the metal) and varying the frequency of the AC between 50 KHz and 2 MHz with a fixed amplitude of 30 mV. The impedance for each sample was then measured and the Nyquist plot was generated. The conductive hydrogels are not homogenous materials, but complex systems composed by a gel matrix with its internal solution (that has an inherent resistance and can exhibit ionic conduction) and a

* The electrochemical characterization was performed by Jonathan Filippi (CNR-ICCOM, Istituto di Chimica dei Composti OrganoMetallici).

conductive polymer network (to which a proper charge transfer resistance should correspond). This means that the impedance itself is constituted by various components (i.e. resistances or capacitances) related to the different parts of the material.[70] In order to discern and evaluate the contribution of each component, the entire system has to be modeled and the Nyquist plot obtained from the experiment must be fitted in accordance with the chosen model. The easiest method is to represent the system as an electronic circuit (called "Randles equivalent circuit")[71] and to describe each single contribution to the global impedance as a basic electrical element (resistance, capacitor, inductor or constant phase element), depending on their physical definition. For example, the charge transfer process inside the conductive polymer and to the electrode is depicted as a resistance, while the ionic conductivity inside the solution as a capacitance (for the migration to the opposite electrodes of the differently charged ions).

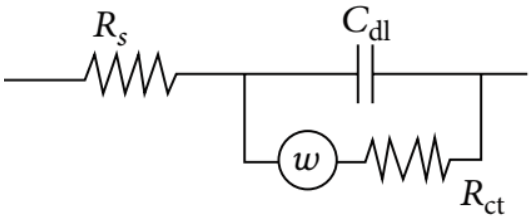

Figure 4.22 Randles equivalent circuit used as model of the conductive hydrogel system.

To choose the right equivalent circuit, the entire structure of the conductive hydrogel has to be taken into account. Starting from the simple model of a non-polarizable electrode in contact with an electrolyte solution, with the introduction of the contribution of the diffusive process present into the system,[72] the equivalent circuit depicted in Figure 4.22 was obtained, where R_s is the inherent resistance of the solution, C_{dl} is the double layer capacitance phase element (used to represent the ionic conduction contribute), *W* is the Warburg element that takes into account the diffusion process inside the liquid phase and R_{ct} is the charge transfer resistance, that is the values from which the resistivity of the material can be determined. This circuit, already employed to model the behavior of similar conductive hydrogels,[73] takes into account a mixed contribution to the total conductivity arising both from the charge transfer pathway and the kinetic processes present in solution. The Nyquist plots obtained from the impedance measurements were then fitted with the chosen equivalent circuit using EC-Lab software and the fitting showed a good agreement with the experimental data (Figure 4.23).

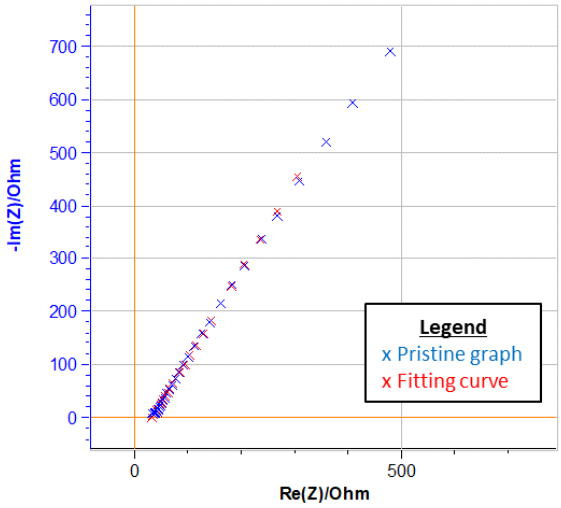

Figure 4.23 Nyquist plot and fitting curve of the experimental data for the sample obtained with procedure 1 before doping.

From the fitting, R_{ct} was determined for all the samples; the value of resistivity and its reciprocal, the conductivity of the material, were then calculated using Equation 2 and 3.

$$\rho = \frac{R_{ct} \times A}{l} \quad \text{Eq. (2)}$$

$$\sigma = \frac{1}{\rho} \quad \text{Eq. (3)}$$

Where ρ is the electrical resistivity (Ω × m), R_{ct} is the measured electrical resistance (Ω), A and l are respectively the area and the length of the samples and σ is the electrical conductivity (S/m). The values of conductivity determined for the different samples are reported in Table 4.8.

Table 4.8 Conductivity values and oxidation potential obtained from the electrochemical characterization.

Hydrogel	**Doping**	**l (cm)**	**A (cm^2)**	**R_{ct} (Ω)**	**σ (mS/cm)**	**Ox. Potential [*vs.* Ag/AgCl, KCl sat.] (V)**
Pristine	-	4.11	29.73	4015	3.3×10^{-2}	-
Conductive (procedure 1)	-	0.35	0.379	1620	0.6	0.353
	√	0.35	0.379	31.5	66	0.460
Conductive (procedure 2)	-	0.41	0.103	856	4.7	0.321
	√	0.41	0.103	14.0	126	0.447

All the samples showed a conductivity at least two order of magnitude higher than that of the pristine gel matrix, demonstrating that the introduction of the conductive polymer effectively enhanced the electronic properties of the material without affecting the elastic properties of the starting hydrogel matrix. Particularly interesting is also the comparison between the conductivity of the gels before and after doping: in both cases, the values increase by two orders of magnitude after the process, showing also how the simple tunability of the electronic properties of the conductive polymer inside the hydrogel is retained by the composite material. Notable is also the comparison between the two different procedures adopted to grow the conductive polymer inside the hydrogel matrix. As can be seen in Table 4.8, either with or without doping, the values of conductivity recorded for conductive hydrogels obtained with the second method are one order of magnitude higher than those synthetized with the first one. These data agreed to what already observed for the CP% value (see Table 4.6), showing how there is a direct correlation between the amount of conductive polymer incorporated within the hydrogel matrix and the conductivity of the material.

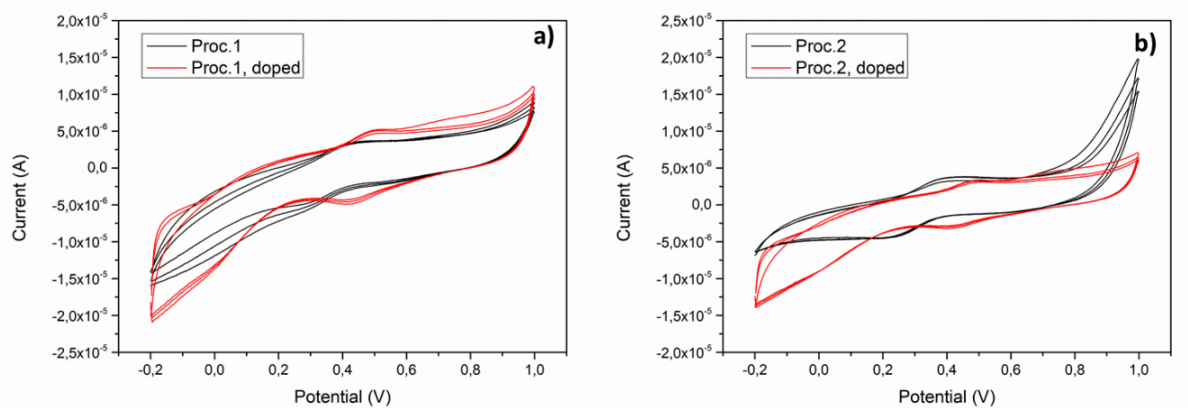

Figure 4.24 Cyclic voltammetry of the conductive hydrogels (vs. RHE) obtained with the two different protocols before and after the doping.

Cyclic voltammetry (CV) of the samples were also measured. CV data could give information of the long-term electrochemical stability (a stable material will have a constant peak size) and can be indicative of the charge storage capacity of the gel (through the size of the redox peaks obtained). Moreover, they can show if the redox process that the materials undergo are reversible or not. The measurements were performed according to the literature,[74] using an Ag/AgCl (KCl sat.) reference electrode, a platinum foil as counterelectrode and $KClO_4$ (ss.) as electrolyte. The CV spectra of the conductive hydrogels before and after the doping were recorded (Figure 4.24) and the corresponding oxidation potentials are reported in Table 4.8. The spectra of the hydrogels obtained in both the two methods exhibit symmetric curves, indicating the presence of one reversible redox process within the active part of the material. The curves were also found to be stable through several cycles, with no signal of degradation of the conductive network being detected. The materials maintained their properties also after the doping: as can be seen, in fact, even if the shape of the curves changed the redox reaction still appears to be reversible and the curves to be stable. A shift of the oxidation potential to higher values was recorded after doping coherently to the protonation of the polymer by the acid. The analysis of the recorded curves showed only one peak instead of the three transitions usually observed in the CV spectrum of PAn.[75] In particular, the registered peak was closed in value to that usually assigned to the formation of its most oxidized form, the pernigraniline[76] (Figure 4.4). The small dimensions of the sample were probably the reason of the extremely low currents recorded, that prevented the detection of the other two peaks.

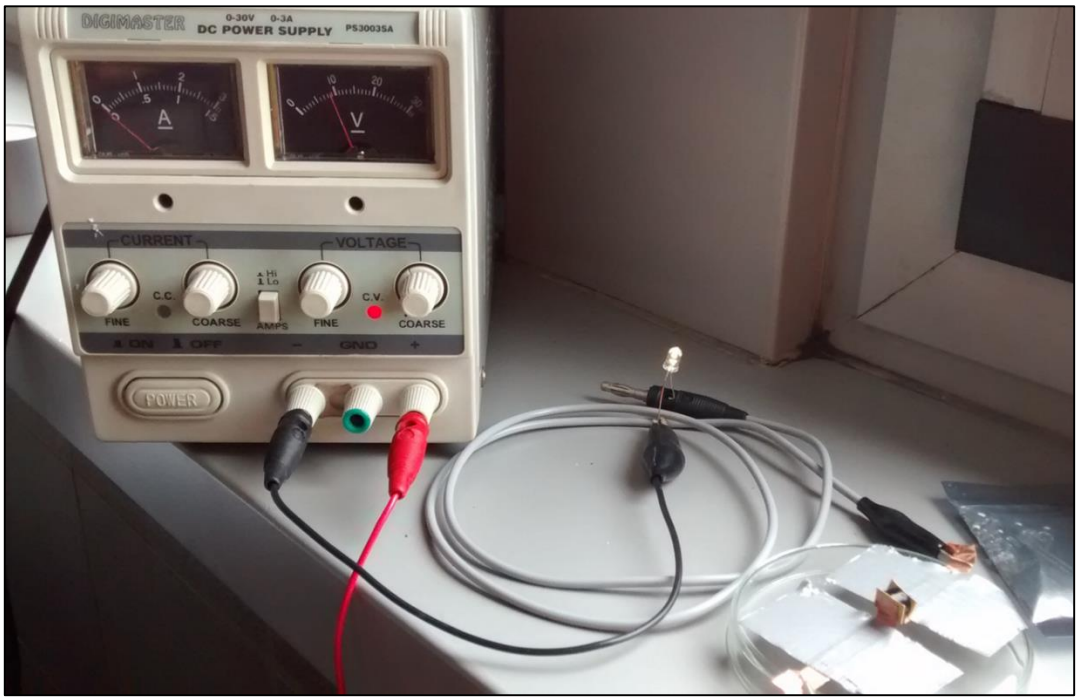

Figure 4.25 Demonstration of the conductibility of the conductive hydrogels developed by powering a small LED.

The above electrochemical characterization suggested that the between the two methods used to prepare the hydrogels the second one (see Table 4.5) is the most promising for obtaining materials with interesting electronic properties. Anyway, all the conductive hydrogels prepared showed a good conductivity and could be used in a simple circuit without interrupting the electric current flow (Figure 4.25).

4.2.2. PAA Hydrogels

Having developed a good procedure for the incorporation of the conductive polymer inside the pre-existing gel matrix, we decided to investigate the scope of the process using another hydrogel as basic component. The new matrix we decided to use is a polyamidoamine (PAA) hydrogel a gel matrix, recently developed in Prof. De Cola's group, at the University of Strasbourg.

This particular matrix (Figure 4.26) can be obtained by *Aza*-Michael reaction between the electron poor double bond of methylenebisacrylamide (MBA), acting as the main monomer of the formulation, and the primary amino groups of pentaethylenehexamine (PEHA), the crosslinker, as well as of γ-aminobutyric acid (GABA).[77] This last component is used to balance the charge inside the hydrogel and for the hydrophilicity that can confer to the hydrogel matrix.[78] The most notable peculiarity of this formulation is the absence of any initiator: the chemical reaction used for the polymerization, in fact, can take place spontaneously also at r.t. once the pH of the solution is basic enough (almost 8-9) to allow deprotonation of the amine groups after nucleophilic attack on the double bond. This requirement is fulfilled by the use of PEHA, which helps also control the pH. The gelation of the polyamidoamine network is in fact achieved at 50°C in few hours without the need to add any other component.

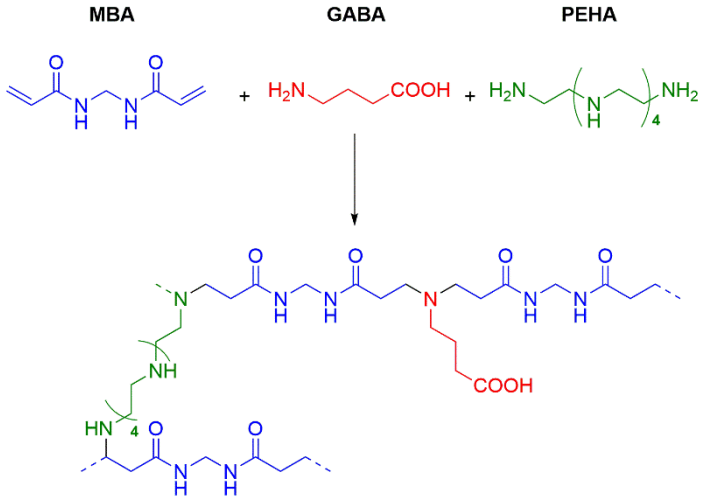

Figure 4.26 Representation of the PAA hydrogel structure.

To start our study, we tried to modify the synthetic procedure in order to evaluate the effect of the reaction temperature on the final polymer. To achieve this goal the reaction temperature was raised to 90°C, thus MBA was dissolved in hot water, then the amino acid and the crosslinker were added to the solution under stirring. The mixture was stirred for 5 min, then the stirring was stopped and we could find that in these conditions, the gelation occurred in only 4h. The hydrogels obtained were yellowish and quite brittle. To check the quality of the material, a swelling study similar to that already conducted for the acrylamide-based hydrogels (see Chapter 4.2.1.2) was performed, and the results obtained for the EDS were compared with whose previously reported in our group.[77]

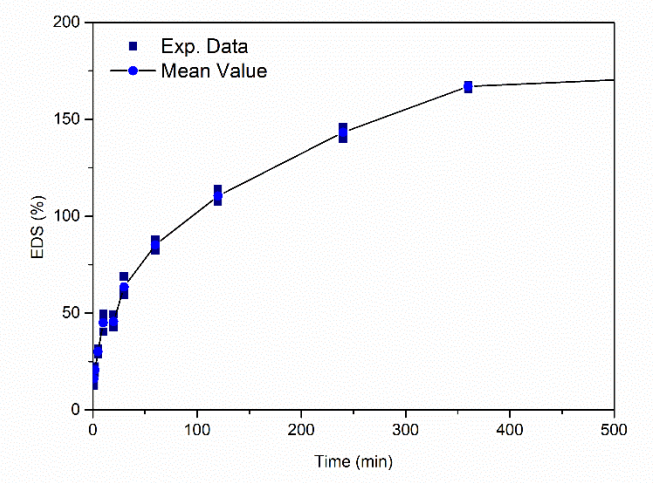

Figure 4.27 EDS kinetic evolution study for the PAA hydrogels.

The curve obtained from the kinetics experiment is showed in Figure 4.27; as can be seen, the trend is similar to those already observed with acrylamide-based hydrogel, even if the maximum EDS value was smaller: after 24h the samples reached a constant weight and a maximum EDS value of 192%. This result could be correlated to a possible different extension of crosslinking present in the two formulations which can be due to the fact that PEHA can react not only with the terminal NH_2 groups (as depicted in Figure 4.26), but also with the "internal" secondary amino groups. This last process would lead to a final network with smaller pores and a more compact structure, due to the shorter length of the crosslinker. The comparison with the EDS value reported in literature for similar network[77] (*ca.* 350%), showed that the changes introduced induced the formation of a network with a larger degree of crosslinking. This could be explained considering that a higher temperature can speed up the *Aza*-Michael reaction also of the secondary amine groups of PEHA, increasing the crosslinking degree of the material.

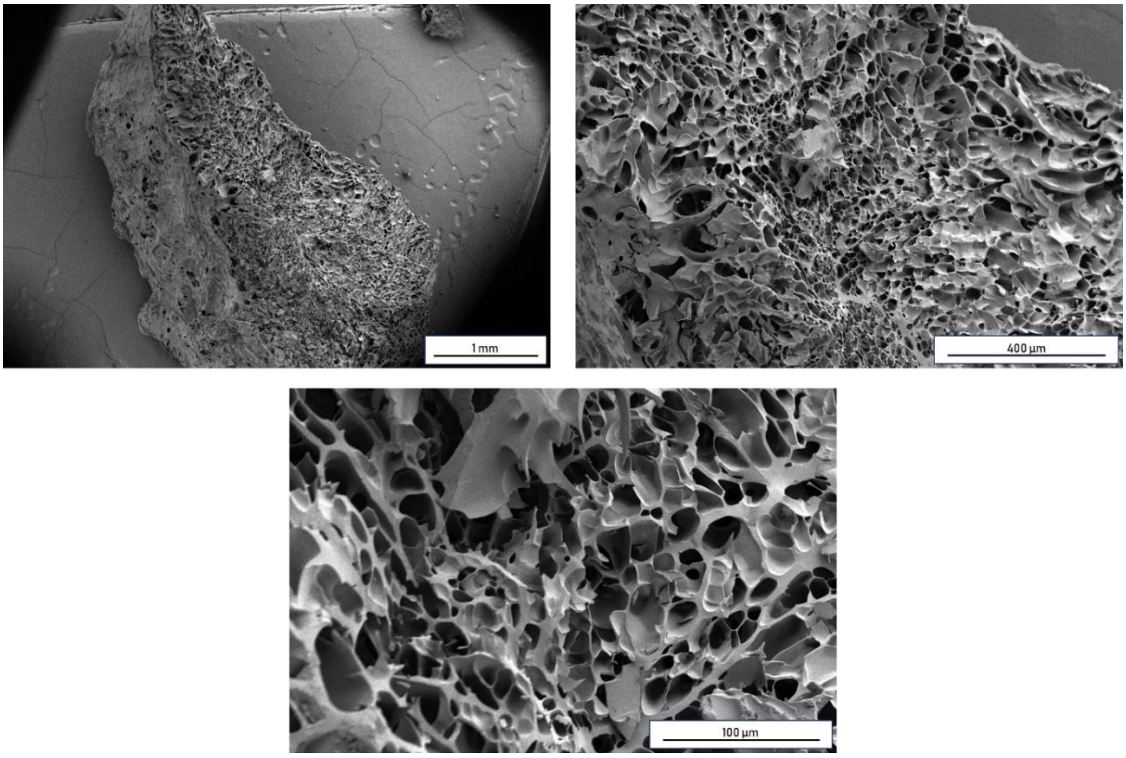

Figure 4.28 SEM of the PAA hydrogel matrix.

The reference hydrogel formulation was then changed aiming to obtain a softer final material capable to store a higher amount of water. To do that, the amount of GABA was slightly reduced and the gelation was performed at 40°C overnight, in verify if using a lower temperature would help in increasing the length of the polymeric chains. The hydrogels obtained with this protocol were softer than those obtained at 90°C and showed an EDS value of *ca.* 750%, even better than the one of the reference hydrogel reported before.[77] This formulation was then used as a reference for all the successive experiments. The morphological characterization of the gel matrix obtained with the new formulation was then carried out by means of SEM analysis (Figure 4.28). The hydrogel showed pores of two main dimensions, the bigger one between 45 and 60 μm and the smaller one comprised in the range 5-25 μm, similar to that observed in the literature formulation (20-70 μm), but displaying a more structured porous system, in agreement with the trend of the EDS value.

4.2.2.1. PAn-Conductive Hydrogels

To grow PAn inside the PAA hydrogels, the same procedure already adopted for the acrylamide-based matrix was tested. Accordingly, the freshly synthetized swollen gel samples were put in water for 2h to remove the unreacted reagents from the gelation process, and were then immersed in a 0.1 M APS solution in HCl 1 M for the entire night. Surprisingly, the next morning all the samples turned darker and appeared to be smaller in dimensions if compared to the night before. Two samples had even been completely dissolved by the solution, leading to the conclusion that the matrix was degraded by reaction with APS in acidic conditions.

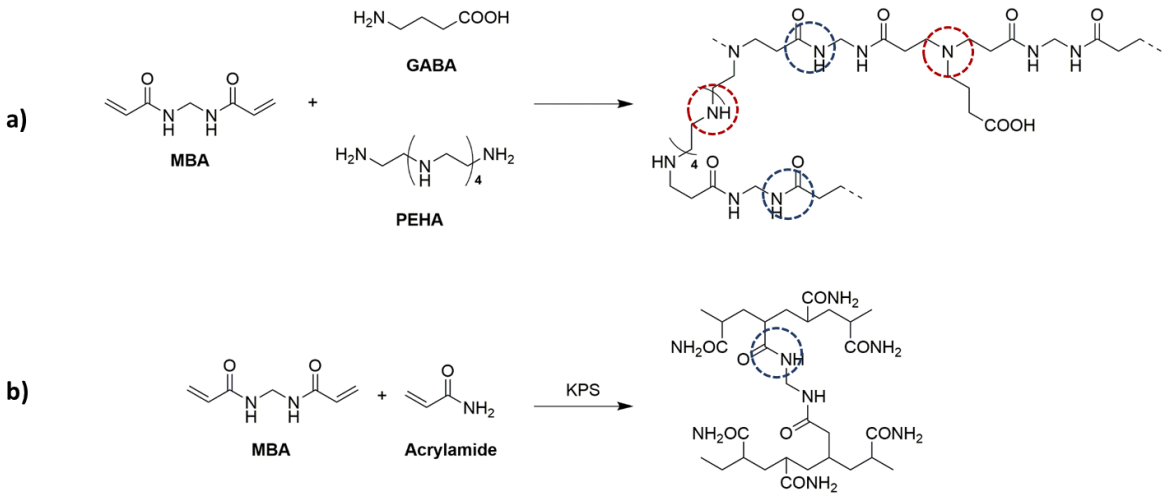

Figure 4.29 Structure similarities (blue circles) and differences (red circles) between (a) the PAA hydrogels and (b) acrylamide-based conductive hydrogels found in literature.[66b]

The analysis of the degraded gels by means of NMR proved impossible due to the insolubility of the residue in the most common organic solvents. In literature,[66] aniline polymerization was described in a hydrogel matrix that showed similarity with that used in our group. Indeed, in both formulations amide bonds were key components of the gel backbone, as part of the crosslink (in the acrylamide-based hydrogel) or in the linear polymer chains (in our PAA gel). The principal difference between the two networks was the presence in the PAA hydrogels backbone of secondary and tertiary amine moieties (Figure 4.29). Amines (especially tertiary amines) are known in literatures for being able to lead to C-C cleavage upon oxidation, following different pathways depending from the oxidizing agents. For

instance, Cope reaction[79] is a common tool in organic chemistry for the production of olefins starting from substitutes amines by oxidation promoted from various peroxides[79,80] (mainly hydrogen peroxide and *m*-chloroperbenzoic acid). In this case, the amine perform a nucleophilic attack on the peroxide bridge leading to the formation of the corresponding amine oxide, which could evolve with the cleavage of a C-C bond near the functional group and the creation of the hydroxylamine (Scheme 4.5). As APS is known for being able to oxidize amines to the corresponding oxides,[81] the event of such process cannot be excluded. Furthermore, the oxidation could be performed also in other ways: metal complexes[82] could extract an electron from the amines, producing an amino cation which could evolve both with the cleavage of one of the C-C bonds near the functional group, or, with other strong oxidants such as Br_2,[83] $KMnO_4$[84] and *o*-iodoxybenzoic acid[85] the principal reaction product is the corresponding imine which, in aqueous environment, could be easily hydrolyzed, leading to the removal of one of the amine substituents. The occurrence of similar oxidation pathways in our hydrogel network cannot be excluded and can be responsible of the destruction of the entire polymeric structure which is mostly constituted by amine bonds on its entire length.

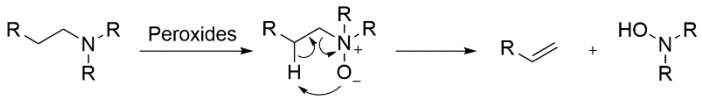

Scheme 4.5 Cope reaction mechanism.[86]

In view of these consideration we needed to modify the two-step procedure, in order to allow aniline polymerization without causing the dissolution of the hydrogel matrix. We tested different conditions which are reported in Table 4.9. The change in weight of the hydrogel after the polymerization was determined in order to evaluated the amount of conductive polymer introduce into the gel matrix and it was calculated according to Equation (4):

$$\text{Change in weight} = \frac{W_{pp} - W_{bp}}{W_{bp}} \times 100 \qquad \text{Eq. (4)}$$

where W_{pp} and W_{bp} are respectively the dry weight after and before the polymerization process. The hydrogels were then dried before in order to record W_{bp} for each sample. After the first step, the hydrogels were washed before immersion into the second solution. Before recording their weight after polymerization, the hydrogels were washed by immersion in water for two days.

Table 4.9 Different conditions tested for the polymerization of the aniline inside the PAA hydrogels.

Entry	1st step		2nd step		Change in weight	Resistance (kΩ)[c]
	Component[b]	Solvent	Component[b]	Solvent		
1	aniline	HCl (10^{-2} M)	APS	HCl (10^{-2} M)	+13%	≈ 10
2	aniline	H_2O	APS	HCl (1 M)	+23%	≈ 5
3	APS	H_2O	aniline	HCl (1 M)	-64%	≈ 10
4	APS	HCl (10^{-3} M)	aniline	hexane	-84%	≈ 60
5	APS	HCl[a] (1 M)	aniline	hexane	+33%	≈ 60

[a] The sample stayed in the APS only 2h instead of the entire night; [b] In all the cases the concentration used was 0.1 M; [c] For comparison, resistance of a pristine hydrogel: ≈ 5 MΩ.

The polymerization of aniline occurred in all cases and the best results were obtained using the conditions reported in Entry 2 and 5. Samples treated according to Entry 3 and 4 showed significant signs of degradation after 1 night in the oxidant solution, becoming darker and smaller in dimensions.

In particular, as can be noticed from the comparison between the data obtained in Entry 3 and 4, the negative effect of the long exposition to the oxidant was even enhanced with the simultaneous use of acidic conditions. On the contrary, samples treated according to Entry 1 and 2 did not show any significant change, while sample reported in Entry 5 showed a darker coloration of the matrix after the first step, but the material seemed to remain intact. The degradation of the matrix treated according to Entry 3 and 4 was confirmed also by the comparison of the weight before and after the entire process. The resistance of all hydrogels was roughly recorded using a common multimeter. As reference, also the resistance of a pristine hydrogel was recorded and resulted to be almost two order of magnitude higher than the values obtained for the conductive hydrogels. Comparing the samples obtained with different protocols it can be noticed how the best conditions in term of electric properties are those of Entry 2 (resistance one order of magnitude lower than all the other samples). The relatively high resistance obtained following the procedure in Entry 5 (showing also the highest increment in weight) could be explained by an insufficient diffusion of the oxidant through the bulk of the gel matrix, leading to insufficient electronic connection of the conductive network.

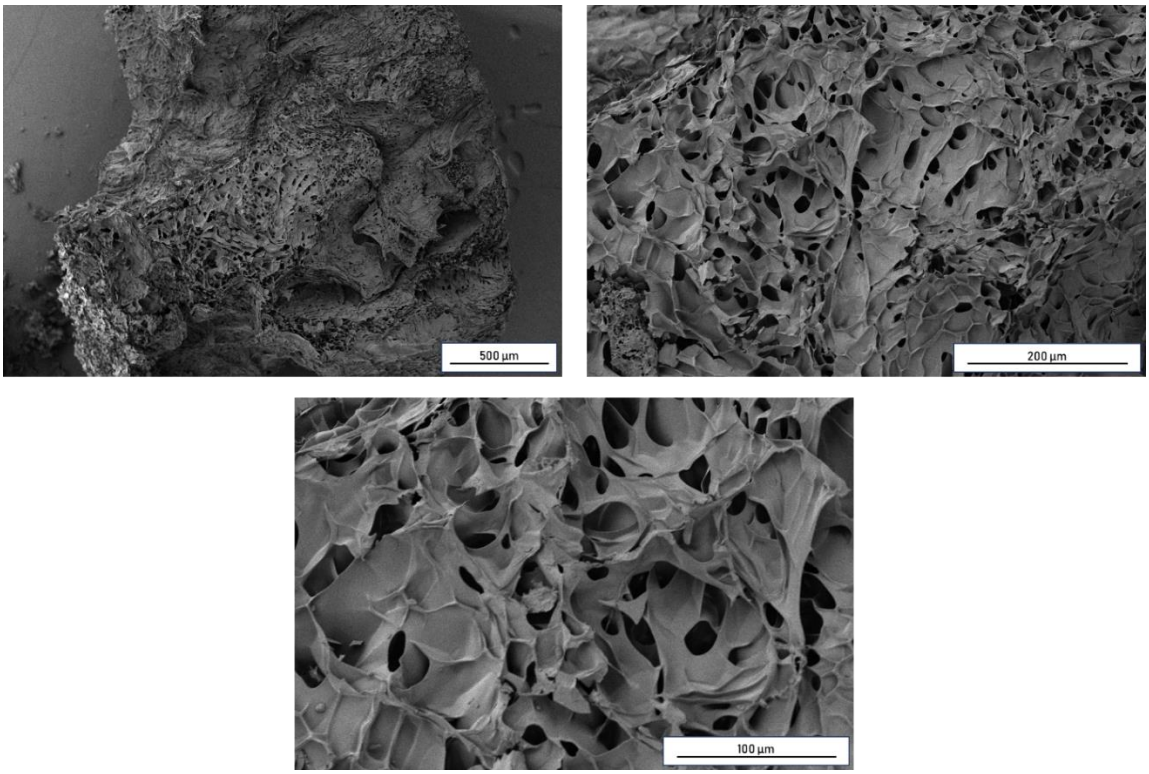

Figure 4.30 SEM of the PAn-condcutive hydrogel.

The topographic characterization of the conductive hydrogels was carried out by means of SEM (Figure 4.30), and the images recorded were compared to those of the pristine hydrogel matrix (Figure 4.28). The pores showed diameters comprised between 7.5 and 25 µm, and by comparing the two samples it could be noticed that the smallest pores of the matrix disappeared after aniline polymerization. This could be due to the presence of the new conductive network, which could have filled and covered the smallest channels.

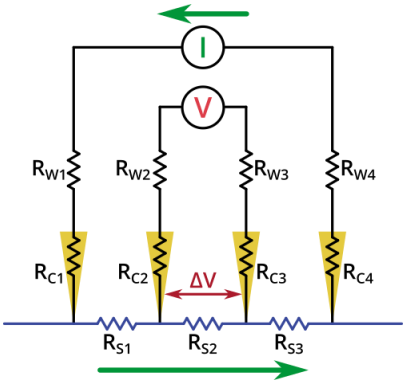

Scheme 4.6 Electric structure of a four-point probes method for the determination of the electric resistance of a material.

In order to gain a better understanding of the electric properties of the materials obtained according with the protocol of Entry 2, we measured their resistance. In this case was used a different technique, namely the four-point probes method† (Scheme 4.6). This measurement allows the direct determination of the electronic resistance of a material by using four different tips, two to generate an electric current flow through the material and the other two to register the voltage drop across the resistance of the material. The separation of the voltage and current electrodes eliminates also the contribution of the lead and contact resistance from the measurement, increasing the overall sensitivity of the technique. Also in this kind of measurements, it is essential to grant a good contact between the tips and the surface of the hydrogels in order to obtain reliable results.

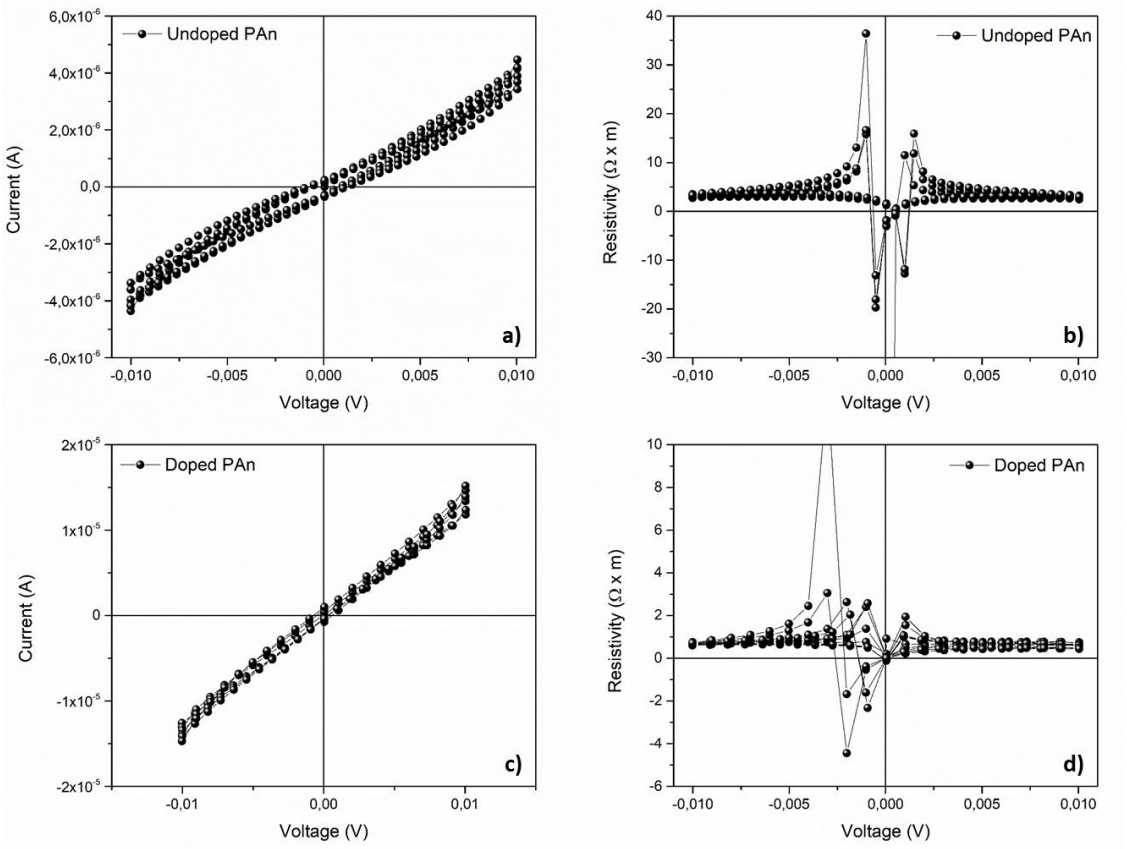

Figure 4.31 Examples of (a,c) current/voltage and (b,d) resistivity/voltage graphs obtained with four-point probes measurements of PAn-conductive hydrogel (a,b) before and (c,d) doping.

† All the four-point probes measurements were performed by Michele Petrecca from University of Florence.

After the measurement, two graphs were generated, the current/voltage curve (showing the stability of the material under the experimental conditions, Figure 4.31a,c) and the resistance/voltage plot (Figure 4.31b,d), which could be transformed into the resistivity/voltage plot after introduction of the samples dimension (according to Equation 2). From the resistivity/voltage graph is possible to extrapolate the resistivity of the material from the average value at high and low voltages recorded. The conductive hydrogel samples were analyzed before and after the doping process, performed as already described above, obtaining, respectively an average resistivity of 2.9 and 0.6 Ω × m (Figure 4.32d). These values were then converted into the reciprocally conductivity values (using Eq.(3)) of 3.4 and 15.4 mS/cm. The average values recorded were comparable with those obtained for the doped and undoped acrylamide-based conductive hydrogels obtained with the analogous procedure, the first (Table 4.10), showing the same trend, with the conductivity exhibit after doping one order of magnitude higher than before the process.

Table 4.10 Summary of the conductivity values recorded for PAn-conductive hydrogels obtained with the two different gel matrix.

Conductive Hydrogel	Doping	σ (mS/cm)
Polyacrylamide (procedure 1)	-	0.6
	√	66
Polyacrylamide (procedure 2)	-	4.7
	√	126
PAA	-	3.4
	√	15.4

4.2.2.2. Other Conductive Polymers

Finally, the possibility to use different kinds of conductive polymers was explored, focusing in particular on polypyrrole (PPy) and polyethylenedioxithiophene (PEDOT), which are well-known highly conductive polymeric materials. The main reason behind this choice was the possibility to achieve the polymerization of the conductive component in milder conditions, in particular without the need to use strong acids or oxidants (Scheme 4.7).

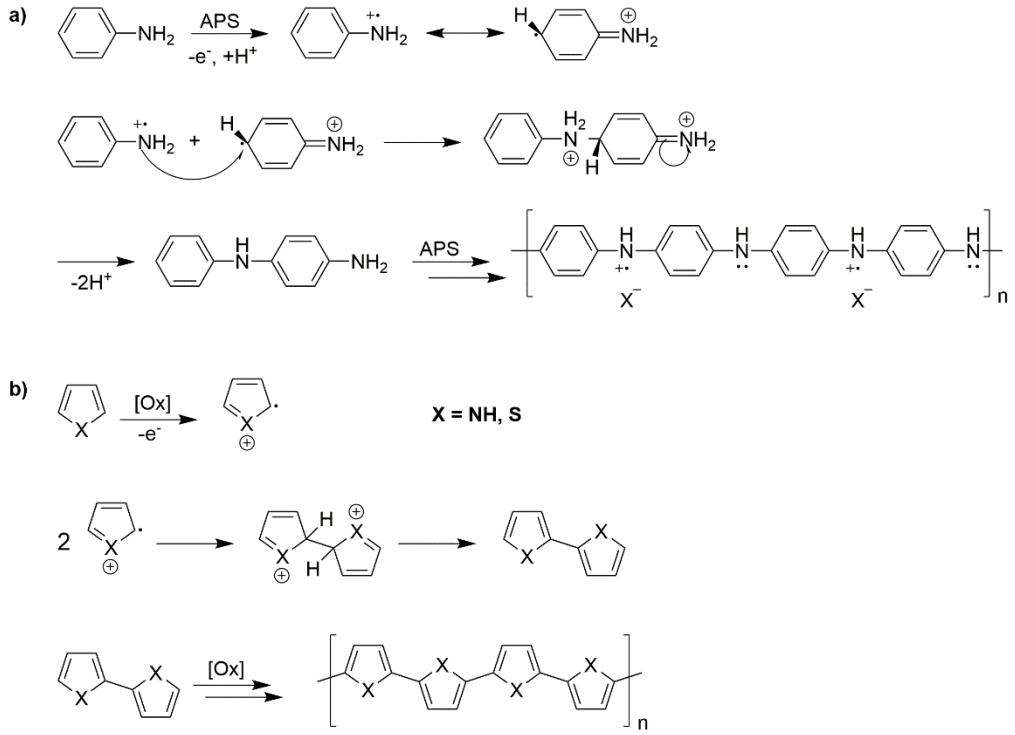

Scheme 4.7 Reaction scheme for the polymerization of PAn, PPy and PEDOT.

Furthermore, in these synthesis persulfate is not required, and weak oxidant species such as $CuCl_2$ or $FeCl_3$ can be used to achieve polymerization.[87] To introduce the two conductive polymers we decided again to use a two-step procedure similar to that optimized for the introduction of polyaniline inside the acrylamide-based hydrogel(see Chapter 4.2.1.3).In this case, the first step was performed in the aqueous solution of the oxidant ($FeCl_3$) and the second one in an organic solution of the monomer (Table 4.11). Due to solubility issues, the second step of pyrrole polymerization was performed in Et_2O instead of hexane. The gel matrix proved able to withstand the oxidative conditions and did not show any sign of degradation after overnight treatment during the first step.

Table 4.11 Summary of the conditions used for the introduction of the different conductive polymers.

Conductive Polymer	1st step (16h)	2nd step
Polyaniline	0.1 M APS in HCl 1 M	0.1 M Aniline in hexane (5h)
Polypryrrole	0.5 M $FeCl_3$ in H_2O	0.5 M Pyrrole in Et_2O (16h)
PEDOT	0.5 M $FeCl_3$ in H_2O	0.5 M EDOT in hexane (16h)

In this case, it was also possible to perform the second step using a longer reaction time thanks to the milder reaction conditions required. In all cases the desired conductive hydrogels were obtained without any sign of degradation. The hydrogels were then washed in water for 2 days and their resistance were measured with the four-point probes methodology. The current/voltage graphs resulted to be extremely similar to those already recorded for doped and undoped PAn (Figure 4.31) and all the hydrogels were stable in the experiment conditions; the resistivity/voltage graphs from which the resistivity values are obtained are reported in Figure 4.32.

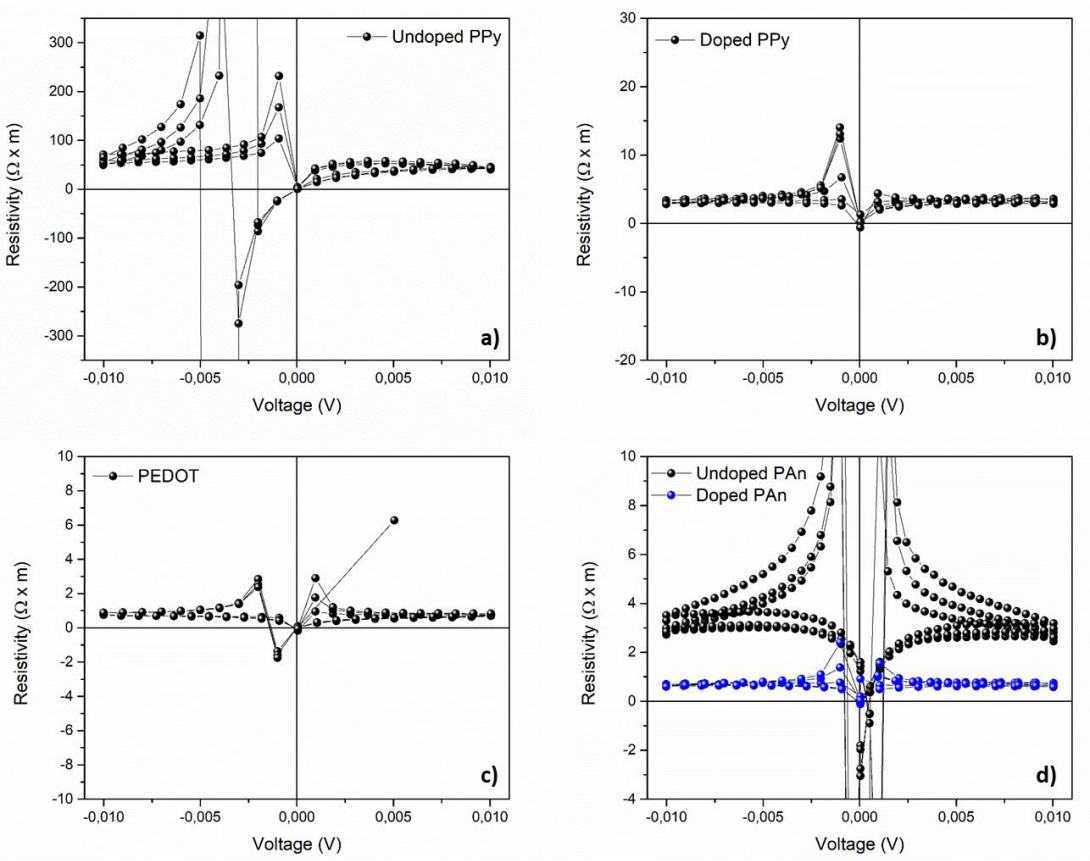

Figure 4.32 Resistivity/voltage graphs recorded for conductive hydrogels with (a) undoped PPy, (b) doped PPy, (c) PEDOT and (d) doped/undoped PAn.

As can be seen in Table 4.12, while the conductivity of the hydrogel/PEDOT composite was similar to that of the analogous conductive hydrogel obtained with doped PAn, the result recorded for the PPy with this method ("PPy undoped") was one order of magnitude lower. To verify if it was possible to enhance the conductive properties of the PPy-conductive hydrogel (as already verified in the case of PAn) we tried to perform the doping of the material. Polypyrrole doping is achieved by over-oxidation of the conductive network in protic solvents;[8,88] in those conditions it is in fact possible to move from the reduced form (called "contracted state") to the oxidized form ("expanded state") of the conductive polymer, which is characterized by an higher conductivity (Scheme 4.8).[89]

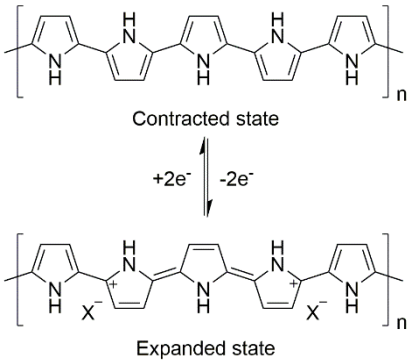

Scheme 4.8 Structural differences in PPy network after doping.

Accordingly, the procedure was changed again and made more similar to that used for PAn, replacing the $FeCl_3$ of the first step with the stronger oxidant APS but avoiding the addition of acids (that can speed up the degradation process of the matrix as observed above). The conductive hydrogel was

synthetized and its resistance was recorded. To summarize, in Table 4.12 the conductivities of all the developed conductive PAA-hydrogels are reported.

Table 4.12 Summary of the conductivity of all the different conductive hydrogels developed.

Conductive Polymer	Conductivity (mS/cm)
Polyaniline (undoped)	3.4
Polyaniline (doped)	15.4
Polypyrrole (undoped)	0.2
Polypyrrole (doped)	3.2
PEDOT	12.6
Pristine	1.0×10^{-3}

To summarize, we were able to successfully introduce inside the PAA hydrogel matrix three different types of conducting polymers obtaining three new conductive hydrogels characterized by a good improvement of the electronic properties of the composite material. Doping of two conductive polymers (PAn and PPy) could be performed without problems and allowed to increase the conductivity of the samples by one order of magnitude. The highest conductivity values were obtained with PEDOT and PAn in its doping state; the comparison with also the PPy showed, obviously, how the nature of conductive polymer introduced was able to influence the properties of the composite material. Unfortunately, even in our best conditions, the conductivity observed remained still order of magnitude lower than that of the most performing conductive hydrogels developed for energetic applications[48a,90] (0.11-0.88 S cm^{-1}), even if the values were in line with the typical range observed for this kind of materials (0.1-10 mS cm^{-1}).[42,91] Further work could then be focused into the optimization of the introduction of PEDOT inside this particular hydrogel matrix, due the good performances exhibited.

4.2.3. Novel PAA-Hydrogel Formulations: Covalent Linkage

A lack of affinity between the two different networks, the hydrophilic hydrogel matrix and the hydrophobic conductive polymer, could be the reason behind the not excellent electronic performances of the conductive hydrogels developed until now. This could be due to a not optimal growth of the conductive network inside the matrix, that can be explained to the different polarity of the material. As a possible solution, we can imagine to introduce new moieties on the backbone of the hydrogel, similar to those present on the second network and maybe able to promote its polymerization. To do that, we decided to add in the hydrogel formulation properly functionalized monomers of the conductive polymers already studied: we focused in particular on PAn and PPy. These monomers were designed having a free primary amino group on their backbone to be capable to react in the *Aza*-Micheal polymerization reaction and thus participate to the formation of the hydrogel backbone. Significantly, with this formulation the conductive polymer could result at the end covalently linked to the hydrogel matrix (and not only trapped inside), reducing the chance of leaking from the final material. Obviously, the functionalization should not be on the same positions reacting in the polymerization process, namely position 4 for the aniline and position 2 for the pyrrole (see Scheme 4.7). Thus, we choose two functional monomers: the 3-aminobenzylamine (**ABA**) and 3-(1*H*-pyrrol-3-yl)propan-1-amine (**3-PPA**), whose structures are shown in Figure 4.33. **ABA** in particular has already been employed as junction

between two different polymeric chains, being able both to polymerize with other aniline molecules in order to obtain polyaniline and to be covalently linked to an hydrophilic chain using its primary amino group, then establishing a covalent bond between the two networks[92] (Figure 4.33).

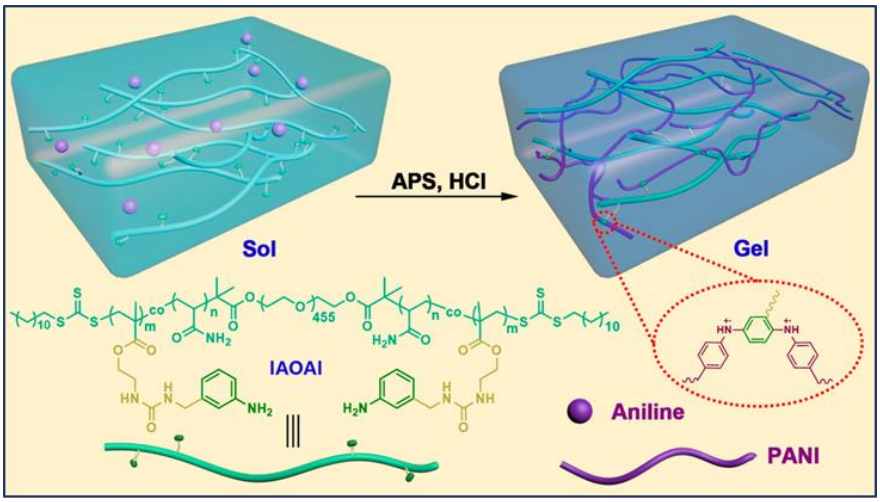

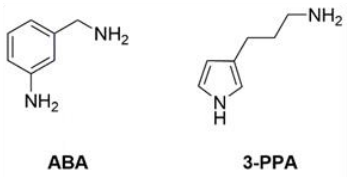

Figure 4.33 (top) Example of the use of ABA as covalent junction between two different networks; (bottom) structure of the two molecules employed.

Despite more difficult to prepare, in the case of **3-PPA**, the choice of putting the amino side chain on the 3 position of the pyrrole ring was made in order to leave the hydrogen on the nitrogen free to interact with the surroundings amines[93] and to favorite the dissolution of the molecule during preparation of the hydrogel.

4.2.3.1. Synthesis of the Additives

While **ABA** was commercially available, **3-PPA** had to be synthetized. The proposed retrosynthetic pathway for **3-PPA** is reported in Scheme 4.9.

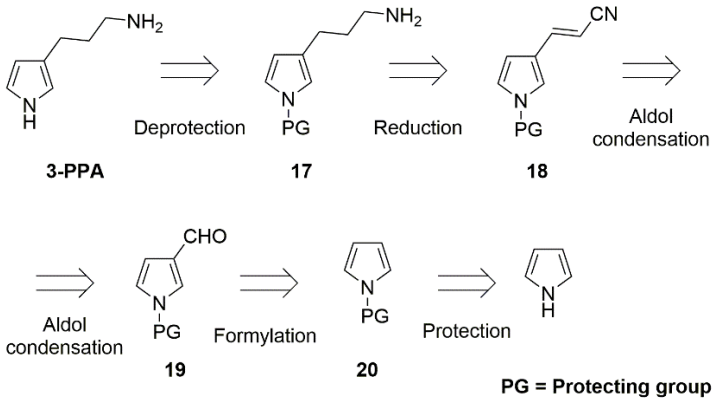

*Scheme 4.9 Proposed retrosynthetic pathway for **3-PPA**.*

Six steps are necessary to build the compound. **3-PPA** can be obtained from the deprotection of amine **17**, which is obtained from the complete reduction of the side chain of conjugated nitrile **18**. The formation of the double bond next the nitrile can be performed by aldol reaction between ACN and compound **19**. The aldehyde can be introduced by formylation in position 3; however, to avoid reaction on position 2 (which is more activated towards electrophilic addition), a bulky protecting group on the nitrogen has to be employed.

According to the hypothesized retrosynthesis, the first step would be the protection of the nitrogen. We decided to employ various silanes (a typical protecting group for pyrrole[94]) in our experiments to determine which one would induce the best selectivity in the following step. The reaction was performed always with the same protocol, involving deprotonation of pyrrole with *n*-BuLi followed by addition of the chosen chlorosilane (Scheme 4.10). The isolated protected pyrrole was then reacted without the need of additional purification with $(COCl)_2$ and DMF in order to introduce the aldehyde function. From analysis of the ^{1}H-NMR spectra of the isolated reaction products it resulted that when $Si(Et)_3$ and $SiMe_2(t\text{-Bu})$ were employed as protecting groups the reaction occurred on both 3- and 2-position (in ratio, respectively, of 3:2 and 2:1, favoring reaction on 3-position); on the other hand, only the product of reaction in 3-position was obtained when the protection was performed with $Si(i\text{-Pr})_3$ (TIPS), which provides a better steric hindrance on the 2-position[95] (Scheme 4.10).

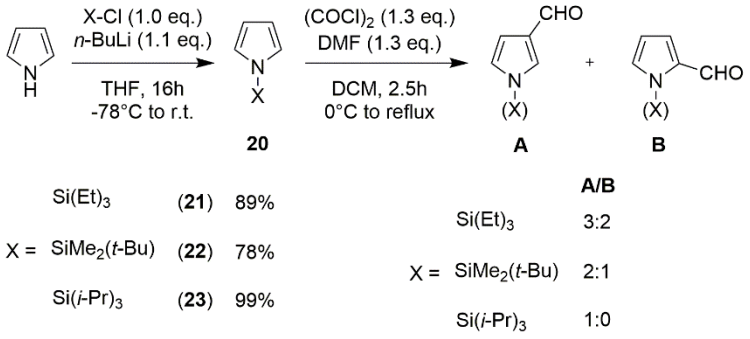

Scheme 4.10 Screening of protecting groups for the pyrrole.

In view of these results, TIPS was then chosen as protecting group. Unfortunately, the basic workup performed after the reaction (quench with an aqueous solution of NaOH 1 M) allowed to recover only the unprotected aldehyde **A** (Scheme 4.10). Even by changing the workup conditions, using H_2O or a smaller amount of base (aq. NaOH 0.4 mM), the right compound could not be isolated, and only reaction intermediate **20** or the deprotected aldehyde **A** were recovered in the two cases, respectively. Even though the functionalization of the pyrrole ring on the 3-position had already been achieved, the protecting group on nitrogen was still important because it could stabilize the molecule, reducing the chance of polymerization and avoiding the occurrence of side reaction in the subsequent steps. For this reason an alternative synthetic pathway was tested,[95] involving introduction of the carbonyl group *via* metalation with *n*-BuLi followed by nucleophilic attack on DMF (Scheme 4.11). To this end, bromine was first introduced on the 3-position of pyrrole **23**, in order to obtain a regioselective metalation by metal-halogen exchange. Bromine introduction was achieved in excellent yield by reaction with NBS leading to the isolation of compound **24**, which was then reacted with *n*-BuLi. The subsequent quench with DMF gave aldehyde **25** in almost quantitative yield.

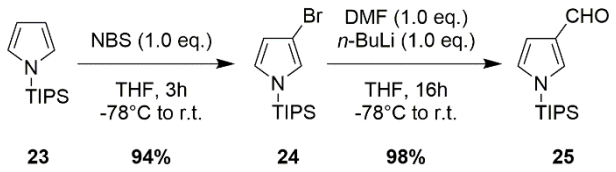

Scheme 4.11 Formylation of the protected pyrrole.

The next step was then the aldol condensation for the introduction of the nitrile group (Scheme 4.12). The reaction was quite straightforward, ACN was deprotonated with *n*-BuLi, then pyrrole **25** was added and after two hours of reaction, the disappearance of the aldehyde spot on TLC was observed. The mixture was then quenched by addition of HCl 3 M and stirred overnight to promote water elimination and the formation of the double bond. Nitrile **26** was then recovered as mixture of isomers *E*/*Z* ≈ 1:1; the two compounds were not separated since they had to be directly reduced in the following step. The reduction of the unsaturated compound **26** to the corresponding aliphatic amine **28** was performed in two steps, due to the impossibility to find suitable reaction conditions for the simultaneous reduction of the double bond and the nitrile. The first step was the hydrogenation of the double bond under H_2 atmosphere, using palladium on charcoal as catalyst, affording compound **27** in good yield, followed by reduction of the nitrile group, carried out with $LiAlH_4$. Protected **3-PPA** (**28**) was then finally isolated.

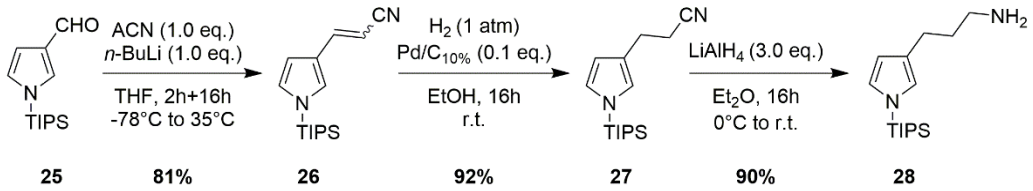

Scheme 4.12 Introduction of the primary amino group.

The last step of the synthetic route to **3-PPA** was TIPS deprotection, which is commonly performed by treatment with tetrabutylammonium floride (TBAF) for 30 min.,[95] followed by purification by column chromatography. In our case, only a small amount of product was recovered after deprotection (equal to 10% yield), accompanied by a large amount of tetrabutylammonium salts. To try to overcome this problem, the deprotection was tried using different deprotecting agents, such as CsF[96] (a fluoride salt more soluble in organic media) and some strong inorganic bases which are known to be usually able remove TIPS (as for instance in the first attempts for the synthesis of the aldehyde **25**).[97] Different reaction times were used and the reaction were all performed at r.t. to hinder the polymerization of the pyrrole derivative. The results obtained are reported in Table 4.13. Unfortunately, deprotection of TIPS was never observed in these conditions and only compounds deriving from the polymerization of the pyrrole derivative were obtained. The last deprotection attempt was performed using TBAF and adding maleic acid to the mixture , hoping to isolated the deprotected product as the corresponding maleate salt.[98] After the end of the reaction, Et_2O was added to the solution as an anti-solvent to trigger the precipitation of the salt, and the mixture was kept at –5°C for 16h. Unfortunately, after filtration of the solid present in suspension, only a small amount of the **3-PPA** ammonium maleate salt was isolated, equal to 2% yield (Entry 5, Table 4.13).

*Table 4.13 Deprotection conditions tested on compound **28**.*

Entry	Reactant	Solvent	Time	Result
1	TBAF 1 M	THF	30min	10% yield
2	NaOH 1 M	H_2O/AcOEt	30min	No deprotection
3	KOH 1 M	H_2O/THF	16h	No deprotection
4	CsF 0.2 M	H_2O/THF	5h	No deprotection
5	TBAF 1 M + Maleic acid (1.0 eq.)	EtOH/Et_2O	50min + 16h	2% yield[a]
[a] calculated by LC-MS on the maleic salt of **3-PPA**.				

Due to these unsuccessful results we decided to focus on a different molecule. Indeed, the low yield obtained in the deprotection step effectively prevented application of **3-PPA** in the hydrogels synthesis, where hundreds of milligrams of compounds would be needed for each sample. The target molecule we chose was **1-PPA** where the aminopropyl chain is moved from the 3-position to the 1-position, on the nitrogen, hoping not to affect the physical properties of the molecule too much. The new compound **1-PPA** could indeed be obtained in only one step by nucleophilic addition of pyrrole on 3-bromopropylamine (**29**) (Scheme 4.13).

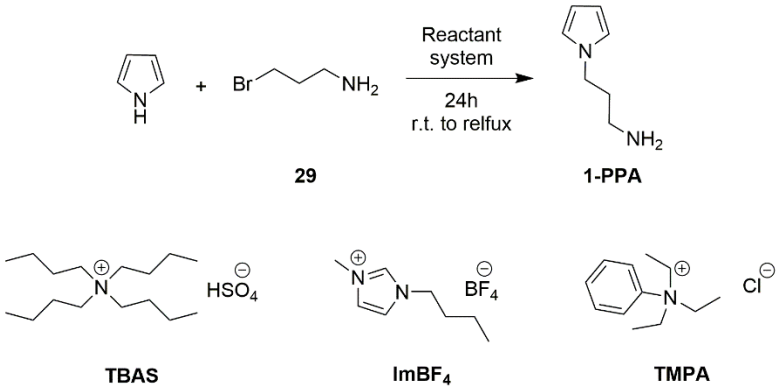

Entry	Reactant system	Solvent	Result
1	TBAS/NaOH	ACN	19% yield
2	$ImBF_4$/NaOH	ACN	No reaction
3	TMPA/NaOH	ACN	15% yield
4	LDA	THF	No reaction
5	EtONa	THF	Side products

*Scheme 4.13 Tested conditions for the synthesis of **1-PPA**.*

In a typical synthesis,[99] pyrrole was deprotonated by NaOH in acetonitrile with the assistance of tetrabutylammonium hydrogensulfate (TBAS) as phase transfer agent, followed by addition of the hydrobromide of amine **29**. After the synthesis, successive extractions allowed to collect the desired product **1-PPA** with 19% yield (Scheme 4.13, Entry 1). In order to increase the yield, different phase transfer agents and bases were tested. Among the heterogeneous systems, a result similar to that obtained with TBAS was observed using NaOH as base and trimethylphenylammonium chloride

(TMPA) as phase-transfer agent, while employment of 1-butyl-3-methylimidazolium tetrafluoroborate ($ImBF_4$) allowed only the recovery of the bare pyrrole (Scheme 4.13, respectively Entry 2 and 3). On the other hand, when we tried to employ an organic base, the desired product was never detected in the reaction mixture: with LDA no reaction at all was observed, while with EtONa only the polymerization of bromoamine **29** occurred (Scheme 4.13, respectively Entry 4 and 5). Trying to avoid this side-process and to simplify the purification, Boc-protected compound **30**[100] was prepared and reacted with pyrrole in the presence of TBAS/NaOH (conditions in Scheme 4.13, Entry 1).

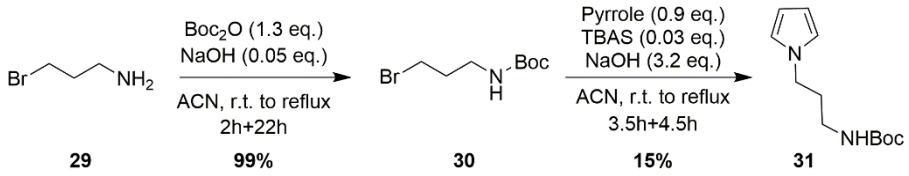

*Scheme 4.14 Synthesis of the protected **1-PPA**.*

Unfortunately, once again, after purification on column chromatography, compound **31** was isolated only with 15% yield. Finally we decided to use conditions reported on Entry 1 (Scheme 4.13) which resulted as the most convenient synthetic pathway for the synthesis of **1-PPA** which was finally prepared, even if with a very low yield, and employed in the next experiments.

4.2.3.2. Synthesis of Covalently Linked Conductive Hydrogels

At this stage, hydrogel synthesis was repeated introducing the two functional monomers (**ABA** and **1-PPA**) in the reaction mixture. Due to its commercially availability, preliminary experiments were performed with **ABA**, in order to find the optimal ratio between the starting materials. To avoid changing the basic structure of the matrix and the original degree of crosslinking, varying amounts of **ABA** were introduced together with GABA in the hydrogel formulation, but their sum was kept constant, so that also the total amount of primary amino group was kept constant during the gelation process (Scheme 4.14).

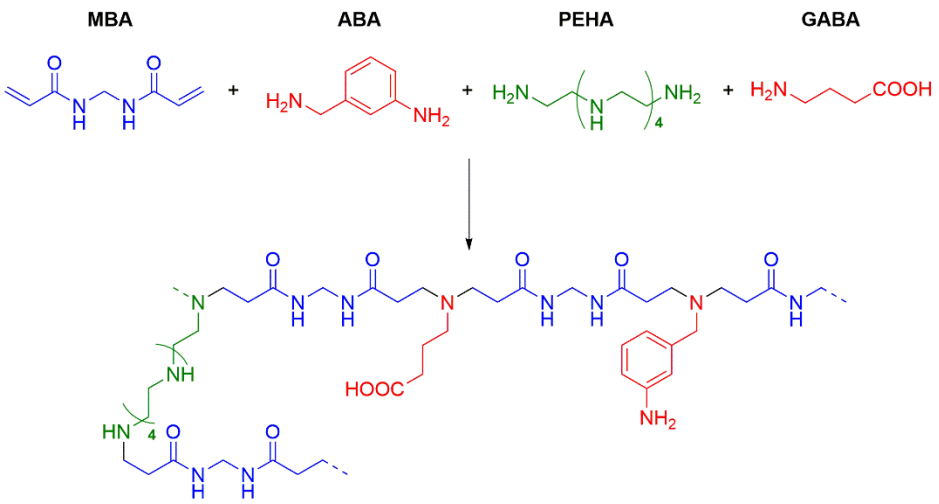

*Figure 4.34 Representation of the structure of the PAA-hydrogel modified with the introduction of **ABA**.*

Table 4.14 Screening on the amount of ABA in the typical hydrogel formulation.

Entry	% ABA	GABA (mmol)	ABA (mmol)	Other reagents
1	0	0.49	-	MBA: 1.3 mmol PEHA: 0.31 mmol H_2O: 1.5 mL
2	10	0.44	0.05	
3	25	0.37	0.12	
4	33	0.33	0.16	
5	42	0.28	0.21	
6	50	0.25	0.25	
7	66	0.26	0.33	
8	75	0.12	0.37	
9	100	-	0.49	

The different amount of **ABA** tested and the hydrogel formulations used are reported in Table 4.14; the procedure employed was the same of the classic PAA-hydrogel, corresponding to the Entry 1 in Table 4.14. The gelation occurred for all formulations and we were able to swell all the samples without observing any leeching of organic compounds.

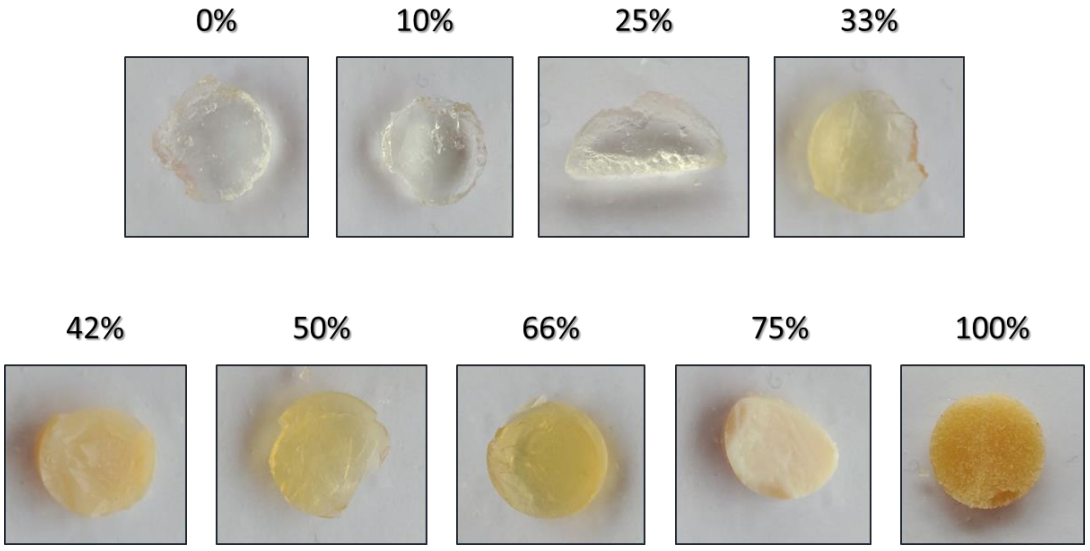

*Figure 4.35 Aspect of the hydrogels containing different amount of **ABA** (% on top of each picture).*

The aspect of the swollen hydrogels is reported in Figure 4.35. As can be seen, hydrogels with an higher amount of **ABA** presented a yellow color, directly depending form the partial oxidation of the functionalized aniline, and were more opaque. This last observation can be explained by the different kind of aggregation and structure that the hydrogels could assume after the introduction of an high amount of an hydrophobic compound. In particular, the sample where all GABA was replaced by **ABA** (100% in Figure 4.35) exhibit a sponge-like structure, completely different from the usual homogeneous aspect of a classical hydrogel. As usual, the EDS value and the morphology (SEM) of each sample were assessed in order to characterize the properties of the novel hydrogels.

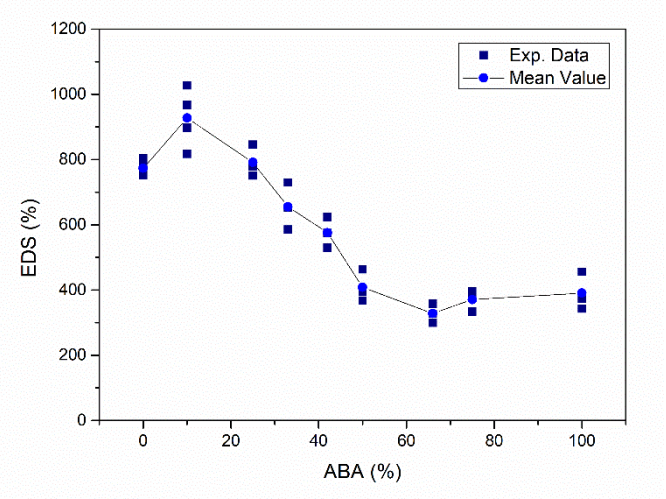

*Figure 4.36 EDS evolution with different amount of **ABA** in the hydrogel.*

As can be seen from Figure 4.36, by increasing the amount of **ABA** inside the hydrogel matrix a drop in the EDS value was observed, until it reached a stable value at *ca.* 370% for %ABA > 60%. This trend could be explained by taking into account that by replacing a hydrophilic molecule with a more hydrophobic one, the affinity towards water of the entire material decreases. Despite that, the amount of aniline monomer used was not enough to drastically change the global wettability of the hydrogel, which could explain why after a certain amount of GABA was replaced by **ABA**, the drop in EDS stopped and the parameter reached a stable value.

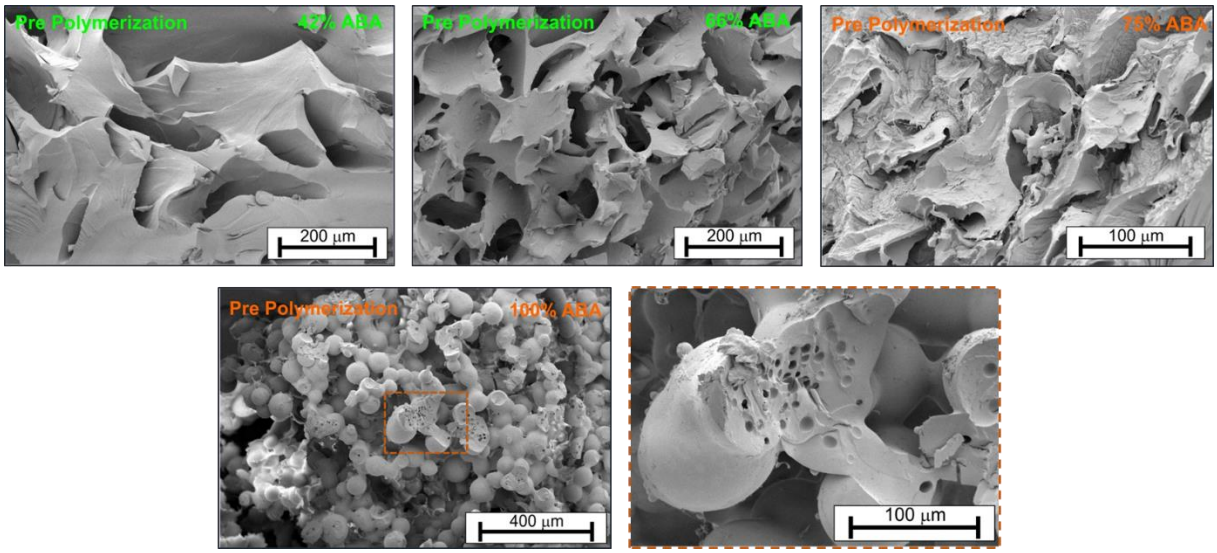

*Figure 4.37 SEM pictures of hydrogels with different amount of **ABA**. On top, from left to right, 42%, 66% and 75%; on bottom, left 100%, right zoom of the previous picture.*

The evolution of the hydrogel structure when increasing the amount of **ABA** during the synthesis can be observed from the SEM pictures in Figure 4.37. When the amount of **ABA** relative to GABA was inferior to the 42%, no substantial change of hydrogel morphology compared to the reference formulation (100% GABA, Figure 4.28) was observed; on the other hand, when higher amounts of aniline monomer were introduced, the structure of the gel matrix began to change. With a percentage of **ABA** comprised between 42% and 75%, a change of the porous structure was observed due to the strengthening of hydrophobic interactions between the various polymer chains (i.e. π-stacking), leading to bigger pores (up to *ca.* 90 µm) with thicker walls. On the other hand, when all GABA was replaced

by the aniline derivative the structure of the hydrogel was completely altered and became almost a "negative" of the classic hydrogel architecture, having only a series of interconnected spheres to construct the matrix rather than a porous network. The cavity between the adjacent spheres formed the "pores" of this particular structure. The spheres appear full, as can be seen from the zoom in Figure 4.37 (bottom, right); indeed, the small holes visible in the figure were not interconnected and part of a bigger network, but seemed to be derived from the evaporation of part of the solvent that was trapped inside the spheres. The reason behind such a great change in the hydrogel structure could be related to the different affinity towards the water of the two components employed: when the hydrophobic **ABA** was used and replaced all the hydrophilic GABA, the polymeric chains tended to organize themselves into a completely different structure from before, in order to maximize the interaction between aromatic rings, exposing the hydrophilic group to the solution and creating the observed spheres. This explanation could also justify the lower EDS value recorded for hydrogels with higher amount of **ABA**, due to the lower hydrophilicity of the aniline co-monomer and to the reduced surface are of the material.

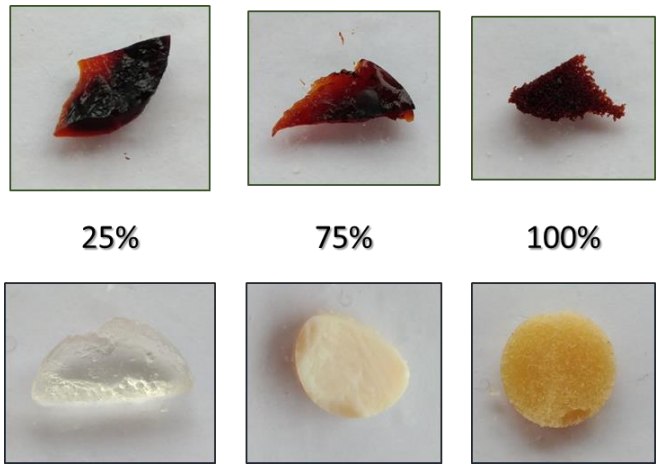

*Figure 4.38 Aspect of the hydrogels containing different amount of **ABA** (% between each pair of pictures) before (bottom) and after (top) the polymerization of the conductive media.*

Subsequently, aniline polymerization was carried out inside the novel hydrogel matrix according to the already optimized two-step procedure (Entry 2, Table 4.9). The aspect of the hydrogels did not differ too much between the different formulations, having the same dark color and compactness (Figure 4.38).Also in this case the novel materials were then characterized recording their EDS and observing their morphology by means of SEM.

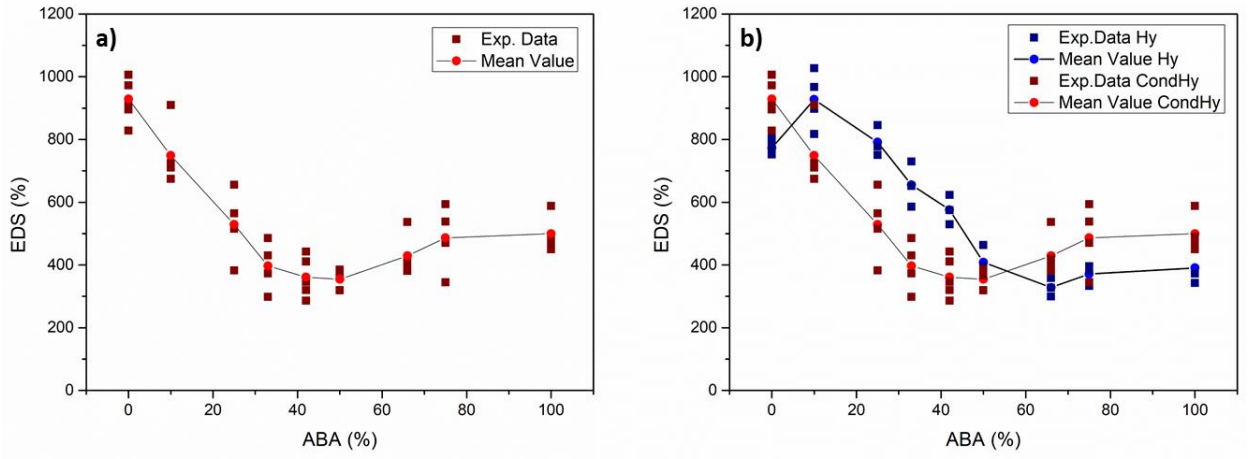

*Figure 4.39 (a) EDS evolution with different amount of **ABA** in the conductive hydrogel, (b) comparison of the EDS trend before and after the polymerization of the conductive polymer.*

In Figure 4.39 the dependence of the EDS value of the conductive hydrogel on the amount of **ABA** used for the synthesis of the pristine hydrogel is reported, alongside a the comparison with the trend observed before the polymerization of the conductive component. The trend in the conductive hydrogels appeared different, with a sudden drop of the swelling degree with the amount of **ABA**, reaching a minimum value around 40% and then increasing again when the percentage was > 60%. This trend could be explained by considering the hydrophobicity of the molecule introduced and the augmented degree of crosslinking due to the polymerization of the aniline chains of the hydrogel matrix with the aniline in solution while the conductive network was formed. After the polymerization, in fact, protonation of the conductive moiety could increase the network hydrophilicity and then counter the reduction of the water uptake capability due to the increased crosslinking degree of the material. The balance of this two effects lead to a different change in the material EDS value after the polymerization, depending from the amount of **ABA** used in the formulation.

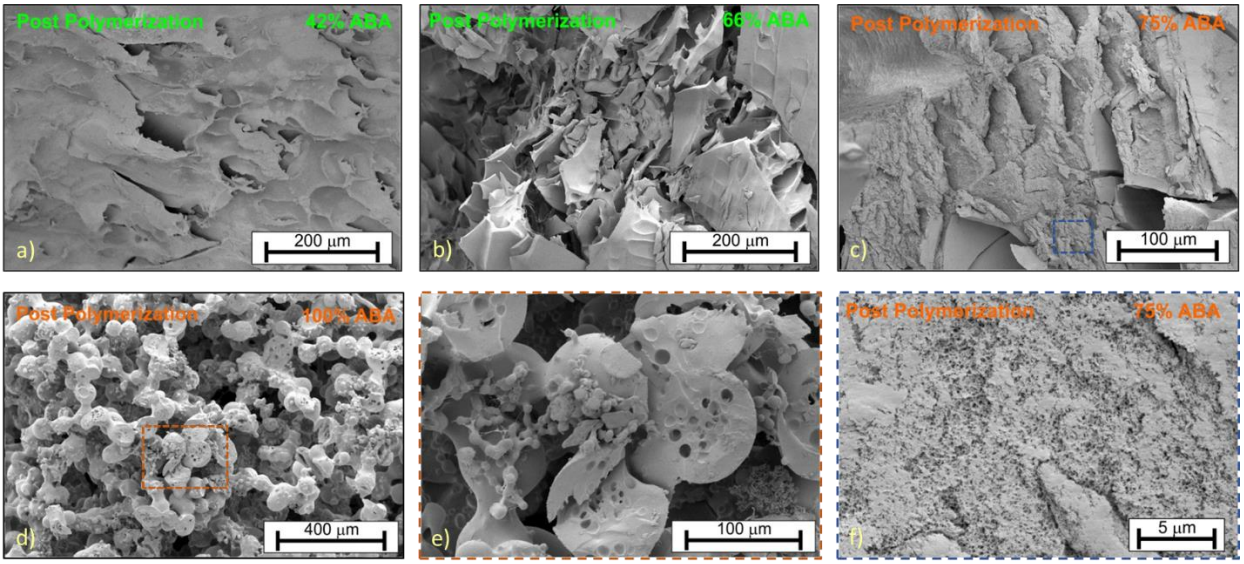

*Figure 4.40 SEM pictures of conductive hydrogels with different amount of **ABA**. On top, from left to right, 42%, 66% and 75%; on bottom, from left to right, 100%, zoom of the 100% **ABA** hydrogel, zoom if the 75% **ABA** hydrogel.*

As can be noticed in Figure 4.40, the hydrogels structure changes a bit after formation of the conductive polymer. The pores were still present, but they were very small in dimensions (as can be seen on the zoom of the conductive hydrogel with 75% **ABA**, Figure 4.40f). This could be caused by the coverage of the pristine hydrogel matrix by a layer of the conductive polymer. The look of the hydrogel with 100% **ABA** (Figure 4.40d) was different: in this case the polymerization of the conductive media caused the formation of other small spheres on the surface of the existing ones (Figure 4.40e), instead of leading to the formation of the homogeneous layer observed for the other hydrogels of the series. The aggregation of PAn in small spheres could be explained in analogy to the considerations already presented for the particular structure of the hydrogel with this formulation. The presence of hydrophobic interactions of the aniline in solution with the **ABA** chains from the hydrogel network could promote the aggregation of the novel polymeric chains of the conductive media into small hydrophobic spheres in order to maximize these interactions and reduce those with the aqueous solution.

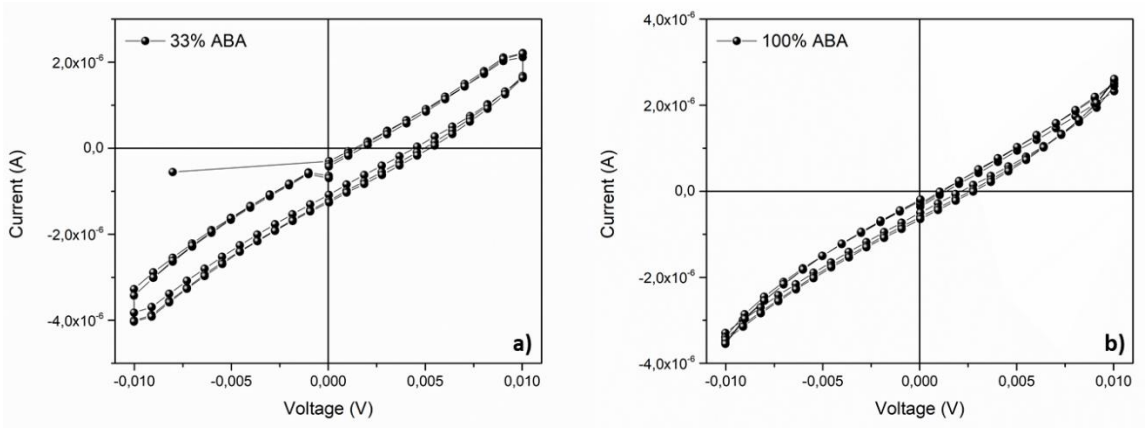

*Figure 4.41 Current/voltage graphs of conductive hydrogels with (a) 33% and (b) 100% **ABA**.*

Finally, the resistance of the ABA-conductive hydrogels was evaluated by means of the four-points probe method. The samples analyzed were those with 33%, 50%, 66% and 100% of **ABA**. In Figure 4.41 two exemplificative current/voltage graphs of the series are reported, while in Figure 4.42 the resistivity/voltage graphs for all the hydrogel samples analyzed are showed.

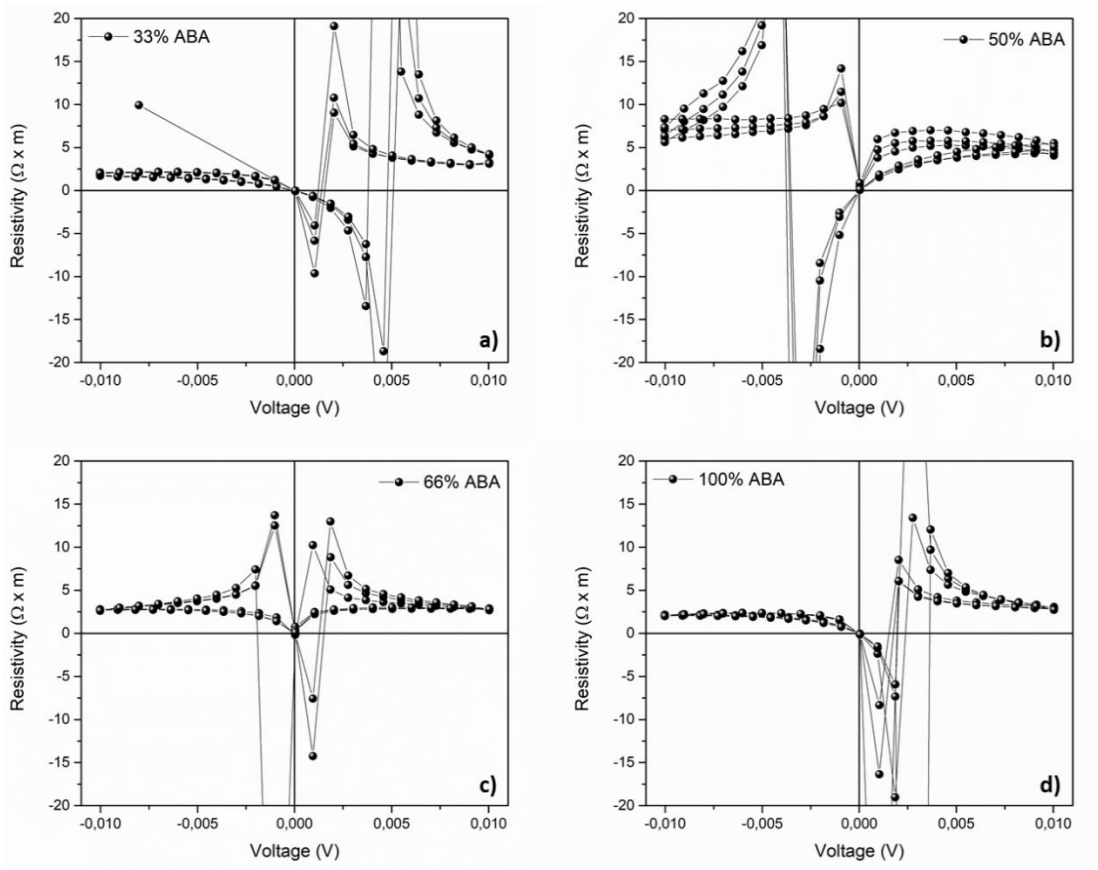

*Figure 4.42 Resistivity/voltage graphs of conductive hydrogels with (a) 33%, (b) 50%, (c) 66% and (d) 100% **ABA**.*

The current/voltage graphs were very similar for all the samples and showed an analogous behavior for the hydrogels with and without **ABA** (see for comparison Figure 4.31). The current registered was low in all the cases, but the all curves did not show any significant drop in activity, sign of the stability of the conducting material. The resistivity was evaluated from the graphs reported in Figure 4.42 and

as can be seen, the values obtained were similar for all the samples (Table 4.15) and, unfortunately, also to those obtained for the undoped PAn-conductive hydrogel without covalent linkage (Table 4.12).

*Table 4.15 Conductivity and resistivity values obtained for the **ABA**-conductive hydrogels of the series.*

Amount of ABA	Resistivity (Ω × m)	Conductivity (mS/cm)
33%	2.8	3.6
50%	5.7	1.7
66%	2.7	3.7
100%	2.5	4.1

To conclude the screening, the employment of **1-PPA** was tested as well. To this end, a hydrogel were all the GABA was replaced with the functionalized pyrrole was synthetized in analogy to what already experimented with **ABA** (Figure 4.43). The pyrrole-based monomer resulted to be not completely soluble in water and the formation of a small drops inside the stirred solution was observed. Anyway, after about 30min, when all the MBA was solubilized due to the start of the *Aza*-Michael reaction, the disappearance of the suspended **1-PPA** was observed as well, implying its participation to the reaction. After gel formation, the polymerization of the pyrrole inside the obtained matrix was carried out following the previously developed procedure with APS (see Chapter 4.2.2.2), leading to the production of the conductive hydrogel with the doped PPy.

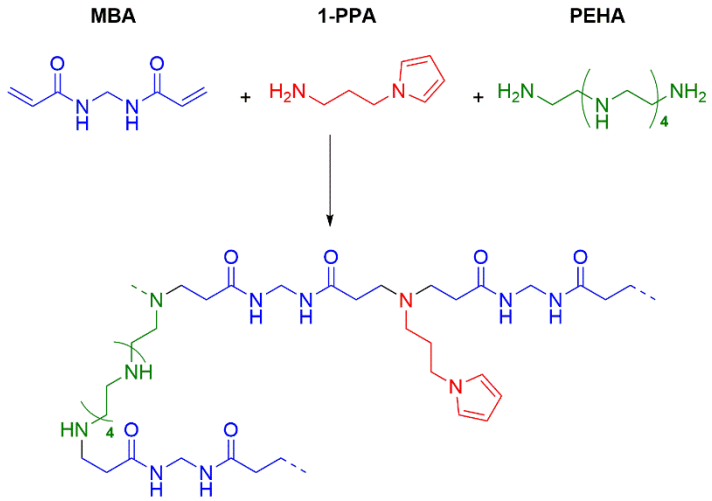

*Figure 4.43 Representation of the structure of the PAA-hydrogel modified with the introduction of **1-PPA**.*

The polymerization of the PPy occurred without problems and the conductive hydrogel was isolated as well. Then, the morphology of the novel material was analyzed by means of SEM to check if also with the pyrrole a structure similar to those observed for the PAn had been obtained (in Figure 4.44 with the SEM picture of the corresponding 100% **ABA** hydrogel).

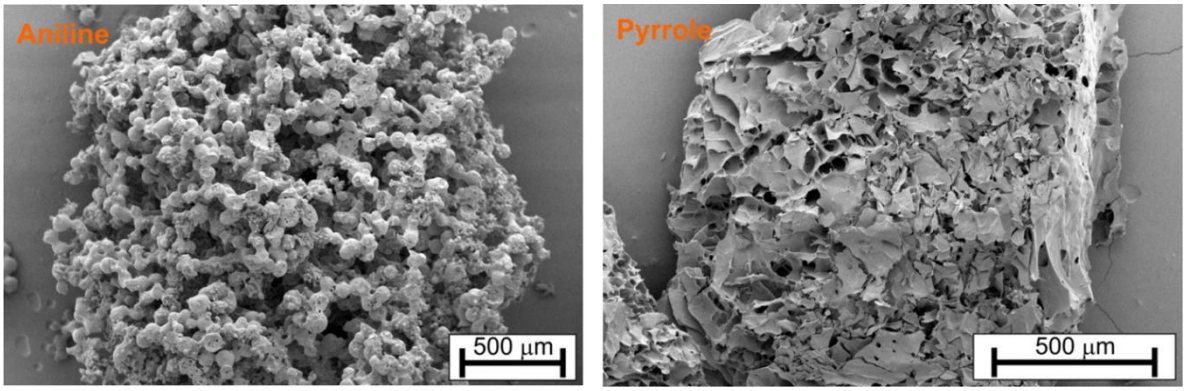

*Figure 4.44 Comparison between (left) the PAn-conductive and (right) the PPy-conductive hydrogels obtained by replacing all the GABA in the basic formulation with, respectively, **ABA** and **1-PPA**.*

The comparison shows how the structure of the PPy-doped hydrogel resulted similar to those of classical hydrogels, namely a polymeric network having a porous structure. Even the pores showed a similar dimensions to those already observed in the pristine hydrogels (see Figure 4.28), with diameter comprised between 25 and 70 µm. The difference relative to the PAn hydrogels (Figure 4.40) could be explained considering the lower degree of aromaticity of the pyrrole derivative, which decreases the efficiency of the π-stacking interactions: if the hydrophobic interactions were not strong enough, probably the lower energy structure for the polymeric chains resulted scattered instead of ordered with a spherical shape, so as to maximize the H-bonds and the electrostatic interactions with the solvent.

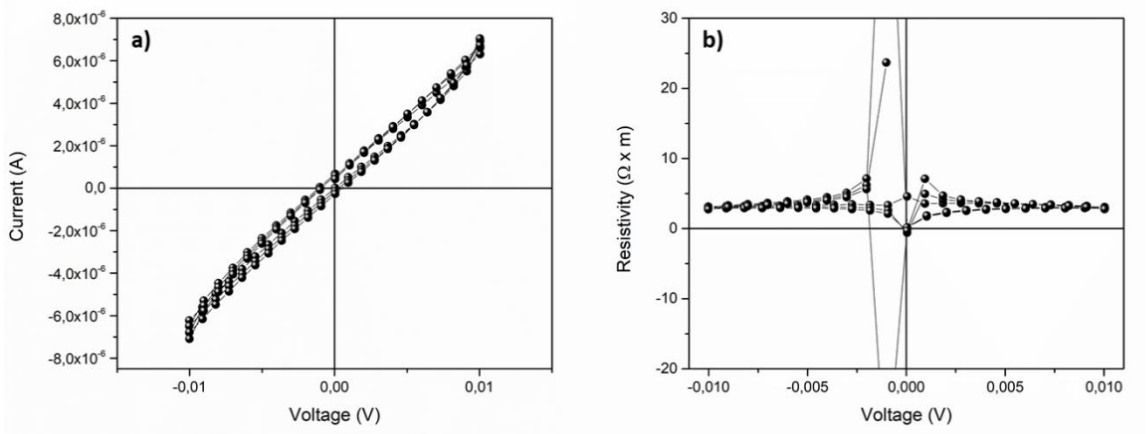

*Figure 4.45 (a) Current/voltage and (b) Resistivity/voltage graph for the **1-PPA** conductive hydrogel.*

Finally, the resistivity was evaluated with the four-points probe method. As can be seen in Figure 4.45, also in this case the resistivity registered (3.5 Ω × m) and the relative conductivity value (2.9 mS/cm) were not different from what previously observed for the traditional PPy-conductive hydrogel not having a covalent link between the two different networks.

The obtained data did not show any significant disadvantage in the use of conductive hydrogels where a stable linkage between the two network was established, if compared to the “classic” ones. The conductivity values did not improved after the modifications on the hydrogel formulation introduced, but a proper rheological characterization could clarify if an increment of the physical properties was achieved. A critical evaluation of this new procedure must take into account the existing difficulties for the identification of the covalent link between the hydrogel matrix and the conductive polymer. Additional work could improve the knowledge of the double network structure properties and give an input to the material design and achieve better electrochemical and physical properties.

4.3. Conclusions

This part of the PhD work was focused on the development of novel conducting hydrogels starting from a non-conductive platform. The first part of the study was focused onto the development of a solid procedure for the introduction of a conductive polymer inside the hydrogel matrix. For this purpose, a novel acrylamide-based formulation was developed upon the synthesis of the right crosslinker, **tEGDA**. Gelation of the matrix was achieved by treatment with APS and the procedure was optimized in order to obtain a good reference material. After that, the introduction of a commonly used conductive polymer, polyaniline, was performed using two different procedures and by varying the polymerization conditions. Physical, morphological and electrochemical characterization of the material allowed us to identify the best conditions to carry out the growth of PAn inside an hydrophilic network. The conductivity of the final hybrid material was obtained by EIS analysis and showed to be order of magnitude higher than that of the pristine hydrogel and to be further enhanced by performing doping of the conductive polymer introduced in the matrix.

The developed methodology has been then applied to another hydrogel matrix with different chemical structure, obtained with another gelation reaction which does not need any initiator (*Aza*-Micheal reaction). The methodology was optimized with the new matrix using the PAn as reference polymer and the novel conductive hydrogel was characterized. The conductivity of the novel materials before and after doping was recorded with a four-points probe method, and was in line with the value registered for the polyaniline in the acrylamide-based formulations. The possibility to introduce PPy and PEDOT conductive polymers characterized with milder polymerization conditions inside the hydrogel matrix was also studied. Also in this case the conductivity was recorded. In general different material showed a similar behavior, but a trend could be individuated, with the PEDOT being the best performing one, along with doped PAn. In general these values were in line with the typical range observed with this kind of material.

In the last part of the work the possibility of introducing a covalent linkage between the two different networks of a conductive hydrogel was attempted with the aim of increasing the interaction among them and maybe enhance the final properties of the material. Two particular monomers (**ABA** and **3-PPA**) were selected to be introduced in the hydrogel backbone for perform the covalent bond. While **ABA** was commercially available, **3-PPA** had to be synthetized and a retrosynthetic plan was designed. Unfortunately, despite several efforts it was not possible to achieve the suitable monomer in reasonable yield. Finally **1-PPA**, which differed from **3-PPA** only for the position of the side chain, was used and a screening on the loading of the new components inside the hydrogel matrix was performed using **ABA** in order to identify the best conditions for maximizing the final material properties. Different amounts of **ABA** were used while replacing GABA and a series of novel hydrogels was synthetized. Their morphology and EDS values were recorded and discussed. Finally, the samples were used to prepare a conductive hydrogels. A conductive hydrogel containing **1-PPA** was also synthetized. In both cases the conductivity value recorded did not show any significant due to the introduction of **ABA** and **1-PPA** moieties.. Further work could be able improve both the design and the electrochemical properties of these hybrid hydrogels.

4.4. Experimental Section

4.4.1. Synthetic Procedures

Triethylene glycol diacrylate (tEGDA)

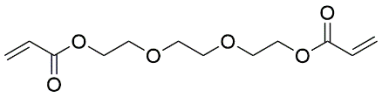

tEGDA

In a flame-dried round bottom flask, under nitrogen atmosphere, triethylene glycol (1.13 g, 7.5 mmol, 1.0 eq.) was dissolved in dry DCM (20 mL) and then, under vigorous stirring, distilled NEt_3 (2.31 g, 22.5 mmol, 3.0 eq.) was added. The solution was cooled down to 0°C and acryloyl chloride (1.56 g, 17.3 mmol, 2.3 eq.) was added dropwise. The obtained suspension was then allowed to react for 16h, while the temperature slowly reached r.t.. The suspension was then filtered through Celite® and the obtained solution was washed with H_2O (2 × 50 mL) and brine (60 mL). The organic phase was finally dried over Na_2SO_4 and the solvent evaporated, giving a dark yellow oil. The purification by flash column chromatography (SiO_2, PE/AcOEt 3:1 to 1:2) allowed to recover the purified product as a pale yellow liquid (1.27 g, 4.9 mmol, 65% yield).

^{1}H-NMR ($CDCl_3$, 300 MHz): δ (ppm) 6.42 (dd, *J* = 17.3, 1.4 Hz, 2H), 6.15 (dd, *J* = 17.3, 10.4 Hz, 2H), 5.83, (dd, *J* = 10.4, 1.4 Hz, 2H), 4.35-4.32 (m, 4H), 3.78-3.74 (m, 5H), 3.69 (s, 3H).

The spectroscopic data were in agreement with those reported in the literature.[64]

4.4.1.1. General Procedure for Pyrrole protection

In a flame-dried round bottom flask, under nitrogen atmosphere, distilled pyrrole (95 mg, 1.42 mmol, 1.0 eq.) was dissolved in dry THF (6.5 mL) and cooled down to –78°C. Then, *n*-BuLi (1.6 M solution in hexanes, 1.0 mL, 1.60 mmol, 1.1 eq.) was slowly added under stirring and the solution was allowed to react for 1h. After that, the proper chlorosilane (1.42 mmol, 1.0 eq.) was added and the mixture was allowed to react for 16h allowing the temperature to rise slowly from –78°C to r.t.. Then, THF was evaporated, $NaHCO_3$ (aq.) (25 mL, ss.) was added and the aqueous solution was extracted with DCM (3 × 25 mL). The reunited organic phases were washed with brine (25 mL) and then dried over Na_2SO_4. Finally, the solvent was removed under reduced pressure, affording the desired product.

1-(Triethylsilyl)-1*H*-pyrrole (21)

21

Prepared starting from triethyl chloride (214 mg). Collected as a pale yellow oil, which was used without further purification for the next step (229 mg, 1.26 mmol, 89% yield).

^{1}H-NMR (C_6D_6, 300 MHz): δ (ppm) 6.75 (s, 2H), 6.52 (s, 2H), 0.80 (t, *J* = 7.5 Hz, 9H), 0.63 (q, *J* = 7.4 Hz, 6H).

The spectroscopic data were in agreement with those reported in the literature.[101]

1-(*tert*-Butyldimethylsilyl)-1*H*-pyrrole (22)

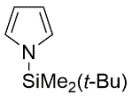

22

Prepared starting from *tert*-butyldimethylsilyl chloride (214 mg). Collected as a brown oil, which was used without further purification for the next step (200 mg, 1.12 mmol, 78% yield).

^{1}H-NMR ($CDCl_3$, 400 MHz): δ (ppm) 6.80 (s, 2H), 6.33 (s, 2H), 0.89 (s, 9H), 0.44 (s, 6H).

The spectroscopic data were in agreement with those reported in the literature.[102]

1-(Triisopropylsilyl)-1*H*-pyrrole (23)

23

Prepared starting from triisopropylsilyl chloride (274 mg). Collected as a brown oil, which was used without further purification for the next step (314 mg, 1.41 mmol, 99% yield).

^{1}H-NMR ($CDCl_3$, 400 MHz): δ (ppm) 6.81 (s, 2H), 6.32 (s, 2H), 1.46 (sept, *J* = 7.6 Hz, 3H), 1.10 (d, *J* = 7.6 Hz, 18H).

The spectroscopic data were in agreement with those reported in the literature.[95]

4.4.1.2. Other synthetic procedures

3-Bromo-1-(triisopropylsilyl)-1*H*-pyrrole (24)

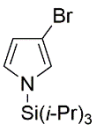

24

In a flame-dried round bottom flask, under nitrogen atmosphere, protected pyrrole **23** (148 mg, 0.66 mmol, 1.0 eq.) was dissolved in dry THF (2.5 mL) and cooled down to –78°C. Then, NBS (118 mg, 0.66 mmol, 1.0 eq.) was added under stirring and the solution was allowed to react for 1.5h at this temperature. After that,

the mixture was kept under stirring for further 1.5h, allowing the temperature to slowly rise to r.t.. Pyridine (25 µL) and hexane (2.5 mL) were then added under stirring to the solution, leading to the precipitation of a white solid. The suspension was filtered on a short pad of Celite®, the solid was washed with hexane and the yellow liquid part was recovered. The solution was then diluted with AcOEt (20 mL) and washed with H_2O (3 × 25 mL). The recovered organic phase was finally dried over Na_2SO_4 and the evaporation of the solvent allowed to collect the desired product **24** as a dark yellow oil which was used without further purification for the next step (187 mg, 0.62 mmol, 94% yield).

^{1}H-NMR ($CDCl_3$, 400 MHz): δ (ppm) 6.73 (bs, 1H), 6.67 (bs, 1H), 6.29 (bs, 1H), 1.42 (sept, *J* = 7.6 Hz, 3H), 1.09 (d, *J* = 7.6 Hz, 18H).

The spectroscopic data were in agreement with those reported in the literature.[95]

1-(Triisopropylsilyl)-1*H*-pyrrole-3-carbaldehyde (25)

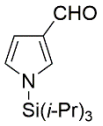

25

In a flame-dried round bottom flask, under nitrogen atmosphere, bromo pyrrole **24** (1.37 g, 4.5 mmol, 1.0 eq.) was dissolved in dry THF (14 mL) and cooled down to –78°C. Then, *n*-BuLi (1.6 M solution in hexanes, 2.8 mL, 4.5 mmol, 1.0 eq.) was slowly added under stirring and the solution was allowed to react for 20min. After that, distilled DMF (0.33 g, 4.5 mmol, 1.0 eq.) was added under stirring and the solution was allowed to react for 20min at –78°C. The mixture was kept under stirring for other 16h, while the temperature was allowed to slowly rise to r.t.. The solution was then diluted with Et_2O (20 mL) and washed with H_2O (3 × 50 mL). The recovered organic phase was finally dried over Na_2SO_4 and the evaporation of the solvent allowed to collect the desired product **25** as a dark yellow oil which was used without further purification for the next step (1.11 g, 4.41 mmol, 98% yield).

^{1}H-NMR ($CDCl_3$, 400 MHz): δ (ppm) 9.82 (s, 1H), 7.41 (bs, 1H), 6.78 (bs, 1H), 6.75 (bs, 1H), 1.48 (sept, *J* = 7.6 Hz, 3H), 1.11 (d, *J* = 7.6 Hz, 18H).

The spectroscopic data were in agreement with those reported in the literature.[95]

3-(1-(Triisopropylsilyl)-1*H*-pyrrol-3-yl)acrylonitrile (26)

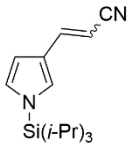

26

In a flame-dried round bottom flask, under nitrogen atmosphere, dry ACN (0.28 g, 4.5 mmol, 1.0 eq.) was dissolved in dry THF (13 mL) and cooled down to –78°C. Then, *n*-BuLi (1.6 M solution in hexanes, 2.8 mL, 4.5 mmol, 1.0 eq.) was slowly added under stirring and the solution was allowed to react for 30 min. In another

flame-dried round bottom flask, under nitrogen atmosphere, aldehyde **25** (1.12 g, 4.5 mmol, 1.0 eq.) was dissolved in dry THF (5 mL) and then added to the first solution; the mixture was allowed to react for 1.5h at –78°C. After that, the solvent was evaporated and the solid dissolved again in DCM (15 mL). HCl 3 M (2 mL) was added and the mixture was stirred for 16h at 35°C. Then the organic phase was collected and washed with H_2O (2 × 80 mL) and brine (80 mL), and finally dried over Na_2SO_4. Evaporation of the solvent allowed to collect the desired product **26** as a mixture of the *E*/*Z* isomers in a ratio ≈ 1:1 in the form of a brown oil, which was used without further purification for the next step (1.06 g, 3.6 mmol, 81% yield).

^{1}H-NMR ($CDCl_3$, 400 MHz): δ (ppm) 7.32 (d, *J* = 16.4 Hz, 1H), 7.22 (s, 1H), 6.78 (s, 1H), 6.75 (s, 1H), 5.45 (d, *J* = 15.3 Hz, 1H), 1.51-1.40 (m, 3H), 1.10 (d, *J* = 7.6 Hz, 9H), 1.09 (d, *J* = 7.5 Hz, 9H).

^{1}H-NMR ($CDCl_3$, 400 MHz): δ (ppm) 7.04 (d, *J* = 12.0 Hz, 1H), 6.97 (s, 1H), 6.93 (s, 1H), 6.46 (s, 1H), 5.01 (d, *J* = 11.3 Hz, 1H), 1.51-1.40 (m, 3H), 1.10 (d, *J* = 7.6 Hz, 9H), 1.09 (d, *J* = 7.5 Hz, 9H).

The spectroscopic data were in agreement with those reported in the literature.[103]

3-(1-(Triisopropylsilyl)-1*H*-pyrrol-3-yl)propanenitrile (27)

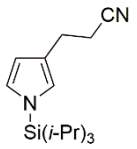

27

In a round bottom flask, under nitrogen atmosphere, pyrrole **26** (1.06 g, 3.6 mmol, 1.0 eq.) was dissolved in EtOH (35 mL) and the catalyst, Pd/C (0.49 g, 0.36 mmol, 0.1 eq.), was added. Then a baloon filled with H_2 (1 atm) was connected to the flask. The mixture was then stirred under these conditions at r.t. for 16h. After that, the suspension was filtered through Celite®; the solid was washed several times with AcOEt and the solution was collected. Evaporation of the solvent allowed to collect the desired product **27** as a brown oil, which was used without further purification for the next step (0.98 g, 3.3 mmol, 92% yield).

^{1}H-NMR ($CDCl_3$, 400 MHz): δ (ppm) 6.70 (s, 1H), 6.63 (s, 1H), 6.17 (s, 1H), 2.83 (dd, *J* = 7.6, 6.9 Hz, 2H), 2.54 (dd, *J* = 7.6, 6.9 Hz, 2H), 1.42 (sept, *J* = 7.6 Hz, 3H), 1.08 (d, *J* = 7.6 Hz, 18H).

^{13}C-NMR ($CDCl_3$, 100 MHz): δ (ppm) 124.7, 122.3, 121.7, 119.9, 110.2, 23.4, 19.5, 17.8, 11.7.

ESI-MS (*m/z*) = 277.24 $[M+1]^+$.

3-(1-(Triisopropylsilyl)-1*H*-pyrrol-3-yl)propan-1-amine (28)

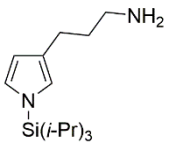

28

In a flame-dried round bottom flask, under nitrogen atmosphere, nitrile **27** (0.62 g, 2.1 mmol, 1.0 eq.) was dissolved in dry Et_2O (35 mL) and the solution was cooled down to 0°C. Then $LiAlH_4$ (0.24 g, 6.3 mmol, 3.0

eq.) was added under stirring and the suspension was allowed to react for 16h, while the temperature slowly rose to r.t.. Then, the reaction mixture was cooled down again to 0°C and H_2O (2.5 mL), NaOH 15% (2.5 mL) and H_2O (7.5 mL) were added in this order under vigorous stirring; the suspension was then kept under stirring for 15 min. Na_2SO_4 (3.5 g) was added and the mixture was stirred for another 15min at r.t.. After that, the suspension was filtered through Celite® and the liquid phase was collected. Evaporation of the solvent allowed to collect the desired product **28** as a brown oil, which was used without further purification for the next step (0.57 g, 1.9 mmol, 90% yield).

^{1}H-NMR ($CDCl_3$, 400 MHz): δ (ppm) 6.69 (bs, 1H), 6.52 (bs, 1H), 6.14 (bs, 1H), 2.71 (t, *J* = 7.0 Hz, 2H), 2.53 (t, *J* = 7.5 Hz, 2H), 1.78-1.69 (m, 2H), 1.41 (sept, *J* = 7.6 Hz, 3H), 1.08 (d, *J* = 7.6 Hz, 18H).

^{13}C-NMR ($CDCl_3$, 100 MHz): δ (ppm) 125.7, 124.2, 121.2, 110.7, 41.9, 35.1, 24.5, 18.0, 11.8.

ESI-MS (*m/z*) = 281.28 $[M+1]^+$.

3-(1*H*-Pyrrol-3-yl)propan-1-amine (3-PPA)

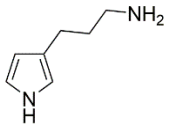

3-PPA

In a flame-dried round bottom flask, under nitrogen atmosphere, protected pyrrole **28** (100 mg, 0.33 mmol, 1.0 eq.) was dissolved in dry THF. Then TBAS (1 M in THF, 350 µL, 0.35 mmol, 1.1 eq.) was added and the solution was kept under stirring at r.t. for 30min. Then, the solvent was evaporated under reduced pressure and the mixture was directly purified by flash column chromatography (SiO_2, DCM + 2% NEt_3). The isolated colorless oil was still not pure, as showed by the ^{1}H-NMR analysis, and therefore it was diluted with DCM (10 mL) and washed with H_2O (2 × 10 mL). The organic phase was dried over Na_2SO_4 and the evaporation of the solvent allowed to collect the desired product **3-PPA** as a brown oil still containing traces of the deprotecting agent (5 mg, 0.03 mmol, 10% yield).

^{1}H-NMR ($CDCl_3$, 400 MHz): δ (ppm) 8.16 (bs, 1H), 6.72 (bs, 1H), 6.59 (bs, 1H), 6,08 (bs, 1H), 2.78 (t, *J* = 7.0 Hz, 2H), 2.55 (t, *J* = 7.4 Hz, 2H), 1.83-1.75 (m, 2H).

ESI-MS (*m/z*) = 125.05 $[M+1]^+$.

3-(1*H*-Pyrrol-1-yl)propan-1-amine (1-PPA)

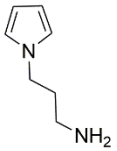

1-PPA

In a flame-dried round bottom flask, under nitrogen atmosphere, distilled pyrrole (0.50 g, 7.5 mmol, 1.00 eq.) was dissolved in dry ACN (5 mL). Then, ground NaOH (1.15 g, 29.0 mmol, 3.80 eq.) and TBAS (0.10 g, 0.3 mmol, 0.04 eq.) were added in order under vigorous stirring and the suspension was stirred at r.t. for 2h.

After that, 3-bromopropylamine hydrobromide (1.91 g, 8.2 mmol, 1.17 eq.) was added (the suspension turned yellow and then red again), the mixture was heated at reflux and then allowed to react for 22h under stirring. The suspension was then filtered through Celite® and the solid washed with a mixture AcOEt/MeOH 1:1. The collected solution was diluted with other AcOEt (70 mL) and then extracted with H_2O (2 × 80 mL). The pH of the aqueous phase was adjusted to 10 with KOH, then the solution was extracted with DCM (2 × 80 mL). The organic phases were reunited and dried, allowing to retrieve a brown oil. To increase the purity of the compound, the oil was dissolved again in a 1:1 mixture of AcOEt / aq. HCl 1M (60 mL in total), the two phases were separated and then the aqueous one was washed with other AcOEt (2 × 30 mL). After that, the solution was alkalinized again with KOH to pH 10 (the colour change from orange to yellow) and then it was extracted with DCM (3 × 40 mL). Evaporation of the solvent allowed to collect the desired product as an orange oil, pure enough for being used in the next experiments without the need of further purification (177 mg, 1.4 mmol, 19% yield).

When the reaction was performed with other base/catalyst systems, the procedure was exactly the same. With TMPA (68 mg, 0.03 mmol, 0.04 eq.) only a yield of 15% was obtained (140 mg, 1.1 mmol).

^{1}H-NMR ($CDCl_3$, 300 MHz): δ (ppm) 6.65 (bs, 1H), 6.13 (bs, 1H), 3.96 (t, *J* = 6.9 Hz, 2H), 2.70 (t, *J* = 6.8 Hz, 2H), 1.94-1.86 (m, 2H).

The spectroscopic data were in agreement with those reported in the literature.[104]

<u>*tert*-Butyl (3-bromopropyl)carbamate (30)</u>

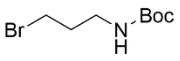

30

In a round bottom flask, under nitrogen atmosphere, 3-bromopropylamine (1.10 g, 5.0 mmol, 1.0 eq.) and di-*tert*-butyl dicarbonate (1.20, 5.5 mmol, 1.1 eq.) were suspended in DCM (25 mL). Then, the mixture was cooled down to 0°C and distilled NEt_3 (0.56 g, 5.5 mmol, 1.1 eq.) was added, allowing to dissolve the solid in suspension. The solution was allowed to react for 16h, while the temperature slowly rose to r.t.. After that, the mixture was diluted with DCM (25 mL) and washed with aq. HCl 0.1M (50 mL), H_2O (2 × 50 mL) and brine (50 mL). The organic phase was finally dried over Na_2SO_4 and the solvent was evaporated under reduced pressure. The desired product was collected as a pale yellow oil, pure enough for being used in the next experiments without the need of further purification (1.15 g, 4.8 mmol, 97% yield).

^{1}H-NMR ($CDCl_3$, 300 MHz): δ (ppm) 4.66 (bs, 1H), 3.44 (t, *J* = 6.6 Hz, 2H), 3.27 (m, 2H), 2.05 (m, 2H), 1.44 (s, 9H).

The spectroscopic data were in agreement with those reported in the literature.[100a]

***tert*-Butyl (3-(1*H*-pyrrol-1-yl)propyl)carbamate (31)**

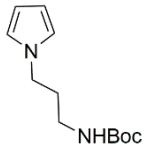

31

In a flame-dried round bottom flask, under nitrogen atmosphere, distilled pyrrole (101 mg, 1.5 mmol, 1.00 eq.) was dissolved in dry ACN (1.5 mL). Then, ground NaOH (230 mg, 5.7 mmol, 3.80 eq.) and TBAS (20 mg, 0.06 mmol, 0.04 eq.) were added in order under vigorous stirring and the suspension was stirred at r.t. for 3.5h. After that, bromide **30** (480 mg, 1.8 mmol, 1.17 eq.) was added (the suspension turned yellow from brown), the mixture was brought to reflux and then allowed to react for 4.5h under stirring. The suspension was then filtered through Celite® and the solid was washed with DCM. The collected solution was purified by flash column chromatography (SiO_2, PE/AcOEt 7:1) and the desired product was obtained as a yellow pale oil in a good purity (52 mg, 0.23 mmol, 15% yield).

^{1}H-NMR ($CDCl_3$, 300 MHz): δ (ppm) 6.65 (d, *J* = 2.0 Hz, 2H), 6.14 (d, *J* = 2.0 Hz, 2H), 4.47 (bs, 1H), 3.93 (t, *J* = 7.0 Hz, 2H), 3.11 (q, *J* = 6.0 Hz, 2H), 2.05 (quint, *J* = 6.8 Hz, 2H), 1.44 (s, 9H).

The spectroscopic data were in agreement with those reported in the literature.[105]

4.4.2. General Procedures for Hydrogels Preparation and Characterization

- **Synthesis of the Acrylamide-based hydrogels; General procedure**

The following procedure[63] reports the amounts of reactants needed in the formulations that showed the best performance (8 and 11, see Chapter 4.2.1.2, respectively Table 4.1 and Table 4.3), but it is valid for all other formulations described in Chapter 4.2.1 by changing the amount of crosslinker and the reaction time according to Table 4.1 and Table 4.3.

In a round bottom flask under stirring, Acr was dissolved in H_2O and the crosslinker, **tEDGA**, was added to the solution. Then, in order, TMEDA and APS were added to the mixture; the stirring bar was removed and the solution kept in static conditions to promote gelation for 30 min. The resulting hydrogel was washed with water several times and kept in water for 2 days (changing the solvent every 6h) before use, to allow the release of all the unreacted starting materials from the gel matrix.

- Large scale procedure (Form. 8): Acr (1.2 g, 16.9 mmol), tEGDA (29 mg, 0.11 mmol), TMEDA (15 mg, 0.13 mmol), APS (7 mg, 0.03 mmol), H_2O (10 mL). The hydrogels were synthetized inside a cylindrical-shape container (volume ≈ 25 mL) and were then cut in pieces of similar dimensions after the synthesis.
- Small scale procedure (Form. 11): Acr (36 mg, 0.5 mmol), tEGDA (8.4 mg, 3.2×10^{-2} mmol), TMEDA (0.45 mg, 3.9×10^{-3} mmol), APS (0.21 mg, 9.0×10^{-4} mmol), H_2O (0.3 mL). The hydrogels were synthetized inside a cylindrical-shape container (volume ≈ 0.5 mL).

- **Sample lyophilization**

Lyophilization, also known as freeze-drying, uses rapid cooling to allow solvent removal by sublimation under vacuum.[106] The scaffolds were swollen in water and frozen at -196 °C in liquid nitrogen for 30min. Then, they were transferred to a lyophilizing jar and lyophilized for 16 hours at a pressure of 150 mT. Lyophilized samples were used right away for SEM analysis and the swelling kinetics. The same procedure was used also for the PAA-based hydrogels.

- **Swelling measurements**

EDS was calculated using the following equation:

$$\mathrm{EDS} = \frac{\mathrm{W_{wet} - W_{dry}}}{\mathrm{W_{dry}}} \times 100$$

where W_{wet} and W_{dry} are, respectively, the weight of the swollen and lyophilized hydrogel measured by gravimetric method. The swollen weight was taken after several measurements when the value was found to be stable (about 2 days), using the hydrogel obtained from the synthesis, not lyophilized. Their surface was blotted free of water using filter paper and their swollen weights were measured on an analytical balance. After that, the samples were lyophilized and the dry weight was recorded. The same procedure was used also for the PAA-based hydrogels.

To determine the stability of the hydrogels at different pH conditions, the samples were incubated in buffer solutions: pH 4.7 (acetate buffer, 0.5 M), pH 9.3 (ammonium buffer, 0.5 M). Their EDS valued were evaluated with the same procedure described above.

- **Swelling kinetics**

Lyophilized cylindrical-shaped hydrogels (diameter of 7 mm and height of 1 mm) were used. The samples were immersed in distilled water and were removed at set time points (after 1, 2, 5, 10, 20, 30 minutes, 1h, 2h, 4h, 8h, 23h, 48h, 72h, 96h). Their surface was blotted free of water using filter paper and their weight was measured on an analytical balance. Then the samples were put again in the same solution. The same procedure was used also for the PAA-based hydrogels.

- **Conductive polymer growth (Polyaniline)**

The samples of pristine hydrogel used could be dried or swollen depending on the particular experiment (see Chapter 4.2.1.3).

- Procedure 1:[68] the samples were put in a solution of distilled aniline (0.1 M) in aq. HCl 1 M for 16h. The samples were then removed, washed with water and put again in a solution of APS (0.1 M) in water for 5h to allow the polymerization of the PAn, in static conditions. After that, the conductive hydrogels were removed from the solution and washed several times with water. The samples were then put in distilled water for 2 days (changing the solvent every 6h) before use, to allow the release of all the unreacted starting materials from the gel matrix.
- Procedure 2:[66b] the samples were put in a solution of APS (0.1 M) in aq. HCl 1 M for 16h. The samples were then removed, washed with water and put again in a solution of distilled aniline (0.1 M) in hexane for 5h to allow the polymerization of the PAn, in static conditions. After that, the conductive hydrogels were removed from the solution and washed several times with water. The

samples were then put in distilled water for 2 days (changing the solvent every 6h) before the use, to allow the release of all the unreacted starting materials from the gel matrix.

- **Determination of the percentage of conducting polymer**

CP(%) was calculated using the following equation:

$$\mathrm{CP}(\%) = \frac{\mathrm{W_{CH}} - \mathrm{W_{PH}}}{\mathrm{W_{CH}}} \times 100$$

where W_{CH} is the dry weight of the conductive hydrogel and W_{PH} is the dry weight of the pristine hydrogel. The hydrogel samples were lyophilized and their W_{PH} was recorded. After that, some samples (see Chapter 4.2.1.3) were rehydrated by immersion in water and kept in the solvent until they reached a constant weight. Both the rehydrated and the dry samples were then used for the polymerization of the conductive moiety as described above. After the polymerization, the conductive hydrogels were kept in water for 2 days (changing the solvent every 6h) to allow the release of all the unreacted starting materials from the gel matrix. After that, they were lyophilized again and the W_{CH} was measured.

- **Environmental scanning electron microscope analysis**

The swollen samples of conductive hydrogel were mounted on aluminum stubs using adhesive carbon tape and directly used for the analysis. ESEM images were captured at 18-20 kV accelerating voltage and 1.00 Torr, using a SEM Philips XL 20 instrument.

- **Doping procedure (Polyaniline)**

To perform the doping, swollen sampled of the conductive hydrogel were put in aq. HCl 1 M and kept in solution for 16h. The samples were then rapidly washed with water before use. The same procedure was used also for PAA-based hydrogels.

- **Electrochemical characterization**

The electrochemical measurements were performed using a Parstat 2273 potentiostat-galvanostat (Princeton Applied Research equipped with a Model 616 rotating disk electrode RDE (PAR-Ametek). The counter electrode was a platinum gauze enclosed in a glass tube with porous bottom. The reference electrode used was commercial Ag/AgCl/KCl_{sat} (Princeton Applied Research).

- Cyclic voltammetry analysis: all cyclic voltammetry potentials are reported against reversible hydrogen electrode (RHE) calculated taking into account the potential-temperature dependence.[107] The potential of silver-silver chloride versus normal hydrogen electrode (NHE) temperature dependence for ranges between 0°C and 95°C is described by:

$$\mathrm{E_{Ag|AgCl|KCl(sat.)}} = 199 - 1.01 \times (\mathrm{T} - 25)$$

with T in °C and $E_{Ag\ |\ AgCl\ |\ KCl(sat.)}$ in mV. The reversible hydrogen electrode (RHE) pH correction temperature dependence is described by:

$$\mathrm{E_{RHE}} = -\frac{\mathrm{RT}}{\mathrm{F}}\, 2.303\ \mathrm{pH}$$

where E_{RHE} is the potential of RHE versus NHE in V, R is the gas constant (8.31 J K^{-1} mol^{-1}), T is temperature in K, F is the Faraday constant (96485 C mol^{-1}). The correction is applied adding $E_{Ag\ |\ AgCl\ |\ KCl(sat.)}$ to the potential referenced *vs.* Ag | AgCl | KCl(sat.) to get the potential *vs.* NHE and then subtracting E_{RHE} in order to get potential versus RHE.

The measurements were performed connecting the conductive hydrogel samples to a platinum wire (working electrode) and immersing it in a $KClO_4$ saturated solution (the electrolyte), taking care to not put in contact the platinum wire with the solution. The scanning was then performed at 60 mV/sec in the range between -0.2 and 1.0 V.

- Electrochemical impedance spectroscopy: the measurements were performed on small parallelepiped-shaped samples with dimensions *ca.* 1.2 × 1.2 cm and thickness of *ca.* 0.5 cm. The gold foils used had an area of 2.25 cm^2. The samples were placed between the two gold foil having care that the entire surface was in contact with the two electrodes. The scanning was then performed in the range 10 KHz < x < 2 MHz with an amplitude of 20 mV and data quad = 2. The Nyquist plots obtained from the impedance measurements were then fitted using EC-Lab software (v 9.46, Bio-Logic), using the equivalent circuit below as reference.[73]

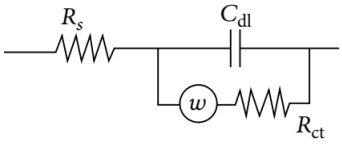

The value of R_{ct} was then employed to calculate the resistivity and the conductivity of the samples using the following equation:

$$\rho = \frac{R_{ct} \times A}{l}$$

$$\sigma = \frac{1}{\rho}$$

where ρ is the electrical resistivity (Ω × m), R is the measured electrical resistance (Ω), A and l are respectively the area and the length of the samples and then σ is the electrical conductivity (s/m).

- **Synthesis of the PAA-based hydrogels; General procedure**

The following procedure reports the amount of reactants needed for the basic formulation of the PAA-based hydrogels, as well for those were all the GABA was replaced by **ABA** or **1-PPA**, but it is valid for all the other formulations comprising both GABA and **ABA**, according to Table 4.14.

In a round bottom flask MBA (200 mg, 1.30 mmol) was suspended in 1.5 ml of distilled water at r.t.. Then the co-monomer and PEHA (72 mg, 0.31 mmol) were added in this order and the temperature was raised to 40°C. The suspension was stirred vigorously until all solids were dissolved (approximately 30 min). Finally, the mixture was transferred into a glass vial and allowed to react in static conditions at 40°C for 16h.

The obtained hydrogel scaffold was subsequently washed with water several times and then kept in water for 2 days (changing the solvent every 6h) before use, to allow the release of all the unreacted starting materials from the gel matrix.

- Basic formulation:[77] co-monomer GABA (50 mg, 0.49 mmol)
- 100% **ABA** formulation: co-monomer **ABA** (60 mg, 0.49 mmol)
- **1-PPA** formulation: co-monomer **1-PPA** (61 mg, 0.49 mmol)

- **Scanning electron microscopy analysis**

The lyophilized samples were mounted on aluminum stubs using adhesive carbon tape. Samples were then sputtered with gold to form a layer of approximately 20 nm on the surface. SEM images were captured at 10-20 kV accelerating voltage using a SEM FEI Quanta FEG 250 instrument.

- **Conductive polymer growth**

The polymerization reactions of the conductive moieties were all performed on swollen samples of the hydrogels by a two-step procedure. Before the second step the samples were always carefully washed with water. After the polymerization, the novel conductive hydrogels were always kept in water for 2 days (changing the solvent every 6h) before the use, to allow the release of all the unreacted starting materials from the gel matrix.

- Polyaniline (PAn): the optimized procedure used for all the subsequent experiments is described (Entry 2, Table 4.9). All other conductive hydrogels were obtained with the same procedure only by exchanging the components between the two steps and the solvents. The procedure was used also for the hydrogels where GABA was (partially) replaced by **ABA**.

  In a vial, a sample of hydrogel was put in a solution of distilled aniline (0.1 M) in aq. HCl 1 M for 16h. The sample was then removed from the solution, washed with water and put in an aqueous solution of APS (0.1 M) for 5h. The beginning of the polymerization process could be noticed in 5 min due to the formation of a black compound inside the hydrogel and the solution.

- Polypyrrole (PPy), undoped:[87b] in a vial, a sample of hydrogel was put in an aqueous solution of $FeCl_3$ (0.5 M) for 16h. The sample was then removed from the solution, washed with water and put in a solution of distilled pyrrole (0.5 M) in Et_2O for 16h. The polymerization of the conductive part started in 10 min.

- Polypyrrole (PPy), doped:[87c] this procedure was also used for the hydrogel were GABA was replaced by **1-PPA**.

  In a vial, a sample of hydrogel was put in an aqueous solution of distilled pyrrole (0.1 M) for 16h. The sample was then removed from the solution, washed with water and put in an aqueous solution of APS (0.1 M) for 5h. The polymerization of the conductive part started in 5 min.

- Polyethylenedioxythiophene (PEDOT):[87c,d] in a vial, a sample of hydrogel was put in an aqueous solution of $FeCl_3$ (0.5 M) for 16h. The sample was then removed from the solution, washed with water and put in a solution of EDOT (0.5 M) in hexane for 16h. The polymerization of the conductive part started in 10 min.

- **Determination of the change in weight after the polymerization of the conductive component**

The change in weight after the inclusion of the conductive polymer inside the hydrogel matrix was calculated according to the following equation:

$$\text{Change in weight} = \frac{W_{pp} - W_{bp}}{W_{bp}} \times 100$$

where W_{pp} and W_{bp} are respectively the dry weight after and before the polymerization process. Lyophilized samples of the hydrogels were used for the polymerization process. After the second step, the samples were kept in water for 2 days (changing the solvent every 6h), to allow the release of all the unreacted starting materials from the gel matrix. Then, the novel conductive hydrogels were lyophilized again and the W_{bp} was recorded for each of them.

- **First resistance measurements**

The first resistance measurements were performed by a normal multimeter in order to check if there were major differences between samples obtained with different polymerization procedures (Table 4.9). The measurements were performed on hydrogel samples of similar dimensions by placing the two electrodes at a distance of *ca.* 0.5 cm, directly recording the displayed value. The measurements were repeated several times in order to determine a mean value.

- **Resistance measurements, 4-points probe method**

Resistivity measurements were carried out using a set-up developed at the laboratory for this purpose. This set-up consists of a voltage generator (Source Meter Unit (SMU) Keithley 2601) and a current flow measuring system (Keithley 6514). The measurements was performed by applying a variable voltage in the -10 to 10 mV range by 1 mV steps, and reading the current flow up to 20 mA maximum value, with a few pA resolution at low current values. The hardware instrumentation was interfaced to a PC through a GPIB cable, which allowed the remote control of the measure using a Visual Basic script. Operatively, the samples parallelepiped-shaped with accurately controlled sized, were connected using silver paste on the two opposite smaller faces to the generator and the current flow meter. The current was then recorded as a function of the applied voltage. The resistance value was extrapolated from the average value at high and low voltages recorded in the resistance/voltage graph. This value was then normalized to the longitudinal size of the sample to obtain the resistivity value.

4.5. References

1 Guiseppi-Elie, A. *Biomaterials* **2010**, *31*, 2701.

2 (a) Akhilesh, K.; Gaharwar, N.; Peppas, A.; Khademhosseini, A. *Biotechnol. Bioeng.* **2014**, *111*, 441; (b) Cirillo, G.; Hampel, S.; Spizzirri, U.G.; Parisi, O.I.; Picci, N.; Iemma, F. *BioMed. Res. Int.* **2014** , *17*, 1; (c) Yang, Z.; Cao, Z.; Sun, H.; Li, Y. *Adv. Mater.* **2008**, *20*, 2201.

3 (a) Zhang, L.; Wang, Z.; Xu, C.; Li, Y.; Gao, J.; Wang, W.; Liu, Y. *J. Mater. Chem.* **2011**, *21*, 10399; (b) Huang, Y.; Zeng, M.; Feng, Z.; Xu, Q.; Fan, L.; Yin, D. *RSC Adv.* **2016**, *6*, 3561.

4 (a) Lutolf, M.P. *Nat. Mater.* **2009**, *8*, 451; (b) Daniel, M.-C.; Astruc, D. *Chem. Rev.* **2003**, 104, 293

5 (a) Kumar, C.S.S.R.; Mohammad, F. *Adv. Drug Delivery Rev.* **2011**, *63*, 789; (b) Meenach, S.A.; Hilt, J.Z.; Anderson, K.W. *Acta Biomater.* **2010**, *6*, 1039.

6 Mohan, Y.M.; Lee, K.; Premkumar, T.; Geckeler, K.E. *Polymer* **2007**, *48*, 158.

7 Zhang, L.; Shi, G. *J. Phys. Chem. C* **2011**, *115*, 17206.

8 Ateh, D.D.; Navsaria, H.A.; Vadgama, P. *J. R. Soc. Interface* **2006**, *3*, 741.

9 (a) Balint, R.; Cassidy, N.J.; Cartmell, S.H. *Acta Biomater.* **2014**, *10*, 2341; (b) Mawad, D.; Lauto, A.; Wallace, G.G. "*Conductive Polymer Hydrogels*", Springer International Publishing Switzerland, S. Kalia (ed.), "*Polymeric Hydrogels as Smart Biomaterials*", Springer Series on "*Polymer and Composite Materials*", **2016**.

10 Shirakawa, H.; Louis, E.J.; MacDiarmid, A.G.; Chiang, C.K.; Heeger, A.J. *Chem. Commun.* **1977**, *0*, 578,

11 (a) Dai, L. *J. Macromol. Sci. Rev. Macromol. Chem. Phys. C* **1999**, *39*, 273; (b) Wallace, G.; Spinks, G. *Soft Matter* **2007**, *3*, 665.

12 Bredas, J.L.; Streer, G.B. *Acc. Chem. Res.* **1985**, *18*, 309.

13 Dai, L. "*Conducting polymers*", in "*Intelligent macromolecules for smart devices: from materials synthesis to device applications*", London: Springer, **2004**, p. 41–80.

14 (a) Guimard, N.K.; Gomez, N.; Schmidt, C.E. *Prog. Polym. Sci.* **2007**, *32*, 876; (b) Cortés, M.T.; Moreno, J.C. *Polymers* **2003**, *4*, 1.

15 Huang, L.; Zhuang, X.; Hu, J.; Lang, L.; Zhang, P.; Wang, Y.; Chen, X.; Wei, Y.; Jing, X. *Biomacromolecules* **2008**, *9*, 850.

16 (a) Ghasemi-Mobarakeh, L.; Prabhakaran, M.P.; Morshed, M.; Nasr-Esfahani, M.H.; Baharvand, H.; Kiani, S.; Al-Deyab, S.S.; Ramakrishna, S. J. *Tissue Eng. Regen. Med.* **2011**, *5*, e17; (b) Shi, G.; Rouabhia, M.; Wang, Z.; Dao, L.H.; Zhang, Z. *Biomaterials* **2004**, *25*, 2477.

17 Liu, X.; Gilmore, K.J.; Moulton, S.E.; Wallace, G.G. *J. Neural. Eng.* **2009**, *6*, 1.

18 Pelto, J.; Haimi, S.; Puukilainen, E.; Whitten, P.G.; Spinks, G.M.; Bahrami-Samani, M.; Ritala, M.; Vuorinen, T. J. Biomed. Mater. Res. **2010**, *93A*, 1056.

19 Gusphyl, J.; Guiseppi-Elie, A. *Biomacromolecules* **2009**, *10*, 2539.

20 (a) Garner, B.; Georgevich, A.; Hodgson, A.J.; Liu, L.; Wallace, G.G. *J. Biomed. Mater. Res.* **1999**, *44*, 121; (b) Garner, B.; Hodgson, A.J.; Wallace, G.G.; Underwood, P.A. J. Mater. Sci. Mater. Med. **1999**, *10*, 19.

21 Kim, D.H.; Richardson-Burns, S.M.; Hendricks, J.L.; Sequera, C.; Martin, D.C. *Adv. Funct. Mater.* **2007**, *17*, 79.

22 Bousalem, S.; Mangeney, C.; Chehimi, M.M.; Basinska, T.; Miksa, B.; Slomkowski, S. *Colloid. Polym. Sci.* **2004**, *282*, 1301.

23 Li, Y.; Neoh, K.G.; Kang, E.T. *J. Colloid. Interf. Sci.* **2004**, *275*, 488.

24 Chronakis, I.S.; Grapenson, S.; Jakob, A. *Polymer* **2006**, *47*, 1597.

25 Akkouch, A.; Shi, G.; Zhang, Z.; Rouabhia, M. *J. Biomed. Mater. Res.* **2010**, *92A*, 221.

26 Meng, S.; Rouabhia, M.; Shi, G.; Zhang, Z. *J. Biomed. Mater. Res.* **2008**, *87A*, 332.

27 Gomez, N.; Lee, J.Y.; Nickels, J.D.; Schmidt, C.E. *Adv. Funct. Mater.* **2007**, *17*, 1645.

28 Zhou, D.D.; Cui, X.T.; Hines, A; Greenberg, R.J. "*Conducting polymers in neural stimulation applications*", in "*Implantable neural prostheses*", vol. 2. Berlin: Springer, **2010**, p.217.

29 (a) Kargirwar, S.R.; Thakare, S.R.; Choudhary, M.D.; Kondawar, S.B.; Dhakate, S.R. *Adv. Mater. Lett.* **2011**, *2*, 397; (b) Borriello, A.; Guarino, V.; Schiavo, L.; Alvarez-Perez, M.A.; Ambrosio, L. *J. Mater. Sci. Mater. Med.* **2011**, *22*, 1053.

30 Manohar, S.R.; Fafadia, C.; Saran, N.; Rao, R. *J. Appl. Phys.* **2008**, *103*, 094501.

31 Godovski, D.Y. *Adv. Polym. Sci.* **1995**, *119*, 79.

32 Bedre, M.D.; Basavaraja, S.; Deshpande, R.; Balaji, D.S.; Venkataraman, A. *Int. J. Polym. Mater.* **2010**, *59*, 531.

33 Mallikarjuna, N.N.; Manohar, S.K.; Kulkarni, P.V.; Venkataraman, A.; Aminabhavi, T.M. *J. Appl. Polym. Sci.* **2005**, *97*, 1868.

34 Tiwari, A.; Kumar, R.; Prabaharan, M.; Pandey, R.R.; Kumari, P.; Chaturvedi, A.; Mishra, A.K. *Polym. Adv. Technol.* **2010**, *21*, 615.

35 Lee, I.S.; Lee, J.Y.; Sung, J.H.; Choi, H.J. *Synth. Met.* **2005**, *152*, 173.

36 Kant, S.; Kalia, S.; Kumar, A. *J. Alloys Compd.* **2013**, *578*, 249.

[37] (a) Leclerc, M.; Faid, K. *Adv. Mater.* **1997**, *9*, 1087; (b) Yamamoto, T.; Sanechika, K.; Yamamoto, A.J. *Polym. Sci., Polym. Lett. Ed.* **1980**, *18*, 9.

[38] Ten Hoeve, W.; Wynberg, H.; Havinga, E.E.; Meijer, E.W. *J. Am. Chem. Soc.* **1991**, *113*, 5887.

[39] Thomas, C.A.; Zong, K.; Schottland, P.; Reynolds, J.R. *Adv. Mater.* **2000**, *12*, 222.

[40] Peramo, A.; Urbanchek, M.G.; Spanninga, S.A.; Povlich, L.K.; Cederna, P.; Martin, D.C. *Tissue Eng. A* **2008**, *14*, 423.

[41] Richardson-Burns, S.M.; Hendricks, J.L.; Martin, D.C. *J. Neural Eng.* **2007**, *4*, L6.

[42] Zhao, Y.; Liu, B.; Pan, L.; Yu, G. *Energy Environ. Sci.* **2013**, *6*, 2856.

[43] Green, R.A.; Lovell, N.H.; Poole-Warren, L.A. *Biomaterials* **2009**, *30*, 3637.

[44] Cui, X. ; Lee, V.A.; Raphael, Y. ; Wiler, J.A.; Hetke, J.F.; Anderson, D.J. *Biomed. Mater. Res.* **2001**, *56*, 261.

[45] Calvo, P.A.; Rodriguez, J.; Grande, H.; Mecerreyes, D.; Pomposo, J.A. *Synth. Met.* **2002**, *126*, 111.

[46] (a) Cao, Y.; Andreatta, A.; Heeger, A.J.; Smith, P. *Polymer* **1989**, *30*, 2305; (b) Pron, A.; Genoud, F.; Menardo, C.; Nechtschein, M. *Synth. Met.* **1988**, *24*, 193.

[47] Sekine, S.; Ido, Y.; Miyake, T.; Nagamine, K.; Nishizawa, M. *J. Am. Chem. Soc.* **2010**, *132*, 1317.

[48] (a) Pan, L.; Yu, G.; Zhai, D.; Lee, H. R.; Zhao, W.; Liu, N.; Wang, H.; Tee, B. C.-K.; Shi, Y.; Cui, Y.; Bao, Z. *Proc. Natl. Acad. Sci. U.S.A.* **2012**, *109*, 9287; (b) Chen, Z.; To, J. W. F.; Wang, C.; Lu, Z.; Liu, N.; Chortos, A.; Pan, L.; Wei, F.; Cui, Y.; Bao, Z. *Adv. Energy Mater.* **2014**, *4*, 1400207.

[49] Wang, Y.; Shi, Y.; Pan, L.; Ding, Y.; Zhao, Y.; Li, Y.; Shi, Y.; Yu, G. *Nano Lett.* **2015**, *15*, 7736.

[50] Pan, L.; Chortos, A.; Yu, G.; Wang, Y.; Isaacson, S.; Allen, R.; Shi, Y.; Dauskardt, R.; Bao, Z. *Nat. Commun.* **2014**, *5*, 3002.

[51] Zhao, F.; Shi, Y.; Pan, L.; Yu, G. *Acc. Chem. Res.* **2017**, *50*, 1734.

[52] Mano, N.; Yoo, J.E.; Tarver, J.; Loo, Y.-L.; Heller, A. *J. Am. Chem. Soc.* **2007**, *129*, 7006.

[53] Green, R.A.; Hassarati, R.T.; Goding, J.A.; Baek, S.; Lovell, N.H.; Martens, P.J.; Poole-Warren, L.A. *Macromol. Biosci.* **2012**, *12*, 494.

[54] Li, L.; Wang, Y.; Pan, L.; Shi, Y.; Cheng, W.; Shi, Y.; Yu, G. A. *Nano Lett.* **2015**, *15*, 1146.

[55] Shi, Y.; Ma, C.; Peng, L.; Yu, G. *Adv. Funct. Mater.* **2015**, *25*, 1219.

[56] (a) Runge, M.B.; Dadsetan, M.; Baltrusaitis, J.; Ruesink, T.; Lu, L.; Windebank, A.J.; Yaszemski, M.J. *Biomacromolecules* **2010**, *11*, 2845 ; (b) Guo, B.; Sun, Y.; Finne-Wistrand, A.; Mustafa, K.; Albertsson, A.-C. *Acta Biomater.* **2012**, *8*, 144.

[57] Liu, X.; Miller II, A.L.; Park, S.; Waletzki, B.E.; Zhou, Z.; Terzic, A.; Lu, L. *ACS Appl. Mater. Interfaces* **2017**, *9*, 14677.

[58] (a) Tsai, T.S.; Pillay, V.; Choonara, Y.E.; du Toit, L.C.; Modi, G.; Naidoo, D.; Kumar, P. *Polymers* **2011**, *3*, 150; (b) Li, Y.; Neoh, K.G.; Kang, E.T. *J. Biomed. Mater. Res.* **2005**, *73A*, 171.

[59] Lira, L.M.; de Torresi, S.I.C. *Electrochem. Commun.* **2005**, *7*, 717.

[60] Choi, E.J.; Shin, J.; Khaleel, Z.H.; Cha, I.; Yun, S.-H.; Cho, S.-W.; Song, C. *Polym. Chem.* **2015**, *6*, 4473.

[61] (a) Shi, Y.; Peng, L.; Yu, G. *Nanoscale* **2015**, *7*, 12796; (b) Sun, K.; Zhang, S.; Li, P.; Xia, Y.; Zhang, X.; Du, D.; Isikgor, F.H.; Ouyang, J.J. *Mater. Sci.-Mater. El.* **2015**, *26*, 4438; (c) Shi, Y.; Pan, L.; Liu, B.; Wang, Y.; Cui, Y.; Bao, Z.; Yu, G. *J. Mater. Chem. A* **2014**, *2*, 6086.

[62] Liu, C.; Liu, X.; Xuan, H.; Ren, J.;Ge, L. *Sci. Rep.* **2015**, *5*, 18419.

[63] Saha, S.; Sarkar, P.; Sarkarb, M.; Girib, B. *RSC Adv.* **2015**, *5*, 27665.

[64] (a) Kim, B.H.; Jeong, E.J.; Hwang, G.T.; Venkatesan, N. *Synthesis* **2001**, *14*, 2191; (b) Xun, M-.M.; Xiao, Y-.P.; Zhang, J.; Liu, Y-.H.; Peng, Q.; Guo, Q.; Wu, W-.X.; Xu, Y.; Yu, X-.Q. *Polymer* **2015**, *65*, 45.

[65] da Silva, L.B.J.; Oréfice, R.L. *J. Polym. Res.* **2014**, *21*, 466.

[66] (a) Choi, M-.H.; Ko, E.J.; Han, Y.W.; Lee, E.J.; Moon, D.K. *Polymer* **2008**, *74*, 215; (b) Dai, T.; Quing, X.; Wang, J.; Shen, C.; Lu, Y. *Compos. Sci. Technol.* **2010**, *70*, 498.

[67] Green, R.A.; Baek, S.; Poole-Warren, L.A.; Martens, P.J. *Sci. Technol. Adv. Mater.* **2010**, *11*, 014107.

[68] Rivero, R.E.; Molina, M.A.; Rivarola, C.R.; Barbero, C.A. *Sensor Actuat. B-Chem.* **2014**, *190*, 270

[69] Tang, Q.; Wu, J.; Sun, H.; Lin, J.; Fan, S. ; Hu, D. *Carbohyd. Polym.* **2008**, *74*, 215.

[70] (a) Feig, V.R.; Tran, H.; Lee, M.; Bao, Z. *Nat. Comm.* **2018**, *9*, 2740; (b) Wu, Y.; Chen, Y.X.; Yan, J.; Yang, S.; Dong, P.; Soman, P. *J. Mater. Chem. B* **2015**, *3*, 5352; (c) Aziz, S.B.; Woo, T.J.; Kadir, M.F.Z.; Ahmed, H.M. *J. Sci.: Adv. Mater. Devices* **2018**, *3*, 1.

[71] (a) Randles, J.E.B. *Discuss. Faraday Soc.* **1947**, *1*, 11; (b) Lasia, A. "*Electrochemical impedance spectroscopy and its applications*", in "*Modern Aspects of Electrochemistry*", B.E. Conway, J.O.M. Bockris and R. White, Springer, NY (USA) **2002**, pp. 143-248; (c) Allen, L.R.F.; Bard, J. "Electrochemical Methods: Fundamentals and Applications", Wiley, 2nd edition, **2000**.

[72] Sarker, S.; Ahammad, A.J.S.; Seo, H.W.; Kim, D.M. *Int. J. Photoenergy* **2014**, 851705.

[73] Burrs, S.L.; Vanegas, D.C.; Bhargava, M.; Mechulan, N.; Hendershot, P.; Yamaguchi, H.; Gomesd, C.; McLamore, E.S. *Analyst* **2015**, *140*, 1466.

[74] Kim, B.C.; Spinks, G.M.; Wallace, G.G.; John, R. *Polymer* **2000**, *41*, 1783.

[75] Pruneanu, S.; Veressl, E.; Marian, O.; Oniciu, L. *J. Mater. Sci.* **1999**, *34*, 2733.

[76] Hand, R.L.; Nelson, F. *J. Amer. Chem. Soc.* **1974**, *96*, 850; Shim, V.B.; Won, M.S. Park, S.M. *J. Electrochem. Soc.* **1990**, *137*, 538.

77 (a) Fiorini, F.; Prasetyanto, E.A.; Taraballi, F.; Pandolfi, L.; Monroy, F.; López-Montero, I.; Tasciotti, E.; De Cola, L. *Small* **2016**, *12*, 4881; (b) Rizzi, V.; Fiorini, F.; Lamanna, G.; Gubitosa, J.; Prasetyanto, E.A.; Fini, P.; Fanelli, F.; Nacci, A.; DeCola, L.; Cosma, P. *Adv. Sustainable Syst.* **2018**, *2*, 1700146.

78 Lin, C.; Zhong, Z.; Lok, M.C.; Jiang, X.; Hennink, W.E.; Feijen, J.; Engbersen, J.F.J. *Bioconjugate Chem.* **2007**, *18*, 138.

79 Cope, A.C.; Ciganek, E. *Org. Synth.* **1963**, *4*, 612.

80 Jia, Q-.F; Benjamin, P.M.S.; Huang, J.; Du, Z.; Zheng, X.; Zhang, K.; Conney, A.H.; Wang, J. *Synlett* **2013**, *24*, 79.

81 Zhang, S.; Shi, Z.; Xu, H.; Ma, X.; Yin, J.; Tian, M. *Soft Matter* **2016**, *12*, 2575.

82 (a) Beatty, J.W.; Corey, R.; Stephenson, J. *Acc. Chem. Res.* **2015**, *48*, 1474; (b) Hu, J.; Wang, J.; Nguyen, T.H.; Zheng, N. *Beilstein J. Org. Chem.* **2013**, *9*, 1977.

83 Deno, N.C.; Fruit Jr, R.E. *J. Am. Chem. Soc.* **1968**, *90*, 3502.

84 Rawalay, S.S.; Shechter, H. *J. Org. Chem.* **1967**, *32*, 3129.

85 Nicolaou, K.C.; Mathison, C.J.N.; Montagnon, T. *Angew. Chem. Int. Ed.* **2003**, *42*, 4077.

86 March, J. "*Advanced Organic Chemistry: Reactions, Mechanisms, and Structure*" (3rd ed.), New York: Wiley, **1985**.

87 (a) Zhang, J.; She, Y.; Lu, B.; Zhou, Y.; Fu, K. *Chinese J. Polym. Sci.* **1993**, *11*, 337; (b) Zhang, X.; Bai, R. *Langmuir* **2003**, *19*, 10703; (c) Mawad, D.; Lauto, A.; Wallace, G.G. "*Conductive Polymer Hydrogels*", in "*Polymeric Hydrogels as Smart Biomaterials*" **2016**, Springer; (d) Du, R.; Xu, Y.; Luo, Y.; Zhang, X.; Zhang, J. *Chem. Commun.* **2011**, *47*, 6287.

88 (a) John, R.; Wallace, G.G. J. *Electroanal. Chem.* **1993**, 354, 145; (b) Rhee, H.W.; Jeon, E.J.; Kim, J.S.; Kim, C.Y. *Synthetic Met.* **1989**, *28*, 605.

89 Roy, K.; Mondal, P.; Bayen, S.P.; Chowdhury, P. *J. Macromol. Sci. A* **2012**, *49*, 931.

90 Yao, B.; Wang, H.; Zhou, Q.; Wu, M.; Zhang, M.; Li, C.; Shi, G. *Adv. Mater.* **2017**, *29*, 1700974.

91 (a) Xia, Y.; Zhu, H. *Soft Matter* **2011**, *7*, 9388; (b) Chen, L.; Kim, B.; Nishino, M.; Gong, J.P.; (b) Osada, Y. *Macromolecules* **2000**, *33*, 1232.

92 He, X.; Zhang, C.; Wang, M.; Zhang, Y.; Liu, L.; Yang, W. *ACS Appl. Mater. Interfaces* **2017**, *9*, 36301.

93 (a) Brandstät, E.; George, U.; Kolbe, A. *J. Mol. Liq.* **1985**, *31*, 107; (b) Tuomikoski, P. *J. Chem. Phys.* **1952**, *20*, 1054.

94 Green, T.W.; Wuts, P.G.M. "*Protective Groups in Organic Synthesis*", Wiley-Interscience, New York, **1999**.

95 Bray, B.L.; Mathies, P.H.; Naef, R.; Solas, D.R.; Tidwell, T.T.; Artis, D.R.; Muchowski, J.M. *J. Org. Chem.* **1990**, *55*, 6317.

96 Frederich, J.H.; Matsui, J.K.; Chang, R.O.; Harran, P.G. *Tetrahedron Lett.* **2013**, *54*, 2645.

97 (a) Gu, Z.; Zakarian, A. *Org. Lett.* **2010**, *12*, 4224; (b) Outlaw, V.K.; Townsend, C.A. *Org. Lett.* **2014**, *16*, 6334.

98 Bach, N.J.; Kornfeld E.C.; Jones, N.D.; Chaney, M.; Dorman, D.E.; Paschal, J.W.; Clemens, J.A.; Smalstig, E.B. *J . Med. Chem.* **1980**, *23*, 481.

99 Ayça, D.; Özel, E.; Dikici, L.; Bachas, G. *Monatsh. Chem.* **2013**, *144*, 781.

100 Noguchi, T.; Shiraki, T.; Dawn, A.; Tsuchiya, Y.; Thi, Le.; Lien, N.; Yamamoto, T.; Shinkai, S. *Chem. Comm.* **2012**, *48*, 8090.

101 David, C.; Königs, F.; Müller, M.F.; Aiguabella, N.; Klare, H.F.T.; Oestreich, M. *Chem. Commun.* **2013**, *49*, 1506.

102 Dhanak, D.; Reese, C.B. *J. Chem. Soc. Perkin Trans. 1* **1986**, *0*, 2181.

103 Beck, E.M.; Grimster, N.P.; Hatley, R.; Gaunt, M.J. *J. Am. Chem. Soc.* **2006**, *128*, 2528.

104 Marks, R.; Cosnier, S.; Polyak, B.; Ionescu, E.R.; Abu-Rabeah, K.; "*Hydrogel functionalized with a polymerizable moiety and their uses as biosensors or bioreactors*" **2008** US 2,008,242,738.

105 Le Gall, T.; Passos, M.S.; Ibrahim, S.K.; Morlat-Therias, S.; Sudbrake, C.; Fairhurst, S.A.; Queiros, M.A.; Pickett, C.J. *J. Chem. Soc. Perkin Trans. 1* **1999**, *0*, 1657.

106 Thomson, R.C.; Wake, M.C.; Yaszemski, M.J.; Mikos, A.G. in "*Biopolymers II*" (Eds.: Peppas, N.A.; Langer, R.S.), Springer Berlin Heidelberg, Berlin, Heidelberg, **1995**, pp. 245

107 Sawyer, D.T.; Sobkowiak, A.; Roberts, J. "*Electrochemistry for Chemists*", 2nd ed., **1995**, ISBN-13: 978-0471594680.

Chapter 5

Light-Responsive Hydrogels

5.1. Background

Among all the external inputs able to induce a response by a stimuli-responsive materials,[1] light is an interesting option because it can act instantly and be controlled both temporally and spatially with high precision. Furthermore, this resource is safe, readily available, inexpensive, clean and easily manipulated, especially in the visible and near-infrared (NIR) range. For these reasons, the interaction with light has been exploited also in the field of biocompatible materials, in particular with hydrogels, leading to the development of several new systems, especially in the engineering and biomedical fields, with potential applications in optical switches, display units and drug delivery devices. Among them, a difference can be recognized between the light-responsive and the photosensitive hydrogels, which constitute two separated categories. Indeed, while in the light-responsive systems upon the irradiation a change in the physical or chemical properties of the material can be observed,[2] within the photosensitive hydrogels the light plays a different role, acting as the main factor inducing either the formation (photocrosslinkable gels) or the destruction (photodegradable gels) of the covalent bonds of the network.[3] While photosensitive hydrogels have already been the subject of an intense research and many synthetic alternatives have been developed,[4] in the case of light-responsive hydrogels the options are still limited. Based on these considerations, we decided to focus our attention on this last class of smart materials. Usually, depending on the kind of light used to induce the desired effect, different compounds are used as photoactive species and different modifications are triggered inside the hydrogel matrix. If UV light is used, usually the photoactive systems are molecules capable to undergo to photoisomerization or photodimerization processes (Figure 5.1). Among them, the azobenzenes[5] and the spyropiranes[6] are the most used; the double bond isomerization they undergo after the light exposure is often used to change the hydrophilicity of the system[7] or the strength of host-guest interactions they establish with another component of the network[8] (typically a cylodextrin), in order to achieve a UV-induced discontinuous reversible volume and shape transition. Other process often employed in this field to achieve the same objective are photodimerization (i.e. coumarines) or photocleveage of labile bond (i.e. triphenylmethanes).

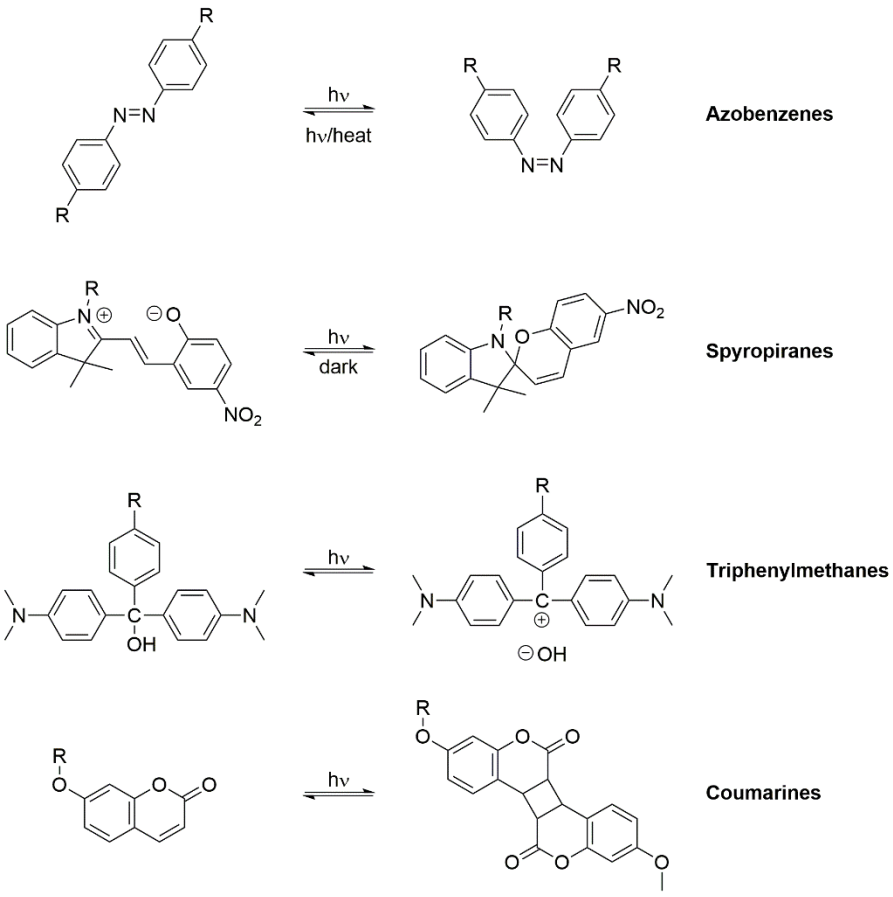

Figure 5.1 Common UV photoactive molecules used in light-responsive hydrogels.

On the other hand, light in the visible and NIR region is not able to the double bond isomerization due the low energy of its photons. For this reason, a different approach is needed to exploit light in such wavelength range. In particular, what is used are tandem systems in which a compound displaying a photothermal effect (defined as the production of thermal energy after the photoexcitation of the material) is coupled with an thermosensitive hydrogel matrix. The latter is usually composed by poly(*N*-isopropylacrylamide), a polymer well-known for being able to shrink upon heating[9] (Figure 5.2). The photoactive system can be constituted either by a metalorganic complex[10] (Figure 5.2) or nanostructured materials, such as graphene oxide[11] and metal nanorods.[12]

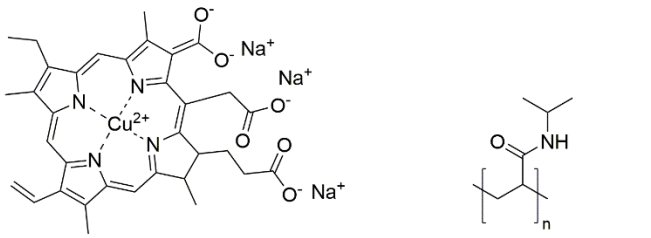

Figure 5.2 Structures of (left) a light-sensitive metalorganic chromophore and (right) poly(N-isopropylacrylamide).

Inspired by this kind of tandem systems, we decided to develop a similar material, but exploiting a different key property from the photothermic effect to induce a macroscopic change of its physical characteristics after light irradiation. In this context, we considered oxidation as the optimal tool. In fact, oxidation of a polymeric material is well known[13] to induce a sharp increase in its hydrophilicity, causing major alterations of its

structure and its interaction with water; in addition, the process can be carried out on almost all the existing compounds. Singlet oxygen was chosen as the optimal specie for this purpose, because it is a strong oxidant which can be generated by excitation of a O_2 molecule (whose ground state is a triplet state) upon charge or energy transfer from another photoexcited compound.[14] Singlet oxygen is already vastly employed in several fields for its high activity and wide reaction scope, with examples ranging from organic synthesis[15] to photodynamic therapy.[16] Several compounds are capable to produce singlet oxygen upon irradiation[14b,17] (Figure 5.3) with different efficiency, which is influenced both by the solvent used in the experiment and the aggregation state of the sensitizer.

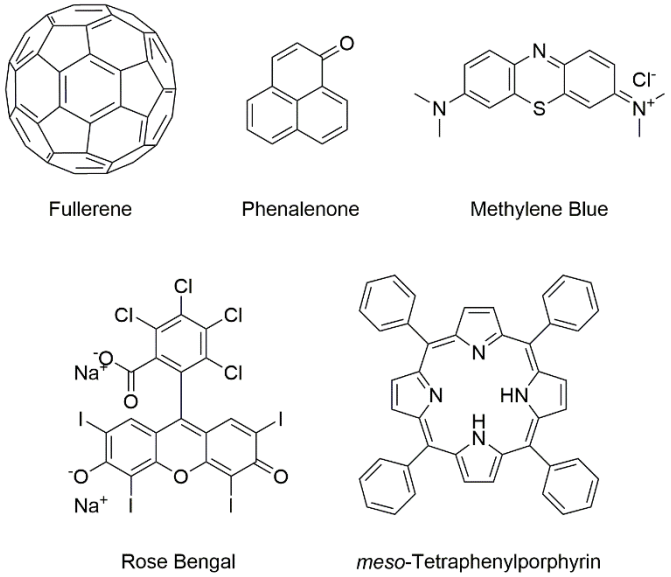

Figure 5.3 Examples of molecules capable to produce singlet oxygen.

Among them, fullerene is one of those showing the highest quantum yield in singlet oxygen production (≈ 1 in organic solvents).[18-22] Furthermore, it also possesses a large absorption spectrum, capable to cover the electromagnetic spectrum from the UV region almost to the NIR region,[19] and can be easily functionalized with various substituents in different ways.[20] The high efficiencies for $^1O_2$ production derives from its particular electronic structure which highly stabilizes the excited state from which the energy transfer to the O_2 takes place. That means that modifications to the π-conjugated system of the molecule usually lead to a reduction of the quantum yield of the charge and energy transfer process to molecular oxygen. The reduction of quantum yield depends on the kind of functionalization performed and on its extent. For example, it has been measured that for dihydrofullerenes (the C_{60} monoadducts) the quantum yield value for the process in organic solvents ranges from ≈ 0.95[21] to ≈ 0.75,[22] while smaller values were recorded for higher adducts (Figure 5.4).[22]

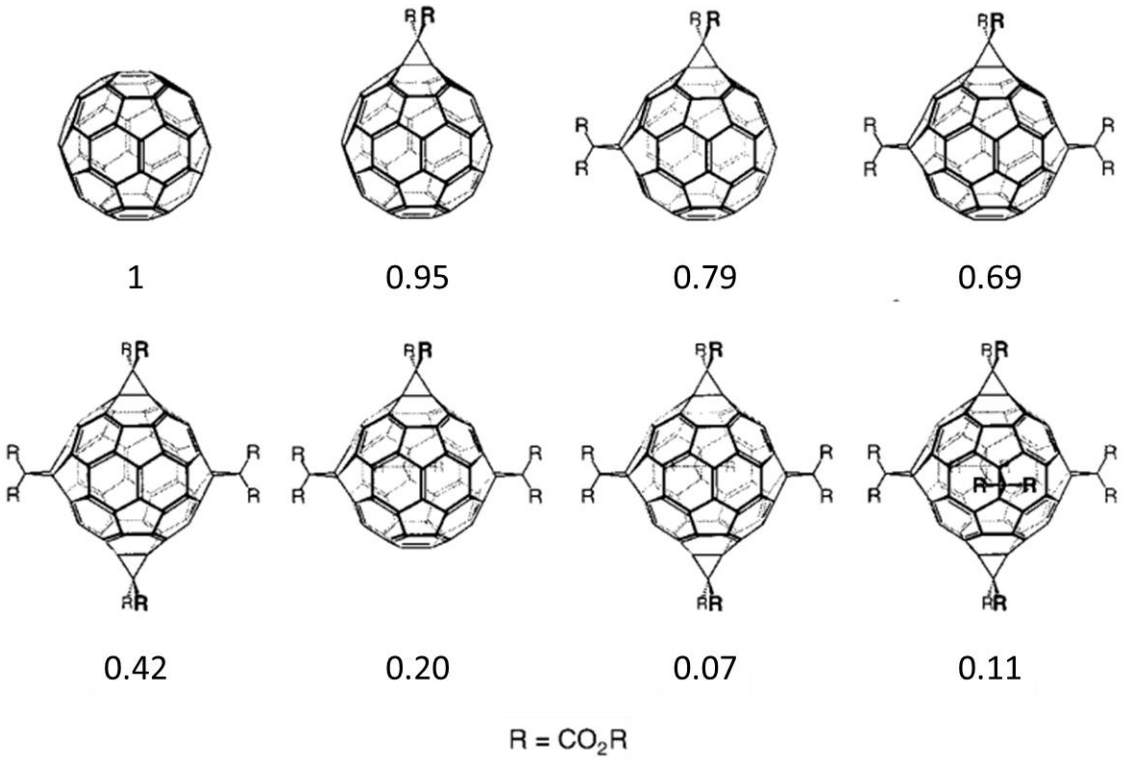

Figure 5.4 Singlet oxygen production quantum yield for various adducts of fullerene in toluene.[22]

The use of fullerene and its adducts in water (the environment present inside the hydrogel matrix) is not common due to their low solubility in that medium. For this reason, usually, recorded quantum yields are referred either to fullerene aggregates[18] (micelles or nanoparticles) or to fullerols[23] (fullerene compounds whose surface is almost entirely covered by OH groups). The low values recorded in these cases have to be attributed to the quenching process taking place in the aggregate forms (strongly reducing the lifetime of the excited states generated upon the photoexcitation) and to the major alteration of the electronic structure of the fullerene cage which is also reflected on the electronic state of the molecule. In fact, if a dispersion of fullerene in water is realized using particular care to avoid the formation of aggregates (i.e. by using either γ-cyclodextrins or poly(vinylpyrrolidone), hydrophilic compounds capable to establish host-guest or complexation interactions with C_{60}), the quenching process cannot take place, the quantum yield rises and the efficiency of singlet oxygen production can reach values 2-3 times higher than Rose Bengal.[24] Then, if the fullerene molecules are enough dispersed, C_{60}-derivatives could be properly employed also in aqueous environment.

The next step was the identification of a proper substrate capable to be oxidized by the singlet oxygen produced by the fullerene. Besides that, the molecule had to fulfill another requisite, namely the capability to be inserted into an hydrogel matrix, such as the polyamidoamine already used for the synthesis of the electroconductive hydrogels (see Chapter 4).[25] This specific matrix was chosen taking into account the possibility to fine tune its characteristics by easily replace its components with other molecules having the proper functional groups, as already explored in Chapter 4.2.3 with the introduction of compounds **ABA** and **1-PPA**. The mild conditions required for the gelation reaction to occur are another good quality, conferring a high tolerance to different functional groups (i.e. no oxidation reaction is needed). To avoid degradation of the matrix, the fragment to be oxidized has to possess a lower redox potential if compared to those of the major components of the network, mostly secondary and tertiary amines. Sulfur compounds were thus identified as the optimal candidates for this role, since they are usually easier to oxidize compared to amines.[26] Accordingly, singlet oxygen

oxidation of sulfur compounds is widely used[27] and even its mechanism has been explained.[28] Based on these considerations, methionine was individuated as the most suitable substrate: it possesses a sulfur-containing hydrophobic moiety (capable to be oxidized), a primary amino group (able to participate to the *Aza*-Michael reaction used for the constitution of the polyamidoamine hydrogel matrix) and also a carboxylic acid, making it extremely similar to the GABA co-monomer used in the original gel formulation. In addition, oxidation of methionine to the corresponding sulfoxide has already been accomplished using singlet oxygen produced by fullerene moieties,[29] and, once implemented in polymeric vesicles, has already been demonstrated to enhance the hydrophilicity of the entire system,[13a] creating an interesting premise for the hypothesized application.

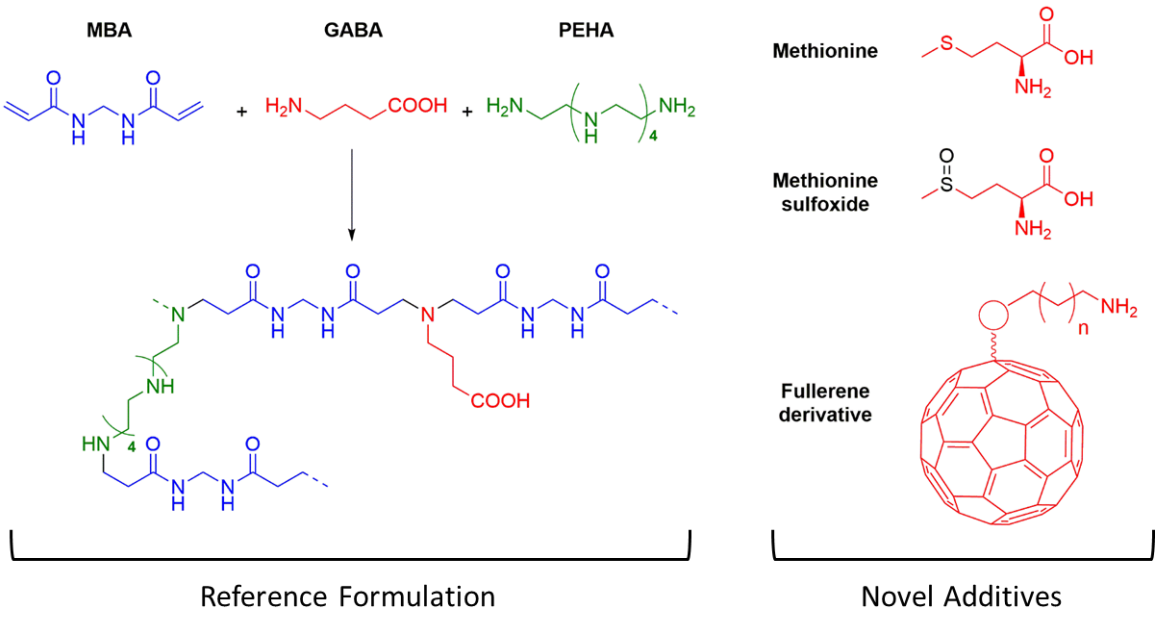

Figure 5.5 Structural design of the reference formulation and of the novel additives employed in the work.

This part of the PhD work will then be focused onto the development of a novel light-responsive hydrogel starting from a polyamidoamine gel matrix by implementation of a tandem system in which a proper designed fullerene-derivative upon photoexcitation will be able to produce singlet oxygen, thereby oxidizing methionine moieties also included in the hydrogel network (Figure 5.5). Such molecular oxidation process is then supposed to induce a macroscopic change of the hydrophilicity of the material, in turn altering its water uptake capability.

5.2. Results and Discussion

Before starting the synthesis of the novel fullerene derivative to be inserted into the hydrogel network, the feasibility of the idea had to be proven. The first step, then, was to determine what was the difference in terms of physical properties between two materials built with the same procedure but incorporating methionine derivatives bearing sulfur in two different oxidation states (sulfide vs. sulfoxide).

5.2.1. Sulfide *vs.* Sulfoxide Formulation

Starting from the reference formulation reported in Figure 5.5, two different series of hydrogels were developed, one incorporating methionine and the other bearing its sulfoxide analogue. The methodology was the same already explored with conductive hydrogels described in Chapter 4, in which GABA was replaced, partially or entirely, with other molecules (**ABA** and **1-PPA**, in that case). Here, four new formulations were developed (Figure 5.6): the first two kept the same ratio of co-monomer (methionine or methionine sulfoxide, respectively) relative to the other components as in the reference formulation with GABA; the other two, instead, contained an increased amount of co-monomer (0.64 mmol vs. 0.49 mmol for the original formulation). These last two formulations were investigated to see if the difference in physical properties (i.e. the EDS) between the two hydrogels could be enhanced by increasing the amount of co-monomer.

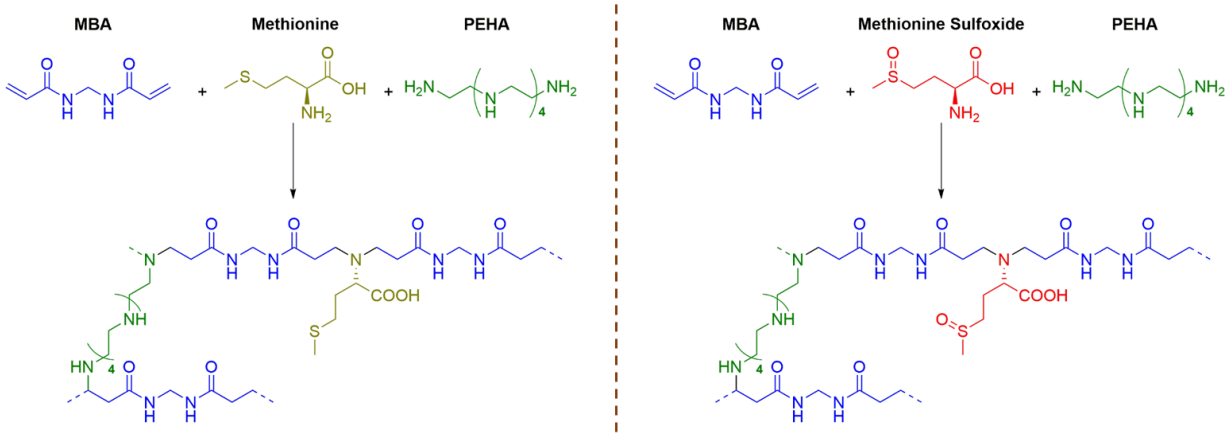

Figure 5.6 Representation of the hydrogel structure of the new formulations with (left) methionine and (right) methionine sulfoxide.

The four new formulations tested are reported in Table 5.1 along with their measured EDS values, reported as an average of the analysis of 3 different samples synthetized with the same formulation. The hydrogels were always synthetized in vials using 1.5 mL of H_2O. All formulations led to the isolation of self-standing soft materials, transparent and slightly yellow in color.

Table 5.1 New formulations with methionine and methionine sulfoxide tested.

Entry	Formulation		Co-monomer (mmol)	EDS (%)
1	Methionine	A	0.64	1000 ± 30
2		B	0.49	600 ± 60
3	Methionine sulfoxide	A	0.64	1010 ± 150
4		B	0.49	760 ± 20
Both for A and B formulations the other components amount is MBA: 1.30 mmol and PEHA: 0.31 mmol				

The swelling data were determined as already explained in Chapter 3.4.1: the hydrogels were kept in water until they reached a stable weight, having care to frequently change the water in the first 2 days to remove all the unreacted starting materials from the gelation process. After the swollen weight was recorded, the samples were lyophilized and then the dry weight was registered. As can be seen from Table 5.1, the amount of co-monomer used during the synthesis had a huge impact on the EDS value,

since by increasing it of *ca.* 30% an increment of almost 50% of the EDS value was obtained. On the other hand, the effect exerted by the different co-monomers was more contradictory: in the case of the higher co-monomer concentration (0.64 mmol) the EDS values obtained with methionine and its sulfoxide resulted substantially identical (Entry 1 and 3 of Table 5.1); on the contrary, when considering hydrogels obtained according to the formulation B (with less co-monomer, Entry 2 and 4 of Table 5.1), a significant difference in the swelling degree of the samples could be recognized. Taken together these results suggest that increasing the amount of non-crosslinking monomer led to a reduction of the network crosslinking degree which could make the more or less hydrophilic nature of the material less relevant for its water uptake capability.

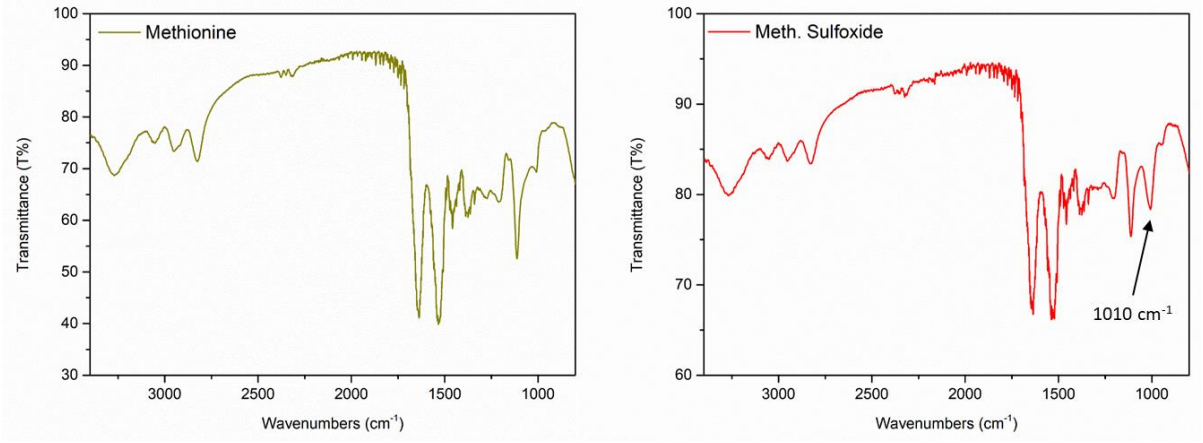

Figure 5.7 ATR-IR spectra of the hydrogel containing (left) methionine and (right) methionine sulfoxide.

The new hydrogels were then characterized by means of two different spectroscopic techniques, namely ATR-IR and XPS* (X-ray Photoelectron Spectroscopy). The main purpose of this study was to identify the best technique to completely distinguish methionine and methionine sulfoxide in the hydrogels, while also obtaining a semi-quantitative evaluation of their abundance into the sample. In general, ATR-IR can be performed easily and is able to give information about the composition of the entire material, while XPS can recognize the different oxidation states of the atoms present in the sample and allows also an evaluation of their ratio by the comparison of the area under each peak. Indeed in an XPS experiment, by irradiating the sample with a high energy source (such as X-rays), it is possible to directly remove the core electrons of the atoms; by measuring the kinetic energy of each electron and their number it becomes possible to extract the binding energy of each particular electron (the energy required to remove the electron from the nuclear attraction), which is directly dependent on the atomic number and the oxidation state of the atoms. In that way it is possible to observe which kind of atoms constitute the sample and their oxidation states. The principal drawback of this last technique is that the analysis can be performed only on the surface of the material, leaving the composition of the inner part unknown. For this reason, hydrogel samples were all ground and, to correct for ample inhomogeneity, the measure was repeated two times. In both cases hydrogel samples were lyophilized before recording the spectra. In Figure 5.7 are reported the ATR-IR spectra of the novel hydrogels, while the XPS spectra of the same materials are showed below, both the survey spectrum (Figure 5.8) and the high-resolution spectrum on the sulfur channel (Figure 5.9).

* The XPS analysis was performed by Simone Silvestrini (Institut de Science et d'Ingénierie Supramoléculaires)

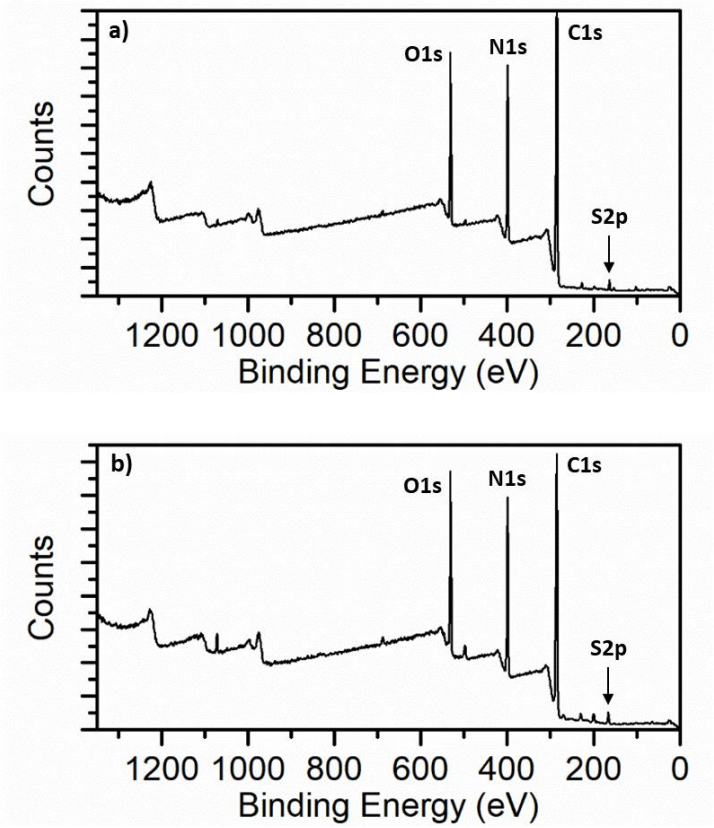

Figure 5.8 Survey XPS spectra of hydrogels synthetized with (a) methionine and (b) methionine sulfoxide formulations.

As can be seen from Figure 5.7, the ATR-IR spectra of the two different hydrogels did not present substantial differences. The only difference was the peak at 1010 cm^{-1} (which can be ascribed to the S=O stretching of the sulfoxide group)[30], which was absent in the formulation with methionine and could be used as a marker to monitor the oxidation of the sulfide moieties to the corresponding sulfoxides.

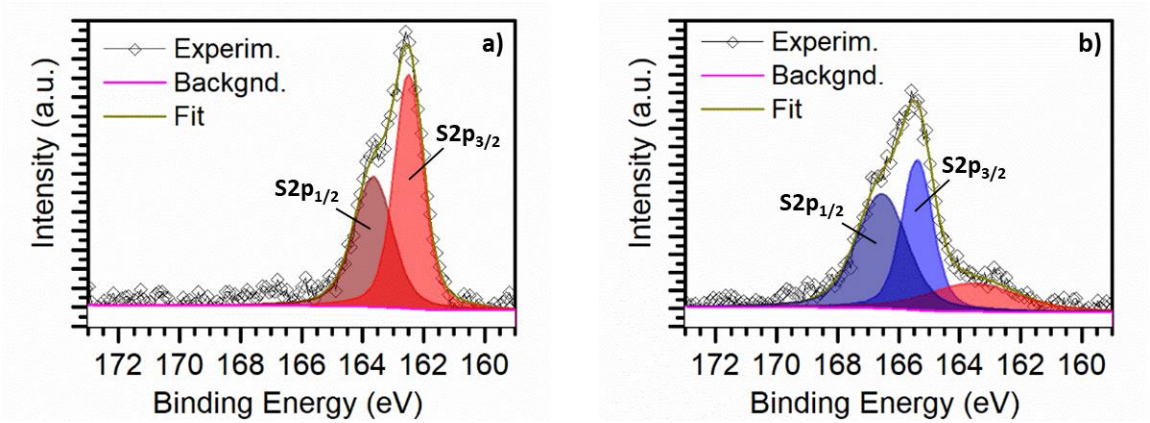

Figure 5.9 HD-sulfur XPS spectra of hydrogels with (a) methionine and (b) methionine sulfoxide. The colored areas correspond to the fitting of the different components of sulfur, in red the reduced form (sulfide) and in blue the oxidized (sulfoxide).

The XPS analysis showed more interesting results. In Figure 5.8 the survey spectra is reported, which shows all the atoms recognized inside the sample, thus giving information about the material composition. As expected from the formulation used, the sulfur peak was very small if compared to those of the main constituents of the hydrogel (C, N and O), but still recognizable and analyzable. It was then possible to record the high-resolution spectra on the sulfur channel (Figure 5.9), which allowed to distinguish the different oxidation states of the atoms based on the energy required to remove the a

specific core electron (in the case of the sulfur the electrons always belong to the 2p orbitals): the more the atoms is positively charged, the more energy will be necessary to take the electron away. The acquired spectra must then be fitted in order to separate the different components. In the case of sulfur, the 2p peaks always show closely spaced spin-orbit components (Δ = 1.16 eV with an intensity ratio of $\approx$ 0.5) ascribed to the two different possible spin states of the electrons (1/2 and 3/2), displayed in the reported spectra. The spectrum of the sample with methionine (Figure 5.9a) shows the two expected components around 163 eV,[31] which are well-separated from the two components of the samples with the sulfoxide (Figure 5.9b), localized at *ca.* 166 eV.[32] Noteworthy was the presence of a large component peaked around 163 eV in the spectrum of the sulfoxide-samples which could still be assigned to a reduced form of the methionine, which probably present as an impurity in the methionine sulfoxide used as the starting material. The simultaneous presence of the two different compounds in the spectrum in Figure 5.9b confirms the good separation of the related peaks in the XPS spectra and renders this kind of analysis an excellent tool to detect the methionine oxidation state inside the hydrogels.

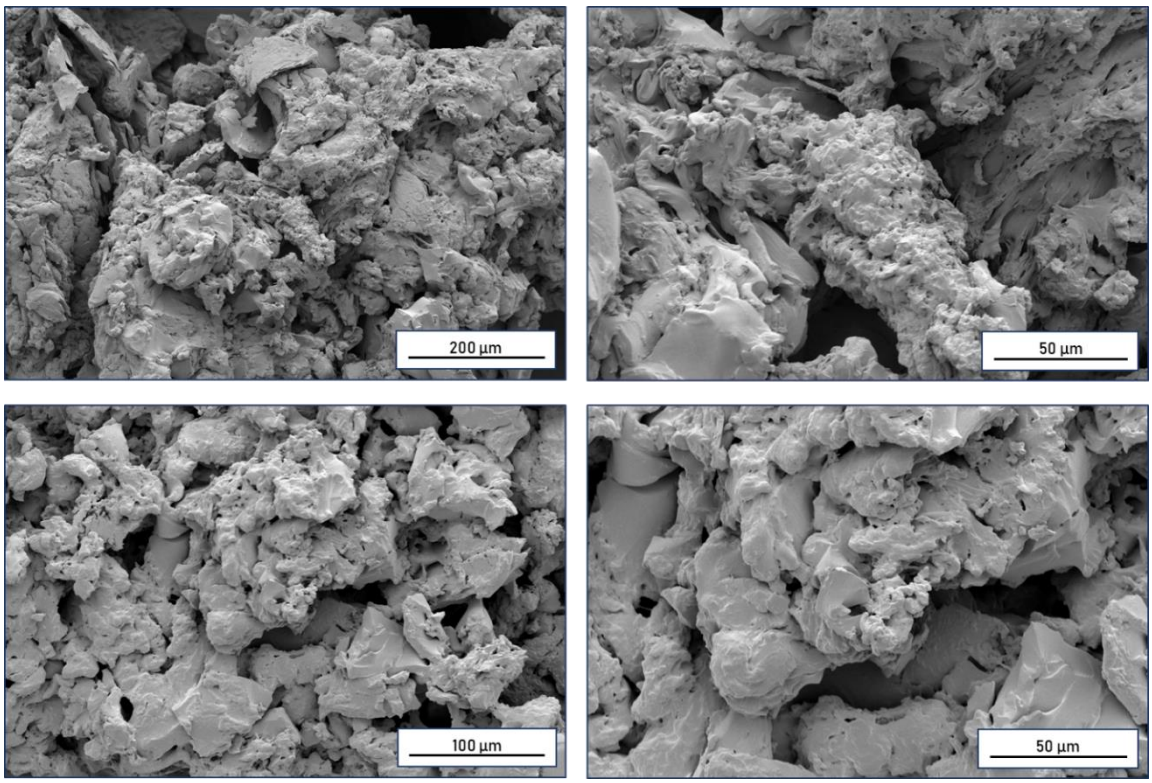

Figure 5.10 SEM pictures of (top) the sulfide- and (bottom) sulfoxide-based hydrogel formulations.

Finally, some SEM pictures of the novel samples were taken. As can be seen from Figure 5.10, both formulations produced hydrogels characterized by an uncommon non-porous structure, where only extremely tiny holes were present. Considering the overall look of the structure, the bigger holes showed in the pictures could indeed be derived from fractures generated upon the lyophilization process which the samples underwent before performing the SEM experiments. Clearly, the two structures were extremely similar, and no macroscopic difference could be recognized from the recorded pictures.

5.2.2. Development of the Oxidizing Agent

5.2.2.1. Design & Retrosynthesis

After having identified fullerene as the possible active moiety for the hypothesized tandem system, the following step was represented by the design of a proper derivative capable to be inserted into the hydrogel network. According to the optimized strategy used to prepare PAA-hydrogels (see Chapter 4.2.3) a C_{60} derivative bearing a terminal amine group was necessary. Due to the ample use of fullerene derivatives in various branches of chemistry and materials science, several functionalization methodologies have been developed during the years.[33] Among them, we decided to employ the Bingel reaction[34] as synthetic tool for the insertion of the amino group on the C_{60} scaffold. The choice was made by taking into account the mild reaction conditions and the simple preparation of the reagent required for the introduction of the amino group. The planned retrosynthesis of the aminofullerene derivative is reported in Figure 5.11.

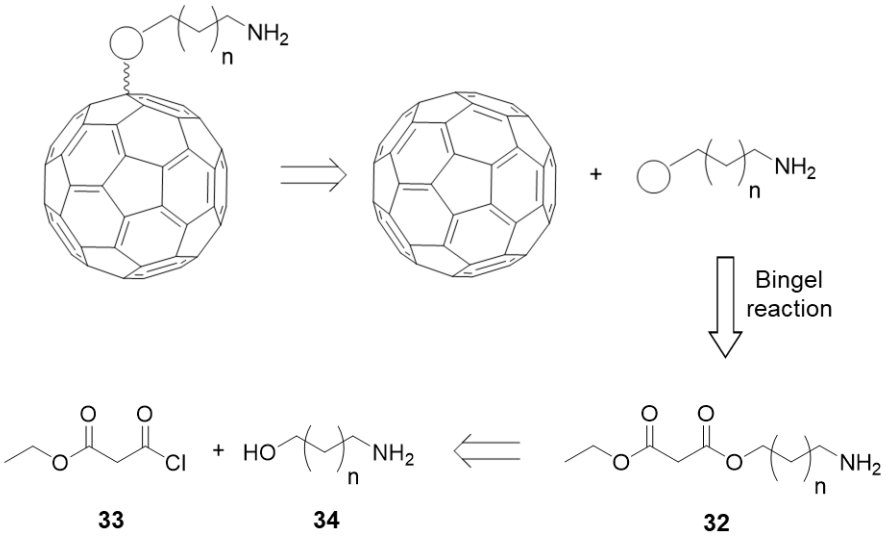

Figure 5.11 Designed retrosynthetic pathway for the synthesis of the aminofullerene.

The reagent necessary for the Bingel reaction was identified with amino malonate **32**, which could be easily obtained by acylation of the proper aminoalcohol **34** with ethylmalonyl chloride (**33**). We decided to use 6-amino-1-hexanol (n = 4) to confer a good flexibility to our fullerene co-monomer, in order to increase the possibility of interaction with methionine fragments inside the gel matrix.

5.2.2.2. Synthesis of the Amino-C_{60} Derivative

According to the retrosynthesis pathway, the first step would be the acylation of the chosen aminoalcohol **34**; however, due to the simultaneous presence of two nucleophilic groups, the NH_2 and the OH, such reaction on the unprotected substrate would probably not be chemoselective. Therefore, the first step was actually the protection of the amino group with Boc_2O (Scheme 5.1).

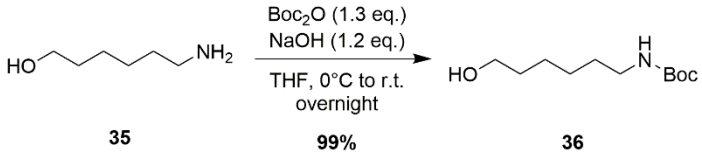

Scheme 5.1 Protection of the chosen aminoalcohol.

Protected alcohol **36** was obtained in excellent yield using a standard procedure for the Boc-protection of primary amines[35] and was then reacted with acyl chloride **33** in the presence of pyridine[36] to access malonate **37**, to be employed for the functionalization of the C_{60} (Scheme 5.2).

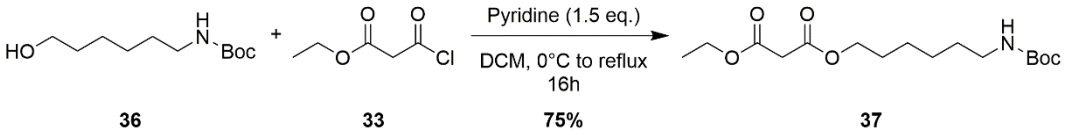

Scheme 5.2 Synthesis of the target malonate.

Malonate **37** was isolated in good yield after purification by means of flash column chromatography and used in the next step, the Bingel reaction (Scheme 5.3).

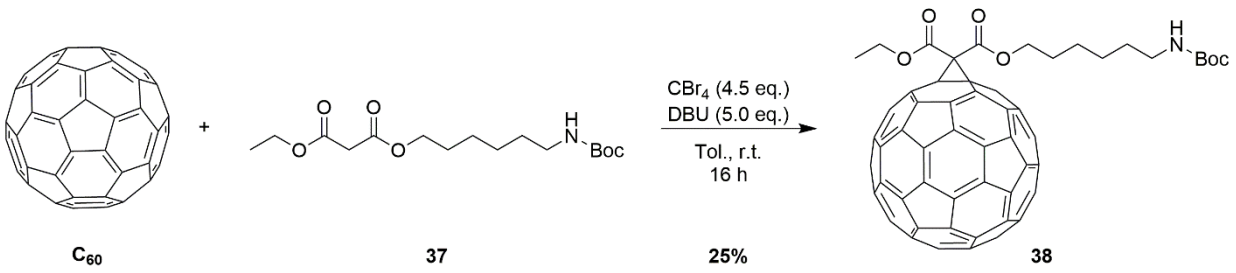

*Scheme 5.3 Synthesis of the desired fullerene monoadduct **38** by Bingel reaction.*

The reaction proceeded smoothly and monoadduct **38** was isolated after purification by means of column chromatography. The relatively low yield could be explained by the particular reactivity of C_{60} itself: after addition of the first molecule of malonate, monoadduct **38** exhibits the same reactivity towards the other reactants as the bare fullerene. As a consequence, if 1 eq. of malonate is used, the bisadduct is always present as byproduct of the reaction together with a certain amount of pristine fullerene which can be recovered.[37] The use of an excess of malonate (which will also generate a higher amount of bisadduct) is generally avoided to be able to recover the maximum possible amount of unreacted fullerene and re-use it in the next batch.

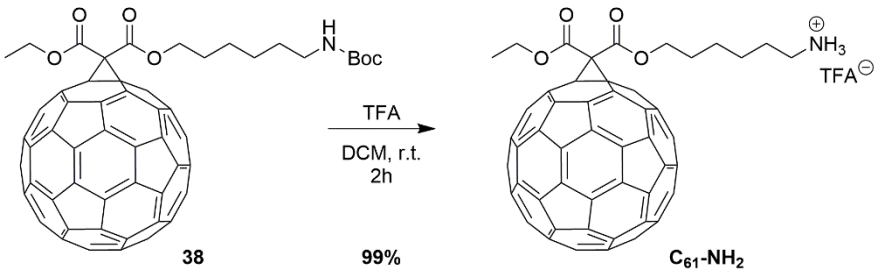

Scheme 5.4 Deprotection of the fullerene amino derivative

Finally, Boc-protected compound **38** was treated with trifluoroacetic acid (TFA) in order to remove the protecting group[38] and obtain the desired fullerene derivative **C_{61}-NH_2** (Scheme 5.4). A huge excess of TFA was employed and after 2h of stirring at r.t. the salt of the amino adduct was isolated in quantitative yield.

The obtained salt was then used directly in this form for the synthesis of the light-responsive hydrogel, due to the basic conditions used during the gelation process, which could directly release *in situ* the corresponding free amine.

5.2.3. Tandem Light-Responsive Hydrogel

5.2.3.1. Synthesis and Characterization

As soon as fullerene derivative **C_{61}-NH_2** was synthetized, it was added to the chosen hydrogel formulation (Entry 2, Table 5.1) in a ratio 1:10 compared to the amount of methionine present. The compound was added to the mixture together with the methionine after being dissolved in few drops of MeOH. **C_{61}-NH_2** did not precipitate after the dissolution in water and the novel light-responsive hydrogel was synthetized without problems (Figure 5.12). The gelation was performed in the dark in order to avoid to trigger the production of the oxidant species from the fullerene before the measurements. For the same reason, the samples of the synthetized hydrogel were always kept in the dark and were exposed to the light only while handling the sample for the measurements. The gel appeared dark brown in color (due to the presence of the fullerene monoadduct) and not particularly transparent. The same characterization previously performed on the methionine-hydrogels was repeated for comparison.

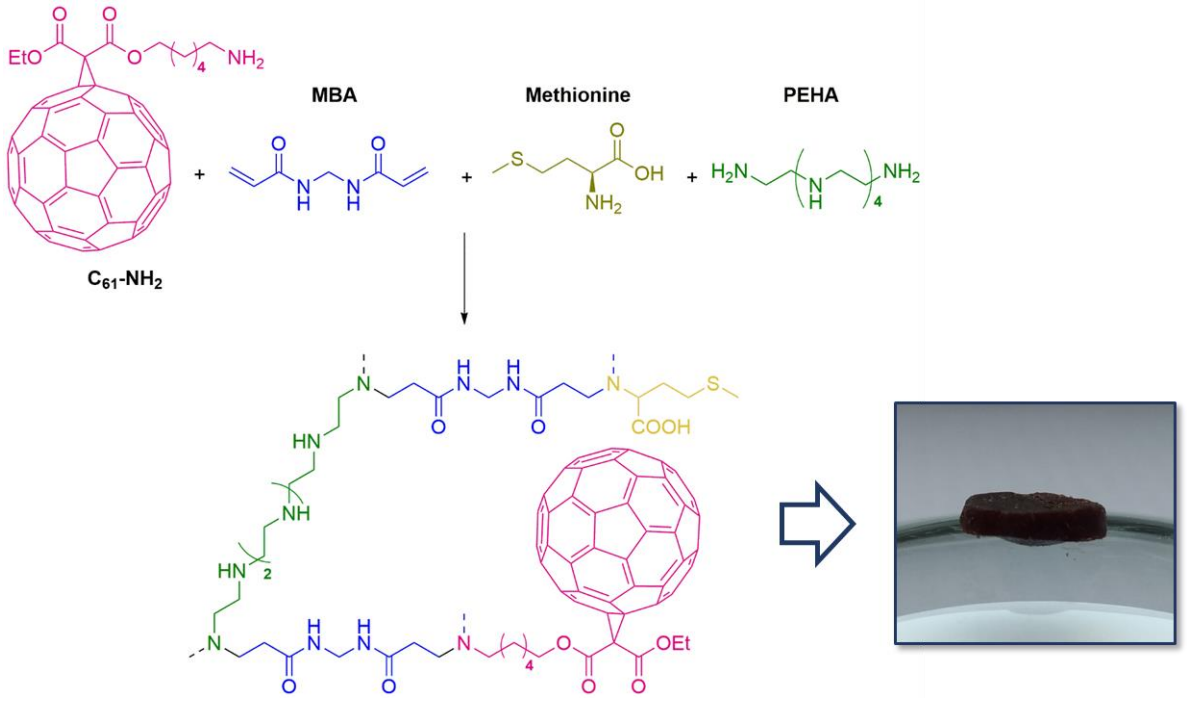

*Figure 5.12 Representation of the novel hydrogel matrix containing the fullerene derivative **C_{61}-NH_2** and photo of the obtained material.*

First of all, various samples of the hydrogels were put in different solvents (acetone, MeOH, DCM, THF, AcOEt) to test if a leaking of the fullerene moiety could be observed; the solution remained colorless and the subsequent mass spectroscopy analysis did not show the presence of the compound in solution. Then, the EDS value was calculated, with the same methodology already employed for the other hydrogels (see Chapter 4). The recorded value for the EDS was of 940 ± 60%, higher than those obtained with methionine- and methionine sulfoxide-based hydrogels of formulation (Entry 2 and 4 of Table 5.1), containing the same amount of sulfur co-monomers. This result could be explained by taking

into account that by adding the fullerene derivative to gel formulation the number of primary amino groups present during the gelation process increased and reached a value half-way between the two original formulations (A and B, Table 5.1).

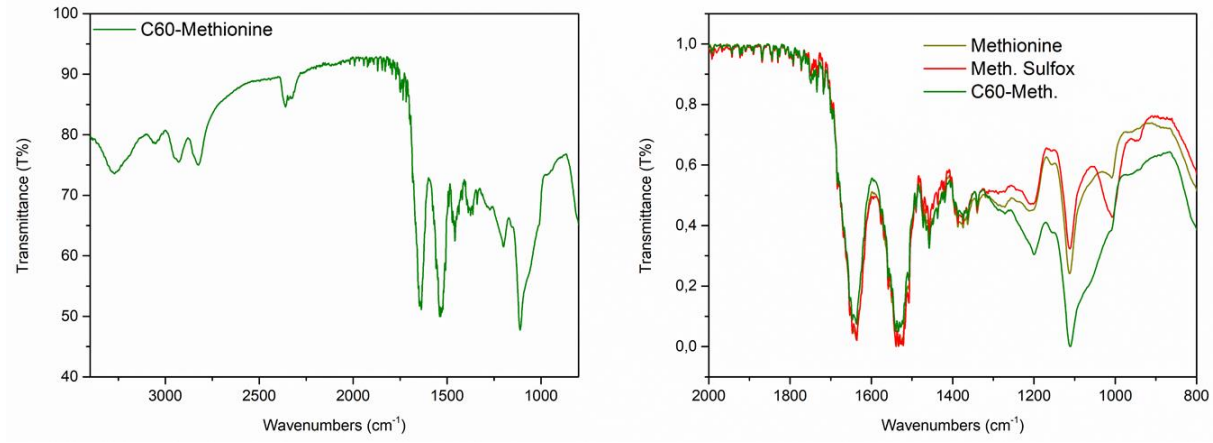

Figure 5.13 (left) ATR-IR spectrum of the novel fullerene-based hydrogel formulation, (right) comparison between the ATR-IR spectra of the different sulfur-based hydrogel formulations in the 800-2000 cm^{-1} range.

In Figure 5.13, the ATR-IR spectrum of the novel fullerene-based formulation is shown alongside the comparison with the recorded spectra of the sulfide- and sulfoxide-based formulations. As can be seen, introduction of the C_{60} moiety inside the matrix produced a new broad band right in the region where the diagnostic peak of the sulfoxide moiety is present (1010 cm^{-1}, see also Figure 5.7). As a consequence, ATR-IR was ruled out as an appropriate diagnostic tool to evaluate the sulfur oxidation state inside the hydrogel matrix.

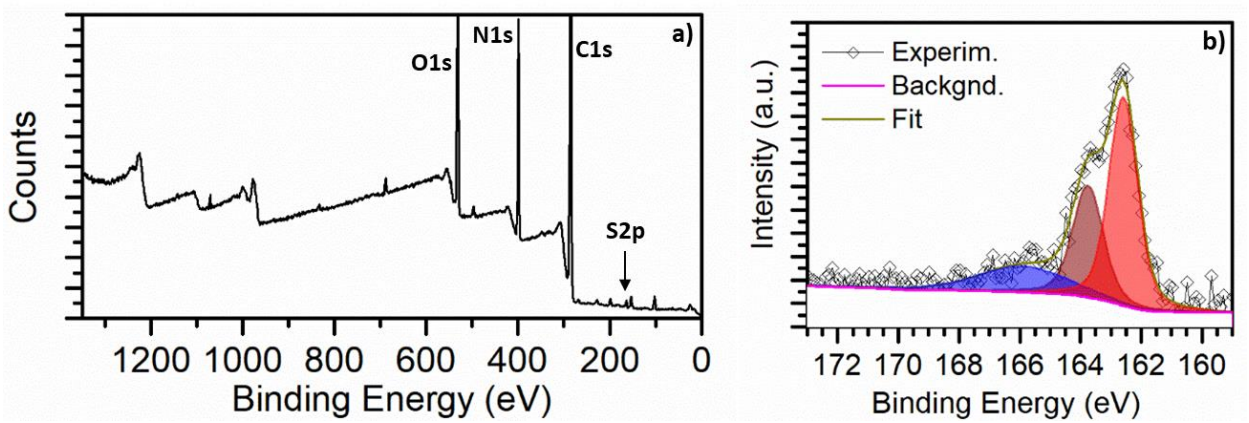

Figure 5.14 (a) Survey and (b) sulfur-HD spectrum of the tandem hydrogel formulation; the colored areas correspond to the fitting of the different components of sulfur, in red the reduced form (sulfide) and in blue the oxidized (sulfoxide).

XPS analysis gave a more interesting result. The survey spectrum (Figure 5.14a) showed the presence of sulfur inside the material, even if in lower amount if compared to the corresponding spectra of the two fullerene-free sulfur-based hydrogels (Figure 5.8), in line with the addition of another component to the same formulation. The HD spectrum on the sulfur channel showed the expected two components of the methionine sulfur present in the hydrogel (in red) along with another peak (in blue), which was assigned to the presence of some sulfoxide. As can be seen in Figure 5.8, the latter was not present in the original, fullerene-free methionine formulation, and the same aminoacid was used also in the synthesis of the tandem hydrogel. This observation thus led to the conclusion that the small amount of sulfoxide present inside the tandem hydrogel (less than 20% of the total amount of sulfur) derived from

the *in situ* oxidation of the methionine mediated by the fullerene moieties when the sample was handled (and then exposed to the ambient light) for preparing SEM experiments. After this result, more precautions were taken while handing samples of this hydrogel to avoid the uncontrolled oxidation of the methionine.

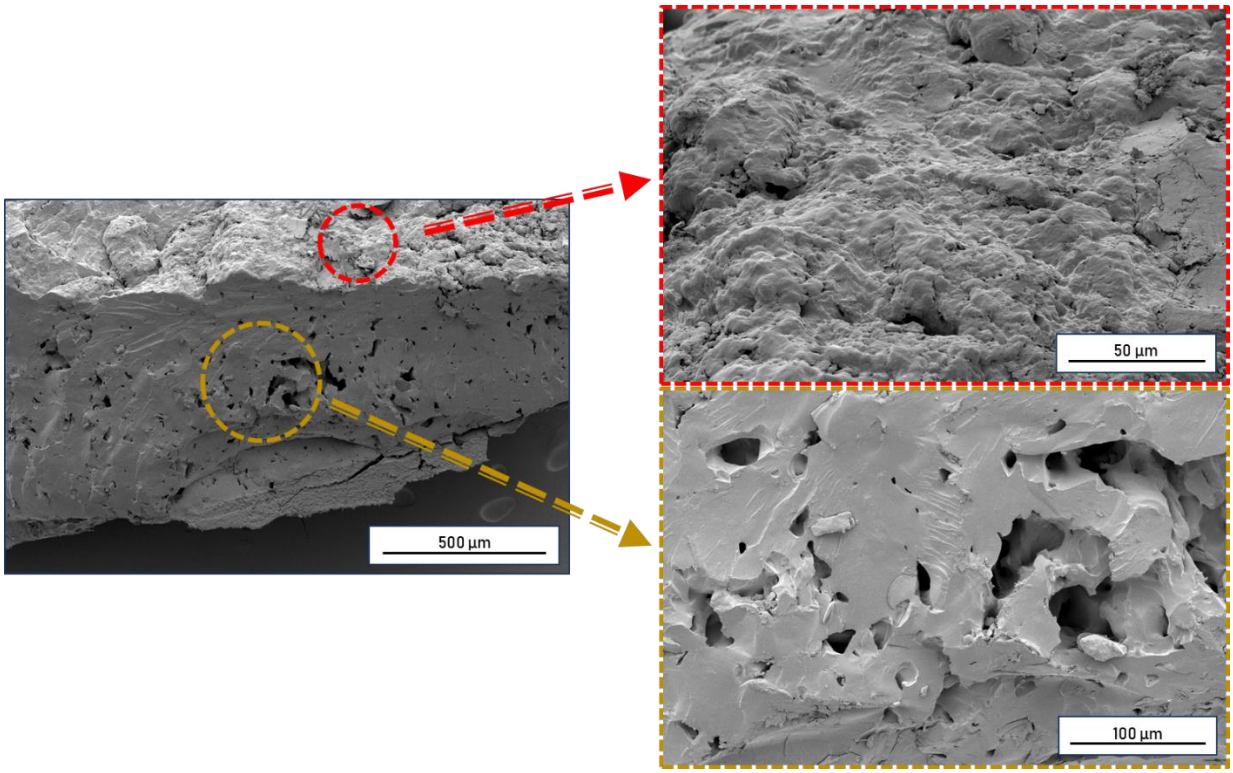

Figure 5.15 SEM pictures of the tandem hydrogel, on right the zoom of (top) the surface and (bottom) the section of the sample.

Finally, SEM pictures of the sample were recorded (Figure 5.15). The hydrogel showed a similar structure to those already observed in the case of the other two sulfur-based formulations. The matrix did not present a highly porous structure, most of the surface seemed a continuous layer of polymer with only some sporadic big holes, while the inner part of the sample appeared more porous if compared to the external part, even if the amount of channels observed was much lower if compared to those observed in the reference hydrogel matrix. On the other hand, the filled and thick matrix structure could help to observe eventual modifications that could take place after oxidation of the methionine moieties.

5.2.3.2. Oxidation Experiments

The first oxidation experiment was performed by exposing the tandem fullerene/methionine hydrogel to UV light (365 nm) using a low power lamp (6 W). Four different samples of the material were used; they were put in open glass vials filled with distilled water and placed under the UV lamp for 5h. After the end of the experiment, the pH of each vial was measured and found to be different: indeed, two samples had a neutral pH, while the other two had basic pH, in particular 8 and 10, sign that the experimental setup had to be optimized. The hydrogels were then transferred in fresh distilled water and kept there until they reached a constant weight. The subsequent lyophilization allowed to calculate the EDS value of the sample after the experiment (Table 5.2). The XPS and SEM characterization was then performed as well.

Table 5.2 Hydrogel characterization before and after the exposition to the UV lamp.

Sample	EDS	XPS Analysis	
		Ox. State	% Sulfur
Before UV exposure	940 ± 60%	sulfide	80.4
		sulfoxide	19.6
After UV exposure	830 ± 150%	sulfide	47.2
		sulfoxide	26.7
		sulfone	26.1

EDS values of the hydrogels matrix before and after the exposure to the UV lamp, unfortunately, did not significantly differ. As can be seen from the large error (calculated as average deviation) reported in Table 5.2, there was a significant difference in EDC values between the various hydrogel samples analyzed, with those presenting a higher pH also showing better EDS. This last observation showed us how a correct and uniform exposure of the samples to the lamp was necessary to the experiment.

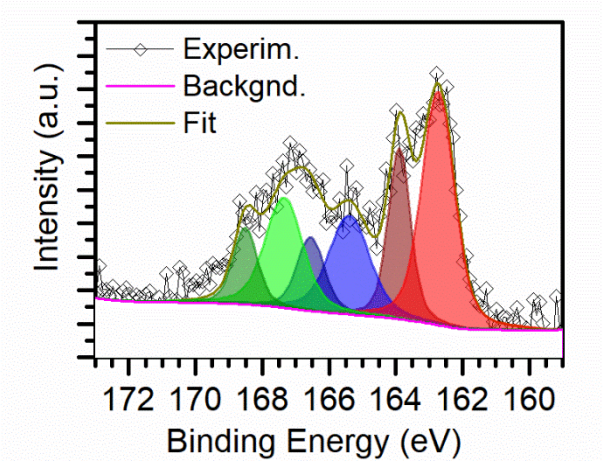

Figure 5.16 HD XPS spectrum on the sulfur channel of the tandem hydrogel after the exposure to the UV lamp. The colored areas correspond to the fitting of the different components of sulfur, in red the reduced form (sulfide), while the oxidized form are in blue (sulfoxide) and green (sulfone).

The XPS spectrum on the sulfur channel showed an unexpected result (Figure 5.16). If compared to the recorded spectrum before the oxidation (Figure 5.14), it can be seen that the amount of sulfur in reduced form (methionine) decreased after exposition to the UV light, going from more than the 80% of the total sulfur present in the sample to ≈ 47% (Table 5.2), in line with expectations. What was unpredicted was the appearance of another pair of peaks at higher energy than those related to methionine sulfoxide. By comparison with other works reported in literature,[39] the two new peaks could be assigned to the even more oxidized form of methionine, namely its sulfone (Figure 5.17).

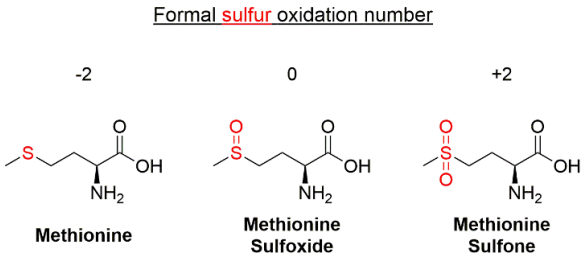

Figure 5.17 Chemical structure of the different forms of methionine observed.

Also the SEM picture taken on samples irradiated by the UV lamp showed some changes in the structure of the material. In fact, as can be seen in Figure 5.18, while the surface of the hydrogel did not show any significant difference after the exposure to the light (see for comparison Figure 5.15), the inner part of the material presented a large number of small pores, which were almost completely absent before the experiment. The formation of these holes could be explained by a more hydrophilic structure causing a stronger interaction with water and thus a larger separation between the polymeric chains of the network. Notably, the change was observed only in the inner part of the material, compatible with the *in situ* production of the oxidant species form the fullerene moieties.

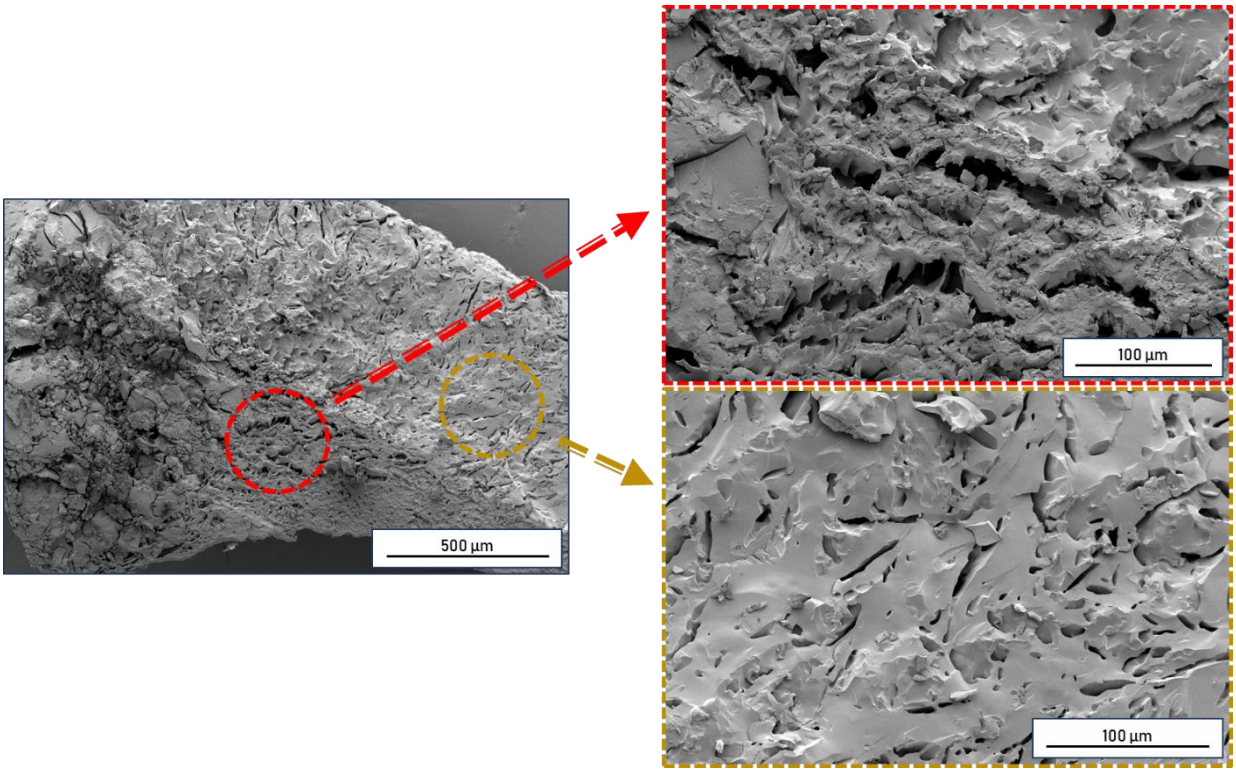

Figure 5.18 SEM pictures of the tandem hydrogel after he exposition to the UV lamp, on right the zoom of (top) the surface and (bottom) the section of the sample.

Fullerene excitation had thus proved capable to trigger also the further oxidation of the sulfoxide and change the macroscopic structure of the hydrogel. These observations suggested us that the constant EDS value recorded could be actually due only to the low amount of light irradiated to the sample; to test this hypothesis we tried to perform the experiment for longer times and with a more powerful lamp. The samples were also placed in a different position relative to the lamp (not under, but in front of it) in order to allow a more homogeneous irradiation and a PBS buffer solution was used to maintain the same pH (7.4) in all the samples. The lamp used was a white-light one (high pressure mercury lamp, chosen to be able to cover all the fullerene absorption spectrum) with higher power (100 W) and the exposure time was increased to 20h. Due to the power of the lamp, a sample of the pristine hydrogel was also exposed to the light for the entire experiment, in order to verify eventual degradation processes taking place on the hydrogel network.

Table 5.3 Hydrogels characterization after the exposure to the high energy lamp.

Formulation	**EDS**	**XPS Analysis**	
		Ox. State	**% Sulfur**
Tandem Light-responsive	1700 ± 200%	sulfide	34.3
		sulfoxide	32.6
		sulfone	33.8
Pristine (GABA)	700 ± 100%	-	-
		-	-

At the end of the experiment, the hydrogel samples were removed from their solution and kept in distilled water until they reached a stable weight, in order to determine the EDS value as usual. The pH of the solution of each sample was measured and did not differ from the value recorded before the experiment. The lyophilized samples were then used also for the SEM and XPS characterization. As can be seen from Table 5.3, while the EDS value of the original hydrogel did not significantly differ from that recorded before the exposure (see Chapter 4.2.2), in the case of tandem hydrogel the EDS greatly increased after irradiation with the white-light (see Table 5.2 for comparison). The value increased also if compared to that recorded in the previous experiment with the low energy lamp (still see Table 5.2), in agreement with our initial hypothesis. The huge increment of the EDS value recorded was also sign of a great change in the hydrogel structure, which was confirmed by SEM and XPS analysis.

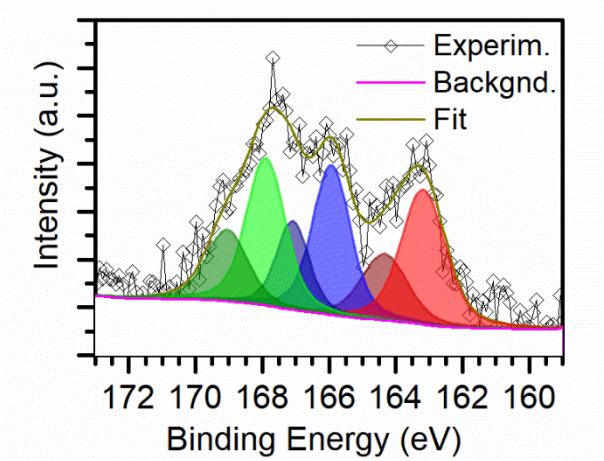

Figure 5.19 HD XPS spectrum on the sulfur channel of the hydrogel after the second experiment of exposure to white light. The colored areas correspond to the fitting of the different components of sulfur, in red the reduced form (sulfide), while the oxidized form are in blue (sulfoxide) and green (sulfone).

XPS analysis on the sulfur channel (Figure 5.19) showed an increment of the oxidized forms of the methionine at the expense of the reduced form, representing now only 34% of the total sulfur present inside the hydrogel (Table 5.3). The amount of both the sulfoxide and sulfone increased if compared to the results of the previous experiment (Table 5.2) and justifies the increase observed in the EDS value.

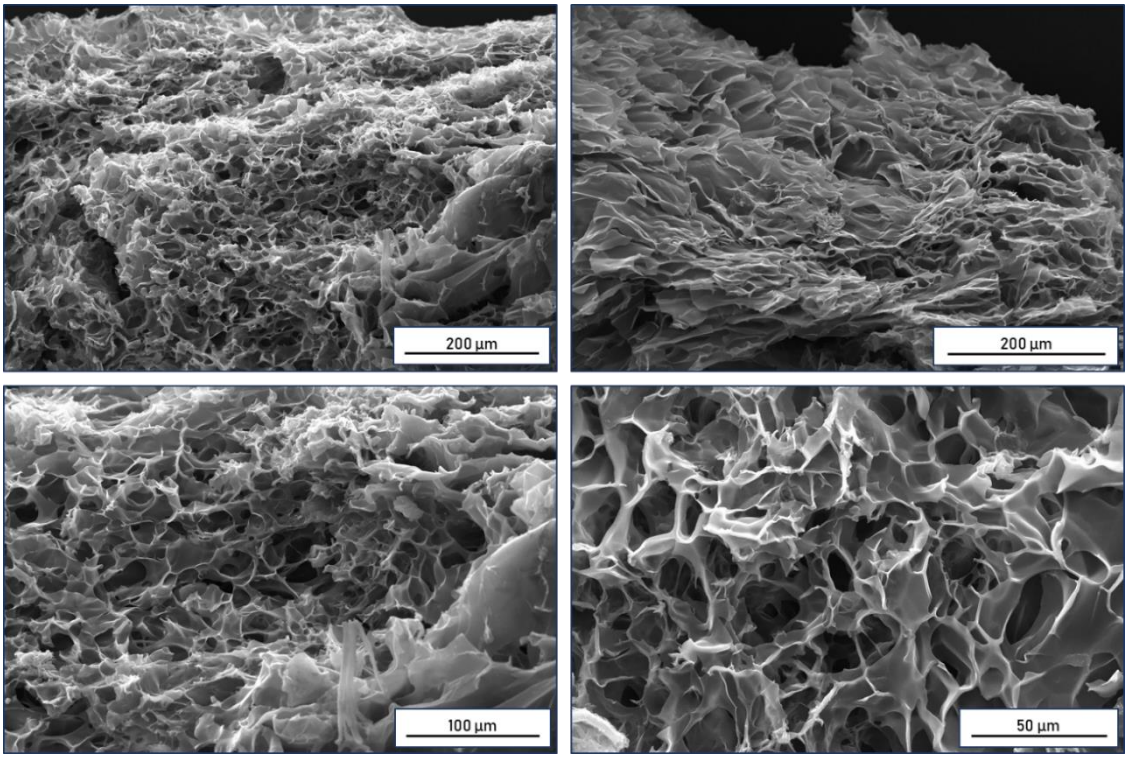

Figure 5.20 SEM picture of the light-responsive hydrogel after the exposure to the high energy lamp.

Finally, SEM analysis confirmed the previous observation. After 20h of exposure to the 100 W white-light lamp, the structure of the hydrogel greatly changed, leading to the formation of a highly porous network which was consistent with the increment of the EDS value. The pores were equally and uniformly distributed within the material and seemed to be interconnected, as already observed in the pristine hydrogel. By comparison with the pictures taken after the previous experiment (Figure 5.18), this results suggests that the increase in the amount of oxidized methionine present inside the network had a huge effect on the gel hydrophilicity and the polymer chains separation (Scheme 5.5).

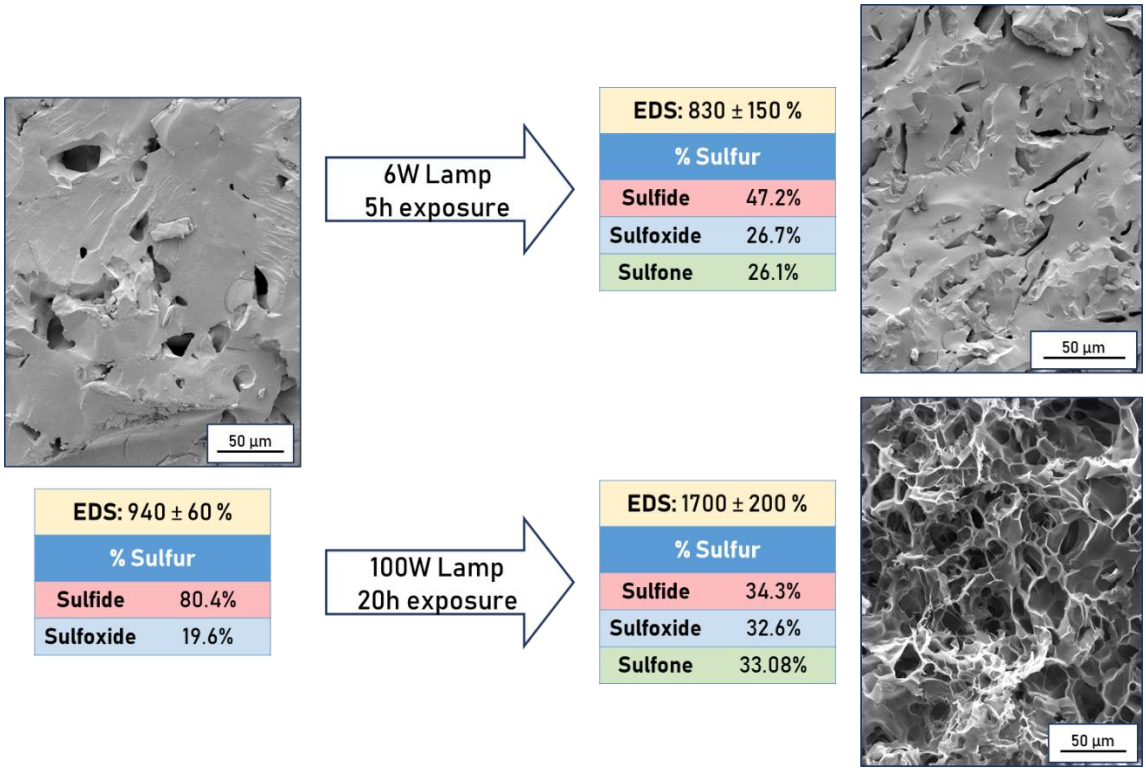

Scheme 5.5 Summary of the properties of the light-responsive hydrogel before and after exposure to light in different conditions.

SEM pictures of the pristine hydrogel were also taken to monitor the effect of the long exposure of the reference matrix to an high energy lamp and exclude that the pores observed in the light-responsive hydrogel samples derived from the degradation of the poliamidoamine network. As can be seen in Figure 5.21, the structure did not present any significant change after the exposure to the lamp. The highly porous system was maintained and also the pores dimensions (5-70 µm) were similar to those previously observed. Along with the EDS value registered, we could conclude that no sign of degradation of the hydrogel matrix was detected as a result of the exposure to the high-energy lamp.

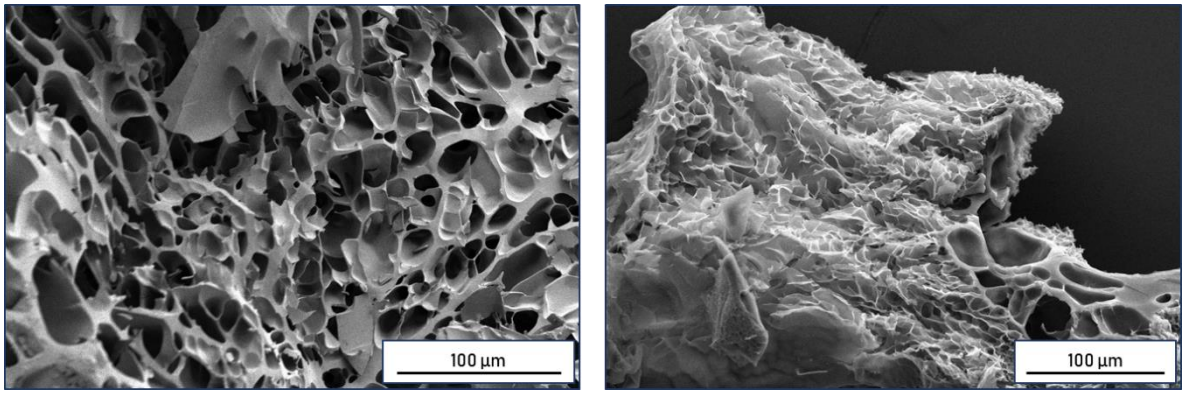

Figure 5.21 SEM pictures of the original hydrogel (left) before and (right) after the exposition to the high energy lamp.

Finally, a sample of methionine-based hydrogel was used to test if the same effect observed on the physical properties and the structure of the methionine/fullerene system could also be obtained in the absence of fullerene by means of a classical chemical oxidation. The compound chosen for the test was KO_2, a common strong oxidant. Such oxidizing species could diffuse inside the hydrogel network, mimicking the effect of the singlet oxygen produced by the fullerene moieties under irradiation. A

sample of the original, GABA-containing polyamidoamide hydrogel was also used as reference. The experiment was carried out by immersing the hydrogel samples inside a aqueous solution of KO_2 10 mM for one night. After that, the hydrogels were put in water and their EDS values were measured. Subsequently, the corresponding dry samples were also used for the SEM and XPS analysis.

Table 5.4 Hydrogels characterization after the treatment with KO_2.

Formulation	EDS	XPS Analysis	
		Ox. State	% Sulfur
Methionine	550 ± 50%	sulfide	30.5
		sulfoxide	50.2
		sulfone	18.3
Pristine (GABA)	1900 ± 100%	-	-
		-	-

Table 5.4 summarize the data obtained from the EDS and XPS analysis. As it can be seen, the formulation with methionine did not show any significant change in the EDS value if compared to the untreated samples of the same hydrogel (for comparison see Table 5.1). On the other hand, the case of the pristine hydrogel (in which only GABA was used) was different, showing a great increment of the EDS value after the exposure to the strong oxidant. This observation was consistent with what already observed in Chapter 4.2.2 for the synthesis of the conductive hydrogel, where the degradation of the hydrogel matrix was observed after treatment with a solution of APS. Probably in this case the same degradation occurred, which did not seem to take place once the GABA was totally replaced by the methionine. The explanation could be related to the fact that in the methionine formulation of an easily oxidisable component is present in the matrix (methionine itself) acting as "sacrificial agent", which is oxidized more quickly than the hydrogel matrix, thus avoiding the massive degradation of the network.

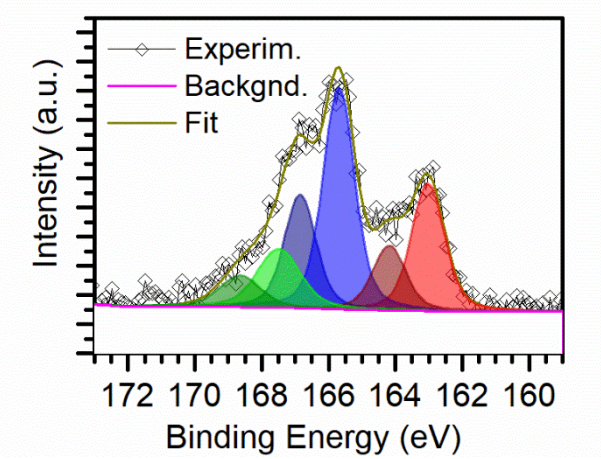

Figure 5.22 HD XPS spectrum on the sulfur channel of the hydrogel after treatment with KO_2. The colored areas correspond to the fitting of the different components of sulfur, in red the reduced (sulfide), while the oxidized form are in blue (sulfoxide) and green (sulfone).

The XPS spectrum of the methionine-hydrogel supports this hypothesis as well. As it can be seen in Figure 5.22 and Table 5.4, exposure to the oxidizing agent caused formation not only of the sulfoxide, but also of the sulfone. Notably, a different ratio between the three sulfur components was recorded in this case relative to the values observed for the fullerene-mediated photooxidation (for comparison see Table 5.3 and Figure 5.19). In particular, while the amount of methionine left was comparable, there was

less sulfone present in the case of the oxidation with KO_2, indicating that the reaction principally led to the formation of the sulfoxide. This difference could explain the discrepancy in the EDS value, due to the more hydrophilic properties of the sulfoxide.[13a]

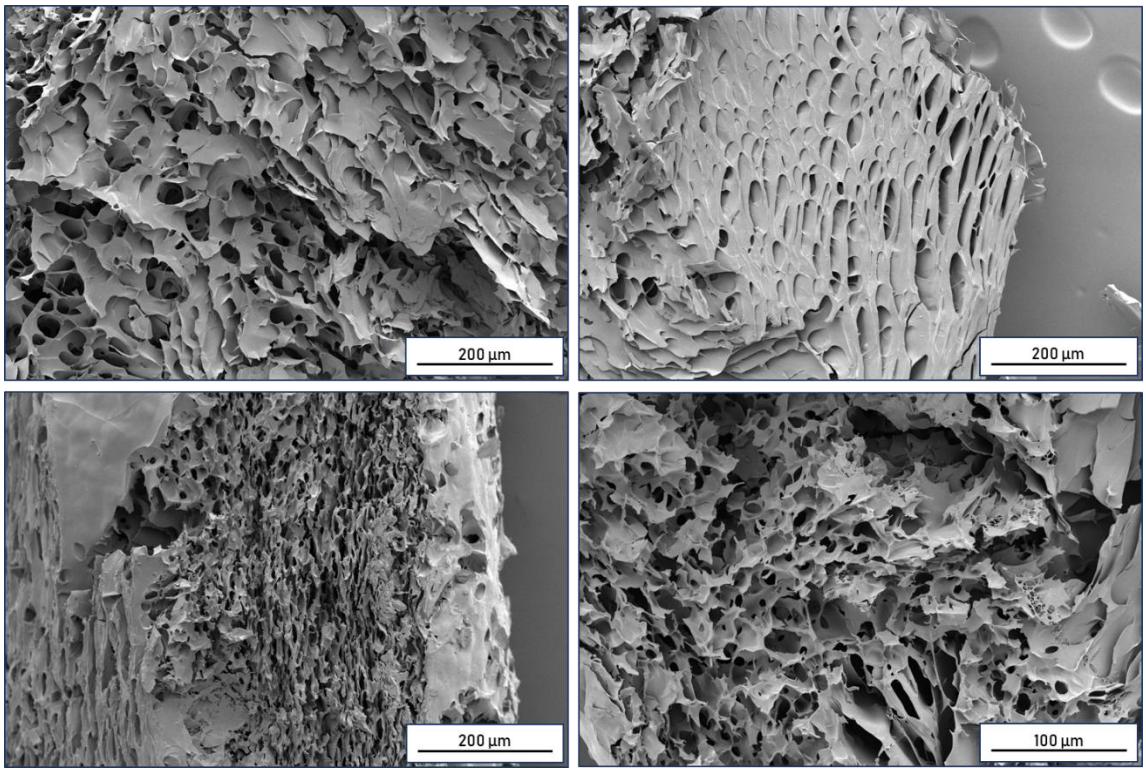

Figure 5.23 SEM pictures of (top) the original and (bottom) the methionine-based hydrogel after treatment with KO_2.

SEM analysis showed the different behavior of the two hydrogel formulations tested. The original hydrogel (Figure 5.23, top) did not show significant changes in the structure, even if the hydrogel layer seemed thinner than those previously observed (i.e. in Figure 5.21). On the other hand, the hydrogel obtained from the methionine-based formulation (Figure 5.23, bottom) showed large morphological differences within the same sample. As it can be seen in the bottom left picture in Figure 5.23, two separated regions were present, one in which the hydrogel presented a more porous structure (zoomed in the bottom right picture of Figure 5.23) and another one constituted by thick wall of polymeric matrix with only some big holes. The two different morphologies could derive from a different exposition to the oxidizing agent: where the latter was present in larger amount a more pronounced oxidation of the matrix could be recognized, leading to the porous system, while where it was almost absent the hydrogel structure mostly resembled the initial one (see Figure 5.10 for comparison). Noteworthy is that in the case of the light-responsive hydrogel, after exposure to the high energy lamp (Figure 5.20), only one structural pattern was observed (the porous network), homogeneously distributed along all the material. The different oxidation patterns observed either at the XPS and with the SEM could be related to the fact that the oxidation promoted by the fullerene moieties in the light-responsive hydrogel took place *in situ,* while KO_2 had to diffuse inside the matrix from the external solution. This difference led to a more efficient oxidation in the case of bound fullerene, which was also reflected in the higher EDS value and the more porous structure observed in SEM.

5.3. Conclusions

This part of the PhD work was focused on the development of a novel light-responsive hydrogel, starting from a reference, not stimuli-responsive material. The hydrogel was designed as a tandem system were two different moieties had to interact in order to use light to change the physical properties of the system. We decided to use oxidation as the process able to induce the desired macroscopic change in the material: by changing the oxidation state of a particular compound inside the hydrogel network we hoped to increase the hydrophilicity of the system and then its water uptake capability. To trigger the oxidation, we decided to employ an organic compound with a wide absorption spectrum and amenable to easy functionalization to facilitate its covalent linkage to the hydrogel network. The compounds chosen for the two roles were methionine and fullerene: the first one could be easily oxidized to the corresponding sulfoxide and sulfone and possesses a structure similar to GABA, which was originally employed in the polyamidoamine hydrogel formulation (Chapter 4). The second compound, fullerene, is able to absorb visible and UV light, and use it to generate singlet oxygen, a strong oxidant specie; in addition, it can also be easily functionalized in various manner in order to tune its properties.

First of all, we synthetized hydrogels containing methionine and the corresponding sulfoxide, to check if they displayed a different water uptake capability. This first experiment allowed us to identify a particular formulation for which the EDS values of hydrogels containing the methionine and methionine sulfoxide were significantly different. The next step was the synthesis of the proper fullerene derivative capable to be introduced into the hydrogel network. To this end, we designed amino fullerene **C_{61}-NH_2** and then synthetized it using a Bingel reaction as the key step after preparation of a proper malonic intermediate bearing a primary amino group. The fullerene moiety was then successfully introduced in a hydrogel containing also methionine, with no leakage occurring in water or other organic solvents. Initial characterization of this material showed that exposure to ambient light during its handling was already sufficient to start production of singlet oxygen and then trigger the oxidation of the methionine. The oxidation experiments were carried out by exposing samples of the fullerene-hydrogel to the light of different lamps: the first experiment was performed with a low energy UV lamp (6 W) and an exposure time of 5h, while later the procedure was repeated with a more powerful white-light lamp (100 W) for a longer time (20h). The analysis carried out (EDS, XPS and SEM) showed a progressive change in the physical and morphological structure of the hydrogels moving from the first to the second experiment. In fact, if irradiation with the low power UV lamp did not affect the EDS value to a large extent, after the longer exposition to the second lamp a significant increase of water uptake was observed. This change was explained by the SEM and XPS analysis, which showed how the morphological structure became more porous and the oxidation more pronounced with longer exposition time and more powerful lamp. No change was observed when a sample of the original hydrogel, with no fullerene or methionine, was exposed to the lamp, verifying our hypothesis of the existence of a tandem process inside the samples. Increasing the exposure time and the power of the lamp resulted in an increased singlet oxygen production, enhancing methionine oxidation and producing a more hydrophilic material. Finally, a sample of the methionine-base hydrogel was treated with a good oxidant (KO_2) to check if an chemical oxidation process could lead to the same changes observed before in the light-responsive system. The experiment showed how, even if methionine oxidation was similar to that observed in the tandem hydrogel, the process was not uniform in the entire material (as easily detectable from the SEM pictures), thereby not leading to similar changes of the physical properties, in particular the water uptake capability. The reference experiment performed with the original, GABA-containing polyamidoamine hydrogel formulation, showed a vast degradation process, confirming the above observation. Thus, it appears that the different oxidation patterns observed for the two methodologies

(photooxidation *vs.* chemical oxidation) could be related to the fact that the fullerene-promoted reaction in the light-responsive hydrogel took place *in situ*, leading to a more efficient and homogeneous process, while the outcome of the KO_2-mediated reaction was strongly affected by the different distribution of the oxidant within the gel matrix. We can then conclude that the light-responsive hydrogel incorporating a tandem fullerene/methionine system could undergo a significant change in water uptake capability upon exposure to a light source and that this change was general and homogeneous in the entire network. The easy alterability of the chosen hydrogel matrix should allow its future employment for the development of more optimized tandem systems.

5.4. Experimental Section

5.4.1. Synthetic procedures

<u>*tert*-Butyl (6-hydroxyhexyl)carbamate</u>

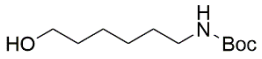

36

In a flame dried round bottom flask, 6-amino-1-hexanol (1.5 g, 12.8 mmol, 1.0 eq.) was dissolved in dry THF (45 mL) and cooled to 0°C in an ice bath under nitrogen atmosphere. Then, NaOH (aq.) 1 M (15 mL) and Boc_2O (3.6 g, 16.6 mmol, 1.3 eq.) were added in this order, and the reaction mixture was stirred for 16h at room temperature. The solvent was removed by rotary evaporation and the aqueous phase was first diluted with water (60 mL) and then extracted with Et_2O (3 × 60 mL). The combined organic phases were dried over Na_2SO_4 and concentrated under reduced pressure to yield **36** (2.8 g, 12.7 mmol, 99% yield) as a pale yellow oil.

^{1}H-NMR ($CDCl_3$, 400 MHz): δ (ppm) 4.54 (bs, 1H), 3.62 (t, *J* = 6.4 Hz, 2H), 3.12 (q, *J* = 6.4 Hz, 2H), 1.61-1.32 (m, 17H).

The NMR spectrum is in agreement with that reported in the literature.[40]

<u>6-((*tert*-Butoxycarbonyl)amino)hexyl ethyl malonate</u>

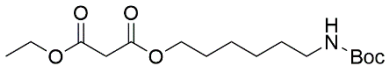

37

In a flame dried round bottom flask, ethylmalonyl chloride (1.92 g, 12.7 mmol, 1.0 eq.) was added dropwise to a solution of protected amino alcohol **36** (2.8 g, 12.7 mmol, 1.0 eq.) and pyridine (1.50 g, 19.2 mmol, 1.5 eq.) in dry DCM (115 mL) at 0°C, under nitrogen atmosphere. After 1h, the mixture was allowed to slowly warm up to r.t., then stirred for 16h, concentrated under reduced pressure and diluted with Et_2O (70 mL). The solution was then washed with water (3 × 70 mL) and, after that, the reunited organic phases were dried over Na_2SO_4 and concentrated under reduced pressure. Flash column chromatography (SiO_2, P.E./AcOEt 3:1) gave ester **37** (1.06 g, 11.4 mmol, 90% yield) as a yellow oil.

IR (neat): v = 3396, 3362, 2976, 2937, 2864, 1731, 1712, 1516, 1147 cm^{-1}.

^{1}H-NMR ($CDCl_3$, 400 MHz): δ (ppm) 4.52 (bs, 1H), 4.20 (t, *J* = 6.9 Hz, 2H), 4.14 (q, *J* = 7.0 Hz, 2H), 3.36 (s, 2H), 3.13-3.08, (m, 2H), 1.65 (quint, *J* = 7.0 Hz, 2H), 1.57 (s, 2H), 1.44 (s, 9H), 1.38-1.33 (m, 4H), 1.28 (t, *J* = 6.9 Hz, 3H).

^{13}C-NMR ($CDCl_3$, 100 MHz): δ (ppm) 166.6, 166.6, 156.0, 78.9, 65.4, 61.4, 41.6, 40.4, 29.9, 28.4, 28.3, 26.3, 25.4, 14.0.

ESI-MS (*m/z*) = 354.01 $[M+Na]^+$.

Monoadduct of malonate 37 (38)

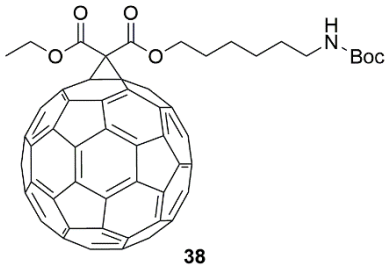

38

In a flame dried round bottom flask, DBU (0.21 mL, 1.40 mmol, 5.0 eq.) was added under nitrogen atmosphere to a stirred solution of C_{60} (200 mg, 0.28 mmol, 1.0 eq.), malonate ester **37** (94 mg, 0.28 mmol, 1.0 eq.) and CBr_4 (400 mg, 1.20 mmol, 4.5 eq.) in dry toluene (200 mL). The resulting solution was stirred for 16h at r.t. and then filtered through a short plug of SiO_2, which was subsequently washed with DCM. The solvent was evaporated under reduced pressure and then the mixture was separated by means of flash column chromatography (SiO_2, AcOEt/cyclohexane from 1:6 to 1:1), which gave fullerene derivative **38** (73 mg, 25%) as a brown glassy solid.

^{1}H-NMR ($CDCl_3$, 400 MHz): δ (ppm) 4.56 (q, *J* = 7.0 Hz, 2H), 4.49 (t, *J* = 6.3 Hz, 2H), 3.18-3.06 (m, 2H), 1.85 (quint, *J* = 6.9 Hz, 2H), 1.54-1.38 (m, 18H).

^{13}C-NMR ($CDCl_3$, 100 MHz): δ (ppm) 163.8, 163.7, 156.1, 145.5, 145.4, 145.4, 145.3, 145.0, 144.9, 144.8, 144.8, 144.1, 143.2, 143.2, 143.2, 142.4, 142.1, 142.1, 141.1, 139.2, 139.1, 79.3, 71.8, 67.4, 63.6, 52.4, 40.6, 30.2, 29.9, 28.7, 28.6, 26.6, 25.8, 14.4.

ESI-MS (*m/z*) = 1049.49 $[M-1]^+$.

Deprotected monoadduct (C_{61}-NH_2)

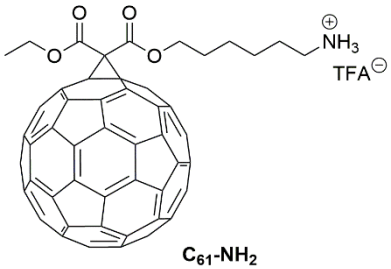

C_{61}-NH_2

In a round bottom flask, protected fullerene derivative **38** (51 mg, 0.049 mmol) was dissolved in DCM (5 mL). Then, under stirring, TFA (1.5 mL) was added and the solution was stirred for 2h.TLC analysis (DCM/MeOH 10:1 + 1% NEt_3) showed the complete disappearance of the starting material (brown coloured spot, Rf ≈ 0.93) and the formation of another brown coloured spot attributable to a more polar compound (Rf ≈ 0.12). The solvent was then evaporated and the product **C_{61}-NH_2** was collected as a red solid and used directly for the hydrogel synthesis (51 mg, 0.049 mmol, 99% yield).

5.4.2. Other Procedures

- **Synthesis of the hydrogels; General procedure**

The following procedure is valid for all formulations reported in the text. By varying the co-monomer and its amount according to Table 5.5 it is possible to synthetize all the previously described hydrogels.

In a round bottom flask, MBA (200 mg, 1.30 mmol) was suspended in 1.5 ml of distilled water at r.t.. Then, in order, the co-monomer(s) and PEHA (72 mg, 0.31 mmol) were added and the temperature was raised to 40°C. The suspension was stirred vigorously until all solids were dissolved (approximately 30min). Finally, the mixture was transferred into a glass vial and allowed to react in static conditions at 40°C for 16h.

The obtained hydrogel scaffold was subsequently washed with water several times and then kept in water for 2 days (changing the solvent every 6h) before use, to allow the release of all the unreacted starting materials from the gel matrix.

Table 5.5 Amount of co-monomers used in the different hydrogel formulations tested.

Formulation	Co-monomer(s)	Amount
Methionine-based A	Methionine	100 mg (0.64 mmol)
Methionine-based B	Methionine	72 mg (0.49 mmol)
Sulfoxide-based A	Methionine sulfoxide	106 mg (0.64 mmol)
Sulfoxide-based B	Methionine sulfoxide	80 mg (0.49 mmol)
Light-responsive	Methionine C_{61}-NH_2	72 mg (0.49 mmol) 57 mg (0.049 mmol)
Pristine	GABA	50 mg (0.49 mmol)

- **Sample lyophilization**

Lyophilization, also known as freeze-drying, uses rapid cooling to allow solvent removal by sublimation under vacuum.[41] The scaffolds were swollen in water and frozen at -196 °C in liquid nitrogen for 30min. Then, they were transferred to a lyophilizing jar and lyophilized for 16 hours at a pressure of 150 mT. Lyophilized samples were used right away for SEM, XPS and ATR-IR analysis.

- **Swelling measurements**

EDS was calculated using the following equation:

$$\mathrm{EDS} = \frac{\mathrm{W_{wet}} - \mathrm{W_{dry}}}{\mathrm{W_{dry}}} \times 100$$

where W_{wet} and W_{dry} are, respectively, the weight of the swollen and lyophilized hydrogel measured by gravimetric method. The swollen weight was taken after several measurements after the value stayed stable (about 2 days), using the hydrogel obtained from the synthesis, not lyophilized. After that, the samples were lyophilized and the dry weight was recorded. Their surface was blotted free of water using filter paper and their swollen weights were measured on an analytical balance.

- **Scanning electron microscopy analysis**

The lyophilized samples were mounted on aluminum stubs using adhesive carbon tape. Samples were then sputtered with gold to form a layer of approximately 20 nm on the surface. SEM images were captured at 10-20 kV accelerating voltage using a SEM FEI Quanta FEG 250 instrument.

- **Oxidation experiments**

- with low power UV lamp

Cylindrical samples (≈ 3 mm diameter and ≈ 1 mm thickness) of the hydrogel were put in vials filled with distilled water. The vials were left open and then placed under a UV lamp (6 W, 365 nm, distance ≈ 15 cm) for 5h in static conditions. After the end of the experiment the samples were removed from the solution and kept in fresh distilled water for 2 days before any other use. The pH of the solution used was measured right after the end of the experiment.

- with high energy white-light lamp

Cylindrical samples (≈ 3 mm diameter and ≈ 1 mm thickness) of the hydrogel were put in vials filled with PBS buffer (Gibco™, pH = 7.4). The vials were closed and then placed in front of a high pressure mercury lamp (100 W, white light, distance ≈ 30 cm) for 20h in static conditions. After the end of the experiment the samples were removed from the solution and then kept in fresh distilled water for 2 days before any other use. The pH of the solution used was measured right after the end of the experiment.

- with KO_2

Cylindrical samples (≈ 3 mm diameter and ≈ 1 mm thickness) of the hydrogel were put in vials filled with an aqueous solution of KO_2 10 mM. The vials were closed and left in static conditions for 20h. The samples were removed from the solution and then kept in fresh distilled water for 2 days before any other use.

5.5. References

1 Qiu, Y.; Park, K. *Adv. Drug Delivery Rev.* **2001**, *53*, 321.

2 (a) Tomatsu, I.; Peng, K.; Kros, A. *Adv. Drug Delivery Rev.* **2011**, *63*, 1257; (b) Katz, S.; Burdick, J.A. *Macromol. Biosci.* **2010**, *10*, 339.

3 (a) Kloxin, A.M.; Kasko, A.M.; Salinas, C.N.; Anseth, K.S. *Science* **2009**, *324*, 59; (b) Zhang, X.; Liu, M.; Li, Y.; Dong, Y.; Pingguan-Murphy, B.; Lu, T.; Xu, F. *Eur. Polym. J.* **2015**, *72*, 590.

4 Annabi, N.; Tamayol, A.; Uquillas, J.A.; Akbari, M.; Bertassoni, L.E.; Cha, C.; Camci-Unal, G.; Dokmeci, M.R.; Peppas, N.A.; Khademhosseini, A. *Adv. Mater.* **2014**, *26*, 85.

5 Zhao, Y-.L.; Stoddart, J.F. *Langmuir* **2009**, *25*, 8442.

6 Schiphorst, J.; Coleman, S.; Stumpel, J.E.; Azouz, A.B.; Diamond, D.; Schenning, A.P.H.J. *Chem. Mater.* **2015**, *27*, 5925.

7 (a) Lee, I-.N.; Dobre, O.; Richards, D.; Ballestrem, C.; Curran, J.M.; Hunt, J.A.; Richardson, S.M.; Swift, J.; Wong, L.S. *ACS Appl. Mater. Interfaces* **2018**, *10*, 7765; (b) Unger, K.; Salzmann, P.; Masciullo, C.; Cecchini, M.; Koller, G.; Coclite, A.M. *ACS Appl. Mater. Interfaces* **2017**, *9*, 17408.

8 (a) Wang, J.; Li, Q.; Yia, S.; Chen, X. *Soft Matter* **2017**, *13*, 6490; (b) Wang, D.; Wagner, M.; Butt, H-.S.; Wu, S. *Soft Matter* **2015**, *11*, 7656.

9 (a) Halperin, A.; Krçger, M.; Winnik, F.M. *Angew. Chem. Int. Ed.* **2015**, *54*,15342; (b) Shi, Y.; Ma, C.; Peng, L.; Yu, G. *Adv. Funct. Mater.* **2015**, *25*, 1219.

10 (a) Suzuki, A.; Ishii, T.; Maruyama, Y. *J. Appl. Phys.* **1996**, *80*, 131; (b) Suzuki, A.; Tanaka, T. *Nature* **1990**, *346*, 345.

11 Huang, K.; Wu, H.; Jiang, F.; Shen, G.; Wang, L. *Polym. Degrad. Stabil.* **2018**, *156*, 228.

12 (a) Lv, S-.W.; Liu, Y.; Xie, M.; Wang, J.; Yan, X-,W.; Li, Z.; Dong, W-.G.; Huang, W-.H. *ACS Nano* **2016**, *10*, 6201; (b) Zhang, H.; Guo, S.; Fu, S.; Zhao, Y. *Polymers* **2017**, *9*, 238.

13 (a) Napoli, A.; Valentini, M.; Tirelli, N.; Müller, M.; Hubbell, J.A. *Nat. Mater.* **2004**, *3*, 183; (b) Yang, P.; Deng, J.Y.; Yang, W.T. *Polymer* **2003**, *44*, 7157.

14 (a) Schweitzer, C.; Schmidt, R. *Chem. Rev.* **2003**, *103*, 1685; (b) DeRosa, M.C.; Crutchley, R.J. *Coord. Chem. Rev.* **2002**, *233/234*, 351.

15 (a) Wasserman, H.H.; Ives, J.L. *Tetrahedron* **1981**, *37*, 1825; (b) Clennana, E.L.; Pace, A. *Tetrahedron* **2005**, *61*, 6665.

16 (a) Li, B.; Lin, L.; Lin, H.; Wilson, B.C.; *J. Biophotonics* **2016**, *9*, 1314; (b) Wang, S.; Gao, R.; Zhou, F.; Selke, M. *J. Mater. Chem.* **2004**, *14*, 487.

17 Kochevar, I.E.; Redmond, R.W. *Methods Enzymol.* **2000**, *319*, 20.

18 Stasheuski, A.S.; Galievsky, V.A.; Stupak, A.P.; Dzhagarov, B.M.; Choi, M.J.; Chung, B.H.; Jeong, J.Y. *Photochem. Photobiol.* **2014**, *90*, 997.

19 Franskevych, D.; Palyvoda, K.; Petukhov, D.; Prylutska, S.; Grynyuk, I.; Schuetze, C.; Drobot, L.; Matyshevska, O.; Ritter, U. *Nanoscale Res. Lett.* **2017**, *12*, 40.

20 (a) Hirsch, A.; Bellavia-Lund, C. "*Fullerenes and Related Structures*" in "*Topics in Current Chemistry*", Berlin: Springer, **1993**; (b) Diederich, F.N. *Pure Appl. Chem.* **1997**, *69*, 395; (c) Prato, M. *J. Mater. Chem.* **1997**, *7*, 1097.

21 Prat, F.; Stackow, R.; Bernstein, R.; Qian, W.; Rubin, Y.; Foote, C.S. *J. Phys. Chem. A* **1999**, *103*, 7230.

22 Prat, F.; Santi, C.; Mart, N.; Zhang, X.; Foote, C.S.; Moreno, R.; Jose, G.; Bourdelandec, L.; Font, J. *Phys. Chem. Chem. Phys.* **2001**, *3*, 1638.

23 Hotze, E.M.; Labille, J.; Alvarez, P.; Wiesner, M.R. *Environ. Sci. Technol.* **2008**, *42*, 4175.

24 Iizumi, Y.; Okazaki, T.; Zhang, M.; Yudasaka, M.; Iijima, S. *Bull. Chem. Soc. Jpn.* **2008**, *81*, 1584.

25 Fiorini, F.; Prasetyanto, E.A.; Taraballi, F.; Pandolfi, L.; Monroy, F.; López-Montero, I.; Tasciotti, E.; De Cola, L. *Small* **2016**, *12*, 4881.

26 Weinberg, N.L.; Weinberg, H.R. *Chem. Rev.* **1968**, *68*, 449.

27 (a) Lacombe, S.; Cardy, H.; Simon, M.; Khoukh, A.; Soumillion, J.P.; Ayadim, M. *Photochem. Photobiol. Sci.* **2002**, *1*, 347; (b) Bonesi, S.M.; Manet. I.; Freccero, M.; Fagnoni, M.; Albini, A. *Chem. Eur. J.***2006**, *12*, 4844.

28 Jensen, F.; Greer, A.; Clennan, E.L. *J. Am. Chem. Soc.* **1998**, *120*, 4439.

29 Carofiglio, T.; Donnola, P.; Maggini, M.; Rossetto, M.; Rossi, E. *Adv. Synth. Catal.* **2008**, *350*, 2815.

30 Ravi, J.; Hills, A.E.; Cerasoli, E.; Rakowska, P.D.; Ryadnov, G.M. *Eur. Biophys. J.* **2011**, *40*, 339.

31 Reyanaud, J.A.; Malfoy, B. *J. Electroanal. Chem.* **1980**, *114*, 195.

32 Ji, H.; Wang, T.; Liu, Y.; Lu, C.; Yang, G.; Ding, W.; Hou, W. *Chem. Commun.* **2016**, *52*, 12725.

33 (a) Yan, W.; Seifermann, S.M.; Pierratd, P.; Bräse, S. *Org. Biomol. Chem.* **2015**, *13*, 25; (b) Collavini, S.; Delgado, J.L. *Sust. Energy Fuels* **2018**, DOI: 10.1039/c8se00254a.

34 Bingel, C. *Chem. Ber.* **1993**, *126*, 1957.

35 Buchini, S.; Buschiazzo, A.; Withers, S.G. *Angew. Chem. Int. Ed.* **2008**, *47*, 2700.

36 Muñoz, A.; Sigwalt, D.; Illescas, B.M.; Luczkowiak, J.; Rodríguez-Pérez, L.; Nierengarten, I.; Holler, M.; Remy, J-.S.; Buffet, K.; Vincent, S.P.; Rojo, J.; Delgado, R.; Nierengarten, J-.F.; Martín, N. *Nat. Chem.* **2016**, *8*, 50.

37 Silvestrini, S.; Dalle Nogare, D.; Carofiglio, T.; Menna, E.; Canu, P.; Maggini, M. *Eur J. Org. Chem.* **2011**, *28*, 5571.

[38] Green, T.W.; Wuts, P.G.M. "*Protective Groups in Organic Synthesis*", Wiley-Interscience, New York, **1999**.
[39] Zhang, G.; Yuan, S-.S.; Li, Z-.M.; Longa, S-.R.; Yang, J. *RSC Adv.* **2014**, *4*, 23191.
[40] Fisher, B.F.; Gellman, S.H. *J. Am. Chem. Soc.* **2016**, *138*, 10766.
[41] Thomson, R.C.; Wake, M.C.; Yaszemski, M.J.; Mikos, A.G. in "*Biopolymers II*" (Eds.: Peppas, N.A.; Langer, R.S.), Springer Berlin Heidelberg, Berlin, Heidelberg, **1995**, pp. 245.

Annex

Abbreviation

^{13}C-NMR	^{13}Carbon-nuclear magnetic resonance
^{1}H-NMR	^{1}Proton-nuclear magnetic resonance
1-PPA	3-(1*H*-pyrrol-1-yl)propan-1-amine
3-PPA	3-(1*H*-pyrrol-3-yl)propan-1-amine
(aq.)	Aqueous solution
ABA	4-Aminobenzylamine
Ac_2O	Acetic anhydride
AcOEt	Ethyl acetate
ACN	Acetonitrile
Acr	Acrylamide
An	Aniline
APS	Ammoniumpersulfate
ATR FT-IR	Attenuated total reflectance Fourier transform infrared spectroscopy
Boc_2O	Di-*tert*-butyl dicarbonate
CDCA	Chenodeoxycholic acid
CNT	Carbon nanotube
CV	Cyclic voltammetry
dba	Dibenzylideneacetone
DBU	1,8-Diazabicycloundec-7-ene
DCM	Dichloromethane
DFT	Density functional theory
DMAP	4-Dimethylaminopyridine
DMF	*N*,*N*-Dimethylformamide
DMSO	Dimethylsulfoxide
DRS	Diffuse reflectance spectra
DSC	Differential scanning calorimetry
DSSC	Dye-Sensitized Solar Cells
EADS	Evolution associated decay spectra
EDC-CI	*N*-(3-Dimethylaminopropyl)-*N*'-ethylcarbodiimide hydrochloride

EDOT	Ethylenedioxythiophene
EDS	Equilibrium degree of swelling
EDTA	Ethylenediaminetetraacetic acid
EIS	Electrochemical impedance spectroscopy
ESEM	Environmental scanning electron microscope
ESI-MS	Electrospray ionization-mass spectrometry
Et_2O	Diethyl ether
EtOH	Ethanol
EtONa	Sodium ethoxide
FMOs	Frontier molecular orbitals
FTO	Fluorine-Tin oxide
GABA	γ-Aminobutyric
HOMO	Highest occupied molecular orbital
HRMS	High-resolution mass spectrometry
ICT	Intramolecular charge transfer
$ImBF_4$	1-Butyl-3-methylimidazolium tetrafluoroborate
IPCE	Incident photon-to-current conversion efficiency
IPN	Multipolymer interpenetrating polymeric hydrogel
IR	Infrared
ITO	Indium-Tin oxide
LDA	Lithium diisopropylamide
LFE	Light-to-fuel efficiency
LUMO	Lowest unoccupied molecular orbital
MBA	*N*,*N*'-Methylenbis(acrylamide)
MeOH	Methanol
min	Minutes
MS-4Å	Molecular sieves – 4 angstrom
NBS	*N*-Bromosuccinimide
***n*-BuLi**	*n*-Butyllithium
NHE	Normal hydrogen electrode
NIR	Near infrared
NIS	*N*-Iodosuccinimide
PAA	Polyamidoamine
PAm	Polyacrylamide

PAn	Polyaniline
PE	Petroleum ether
PEDOT	Polyethylenedioxythiophene
PEG	Poly(ethylene glycol)
PEHA	Pentaethylenehexamine
PHEMA	Poly(hydroxyethyl methacrylate)
PPy	Polypyrrole
ProDOT	Propylenedioxythiophene
PSS	Polystyrenesulfonate
PTh	Polythiophene
PVA	Poly(vinyl alcohol)
Py	Pyrrole
PyBOP	Benzotriazol-1-yl-oxytripyrrolidinophosphonium hexafluorophosphate
PV	Photovoltaics
RHE	Reversible hydrogen electrode
SED	Sacrificial electron donor
ss.	Saturated solution
TBAF	Tetrabutylammonium floride
TBAS	Tetrabutylammonium hydrogensulfate
TBP	4-*tert*-Butylpyridine
TBTU	2-(1*H*-Benzotriazole-1-yl)-1,1,3,3-tetramethylaminium tetrafluoroborate
TCO	Transparent conductive oxide
TD-DFT	Time dependent – density functional theory
tEGDA	Triethyleneglycolediacrylate
TEOA	Triethanolamine
TFA	Trifluoroacetic acid
TGA	Thermogravimetric analysis
THF	Tetrahydrofuran
TIPS	Triisopropylsilane
TMEDA	Tetramethylethylenediamine
TMPA	Trimethylphenylammonium chloride
TOF	Turnover frequency
Tol	Toluene
TON	Turnover number

UV-Vis	Ultraviolet-visible
XPS	X-ray photoelectron spectroscopy

General experimental remarks

All air-sensitive reactions were performed under inert atmosphere in a flame- or oven-dried apparatus using Schlenk techniques.[1] Tetrahydrofuran (THF) was distilled over metallic sodium in the presence of benzophenone, DCM was distilled over CaH_2, toluene, diethyl ether and acetonitrile were dried on a resin exchange Solvent Purification System (*MBraun*). 1,2-dichloroethane, was dried by storing under nitrogen over 4 Å molecular sieves. Aniline and pyrrole were freshly distilled over CaH_2 under reduced pressure and stored under nitrogen, according to the reported procedures.[2] Triethylamine was distilled over CaH_2 according to the reported procedure.[2] Triethylene glycol was kept for 2 days over 4 Å molecular sieves, then distilled under reduced pressure and stored under nitrogen over 4 Å molecular sieves in the drier, according to the reported procedure.[2] Dye **DF15**, **MB25**, **MM62**, **MB56**, **AD418** were prepared according to published procedures.[3,4] **MK-2**, **ABA** and all other chemicals employed were commercially available and used as received. Petroleum ether was the 40-60 °C boiling fraction. Thin-layer chromatography was carried out on aluminum-supported Merck 60 F254 plates; detection was carried out using UV light (λ = 254 and 365 nm) and permanganate followed by heating. Flash column chromatography was performed using Merck Kieselgel 60 (300-400 mesh) as the stationary phase. ^{1}H-NMR spectra were recorded at 300 or 400 MHz, and ^{13}C-NMR spectra were recorded at 75.5 or 100.6 MHz, respectively, on *Bruker* Avance or *Varian* Mercury series instruments. Chemical shifts were referenced to the residual solvent peak ($CDCl_3$, δ 7.26 ppm for ^{1}H-NMR and δ 77.16 ppm for ^{13}C-NMR; C_6D_6, δ 7.16 ppm for ^{1}H-NMR, δ 128.06 ppm for ^{13}C-NMR). FT-IR spectra were recorded with a *Perkin-Elmer Spectrum BX* instrument in the range 4000-400 cm^{-1} with a 2 cm^{-1} resolution. ESI-MS spectra were obtained by direct injection of the sample solution using a *Thermo Scientific* LCQ-FLEET instrument and are reported in the form *m/z* (intensity relative to base = 100). HRMS spectra were measured using a Thermo Scientific LTQ Orbitrap (FT-MS) instrument and are reported in the form m/z. UV-Vis spectra were recorded with a *Varian Cary* 400 spectrometer and a *Shimadzu* 2600 series spectrometer, and fluorescence spectra were recorded with a *Varian Eclipse* instrument, irradiating the sample at the wavelength corresponding to maximum absorption in the UV spectrum. UV-Vis spectra of the compounds on TiO_2 were recorded in transmission mode after sensitization of thin, transparent semiconductor films. ATR-IR spectra of sensitized TiO_2 powders were recorded with a Shimadzu model IRAffinity-1 in the range 4000-800 cm^{-1}. XPS experiments were carried out with a Thermo Scientific K-Alpha X-ray photoelectron spectrometer equipped with an aluminium X-ray source (energy 1486.6 eV) at a base pressure of 10^{-8}–10^{-9} mbar. The X-ray beam spot size was ≈ 400 µm. All spectra have been referenced to C1s adventitious carbon at 284.8 eV. The peak fitting was performed with constraints on the full width half maximum (FWHM) and the peak-area ratio of the spin-orbit components. The lyophilisation was performed at 150 mT for 16h at r.t. with a VirTis BenchTop Pro (SP Scientific).

1 Shriver, D.F.; Dredzon, M.A. "*The Manipulation of Air-Sensitive Compounds*", John Wiley & Sons, Hoboken, **1986.**

2 Armarego, W.L.F.; Chai, C.L.L. "*Purification of Laboratory Chemicals 5th Editions*", Butterworth-Heinemann, Elsevier Science, **2002**.

3 Franchi, D.; Calamante, M.; Reginato, G.; Zani, L.; Peruzzini, M.; Taddei, M.; de Biani, F. F.; Basosi, R.; Sinicropi, A.; Colonna, D.; Carlo, A. D.; Mordini, A. *Tetrahedron* **2014**, *70*, 6285.

4 Dessì, A; Monai, M.; Bessi, M.; Montini, T.; Calamante, M.; Mordini, A.; Reginato, G.; Trono, C.; Fornasiero, P.; Zani, L. *ChemSusChem* **2018**, *11*, 793.

Matteo BESSI

Development of new highly conjugated molecules and their application in the field of renewable energy and biomaterials

Résumé

Ces dernières années, les matériaux fonctionnels hybrides ont commencé à être employés pour des applications de la haute technologie, allant des senseurs bio/médicaux, à la production d'énergie renouvelable. Pour cette raison, ils sont devenus le centre de plusieurs études dans le domaine des sciences des matériaux. Simultanément, des molécules conjuguées ont été examinée intensément à cause de leurs propriétés venant de leurs longs systèmes π, allant de la possibilité de conduire l'électricité, à leur capacité d'absorber la lumière dans une grande fenêtre spectrale. Le travail de cette thèse se concentre sur l'introduction de tels systèmes dans deux sortes de matériaux hybrides, les dispositifs photovoltaïques pour la production d'électricité (en particuliers les cellules solaires à pigment photosensible) et de carburants alternatifs (hydrogène), et pour les hydrogels biocompatibles sensibles aux stimuli (capables de conduire l'électricité et de réagir sous irradiation), et sur l'étude de leur influence sur les caractéristiques du matériau final.

Mots-clés: cellules solaires à pigment photosensible, pigment organique, production d'hydrogène, photocatalyse, spectroscopie d'absorption transitoire, hydrogel, sensibles aux stimuli, polymère conducteur, sensible à la lumière, fullerène

Résumé en anglais

In recent years hybrid functional materials began to be employed in a series of technologically advanced applications spanning from bio/medical sensors, to renewable energy generation. For this reason, they became the focus of several studies in the field of materials science. At the same time, conjugated molecules have also been intensively investigated, due to the properties arising by the presence of long π-conjugated systems, from the possibility to conduct electricity to the ability to absorb light in a wide range of wavelengths. This PhD work focused on the introduction of such systems in two different kinds of hybrid materials, namely photovoltaic devices for the production of electricity (in particular Dye Sensitzed Solar Cells) and alternative fuels (hydrogen), and biocompatible stimuli-responsive hydrogels (capable to conduct electricity and to react upon irradiation), and on the study of their influence on the characteristics of the final material.

Keywords: dye sensitized solar cells, organic dye, hydrogen production, photocatalysis, transient absorption spectroscopy, hydrogel, stimuli-responsive, conductive polymer, light-responsive, fullerene